SCUFFING AND WEAR OF ENGINEERING MATERIALS UNDER DIFFERENT LUBRICATION REGIMES IN THE PRESENCE OF ENVIRONMENTALLY FRIENDLY REFRIGERANTS

BY

EMERSON ESCOBAR NUNEZ

DISSERTATION

Submitted in partial fulfillment of the requirements
for the degree of Doctor of Philosophy in Mechanical Engineering
in the Graduate College of the
University of Illinois at Urbana-Champaign, 2010

Urbana, Illinois

Doctoral Committee:

Professor Andreas A. Polycarpou, Chair
Professor Pascal Bellon
Emeritus Professor Thomas F. Conry
Associate Professor Spyros I. Tseregounis

ABSTRACT

In recent years, the air-conditioning industry has been focusing on alternative refrigerants for the replacement of hydrofluorocarbons (HFCs) due to environmental regulations. HFCs refrigerants have been widely used in the refrigeration industry since the early 1990's as replacement to chlorofluorocarbon (CFCs) refrigerants that were non-flammable and non-toxic, but posses a high ozone depletion potential (ODP). Despite the fact that HFCs have zero ODP, they were found to have a high global warming potential (GWP) being considered one of the green house substances to be banned by the Kyoto agreement. The interest for long term solutions has been towards natural refrigerants. Among different natural refrigerants such as water, air, and ammonia, carbon dioxide (CO_2, R744) is an attractive and possibly the most viable candidate. Although, CO_2 is a non-flammable and non toxic natural refrigerant (being not the case for Hydrocarbons and Ammonia), one of the main drawbacks related to its implementation as a refrigerant in air-conditioning compressors has to do with the high operating working pressures. These working pressures can be around 5 to 6 times higher compared to HFCs systems. One of the important aspects in the design of an air-conditioning compressor is the understanding of the miscibility and solubility of the lubricant and the refrigerant. The incomplete miscibility and solubility of CO_2 with commonly used lubricants in the vapor compression cycle affects the way the lubricant is transported out of the refrigeration circuit. Also, when miscibility and solubility is incomplete, the lubricant accumulates in the system causing pressure drops (especially in the evaporator). Appropriate lubrication of the critical components of the compressor becomes important as the demands for higher efficiency increases. Control of the wear of these components has to be ensured in order to guarantee appropriate

operation of the compressor over a prolonged period of time. Scuffing is another important aspect to be addressed in the design of compressors. This is considered a severe adhesive type of failure that renders the tribocontacts non functional. Interaction of the lubricant, refrigerant, and materials, plays an important role on the scuffing performance since tribochemical reactions might improve or lower the wear resistance at the sliding interfaces. Studies on CO_2 as an alternative refrigerant for air-conditioning systems has been mainly focused on the thermodynamical aspects to ensure that the efficiency and cost will make it suitable as a replacement to HFCs. However, research on the tribological aspects of CO_2 with lubricants and engineering materials is scarce.

The aforementioned drawbacks related to the circulation of lubricant and refrigerant in the refrigeration circuit has raised the possibility of design and development of oil-less compressors. In this direction, it is imperative to design advanced materials able to withstand aggressive sliding conditions in the absence of lubricant.

This research focuses on the study of the friction and wear behavior of different materials and lubricants in the presence of CO_2 for air-conditioning and refrigeration compressors. Bare materials and soft polymeric type of coatings were studied in the presence of lubricants and environmentally friendly refrigerants to understand the role of tribochemistry by using a range of analytical tools that provide answers of the scientific aspects during the characterization of friction and wear.

ACKNOWLEDGEMENTS

I want to thank my advisor Andreas Polycarpou for his continuous motivation, encouragement, challenges, guidance, and endless support during my doctoral studies at Illinois. Professor Polycarpou endorsed me as part of his research group; he opened to me the doors of the field of Tribology which by the time I started my studies was completely unknown to me. He gave me the best advice any single graduate student can ask for, he embraced the opportunity to discover the unknown, he was tolerant and patient with my ignorance, and thanks to his guidance I polished my research skills on a way I could have never imagined when I just started my doctoral studies. I have to admit that most importantly he was like a father in many different aspects during my studies.

To the Fulbright commission and Universidad Autónoma de Occidente for their financial support throughout my doctoral studies in the USA.

I would also want to thank some of the alumni and current graduate students of the Microtribodynamics research group. I want to thank Nick Demas for being the first person to teach me many different aspects of experimental work. We exchanged many ideas in the laboratory and became friends during the last stage of his studies. To Raja Katta who was always kind, helpful, and patient. He gave me a lot of motivation on the most difficult situations of my doctoral studies. To Kyriaki Polychronopoulou who was very helpful and diligent on the chemical analysis and discussions of my work. To Seung Min Yeo, a very promising young graduate student whom I had the opportunity to learn and work with. We spent many hours in the office discussing different aspects of research and life in general. To Jung Kyu Lee, Melih

Eriten, and Antonis Vakis who gave me daily motivation in many different ways to finish my studies.

I would like also to thank the Air Conditioning and Refrigeration Center (ACRC) at the University of Illinois for their financial support through out my studies. To Warner Wagner and Kurt Wagner from Wagner Machine Co., for their cleverness in the design of many different components we used in the experimental setups in the laboratory. They were always efficient and helpful in many different situations. I would also want to express my gratitude to Forest Carignan and Alan Walsh from AMTI who were of valuable help in the fixing and updating of the Ultra High Pressure Tribometer.

I want to thank my parents for their invaluable support. They are the light of my life; they taught me how to be persistent, perseverant, and hard worker. They taught me values and the most elemental tools to achieve any single dream in my life. Finally, I want to thank my sisters who were always a source of motivation and support through out my studies.

TABLE OF CONTENTS

LIST OF FIGURES

LIST OF TABLES

LIST OF SYMBOLS AND ABBREVIATIONS

AES	auger electron spectroscopy
ACT	active control tuning
A_n	nominal contact area
ASTM	american society for testing and materials
FIB	focused ion beam
F_x	tangential force in the x direction
F_y	tangential force in the y direction
F_z	Normal force in the z direction
CFC	chrolofluorocarbon
COP	coefficient of performance
CVD	chemical vapor deposition
ΔV	change of volume of material
DLC	diamond-like carbon
E	Young's modulus
E^*	composite Young's modulus
ECR	electrical contact resistance
EDS	energy dispersive spectroscopy
E_f	activation energy of oxide formation
E_v	activation energy of oxide removal
EHL	elastohydrodynamic lubrication
ϕ	working function (XPS)

GWP	global warming potential
η	dynamic viscosity
η_a	number of asperities per unit area
H	hardness of the softer material of the tribopairs
HFC	hydrofluorocarbon
HFO	hydro fluoro olefin
HPT	high pressure tribometer
K	non-dimensional wear coefficient
k	dimensional wear coefficient
μ	friction coefficient
m	area factor
υ	Poisson's ratio
ODP	ozone depleting potential
OECD	organization of economic cooperation and development
P	ideal gas pressure
P	nominal contact pressure
p	nominal bearing pressure
PAG	polyalkylene glycol
PEEK	polyether ether ketone
PID	proportional integral derivative
POE	polyolester
P_r	Reduced pressure
PTFE	polytetrafluoroethylene

R	ideal gas constant
R_f	rate of oxide formation
Rq	root mean square
R_r	rate of oxide removal
R-134a	tetrafluoroethane
RH	relative humidity
RMS	root mean square
RPM	revolutions per minute
s	sliding distance
S_c	core void volume
S_m	material volume
S_{sk}	skewness
SAE	society of automotive engineers
SEM	scanning electron microscope
T	ideal gas temperature
T	absolute temperature
T_g	glass temperature
T_R	reduced temperature
TOF-SIMS	time of flight
UHPT	ultra high pressure tribometer
UHV	ultra high vacuum
V	ideal gas volume
V	sliding velocity

w	wear volume
W	normal load
ω	rate of rotation
XPS	x-ray photoelectron spectroscopy
XRD	x-ray diffraction
XRF	x-ray fluorescence
Z	compressibility factor

CHAPTER 1
INTRODUCTION

1.1 Background

Chlorofluorocarbon (CFC) refrigerants made their way as alternative refrigerants in the 1930's solving issues related to flammability and toxicity of refrigerants, thus significantly increasing the demand for refrigeration systems [1]. In 1974 researchers proved that the chlorine present in CFC refrigerants was a main factor in the depletion of the ozone layer [2], which led to the replacement of CFC with hydrofluorcarbon (HFC) refrigerants. However, HFCs refrigerants were also proven to have negative effects to the environment, namely contributing to global warming [3]. CO_2 is an alternative environmentally friendly refrigerant as it has no ozone depleting potential and negligible global warming potential compared to synthetic refrigerants [4, 5]. The fact that CO_2 can be obtained from different industrial processes and be recycled and implemented as a refrigerant, constitutes a great advantage since automatically disregard its contribution to global warming. Even when small amounts of CO_2 are released from air-conditioning compressors (i.e., during maintenance and repair), its contribution to global warming will be insignificant compared to that produced during the burning of fossil fuels (such as coal for energy and transportation) or to that generated by HFCs, which is considered 1000-1900 times higher compared to the same amount of CO_2 delivered into the atmosphere [6]. Although, CO_2 is a non-flammable and non toxic natural refrigerant (being not the case for hydrocarbons and ammonia), one of the main drawbacks related with its implementation as a refrigerant in air-conditioning and refrigeration compressors has to do with the high operating

working pressures. High operating working pressures implies smaller clearances and more expensive components because of the difficulties in sealing [7, 8].

1.2 New alternative refrigerants

Implementation of CO_2 as an alternative refrigerant depends on the ability of solving issues related with the efficiency, compatibility with lubricants, and minor changes or ease in the re-tooling transition in the design of these systems [6]. Among several drawbacks associated with the high working pressures in CO_2 systems, the main issues are related to the ability of finding leaks (resulting in a loss of charge of refrigerant), more expensive components to be used in CO_2 systems compared to R-134a, and manipulation of stiffer hoses in the compact compartment of the engine during maintenance [8]. Despite the fact that new alternative refrigerants have been studied, some of them have not met the evaluation criteria. For instance, according to DuPont® , Fluid H® was found to have zero ozone depletion potential, while DP-1® and JDH® refrigerants were found to be toxic [8]. On the other hand, the newly team-developed DuPont-Honeywell HFO-1234yf ($CF_3CF=CH_2$) refrigerant was found to have the best balance of properties and performance [8]. This hydro fluoro olefin refrigerant has a GWP of 4 being much lower than other common refrigerants (see Table 1.1) [8, 9, 10]. Different rigorous experimental tests have shown that HFO-1234yf has low flammability and it is safe to use in automotive air-conditioning and refrigeration systems as a direct replacement [9]. One of the main advantages of this refrigerant compared to CO_2 is that require similar working pressures compared to R-134a resulting in minor conversion changes in the reconversion of engineering manufacture. In addition, HFO-1234yf has similar cooling performance than R-134a in all climates being an advantage compared to CO_2 which has lower efficiency at high temperature (which results in

more power consumption and more emissions in CO_2 systems) [8]. However, the aforementioned advantages of these have not been proven by independent researchers.

Table 1.1–Ozone depletion potential, global warming potential, and atmospheric lifetime for different refrigerants

Refrigerant	ODP	GWP	Atmospheric lifetime (years)
CO_2	0	1	>500
HFO-1234yf	0	4	11
R134a (HFC)	0	1430	14.6
R22 (HCFC)	0.05	4100	13.3
R12 (CFC)	1	7100	102

Advantages and disadvantages of CO_2 and HFO-1234yf as refrigerants for air-conditioning systems can be seen in Table 1.2, where despite the GWP of HFO-1234yf being higher compared to CO_2, the transition and overall advantages on its implementation seem to be higher [8]. Most of the efforts towards the transition to new alternative refrigerants have been focused on the thermodynamical aspects to ensure that efficiency and cost are comparable or superior compared to current HFCs systems. Available literature on the friction and wear aspects of different materials and lubricants in the presence of CO_2 and HFO-1234yf is scarce.

Figure 1.1 shows a typical pressure-enthalpy thermodynamic cycle of carbon dioxide. It can be seen that in a typical thermodynamic cycle of a CO_2 air-conditioning compressor the operating pressure conditions are approximately 3.5 MPa (~507 psi) and 30 °C at the low pressure side of the compressor and 13.5 MPa (~1957 psi) and 160 °C at the high pressure side. These conditions of pressure are 5 to 6 times higher than in conventional R-134a refrigerant and HFO-1234yf systems.

Table 1.2–Comparison between CO_2 and HFO-1234yf as alternative refrigerants for automotive air-conditioning and refrigeration systems [8]

	CO_2	**HFO-1234yf**
Cooling efficiency	The efficiency of CO_2 systems decreases as temperature increases which results in higher fuel consumption to keep the operation of the compressor	Behaves very similar to R-134a and is considered a global solution since it performs well in hot and warm climates
Compatibility with current A/C equipment	CO_2 systems need significant re-engineering due to the high working pressures	As HFO-1234yf is comparable with R-134a in terms of working pressures, minor changes are needed to be implemented
Safety	Because of the high pressures in CO_2 systems, a careful design has to be made to avoid risk to passengers and maintenance personnel	Despite the fact that SAE tests showed no risk associated with the implementation of this refrigerant, appropriate training is needed to account for its mild flammability
Environmental impact	It has more greenhouse gas emissions compared to HFO-1234yf and R-134a because is less efficient due to the high pressure	According to different tests performed on some of the main capitals its life-cycle climate performance is lower compared to CO_2 and R-134a
Ease of leak detection	Is more difficult to detect because it mixes with air. Requires special methods to detect leaks in the system	Since the working pressure of this refrigerant is similar to R-134a, leak detection can easily be implemented

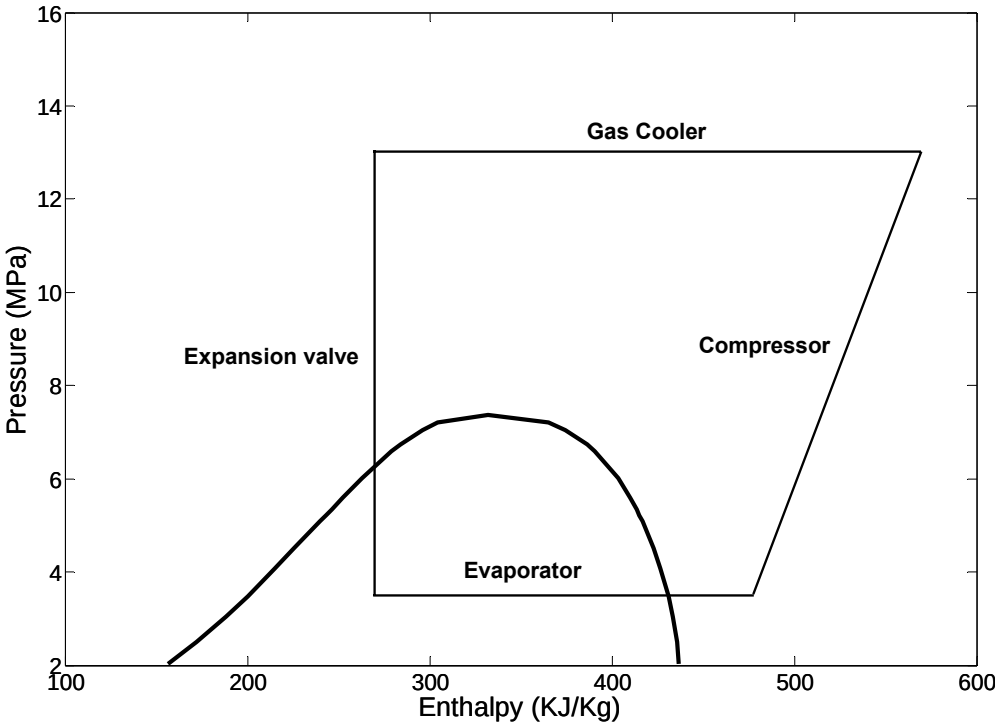

Figure 1.1–Typical thermodynamic operating conditions of a CO_2 air-conditioning system.

1.3 Theories on scuffing

Scuffing is not a well defined phenomenon and there is not much consensus on what its causes and consequences are. In fact, from different known wear mechanisms, scuffing is the least understood one [11]. Some of the experimental observations during scuffing are related to an abrupt increase in friction, vibration, near contact temperature, and noise, which end up rendering the tribopairs non-functional. Salomon and Bolliani defined scuffing as a deviation from Archard's and Amonton's law in the range of sliding speeds between 0.1-2.5 m/s, which corresponds to the transition from mild to severe wear in steel tribopairs [12, 13]. They claimed that during this transition friction coefficient increases from 0.1 to 0.35-0.40 due to the failure of the lubricant film. Similarly, other researchers propose that scuffing is being caused by the destruction of lubricant films under severe conditions of sliding speed and normal load [14, 15].

Ludema [11] defined scuffing as "roughening of surfaces by plastic flow whether or not there is material loss or transfer." One of the most widely used definitions of scuffing, is the one provided by the Organization of Economic Cooperation and Development (OECD) which defined scuffing as "localized damage caused by the occurrence of solid-phase welding between sliding surfaces without local surface melting" [16]. Several hypotheses have been developed to address scuffing phenomena. For instance, Blok was one of the earliest researchers to study scuffing and to propose a hypothesis to explain the experimental observations. In his study he suggested that scuffing would only take place if a critical temperature is reached at the sliding interface [17]. He assumed that the heat flux is applied into an isolated single asperity (mathematical boundary) and also the frictional energy is carried away to the bulk of the sliding tribopairs (rubbing components). Calculations and modeling based on frictional heating are very complex, mainly because of the difficulty of decoupling different parameters that affect the distribution of the heat flux in the bulk of the sliding tribopairs such as thermal conductivity, diffusivity, thermal expansion, and real contact pressure [18]. These parameters might change constantly as a function of the temperature below the sliding interface, which means that considering these thermal properties constant during the sliding process is not accurate [18].

Another hypothesis introduced by Somy Redy et al. in 1994 is the one related to a critical subsurface stress [19]. These researchers investigated the subsurface failure mechanisms in hypereutectic aluminum-silicon alloys observed during scuffing. Based on their experimental results performed under unlubricated conditions, they suggested a ductile type of failure as responsible for scuffing when the shear stress taking place at a critical depth below the sliding interface, surpasses the temperature-dependent shear strength of the material. This hypothesis is

supported by the large plastic flow observed during scuffing [20]. One of the disadvantages of this hypothesis is that does not take into account the load-history.

More recently in 2005, Ajayi and coworkers proposed that scuffing is caused by several events leading to the plastic deformation of the subsurface region (below the sliding interface). They believed this plastic deformation is caused by adiabatic shear plastic instability, which can be explained based on the fact that as the tribopairs experience contact stresses higher than the yield strength, plastic deformation takes place. As sliding continues, deformation will become larger and the density of dislocations will grow as well. As a result, strain hardening will be induced and the work done during the plastic deformation is converted into heat weakening the deformed material. The plastic deformation will become unstable if the rate of weakening (softening) becomes larger than the rate of work hardening. The process is adiabatic due to the fact that the shear instability happens very fast and significant plastic work is present. The absence of the removal of the heat generated will eventually cause an increase in temperature in the region where the shear instability takes place resulting in scuffing [21].

1.4 Air-conditioning and refrigeration compressors

The most common geometries found in air-conditioning and refrigeration compressors include swash plate, scroll, and vane compressors. In a swash plate type compressor (see Figure 1.2) the swash plate connected to the drive shaft moves the pistons back and forth compressing the refrigerant. The 52100 steel shoes transmit the displacement of the incline swash plate to the pistons. The displacement of the pistons can then be modified by changing the inclination of the swash plate. The sliding contact between the swash plate and the 52100 steel shoes is one of the critical tribocontacts, since it constitutes locations more prone to scuff [22]. One of the reasons

why scuffing appears on this location, is related to the fact that under starts and stops of the compressor this tribocontact may have a starved lubrication regime being more susceptible to scuff since most of the contact load is being taken by the contacting asperities. Other causes are related to the solubility of the lubricant and the refrigerant which affects the viscosity of the lubricant reducing its protective role [6].

A scroll type compressor consists of two circular involutes scrolls (one moving and the other one fixed) which are out of phase 180° (see Figure 1.3). This design has several advantages, with the most important ones being; the reduced number of moving parts, reduction in the noise and vibration due to the ease of balancing of the circular involutes. However, one of the main disadvantages is related to the number of cycles of the involutes spiral needed to compress the pocket of refrigerant and raise its pressure to the desired value [23].

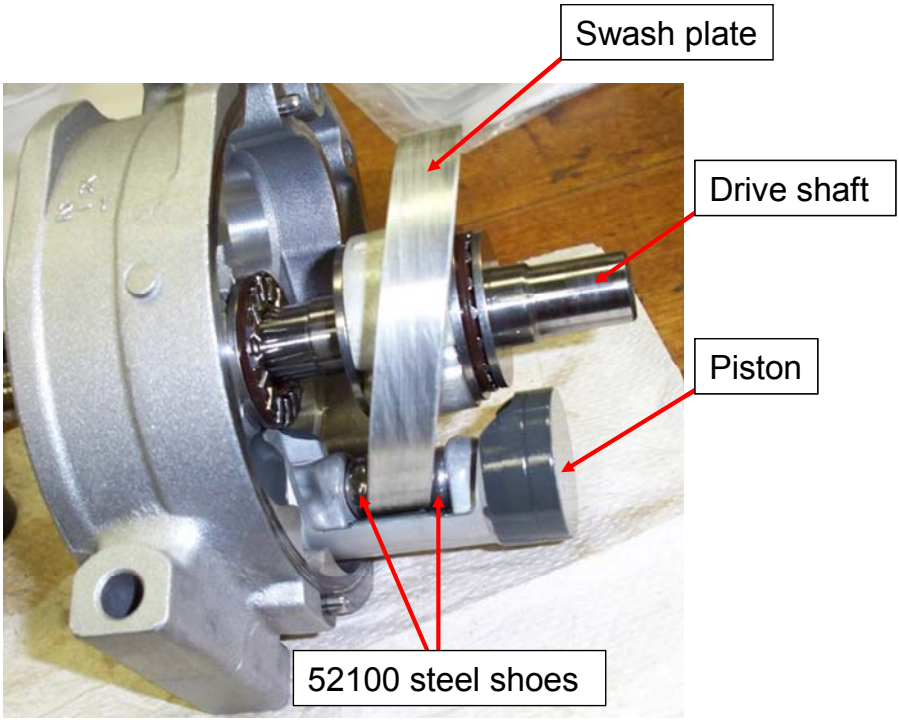

Figure 1.2–Swash plate compressor and some of its components

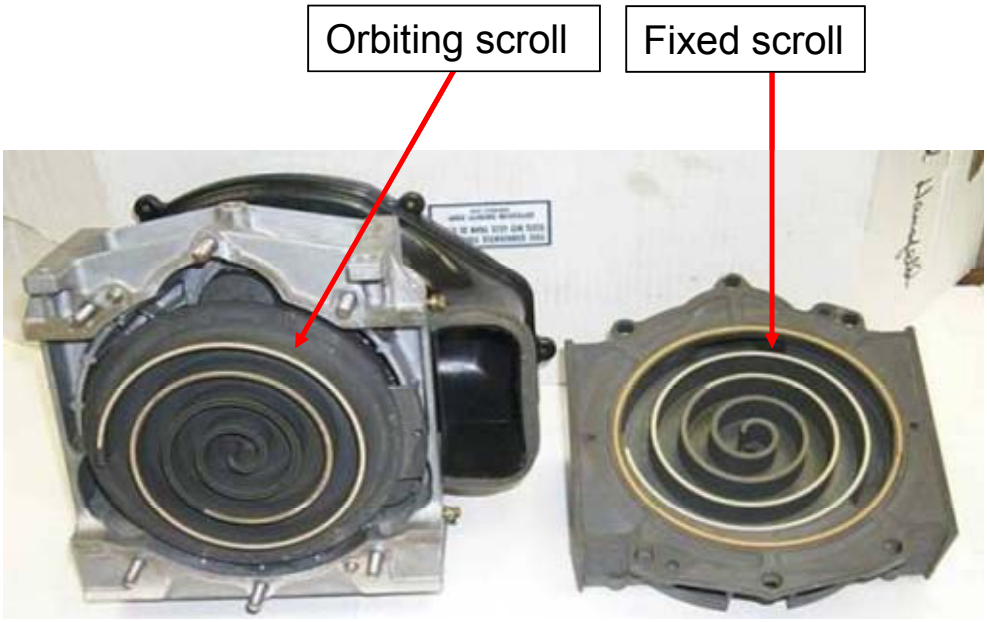

Figure 1.3–Scroll compressor and some of its components [24].

Swash plate and scroll type compressors are prone to scuff making the understanding of friction and wear behavior of their different tribocontacts of critical importance. While Al390-T6 and Mn-Si brass (UNS 67300) are the most common bare materials choices for the plate in swash plate compressors, gray cast iron is the preferable choice for the involute parts in scroll type compressors. Other compressors such as Vane and piston type have similar sliding contact conditions meaning that the tribological studies of this work are more general.

1.5 Tribolayers

Sliding contact of bare materials under unlubricated and boundary mixed lubricated conditions rely on the formation of tribolayers for the prevention of scuffing [25]. The formation of these layers not only depends on the load, but also on the sliding speed and the atmosphere surrounding the tribocontacts [26]. The chemical composition and morphology of such layers, depend on the level of oxidation, plastic flow (or plastic deformation), chemical interaction and

compatibility between sliding materials, and on the way the wear debris are being compressed during sliding [27]. Different researchers have found that the hardness of this layer is higher than the bulk of the material where it is being formed, and can retard the transition from mild to severe type of wear [28, 29]. Also it has been reported that the thickness of these tribolayers can change from nanometers to micrometers depending on the load, atmosphere, and lubrication regime. For instance, an increase in the thickness of a tribolayer from approximately 10 to 70 μm was measured after testing when the load was increased from ~10 to 380 N during testing of A356 alloy against 52100 steel at a sliding speed of 0.8 m/s [29]. By performing tests at high speed and using normal loads in the mild wear regime, a tribolayer 10 times harder than the bulk of A356 was found. However, a tribolayer 2 times harder than the bulk was found when tests were performed at high speed and the normal loads in the severe wear regime. In a different study, it was shown that the thickness of the tribolayers of Al390-T6 tested against 52100 steel in air was of approximately 15 μm having a maximum value of 30 μm. Also, this tribolayer was mainly composed of iron oxides with a hard brittle morphology [30]. In the same study they tested the aforementioned sliding interface under the same parameters of load and sliding speed in Argon atmosphere and showed that the thickness of the tribolayer was more uniform and of approximately 5-10 μm thickness showing less cracks perpendicular to the sliding contact. In addition, the depth of the plastically deformed zone below the tribolayer was 15-20 μm which was lower compared to 40-50 μm depth found in the sample tested in air. Using pins of hypereutectic Al390-T6 against 1018 carburized steel disks under dry sliding conditions in air, other researchers found that the thickness of the tribolayer ranged from 3-30 μm where this thickness was dependant on load and sliding speed [27]. By Auger Electron Spectroscopy (AES) they also pointed out the importance of oxidation in the formation of the tribolayer. It was found

that a rich oxygen tribolayer was formed as a function of depth below the sliding surface. They also showed that the thickness of the plastically deformed region below the tribolayer was of the order of 100-150 μm with microstructural features oriented in the direction of sliding. The boundary between the tribolayer and the plastically deformed region was characterized by a change in angle in the microstructure of the material. Other researchers studied the scuffing behavior of Al390-T6 against 52100 steel shoes under starved lubrication conditions supplying polyolester lubricant (POE) mixed with R410 refrigerant [31]. It was found that the thickness of the tribolayer was less than 1 μm. This thickness was a mix of small silicon particles mixed with the aluminum matrix. The thickness of some of these tribolayers are summarized in Table 1.3 as a function of the tribopair material, lubrication regime, and the product of the nominal contact pressure (P) and the sliding speed (V) [27, 29, 31].

Table 1.3–Thickness of tribolayers as a function of material, lubrication regime, contact pressure (P) and sliding velocity (V)

Tribopair material disk (pin)	**Lubrication regime**	***PV* (MPa.m.s^{-1})**	**Tribolayer thickness (μm)**
1018 carburized steel (Al390-T6)	Unlubricated	8.04	3-30
A356 (52100 steel)	Unlubricated	6.36	30-50
Al390-T6 (52100 steel)	Boundary/mixed	~47	<1

Oxidation plays a very important role in the formation of tribolayers since it protects the surfaces against wear. Research on friction of base metals with asperities covered by oxide films have shown that the sliding distance influence the event of adhesion and junction growth on the

surface [32, 33]. Cutiongco and Chung, proposed that scuffing can be predicted based on the kinetic of oxide formation and oxide destruction. In their scuffing theory, the rate of removal of oxides is higher than the rate at which they are being formed at a certain critical temperature leading to the removal of protective oxide layers and metal adhesion [34]. A different way to express this theory is using the Arrhenius type equations:

$$R_f = v_f \exp^{\left(-\frac{E_f}{RT}\right)} \tag{1.1}$$

$$R_r = v_r \exp^{\left(-\frac{Er}{RT}\right)} \tag{1.2}$$

Where R_f and R_r refer to the rates of oxides formation and oxides removal respectively, the exponential factors E_f and E_r are the activation energies of oxide formation and oxide removal. Other terms in the equation, such as v_f, v_r, R, and T refer to the constant of formation, constant of removal, ideal gas constant, and absolute temperature respectively. According to these equations, scuffing will occur when:

$$R_f \geq R_r \tag{1.3}$$

One disadvantage of this hypothesis is that rates of oxides formation or growth are obtained from static tests, while the rates of oxides removal are acquired from wear tests in vacuum. It was confirmed through experimental data that the rate of formation of oxides can not be used to predict the rate of oxide growth during tribotesting (sliding) [35].

1.6 Lubricants in air-conditioning and refrigeration compressors

Lubricants play an important function in air-conditioning and refrigeration compressors. They allow relative motion between sliding components with reduced friction and wear. Besides reducing friction and wear, other functions of lubricants are related to the removal of heat, inhibition of corrosion, and sealing between moving components [36]. In air-conditioning and

refrigeration systems, the lubricant prevents the occurrence of scuffing and excessive wear in the compressor. Once the lubricant and the refrigerant interact, the mix is carried through out the system and back to the compressor. It has been reported that the presence of lubricant reduces the thermodynamic coefficient of performance (COP) [6]. The ability of a liquid lubricant to reduce friction and wear is mainly dependant on its viscosity. The variation of the friction coefficient as a function of Sommerfeld number (S) is called Stribeck curve (Figure 1.4) and provides information of three different major modes of lubrication [37]. The first mode is called boundary lubrication where there is significant asperity interaction and usually takes place at low Sommerfeld numbers (low speed or low viscosity) with thin lubricant film thickness. The second mode is called partial or mixed lubrication regime, where there is less contact and the number of interacting asperities is reduced. Under this mode (which occurs at intermediate Sommerfeld numbers) a partial fluid film thickness is developed and the sliding surfaces will be partially separated. The last mode of contact takes place at large Sommerfeld numbers and is called hydrodynamic or elastohydrodynamic lubrication. In this mode a full film larger than the combined root mean square (R_q) of the contacting surfaces is developed. Due to the appearance of scuffing and seizure on air-conditioning and refrigeration compressors, it is believed that they work on the boundary/mixed lubrication regime [38]. Natural oils were the only solution to reduce friction and wear until the mid 19^{th} century. However, they suffer from limited viscosity and rapid degradation [39]. Mineral oils on the other hand, have a much wider span of viscosities and more complex chemical structures providing a wider range of viscosities along with the development of chemical additives (anti-oxidants, viscosity improvers, etc). In spite of the fact that chemical additives improve the performance of mineral oils, there are applications where the requirements can not be fully satisfied by mineral oils leading to the design of

synthetic lubricants. Polyolester (POE) and Polyalkylene glycol (PAG) are the most common synthetic lubricants choices in CO_2 air-conditioning systems. In POEs lubricants the presence of the ester group, provides mobility of the lubricant at low temperature, decreases its volatility at high temperature, and provides good absorption on metallic surfaces. PAGs are polymer chains of ethylene and propylene oxides, its chemical structure can be modified in such a way that a great span of viscosities can be obtained. Also, the polarity of PAGs can be changed to make it soluble in different types of media [40].

In air-conditioning and refrigeration systems, the incomplete miscibility of CO_2 with commonly used lubricants in the vapor compression cycle affects the way the lubricant is transported out of the refrigeration circuit [41]. Miscibility of POEs and PAGs is particularly important to avoid accumulation of lubricant in the system. While some research has been reported on the tribological performance of these lubricants under the presence of CO_2, the subject is not completely understood. For instance, a drop in viscosity and subsequent failure of mechanical components in CO_2 compressors lubricated with POE was reported [42]. This drop in viscosity was attributed to the complete miscibility between POE and CO_2. Other researchers documented a failure in a CO_2 compressor lubricated with POE, but reported good performance when the same system was lubricated with PAG [43]. These studies, however, focused on the thermodynamical aspects of the refrigerant-lubricant mixture. Further studies are needed to better understand the tribological performance of PAG and POE in the presence of CO_2 and the new environmental refrigerant HFO-1234yf. Studies on the friction and wear performance of PAGs and POEs lubricants in the presence of CO_2 and tribopairs commonly found in air-conditioning and refrigeration compressors will be studied in this work.

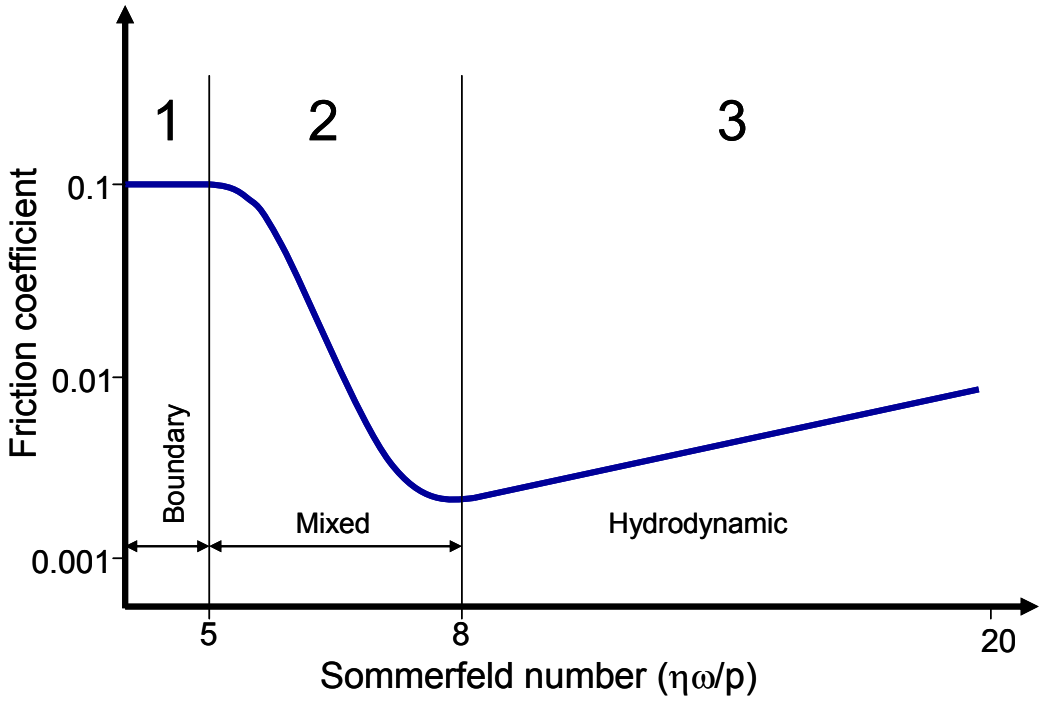

Figure 1.4–Stribeck curve and its three characteristic regions. η is the dynamic viscosity, ω the rate of rotation (rev/s) and p the nominal bearing pressure [37].

1.7 Advanced soft polymeric coatings for oil-less compressors

The air-conditioning and refrigeration industry has been exploring the possibility of oil-less compressors, mainly due to the adverse thermodynamical effects of the liquid lubricant present in the refrigeration circuit. Development of oil-less type compressors requires the search of advanced materials able to withstand unlubricated sliding conditions while keeping friction and wear under acceptable levels. Technological advances on the deposition of polymeric coating materials have found an extraordinary increase in the last decade. Spray gun has made possible to deposit different types of soft polymeric coatings based on Polytetrafluoroethylene (PTFE), Polyether ether ketone (PEEK), and Fluorocarbons onto substrates that posses low surface energy such as gray cast iron. PTFE is characterized by low friction coefficient, but high wear rates. It is believed that the low friction coefficient displayed by PTFE during sliding is

related to the low shear strength of its long -(CF_2-CF_2)- chains [43]. This low friction coefficient along with its high melting point (327 °C) makes this polymer very attractive for unlubricated sliding applications [44]. However, the continuous transfer of PTFE layers to the counterface and its easy removal makes the wear rates of this material unacceptable [45]. PEEK on the other hand, is a thermoplastic polymer that can be blended with PTFE to improve its poor wear performance. The good wear resistance of PEEK can be attributed to its stiff backbone chemical structure and high temperature stability which includes a high melting point (335 °C) and a high glass transition temperature (145 °C) as stated by Blundell and Osborn [46]. Lu and Friedrich showed that friction coefficient and wear rates of blends between PEEK and PTFE have minimum values when the blends are between 10-20% of PTFE [47]. They concluded that 15% partial volume of PTFE was optimum to obtain low values of friction and wear under sliding conditions of 1 m s^{-1} and 1 MPa of contact pressure. They explained that this reduction on friction and wear at 15% volume of PTFE was due to the transfer of a continuous layer to the steel counter face. It was claimed that at this volume a continuous phase of PEEK with PTFE particles was present and the PTFE particles were responsible for the low friction (continuous transfer film) while the PEEK structure still provides good strength and wear resistance. Other researchers found that blended PTFE polymers were suitable for applications where low friction and low wear are required, but only in situations of low normal load [48]. However, on situations of high starting normal loads, PEEK blends where found to be more suitable compared to PTFE blends.

Despite the fact that the studies previously mentioned provide answers of the friction and wear behavior of PTFE and PEEK blends (in bulk form), tribological studies related to the performance of these polymers deposited onto substrates are very limited. For instance, Shaffer

and Rogers found that Xylan® 1014 (a PTFE based polymeric coating) showed a friction coefficient below 0.2 along with a prolonged wear life in a range of temperatures from ambient up to 150 °C under unlubricated conditions [49]. They claimed that this commercially available polymeric coating can be potentially applied to small arm components that require absence of lubricant. Demas and Polycarpou compared the tribological performance of three different commercially available PTFE-based polymeric coatings [50]. Namely, they studied PTFE/pyrrolidone (trade name as Dupont® 958-414), PTFE/pyrrolidone (trade name as Dupont® 958-303), and PTFE/MoS_2 (trade name as Whitford Xylan®). These coatings were coated onto gray cast iron and tested under unlubricated oscillatory conditions. They found that during testing, the thickness of the coating was penetrated and most of the wear took place during the first two minutes of the test. In spite of the fact that the thickness of the different coatings was penetrated, they claimed that the wear debris behaved as a third body and avoided scuffing. In a continuation of the aforementioned study, Dascalescu et al, evaluated the effect of the substrate on the performance of the same three coatings [51]. By using X-ray Photoelectron Spectroscopy (XPS) it was shown that in fact, Whitford Xylan® was the only one of the three different coatings which did not show any sign of scuffing when coated on Al390-T6. They found that metal fluorides formed as a result of fragmentation of PTFE and its interaction with the Al390-T6 substrate had a positive effect on the performance of Whitford Xylan® by improving its adhesion to the substrate. Even though there are some studies on the performance of commercially available PTFE and PEEK deposited coatings, studies dealing with their friction and wear response in the presence of lubricant and refrigerant are scarce. An investigation of the performance of PEEK/PTFE, PTFE/MoS_2, and Fluorocarbon based coatings in the presence of

lubricant under unidirectional conditions will be addressed in the present work to understand the performance of these coatings under harsh sliding conditions.

1.8 Thesis outline

The main objective of this dissertation is to investigate the friction and wear behavior of different material interfaces (bare and soft polymeric coatings) under the presence of different lubricants (namely PAG and POE) and refrigerants (CO_2 R-134a, and HFO-1234yf) as seen in Figure 1.5. To accomplish this objective, each chapter addresses a different aspect of the problem as follows:

a) Chapter two focuses on the instrumentation and experimental conditions employed during tribological testing. The focus is on the description of the technical specifications of the tribometers and the analytical techniques for the chemical characterization of the samples before and after tribological testing.

b) Chapter three presents a direct comparison of the performance of PAG and POE lubricants in the presence of CO_2 using Al390-T6 disks against 52100 steel shoes. Scuffing and wear experiments were performed at different temperatures.

c) Chapter four compares the scuffing and wear performance of three different bare material interfaces (Al390-T6, gray cast iron, and Mn-Si brass) against 52100 steel shoes in the presence of CO_2 under boundary/mixed and submerged lubrication conditions and (using PAG lubricant).

d) The impact of CO_2 pressure and mass on the tribological performance of gray cast iron under unlubricated conditions is addressed in chapter 5.

e) Chapter 6 discusses the friction and wear behavior of four different polymeric coatings based on PTFE, PEEK and Fluorocarbons under boundary/mixed lubricated and unlubrictaed conditions.

f) Chapter 7 will summarize the main findings and ideas for future work.

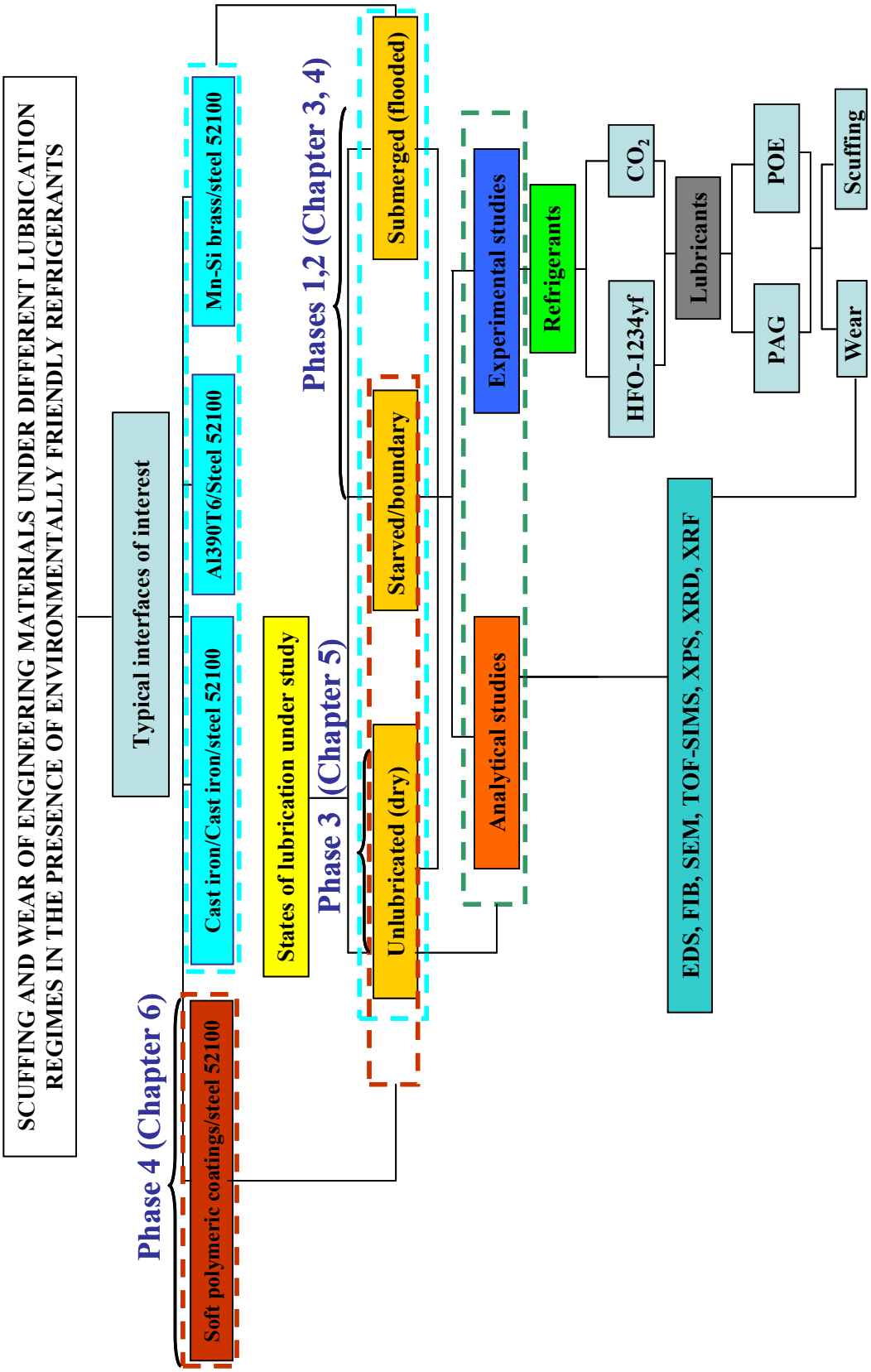

Figure 1.5–Flow chart of PHD studies (chapter 2-6).

CHAPTER 2
INSTRUMENTATION AND EXPERIMENTAL CONDITIONS

2.1 Ultra High Pressure Tribometer (UHPT)

The UHPT is a custom designed equipment for testing at high chamber pressures relevant to CO_2 refrigerant. This machine was specially built for testing of CO_2 at high operating pressures. Compared to the High Pressure Tribomer (HPT) [52], it can be pressurized up to 2000 psi (13.8 MPa). Demas and Polycarpou were the first ones to publish experimental results on testing of CO_2 at high chamber pressures [7]. Conventional refrigerants such as R-134a and the new HFO-1234yf work under working pressures one order of magnitude lower than CO_2 which facilitate their testing on the HPT.

In the UHPT the lower part of the tribometer is hydraulically actuated through a closed loop control system. The UHPT and its components are shown in Figure 2.1 where the testing chamber is composed of an upper rotating part and a lower stationary part. A six axis strain gage force transducers can be mounted on the top of the shaft (covered by the aluminum plate shown in Figure 2.2) and forces on the normal (F_z) and tangential directions (F_x and F_y) can be measured. The friction coefficient can be calculated as:

$$\mu = \frac{\sqrt{(F_x^2 + F_y^2)}}{F_z} \tag{2.1}$$

In the UHPT a thermocouple is inserted up to 2 mm below the surface of the pin to measure the near in-situ contact temperature. This measurement provides information about the thermal heating 2 mm below the sliding interface. Another useful feature on the UHPT is the electrical contact resistance (ECR) which provides information about the regime of lubrication,

formation of protective tribolayers at the sliding surfaces, and indication of metal to metal contact (for instance when the tribolayers are destroyed or coatings are penetrated). The range of the contact resistance is from 10^{-6} to 10^{4} Ω. In situations of boundary/mixed lubrication the contact resistance fluctuates between 10^{-2} to 10^{2} Ω, whereas higher values are expected in the case of submerged lubrication (samples are flooded in lubricant). Indication of penetration of the lubricant film or penetration of the coating will lead to significant asperity interaction and contact resistance values lower than 10^{-2} Ω [52] . Boundary lubrication experiments on the UHPT are performed using a piece of felt inserted in a lubricant reservoir (see Figure 2.3). The lubricant is brought to the surface of the upper rotating disk and the sliding contact by capillarity and centrifugal forces, respectively.

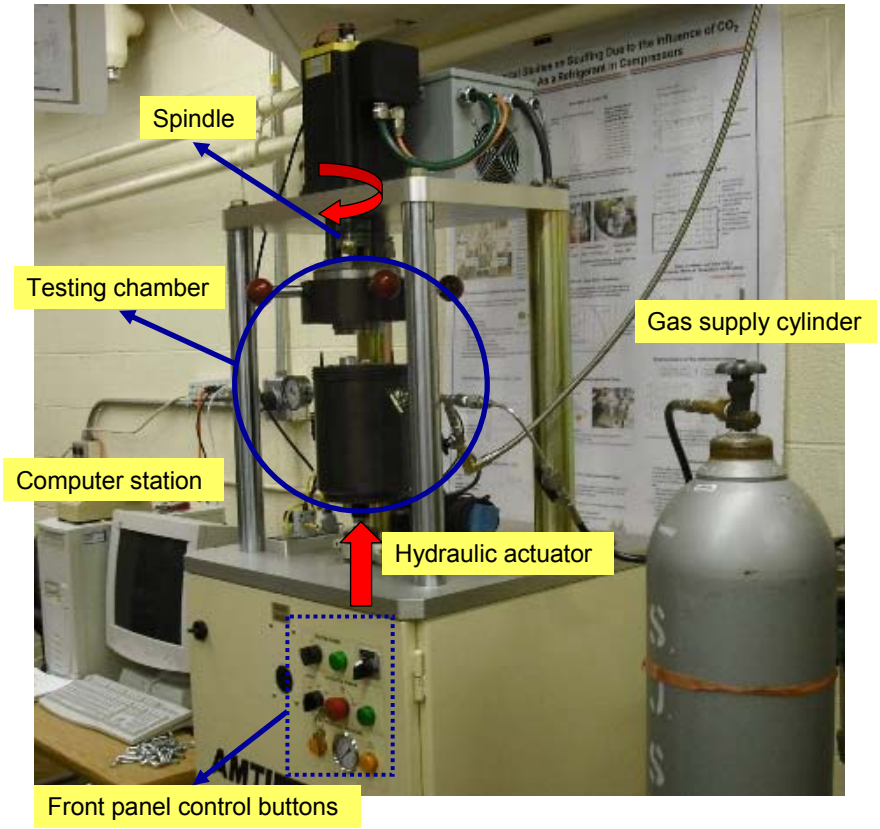

Figure 2.1–Ultra High Pressure Tribomer (UHPT) and its components.

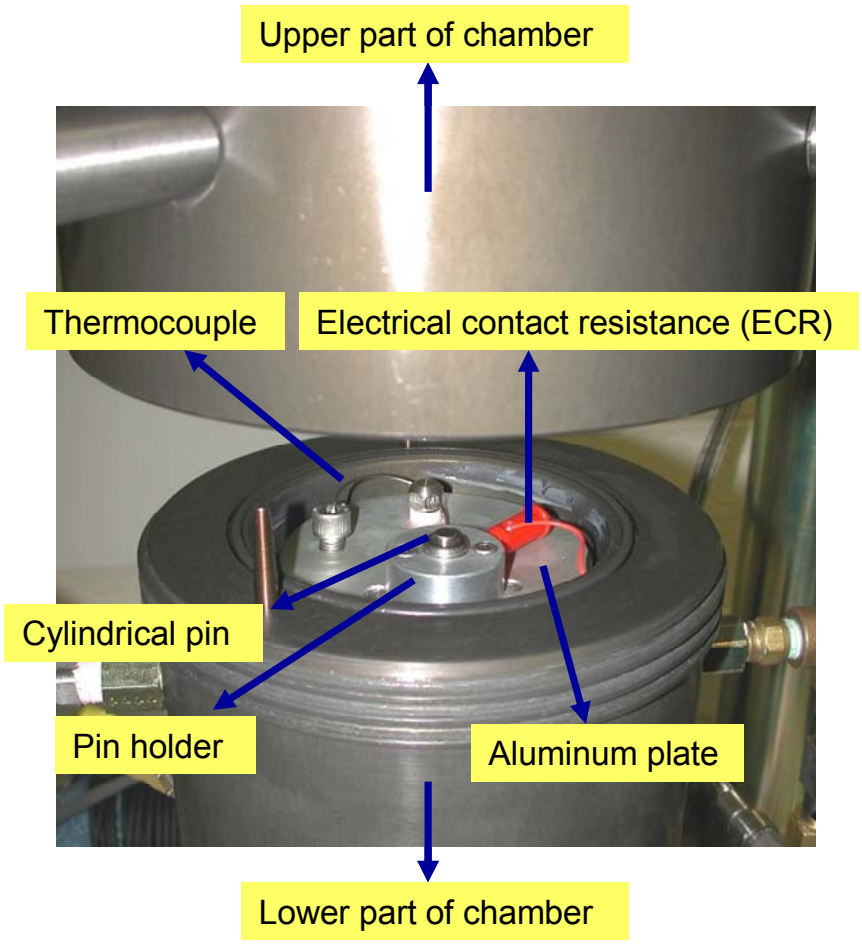

Figure 2.2–View of the testing chamber and its components.

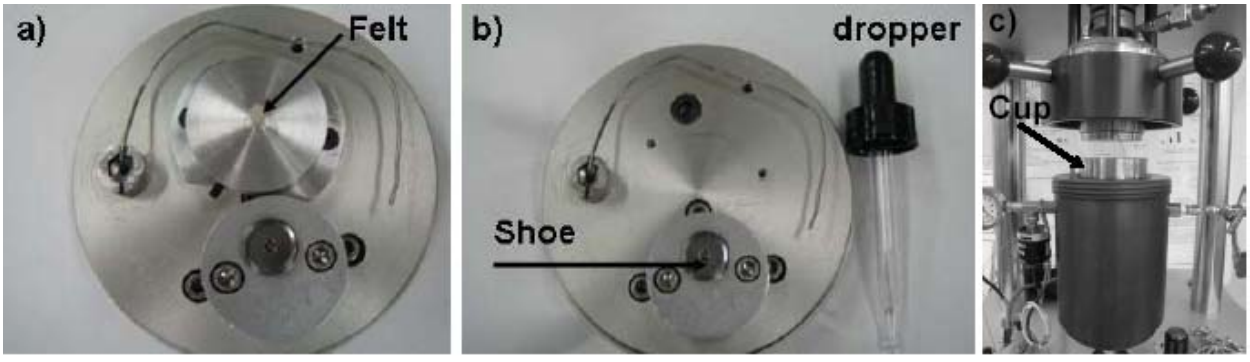

Figure 2.3–Boundary/mixed lubrication device.

The lubricant supply rate is measured by subtracting the weight of the lubricant before and after the experiment and dividing the result by the time duration of the test. Based on trial and error during testing under normal (wear) and step (scuffing) loading, the optimal diameter of the piece of felt to be used was 3/16" (4.76 mm) to obtain a thin lubricant film at the sliding interface. Another way of performing boundary lubrication experiments is by depositing a predefined number of drops of lubricant onto the surface of the pin before initiating a test. However, this method compared to the first one has the disadvantage that does not allow high normal loads and long test durations, reducing the amount of wear that can be obtained on the samples after testing. Under submerged lubrication conditions a removable aluminum cup is used to keep the interface flooded by lubricant during testing. In order to guarantee sealing (or avoid leakage of lubricant), this cup is press fit to the aluminum plate by an O-ring during testing as shown in Figure 2.3c).

In the UHPT, the normal load is controlled through a PID (Proportional Integral Derivative) control loop where the load sensed on the six axis load cell (multi-axis force transducer) is used to drive a servo hydraulic valve which in turn drives a servo hydraulic actuator. The error between the user defined desired waveform (Figure 2.4) and the feedback signal can be corrected by using Active Control Tuning (ACT). This error is measured at many different points along the waveform during one cycle and multiplied by the ACT gain value in the PID file. As a result, the actuator drive signal is modified by the result of the previous calculation and the process is repeated continuously in such a way that each successive waveform is corrected based on the previous one. As can be seen in Figure 2.4, the PID control loop consists of three different parameters. Namely, Kp, Ti, and Td are used to modify the way the user desired wave approaches the feedback signal. From these parameters, the most important one is T_i and K_p which reduce the error between the desired and feedback waves. It is

recommended to use K_p values between 0.4-0.5 during boundary/mixed (222 N~50 lbs) and unlubricated experiments (89 N~20 lbs) using the sensitive transducer (see Table 2.1). In regards to T_i a value of 30000 should be used all the time during testing, while T_d is predefined to zero and usually not modified by the user.

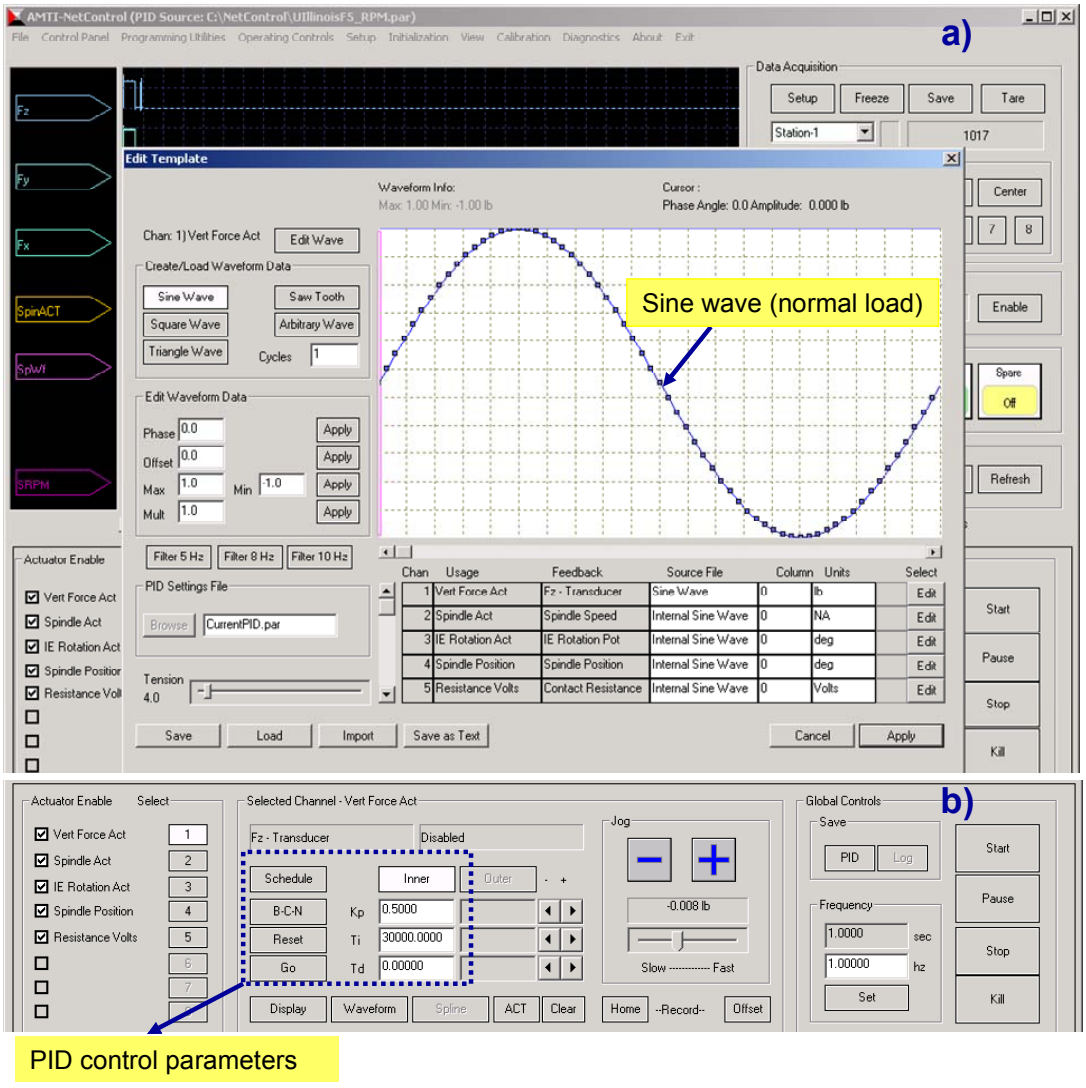

Figure 2.4–Print screen of the Netcontrol software of the UHPT; a) User defined wave form, b) PID control parameters.

In addition, the temperature inside the chamber can be controlled from 0°C to 120°C by recirculation of a heat transfer fluid. Special care has to be taken performing experiments at high

temperature due to thermal fluctuation of the transducer. In order to avoid thermal fluctuation of the normal load, the transducer has to be zero (using the Tare command) before starting a test.

As previously mentioned the UHPT has two different force transducers that can be used to obtain in-situ, friction forces (tangential forces) in the F_x, and F_y directions and normal forces (F_z). The moments produced by these three force components can be obtained from three different components (M_x, M_y, and M_z). A high load transducer should be employed in situations where scuffing resistance wants to be evaluated and situations where the amount of wear after testing under submerged lubrication conditions is under study (in both cases high normal loads are expected to be applied). On the other hand, the sensitive transducer is more suitable for situations where the wear of different materials under unlubricated or boundary/mixed lubrication conditions needs to be obtained. The technical specifications of both transducers are shown in Table 2.1.

Table 2.1–Six-component load cell specifications

Specifications	**Sensitive transducer**	**High load transducer**
Capacity: F_x & F_y, lb (N)	140 (623)	500 (2224.1)
Capacity: F_z, lb (N)	270 (1201)	1000 (4448.2)
Capacity: M_x & M_y, in-lb (Nm)	108 (12.23)	1000 (113)
Capacity: M_z, in-lb (Nm)	73.95 (8.37)	500 (56.5)
Sensitivity: F_x & F_y, µV/[V-lb] (µV/[V-N])	3.0 (0.67)	3.0 (0.67)
Sensitivity: F_z, µV/[V-lb] (µV/[V-N])	0.75 (0.17)	0.75 (0.17)
Sensitivity: M_x & M_y, µV/[V-in-lb] (µV/[V-Nm])	4.0 (35.4)	4.0 (35.4)
Sensitivity: M_z, µV/[V-in-lb] (µV/[V-Nm])	3.0 (26.6)	3.0 (26.6)

In addition, the upper part of the UHPT is controlled by AC servo control motor connected to the spindle by a flexible coupling. Unidirectional and oscillatory type of testing can be performed up to 2000 rpm and up to 10Hz respectively through a user defined routine.

Another tribometer commonly used during wear and scuffing experiments is the High Pressure Tribometer (HPT). A picture of the HPT and the sliding interface is shown in Figure 2.5a) and b) respectively. Tribological experiments can be performed using a sliding configuration where the pin is the lower stationary component and the disk the upper rotating part. The lower pin and upper disk are brought into contact by using a mechanical screw and the stationary lower part is connected to a 6-axis force transducer capable of measuring normal loads from 45 up to 4450 N and friction forces up to 2225 N by strain gages. The spindle (which is driven by a DC servo motor) can be controlled at amplitudes of $\pm 180^{\circ}$ and frequencies up to 5 Hz in the oscillatory mode while 2000 rpm is the maximum rotational speed in the unidirectional mode. The pressure and temperature in the chamber can be controlled up to 1.72 MPa (250 psi) and up to120 °C (with a 0.1 °C accuracy) respectively. Before gas is introduced (or the chamber is pressurized), vacuum can be performed up to 0.1 Torr (13.2 Pa). The temperature of interest during testing can be achieved by recirculating an external heat transfer fluid throughout the hollow spindle. In addition, measurements of the near-contact resistance and near-contact temperature can be also be performed (as in the UHPT) to provide information of the lubrication regime and temperature 2 mm below the sliding interface respectively. The HPT is computer controlled by control boards and solid-state relays, while the Labwindows software provides a different variety of complex load routines and sliding velocities.

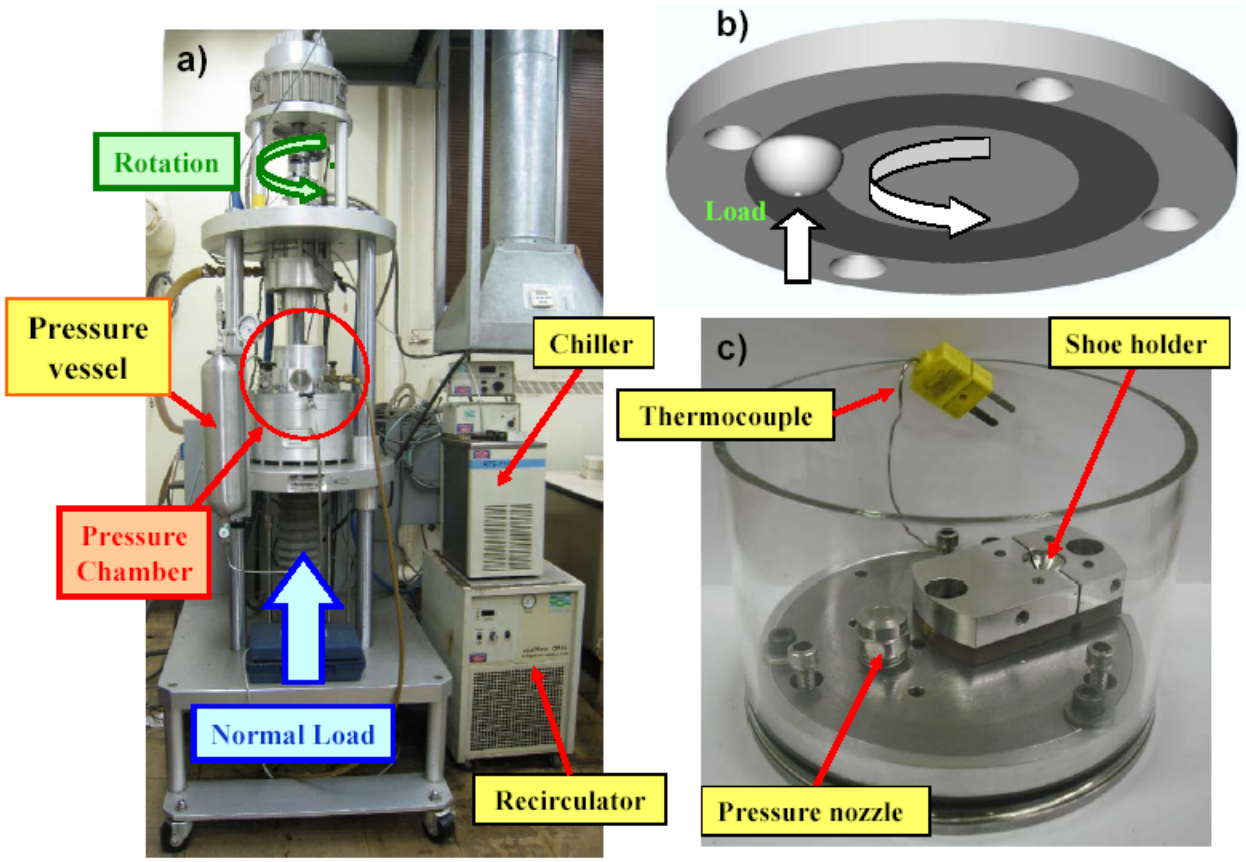

Figure 2.5– a) High Pressure Tribometer (HPT) and its components, b) upper rotating disk, c) lower sample holder.

Two types of experiments can be performed on the UHPT and HPT; namely scuffing and wear tests. In regards to scuffing, there are two methods that can be used to achieve this condition. The first one consists of increasing the normal load in constant steps until a sudden and abrupt change in friction coefficient is reached. The second one consists in measuring the endurance limit or time needed for the samples to scuff for a given set of normal loads and sliding velocities. From these two methods the step-loading is the one more commonly used because of the shorter time needed to achieve the scuffing condition. Through experimental observation is has been found that scuffing follows the relationship:

$$PV = const \tag{2.2}$$

Where P is the nominal contact pressure (scuffing load divided by the nominal area of contact) and V is the sliding velocity [27]. The duration of the step is selected in such a way that scuffing is not affected by temperature and steady state is reached within the step. Scuffing experiments are useful when the maximum resistance up to the point of failure needs to be evaluated. This maximum resistance can be used to compare the performance of different materials, lubricants, and atmospheres during sliding.

Constant load or wear type experiments are used to evaluate the removal of material after testing. During these experiments, the normal load is set constant during a certain period of time and the wear is usually quantified by the amount of mass or volume of material loss after the tests. The wear volume w can be calculated using Archard equation [33] as follows:

$$w = K\frac{W}{H} \tag{2.3}$$

Where K is a non-dimensional constant known as wear coefficient, W the normal load, and H the hardness of the softer material. Since the hardness of the top most layer during the contact may not be known with certainty, usually the dimensional wear coefficient k ($mm^3.N^{-1}.m^{-1}$) is used instead. This can be expressed as:

$$k = \frac{\Delta V}{Ws} \tag{2.4}$$

where ΔV is the change in volume, W is the normal load, and s the sliding distance. Usually wear experiments are performed after the scuffing resistance of the tribopair of interest is known. After that an appropriate set of normal load and sliding speed parameters can be selected to perform the tests.

2.2 Samples and Materials used during tribotesting

Bare materials commonly found in air-conditioning and refrigeration compressors, where used during the studies. Some of these materials where also employed as the substrates to deposit the soft polymeric coatings as will be explained in the last chapter. Three different materials were used, namely; Al390-T6, gray cast iron, and Mn-Si brass. The first one is commonly found in swash plate type compressors, the second one in Scroll type compressors, and the last one is being implemented as a replacement of Al390-T6 in Swash plate compressors. The sample dimensions and chemical composition of the aforementioned materials is listed in Figure 2.6 and Table 2.2. Also, as observed in Figure 2.6 e) and f) the 52100 steel original shoes can be modified to increase the contact stresses and generate more wear during testing.

Table 2.2–Chemical composition of Al390-T6, gray cast iron, and Mn-Si brass (wt %)

Element	**Specified chemical percentage by weight (wt %)**		
	Al-390T6 [28]	**Gray cast iron [31]**	**Mn-Si brass [54]**
Al	76	-	0.01
C	-	3.20-3.70	-
Cu	3.00-4.00	-	60.40
Fe	1.00	Balanced	0.23
Mg	0.40-1.00	-	-
Mn	0.50	0.70-0.80	2.43
Pb	-	-	1.24
Si	16-18.5	2.20-2.55	0.86
Zn	1.00	-	35.58

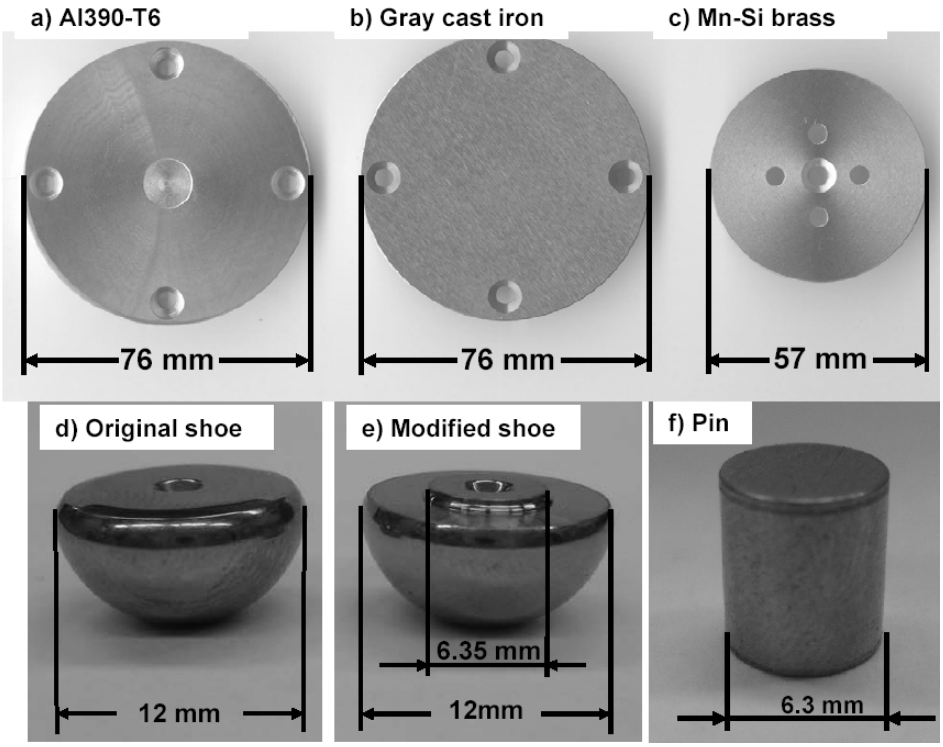

Figure 2.6–Samples used during tribological testing a)-c) disk materials, d)-e) 52100 steel shoes, f) Gray cast iron cylindrical pin 6.5 mm in length.

2.2.1 Al390-T6

The chemical composition of the aluminum alloy used in this study is shown in Table 2.2 [28], indicating that there is a high percentage of silicon (16-18%), which provides good wear resistance. As seen in the Scanning Electron Microscopy (SEM) microphotograph and Energy Dispersive Spectroscopy (EDS) mapping depicted in Figure 2.7a) and Figure 2.7b), respectively, silicon particles in Al390-T6 have a non-uniform morphology: There are primary silicon particles (large dark particles) and eutectic silicon particles (small dark particles) embedded in the Al matrix, Figure 2.7c). Primary silicon particles are responsible for the improvement of the strength of the material and wear resistance, and as measured in [16, 53], their hardness values is 10-12 GPa. The eutectic silicon particles have a more uniform distribution in the matrix than the primary silicon particles, as seen in Figure 2.7a) and Figure 2.7b). Additional elements like

copper (Cu) and magnesium (Mg) forming different phases as seen in Figure 2.7d) and Figure 2.7e) provide additional strength to the alloy. Fe and Mn are not displayed because their percentages are too low to be identified through EDS.

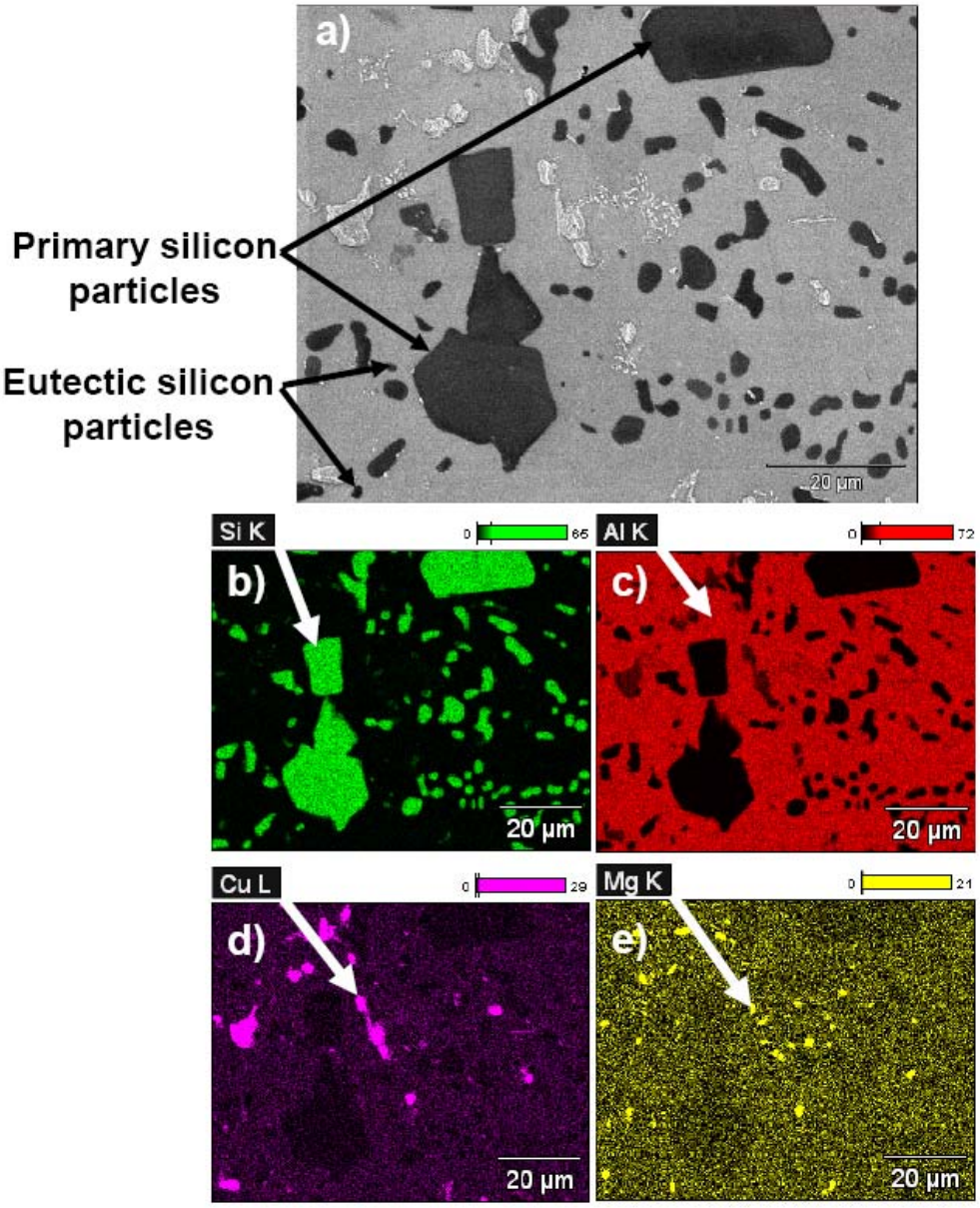

Figure 2.7–a) Surface cross section SEM micrograph of untested Al390-T6 hypereutectic alloy showing primary and eutectic silicon particles, b)-e) EDS mapping showing Si, Al, Cu, and Mg respectively.

2.2.2 Gray cast iron

Gray cast irons are formed by the addition of silicon, which promotes the formation of graphite flakes when its concentration is greater than 1%. Table 2.2 also shows the chemical composition of gray cast iron [31], while Figure 2.8a) and Figure 2.8b) show the microstructure of the pearlitic gray cast iron used in this work. It can be seen that graphite flakes have sharp edges and are surrounded by pearlitic structure where the ferrite phase appears in light color and the cementite in dark color lines.

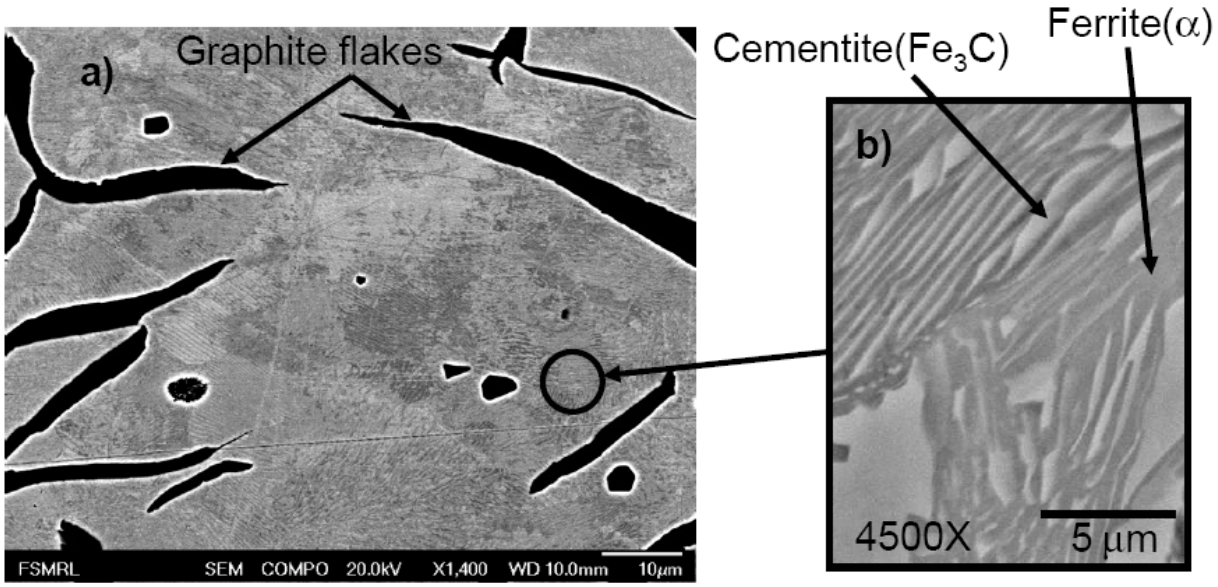

Figure 2.8–SEI surface cross section SEM micrograph of untested pearlitic gray cast iron a) graphite flakes surrounded by pearlitic matrix b) cementite (Fe_3C) light lamellar structure and ferrite (α) dark structure.

2.2.3 Mn-Si Brass

The microstructure of Mn-Si brass consists of a copper rich α soft phase matrix and a manganese silicide phase (Mn_5Si_3) [54] (its composition is also listed in Table 2.2). The low percentage of Al (less than 0.02 %) causes the matrix to be rich in α phase. Silicon increases the wear resistance of Mn-Si brass by forming hard Mn_5Si_3 and improves its performance during

plastic deformation [55]. Primary (longer) and smaller Mn_5Si_3 particles can be seen in Figure 2.9 along with lead (Pb). Pb plays an important role in this alloy since it provides free machining characteristics due to its positive lubricity properties.

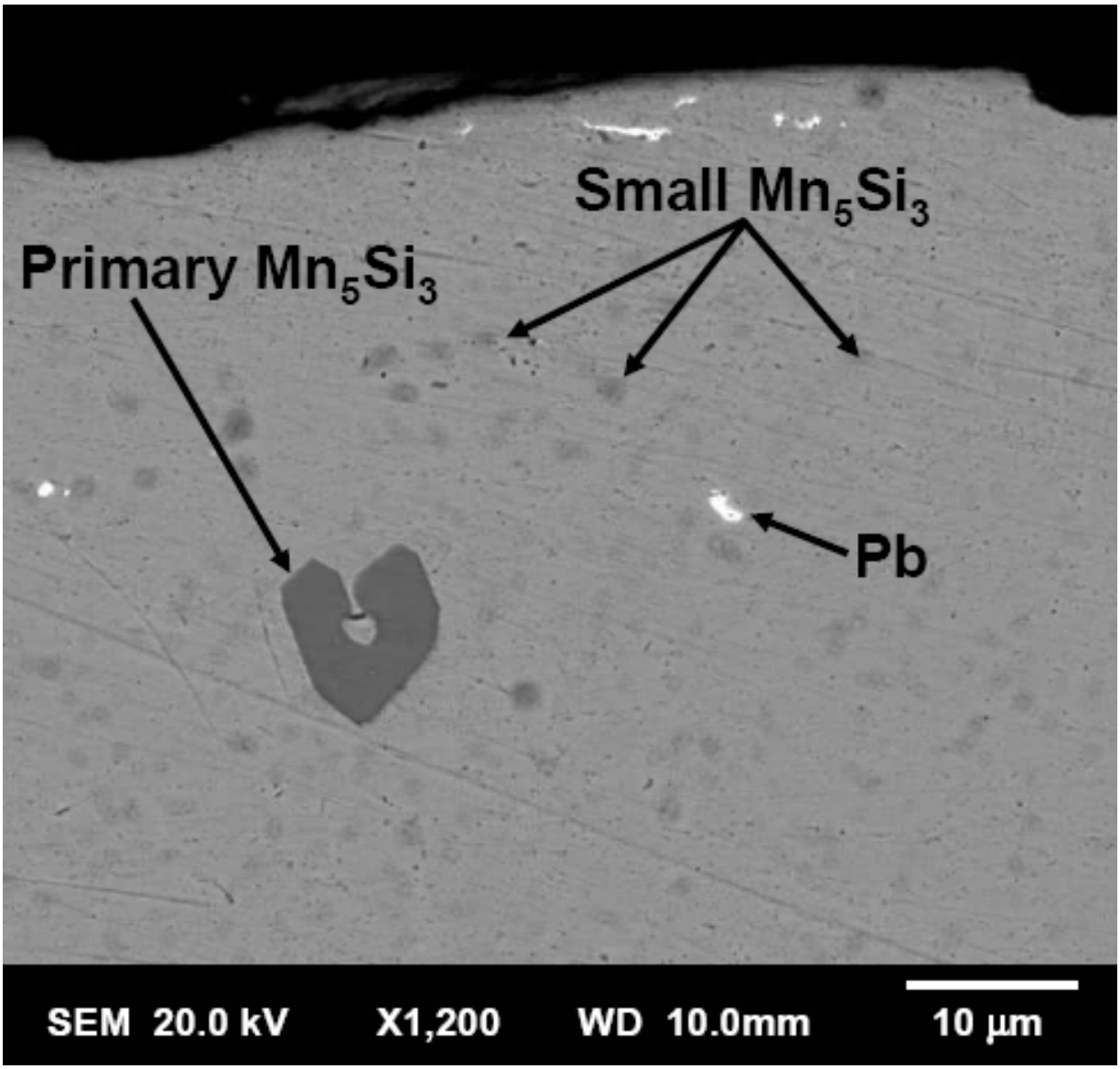

Figure 2.9–SEI surface cross section SEM micrograph of untested Mn-Si brass showing primary and small Mn_5Si_3 particles and lead (Pb).

2.3 Surface analysis techniques

The presence of lubricant or different atmospheres during tribotesting can generate chemical interactions on the sliding surfaces. As a result the topmost layer of the sliding surfaces will be covered by tribolayers composed by adsorbed layers of lubricant, gases, and chemical products due to the interaction of the different surfaces. Different surface and scanning electron microscopy techniques were used during this study and they include: x-ray photoelectron spectroscopy (XPS), time of flight secondary ion mass spectroscopy (TOF-SIMS), x-ray fluorescence (XRF), scanning electron microscopy (SEM), energy dispersive spectroscopy (EDS), and focused ion beam (FIB).

X-ray photoelectron spectroscopy (XPS) is a useful technique to identify surface films in specimens exposed to different types of environments. This technique provides chemical state information from the top nanometer layers of the samples. The principle behind this technique involves the detection of photoelectrons emitted through the adsorption of incident x-rays to the sample. The process involves the transfer of energy from the x-rays to inner shell electrons. As a result the kinetic energy of the emitted photoelectron is equal to that of the x-rays (hv) minus the binding energy of the shell electron, minus the energy required to move an electron from the top of the surface to vacuum *(*working function $\phi_{function}$). This can be expressed throughout the relationship:

$$E_{kinetic} = hv - E_{binding} - \phi_{function} \tag{2.5}$$

Changes in the measured value of the kinetic energy of the photoelectron of 1-10ev denote an alteration of the binding energy (where the electrons were expelled from) and therefore a change in the chemical state. The irradiation of a monoenergetic source on the surface of interest is performed at ultra high vacuum (UHV, 10^{-5}-10^{-6} torr). This source can be composed

of low energy x-rays or electrons. X-rays are typically used due to their lower sample decomposition effect, compared to electrons. From the binding energy and intensity of a photoelectron peak, the chemical state, and quantity of an element are determined. TOF-SIMS compared to XPS is a more sensitive surface technique with higher spatial resolution (1-2 nm) compared to 2-10 nm achieved in XPS. In TOF-SIMS, the time of flight along with the mass of the accelerated secondary ions into the mass spectrometer are measured. This time is measured from the target surface to the analyzer (mass spectrometer). One of the main advantages in TOF-SIMS compared to XPS is that images can be obtained to visualize the distribution of individual species on the surface of interest. XRF compared to XPS uses lower vacuum pressure making this technique useful in the analysis of lubricants (interaction of lubricant, refrigerant, and the sliding tribopairs). SEM was used to study surface morphology before and after testing and EDS for chemical distribution of elements on the polished cross sections of the wear tracks. FIB is useful to measure the thickness of tribolayers after testing. This is done by ion-milling of the surface of interest on the micron range. Another technique used during these studies was x-ray diffraction (XRD). This technique is useful in situations where crystallographic changes of tribopairs take place during testing.

2.4 Surface roughness measurements and analysis

Surface roughness of engineering samples change with tribological testing due to burnishing and wear at the interface. Such changes can be quantified using statistical descriptors calculated from profilometric measurements. The most commonly used amplitude descriptors to characterize surface roughness are the root-mean square and center-line average values. Even though line scans are typically used for these measurements, they do not always capture the variation of surface roughness because the contact at the interface is represented by an area and

line scans do not take into account transverse features. In order to better capture realistic topographical changes in surface roughness, 2D areal scans must be performed. In this work, line scans and detailed 2D areal scans were performed using a contact profilometer (P15-Tencor) as seen in Figure 2.10 a). In general, contact surface profilometers are more accurate but slower than optical profilometers because the shape of the asperities is scanned by a tip in contact with the surface, while optical profilometers rely on imaging techniques that can vary with the reflectivity of the surface [56]. Using the data obtained from the roughness measurements, statistical parameters were extracted in this study. Some of these parameters were calculated from the bearing area curve, which provides valuable information about the topographical changes and fluid retention capacity of surfaces as they undergo burnishing/wear. Three characteristic regions define a bearing area curve when lines at 5% and 80% of the bearing area ratio are drawn, as depicted in Figure 2.10b) [57]. Specifically, these regions are defined as the material volume in the peak zone (Sm) (0-5%), the void volume in the core zone (Sc) (5-80%), and the void volume in the valley zone (Sv) (80-100%). As the sliding interface experiences interaction between contacting asperities, more asperities come into contact. As can be seen in Figure 2.10c) 10% of the bearing area curve means that if a rigid surface is pressed against the deformed asperities, only 10% of the asperities are in contact, distributing the contact pressure. This process will continue until 100% of the asperities are in contact with the rigid surface at 100% of the bearing area curve. Details of these three functional coefficients that characterize material and fluid retention capabilities can be found in Suh et al [58].

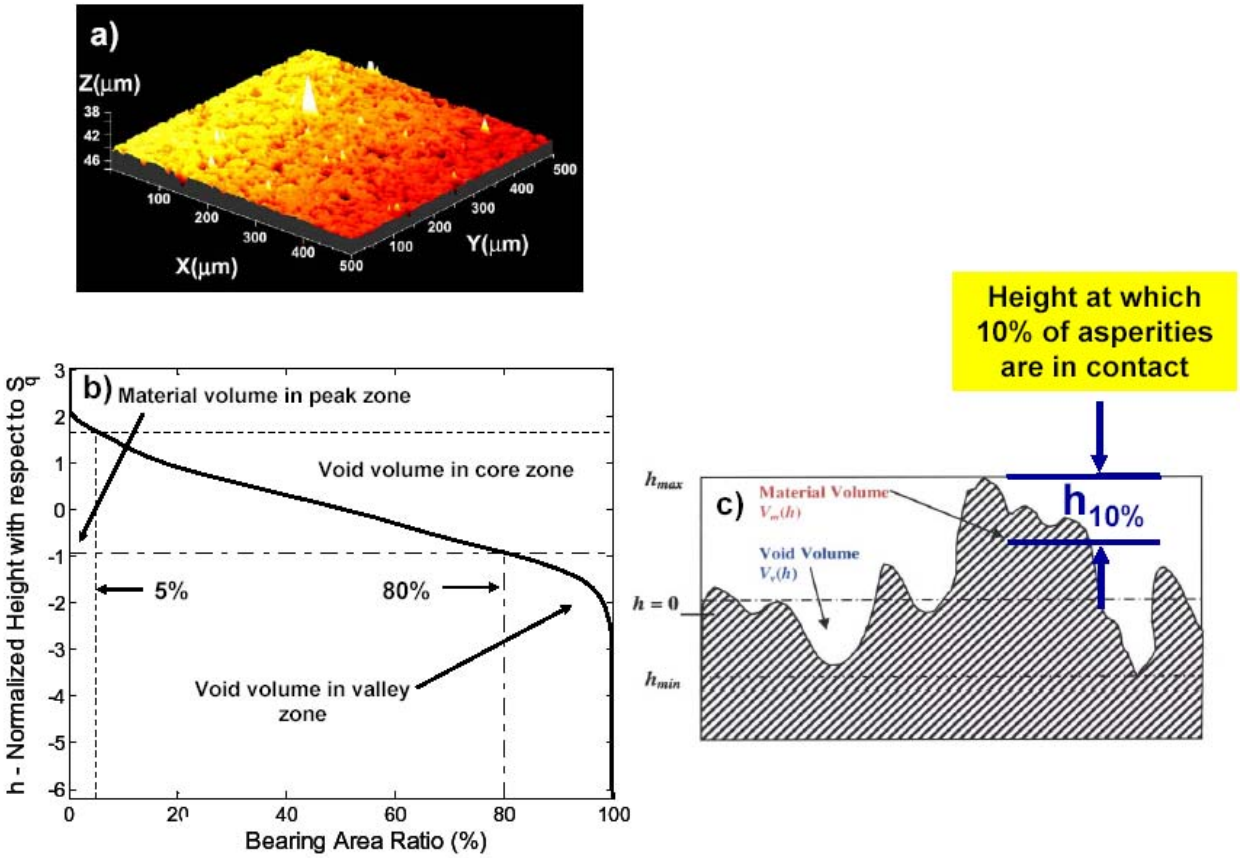

Figure 2.10–a) 2D areal scan, b) bearing area curve with its three characteristic regions, c) representation of the regions on a surface profile

CHAPTER 3
COMPARISON OF PAG AND POE LUBRICANTS USED IN AIR-CONDITIONING COMPRESSORS IN THE PRESENCE OF CO_2

3.1 Background

In air-conditioning systems, understanding the miscibility of CO_2 with polyalkylene glycol (PAG) and polyolester (POE) lubricants is important to design strategies and avoid accumulation of lubricant in the circuit. While some studies related to the tribological performance of these lubricants under the presence of CO_2 are available in the literature [39, 40], the subject is not completely understood. Further studies are needed to better understand the tribological performance of PAG and POE in the presence of CO_2. Chemical structures of PAG and POE lubricants are shown in Figure 3.1a) and b).

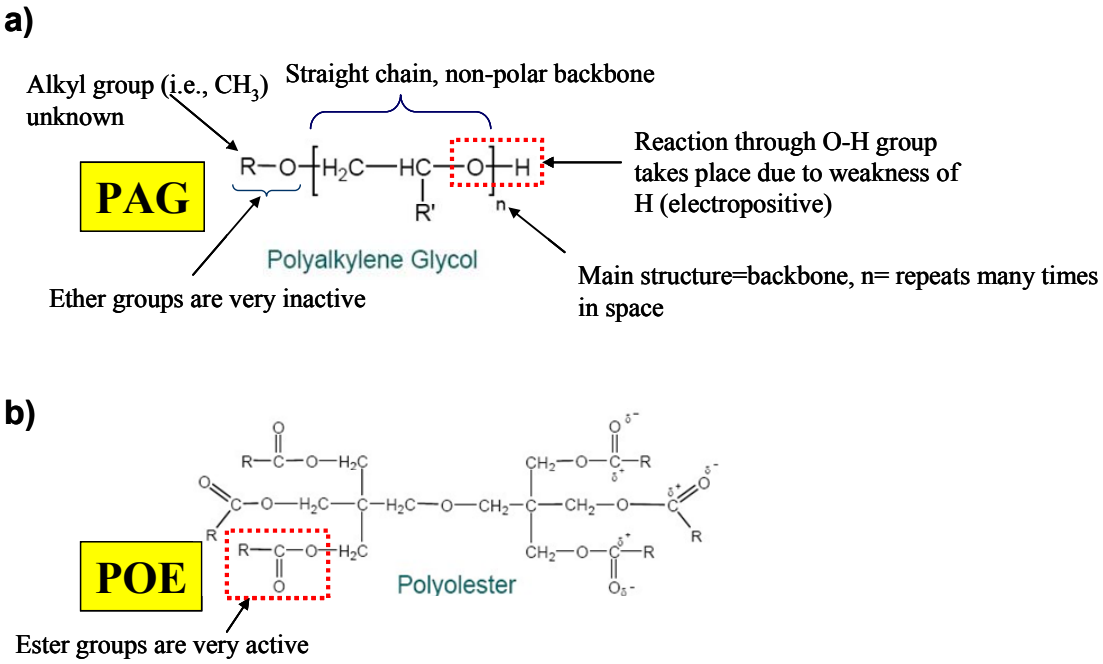

Figure 3.1–Chemical structure of PAG a) and POE b) lubricants.

It is interesting to note that reaction of PAG lubricant with the interacting surface takes place through its ether-oxygen terminal in the backbone (C-O-C), seen in Figure 3.1a), since this terminal is very inactive and weak the mobility of PAG is enhanced. In the case of POE lubricant the carboxylic group (COO^-) of the ester group (see Figure 3.1b)) contributes to the adsorption on the interacting surface because this terminal is very active.

In recent years, boundary lubrication experiments have been used to evaluate the performance of lubricants under the presence of refrigerants [31]. The objective of this chapter is to compare the performance of PAG and POE lubricants using a set of controlled tribological experiments in a CO_2 atmosphere. It is acknowledged that selection of these lubricants for specific applications is based primarily on performance. However, other factors also drive the selection including thermal and hydrolytic stability, compatibility of system materials and cost. The two lubricants were tested using a High Pressure Tribometer (HPT) which is a machine designed to perform tribological tests at high chamber pressures [59]. These experiments were carried out using Al390-T6 disks and SAE 52100 hardened steel pins under starved lubrication conditions. As was previously stated these materials are representative contact pairs commonly found in swash-plate automotive air-conditioning compressors.

Three different sets of experiments were performed to evaluate the scuffing and wear performance of PAG and POE lubricants in a CO_2 atmosphere. In the first and second sets, the scuffing resistance was measured by progressively increasing the load up to the point of scuffing failure at two different temperatures. In the third set of experiments the load was kept constant throughout the test, thus studying the wear performance of the interfaces. In the third set of experiments, the variation of the surface roughness with burnishing/wear was also investigated. Specifically, statistical parameters related to amplitude, as well as bearing area descriptors (such

as lubricant retention indices) were extracted for the untested and burnished samples. Lastly, X-ray Photoelectron Spectroscopy (XPS) measurements were performed to identify chemical changes in the surface of the samples after tribological tests

3.2 Controlled tribological experiments

Using a sliding configuration shown in Figure 3.2, three sets of experiments were performed. In all three sets, two different lubricants, namely, PAG (Idemitsu Kosan Co., Ltd. PZ 68ZL) and POE (Nu Calgon Wholesaler, Inc. RL 68H) were evaluated. The PAG used in this study is oil specifically manufactured for use with CO_2 as a refrigerant while the POE is refrigeration oil for all types of compressors. The actual viscosity of the two lubricants was the same, not the viscosity under CO_2 environment. Under CO_2 pressure the viscosity of the two lubricants would be different as the miscibility/solubility limits are different for the two lubricants. Limited specialized measurements on how the viscosity of the lubricants changes as a function of pressure and temperature have been performed [60]. However such measurements are scarce and specific to lubricant composition, including type of additives.

Experiment sets one and two were scuffing-type experiments (step loading) at room (22 °C) and elevated (90 ^{o}C) temperatures under starved lubrication conditions. The temperature of 90 ^{o}C was selected as this is a typical operating temperature of compressors under idle conditions. The room temperature was selected so that the two lubricants have the same viscosity at that temperature and only the pressure of CO_2 contributes to changes. A small amount of lubricant (40 mg) was applied onto the surface of the shoe (shown in Figure 3.2 b)) at the start of the test. A rotational speed of 1030 rpm, corresponding to a linear speed of 2.4 m/s was used. The CO_2 pressure was kept constant at 1.4 MPa (200 psi) and the normal load was

increased in steps of 67 N every 15 seconds up to the point of scuffing. The scuffing point was characterized by a sudden increase in the friction coefficient leading to scuffing, in which manifests itself via the formation of cold welds between the shoe and disk.

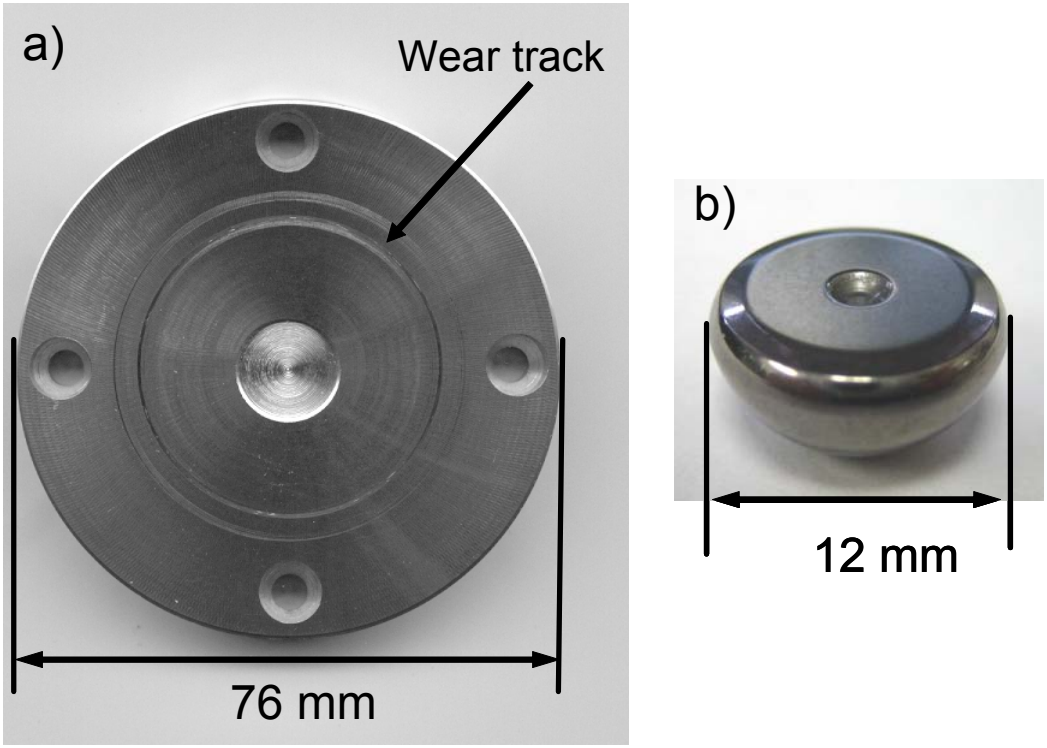

Figure 3.2─Samples used for testing; a) Al390-T6, b) SAE 52100 steel shoe

The third set of starved lubrication experiments was carried out keeping the load constant at 600 N (equivalent to a contact pressure of 6.82 MPa) for 10 minutes. The rotational speed, CO_2 pressure, temperature and amount of lubricant were the same as in the first set of experiments. The conditions of the three sets of experiments are summarized in Table 3.1. In the contact geometry used for these experiments, the shoe was the lower stationary part, while the disk was the upper rotating part. The disk diameter was 75 mm and the shoes had a dimpled geometry with a radius of curvature of 0.3 m [28]. Before initiating a test, the samples were

immersed in a pool of acetone and ultrasonically cleaned, then rinsed with alcohol and dried using warm air. To ensure repeatability each condition was repeated at least twice, and in most cases three times. The root-mean square roughness (Rq) of the samples was also kept approximately constant. Specifically, surface roughness values for Al390-T6 were Rq=0.2-0.4μm determined using 10 mm-long profilometric scans, while the SAE 52100 hardened steel shoes had an Rq=20nm (using 1 mm-long profilometric scans).

Table 3.1–Summary of experimental conditions in the three set of tests

Conditions	**Set 1**	**Set 2**	**Set 3**
Type of experiment	**Scuffing**	**Scuffing**	**Constant Load**
CO_2 Pressure: psi, (MPa)	200 (1.4)	200 (1.4)	200 (1.4)
Temperature (°C)	22	90	22
Step Loading Conditions: N/s	67/15	67/15	-
Constant load: N	-	-	600
Time (s)	-	-	600
Lubricant Amount (mg)	40	40	40
Linear Speed (m/s)	2.4	2.4	2.4

3.3 Experimental results

3.3.1 Controlled tribological scuffing experiments

Typical experimental results of scuffing load and resulting friction coefficient for the first series of scuffing experiments are shown in Figure 3.3. Two typical scuffing experiments for each case are shown to demonstrate repeatability. As seen in Figure 3.3a) the scuffing resistance of Al390-T6 disk lubricated with POE was approximately 800 N in both tests with PV~24.8 MPa.m.s^{-1}. For the case of PAG, the scuffing resistance was significantly higher than POE at 1872 N (PV~51 MPa.m.s^{-1}) as shown in Figure 3.3c). The friction coefficient for the case of POE started at approximately 0.17 and decreased to approximately 0.14 before scuffing was reached (Figure 3.3b)). In the case of PAG, the friction coefficient started at approximately 0.15 and decreased to 0.1 before scuffing (Figure 3.3d)). Even though these experiments were of very short duration without experiencing significant wear, they were designed to determine the scuffing resistance of the two different lubricants. Clearly, the samples lubricated with PAG showed better performance compared to the samples lubricated with POE at room temperature in terms of significantly higher scuffing resistance and lower friction coefficient.

Experimental results for the second set of scuffing experiments at higher temperature are shown in Figure 3.4. As can be seen in Figure 3.4a), a scuffing resistance of 380 N was obtained in the case of POE resulting on a PV~10.4 MPa.m.s^{-1}. This resistance was lower compared to the samples lubricated with PAG for which the scuffing load was 535 N (14.6 MPa.m.s^{-1}), shown in Figure 3.4c). The initial friction coefficient values in the case of the two POE tests are different due to differences in the run-in behavior. However, for both cases the friction coefficient reaches 0.15 before scuffing. Note that the spikes in the raw (unfiltered) data of Figure 3.4 are due to electrical noise and should be ignored. In the case of PAG, the initial

friction coefficient was 0.1 and increased slightly during the test (to 0.15). Towards the latter part of the tests, it decreased to 0.12, as seen in Figure 3.4d). As with the low temperature testing, at high temperature the friction coefficient values for the case of PAG tend to decrease as time progresses, which is not the case for POE. As will be explained through XPS, this behavior is related with the formation of tribolayers which decrease the event of asperity interaction. Also, PAG offers higher scuffing resistance compared to POE, as was the case for ambient temperature testing. Experimental results are summarized in Table 3.2.

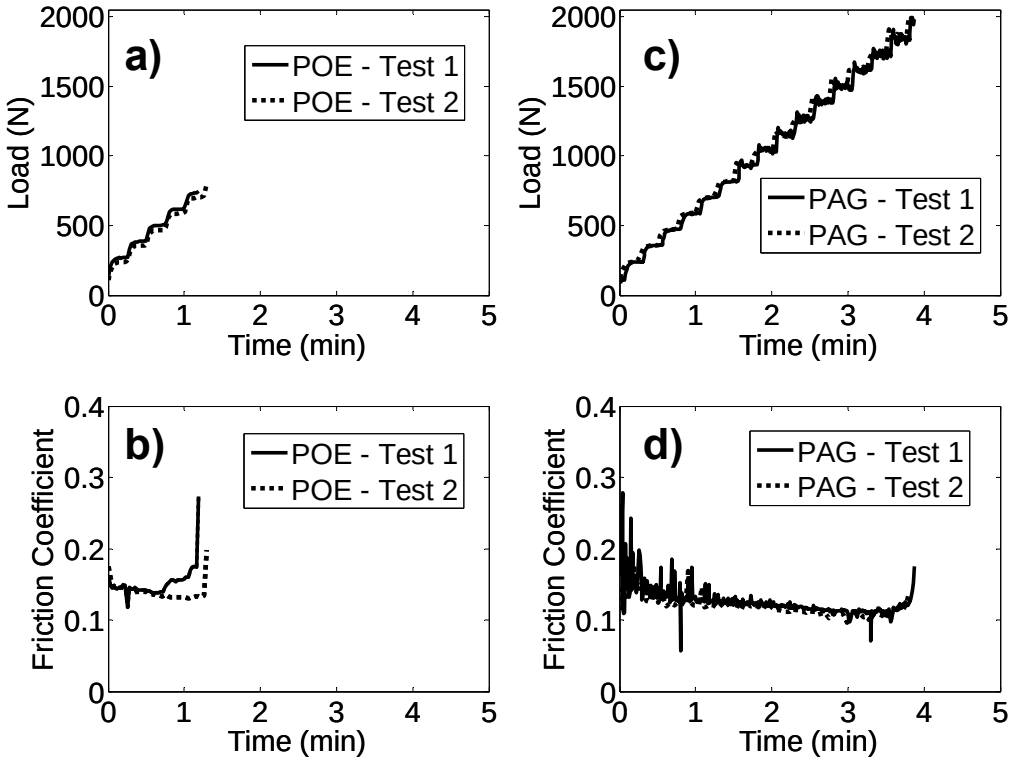

Figure 3.3─Scuffing experiments (Set 1) for POE and PAG lubricants at room temperature (22 °C)

Comparing both lubricants at the two different temperatures, we note that both PAG and POE display lower scuffing resistance at high temperature (90 °C) when compared to ambient

temperature (22 °C), possibly due to the decrease of lubricant viscosity. Even though the near-contact temperature was not recorded in these experiments, from previous studies it has been found that the temperature does not show any drastic changes throughout these tests, until the point of scuffing [59]. Also, for submerged experiments, the temperature variation due to frictional heating is small throughout the test [22]. As stated earlier, the boundary lubrication experiments reported in this study are short term tests and do not provide information about the evolution of the lubricant in time, however, they clearly determine the scuffing resistance. The higher scuffing resistance of PAG has been attributed to its low miscibility with CO_2 [42], but as it will be explained through XPS analysis in this work, chemical changes on the surfaces also contribute to the scuffing resistance.

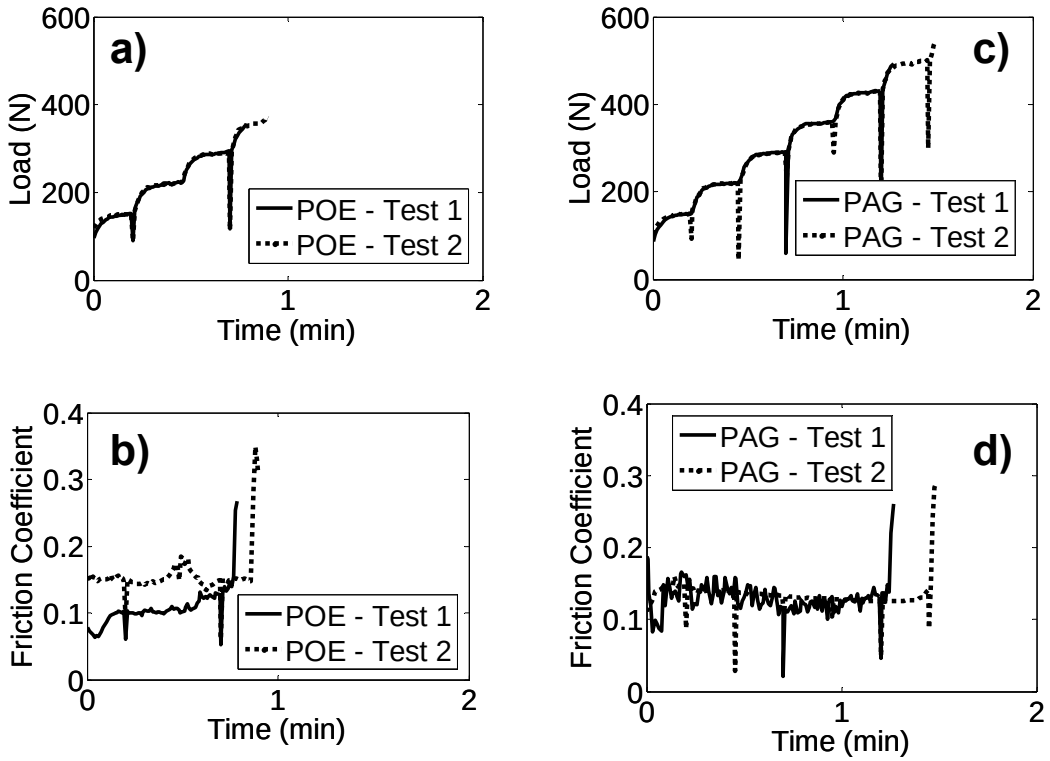

Figure 3.4─Scuffing experiments (Set 2) for POE and PAG lubricants at high temperature (90 °C)

Experimental results for Set 3 are shown in Figure 3.5. As can be observed, friction coefficient under conditions of constant normal load was similar for PAG and POE and approximately ~0.15. However, as will be explained through microscopy images and roughness parameters there are differences in burnishing between the surfaces of Set 3 after testing. Experimental results are summarized in Table 3.2.

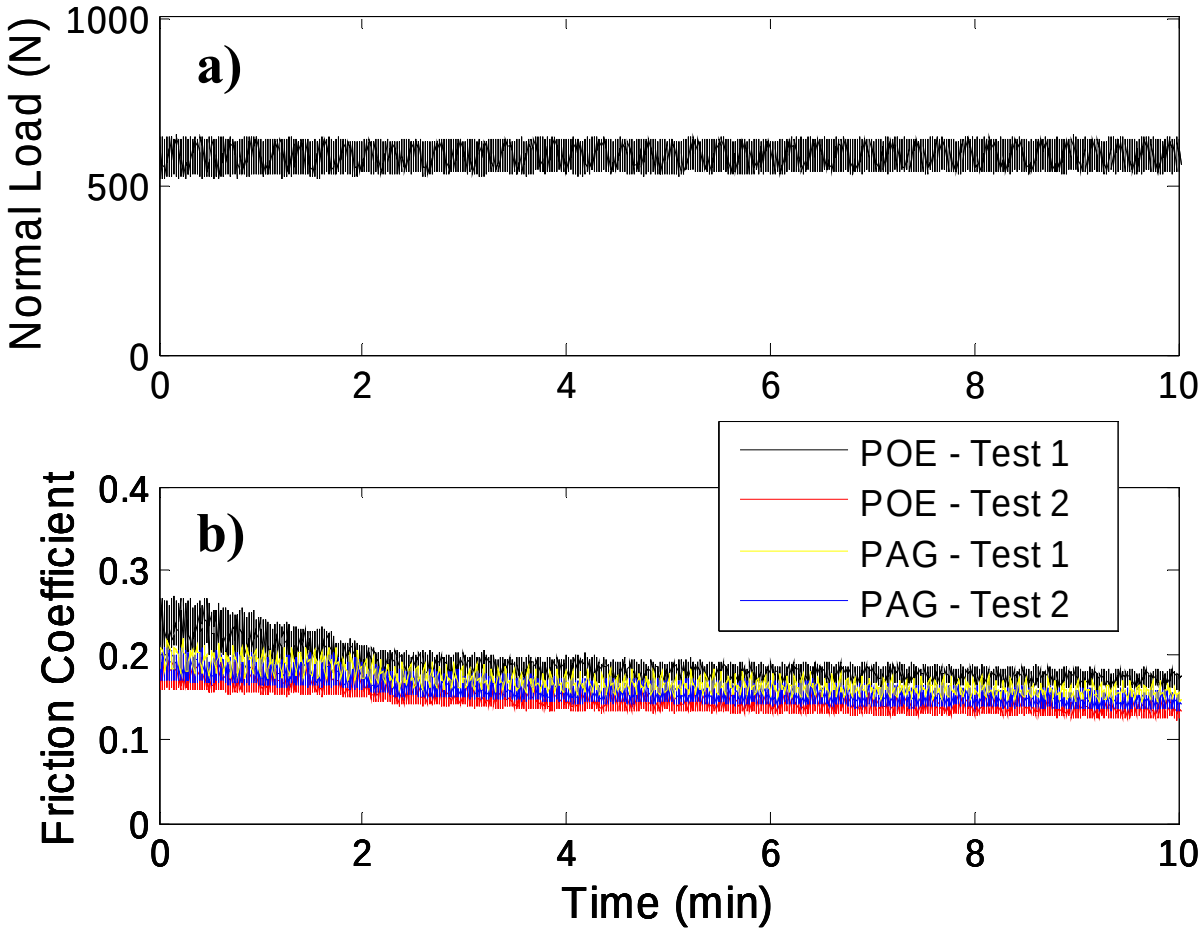

Figure 3.5—Wear experiments (Set 3) for POE and PAG lubricants at room temperature (22 °C)

Table 3.2–Summary of experimental results in the two set of tests

Conditions	**Set 1**	**Set 2**	**Set 3**
Type of experiment	**Scuffing**	**Scuffing**	**Wear**
CO_2 Pressure: psi, (MPa)	200 (1.4)	200 (1.4)	200 (1.4)
Temperature (°C)	22	90	22
Step Loading Conditions: N/s	67/15	67/15	-
Normal load (N)	-	-	600
Lubricant Amount (mg)	40	40	40
Linear Speed (m/s)	2.4	2.4	2.4
Scuffing resistance ($MPa.m.s^{-1}$), POE	24.8	10.4	-
Scuffing resistance ($MPa.m.s^{-1}$), PAG	51	14.6	-
Friction coefficient, POE	0.14	0.15	0.15
Friction coefficient, PAG	0.10	0.12	0.15

Microscopy images of the worn samples after testing in set 3 are shown in Figure 3.6a) confirms that indeed the PAG lubricated disk suffered less burnishing and wear compared to POE (Figure 3.6b)). The thick vertical arrows show the sliding direction, which is perpendicular to the machining marks. A similar trend was observed for the steel pins lubricated with PAG and POE, as seen in Figure 3.7.

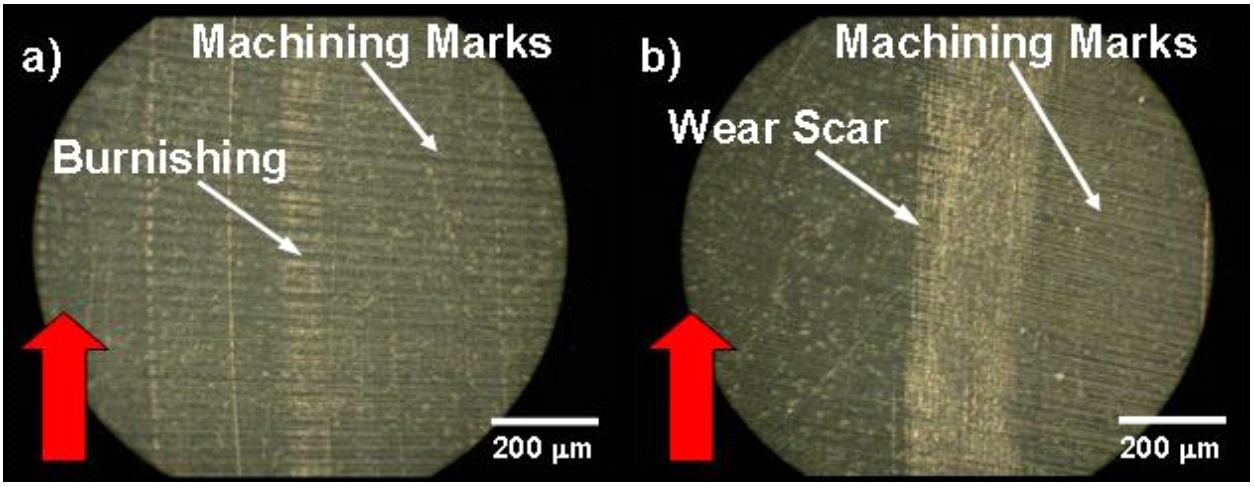

Figure 3.6─Optical microscopy images of disk samples for Set 3 wear experiments lubricated with; a) PAG, b) POE

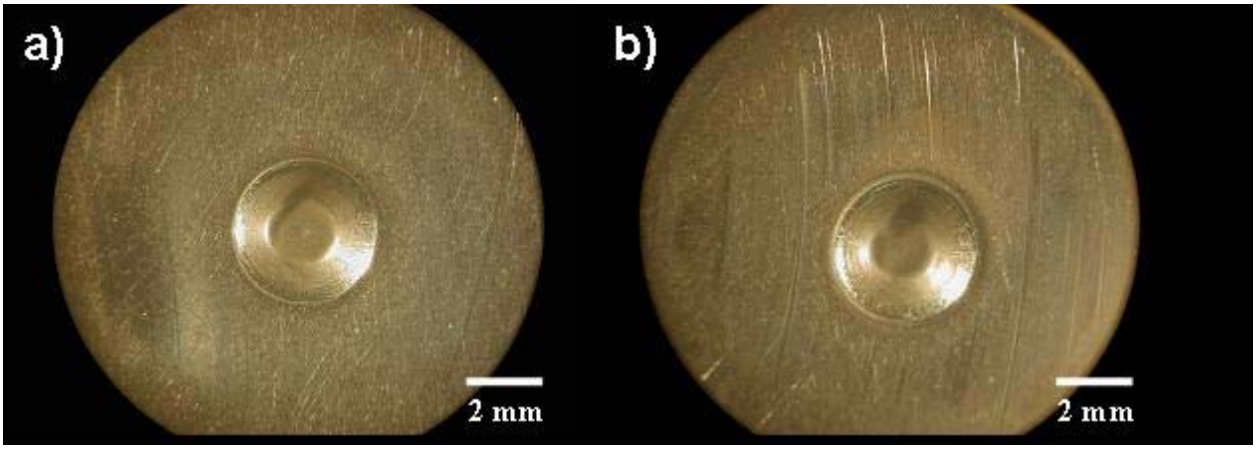

Figure 3.7─Optical microscopy images of shoes samples for Set 3 wear experiments lubricated with; a) PAG, b) POE

3.3.2 Surface topographical measurements

Using a contact profilometer, 2D scans of the Al390-T6 samples tested with PAG and POE in the third set of wear experiments (at constant load) were carried out. A typical 2D image from the untested (virgin) region of the disk is shown in Figure 3.8a) while an image inside the wear track is shown in Figure 3.8b). After testing there are obvious changes in the roughness of the surface due to mild burnishing but no major wear is observed. From these data, root-mean

square (R_q) and skewness (S_{sk}) values were extracted and summarized in Table 3.3. After testing, the value of S_q of the sample lubricated with PAG was reduced by 34% while the reduction of S_q for the sample lubricated with POE is higher at 57%. Skewness values (which are typically negative for engineering samples [58]) decreased by 128% for the disk lubricated with PAG, and by 196% for the disk lubricated with POE. The larger changes of the R_q and S_{sk} values for the case of POE lubricated disks are indicative of a higher degree of burnishing, thus confirming the better performance of the PAG lubricant as it exhibits less burnishing.

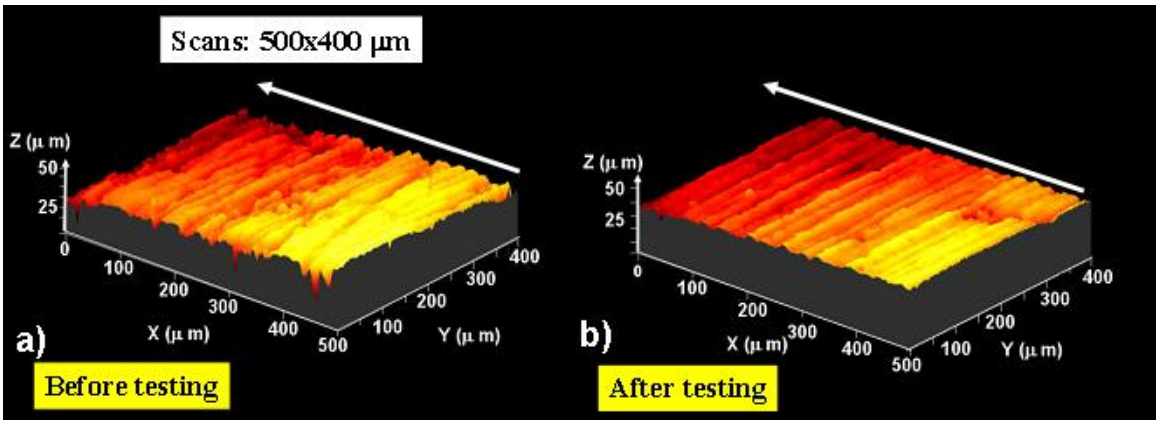

Figure 3.8—Typical 2D roughness measurements for Set 3 wear experiments; a) before testing, b) after testing

Functional volume parameters for the characterization of material and fluid retention on the surfaces were also extracted to provide insight on the functional performance of these surfaces. The core void volume is defined between 10% and 80% of the bearing area curve and is the "empty" volume contained when 10% to 80% of the asperities are in contact. As can be seen in Table 3.2, after testing, the core void volume of the surface (S_c) decreased by 30% for the disk lubricated with PAG and 59% for the disk lubricated with POE. Similarly, the material volume of the surface (which is the material of the asperities at 100% of the bearing area curve)

for the disk lubricated with PAG decreased by 35% and by 57% for the case of POE. These results can be explained by the fact that as the top of the asperities get burnished there is a decrease in their mass and volume. Similarly, the valley void volume of the surface (defined between 80-100% of the bearing area curve) decreased by 18% for PAG and 46% for POE lubricants. Clearly, the case of POE lubricated interface experiences more burnishing compared to PAG.

Table 3.3–Surface roughness parameters of the samples tested in the last set of experiments

Parameter	**PAG Lubricant**			**POE Lubricant**		
	Virgin Region	**Wear Track**	**% Change**	**Virgin Region**	**Wear Track**	**% Change**
R_q (μm)	0.42	0.31	34	0.49	0.22	57
S_{sk}	-0.25	-0.57	128	-0.24	-0.71	196
S_c (nm^3/nm^2)	509	355	30	591	239	59
S_m (nm^3/nm^2)	9.2	6.0	35	18.8	8.0	57
S_v (nm^3/nm^2)	38.8	31.7	18	60	32.4	46

Note that unlike traditional wear analysis where significant amount of material wear allows its quantification by weight (or material) loss, in the cases presented in this research no significant wear was observed. In such cases, the technique of topographical analysis, especially via the simple indices extracted from the bearing area curve could be used as a means to quantify the

robustness of an interface [58]. A similar effect showing that PAG performs better than POE during submerged lubrication experiments in a CO_2 atmosphere has been reported by Lee et al [22]. These tests were much longer than the 10 minute tests performed in Set 3 as they were performed over 60 minutes duration with the interface flooded in lubricant and the load increasing in constant steps.

3.3.3 XPS results

XPS experiments were conducted on a Perkin Elmer PHI 5400 spectrometer equipped with a hemispherical electron analyzer and a non monochromatic Mg Kα X-ray source (1253.6 eV). All reported photoelectron binding energies are referenced to the C 1s feature of adventitious carbon at 285 eV (internal standard) to take into account charging effects. XPS studies were performed inside the wear track of the samples tested in the third set of wear experiments. A certain region of the spectrum was scanned a number of times in order to obtain a good signal-to-noise ratio. The measurements were performed in three different points inside the wear track in each individual sample for repeatability purposes.

Figure 3.9a) and c) presents the C 1s and Figure 3.9b) and d) the O 1s photoelectron spectra obtained from the samples tested in Set 3 of constant load experiments (see Table 3.1). The binding energy of the most intense C 1s peak at 285 eV is attributed to C-C bonds (contamination), while that at 287 eV to C-containing organic molecules (C-O bonds) due to lubricant fragmentation-interaction with refrigerant [61]. The peak at 289 eV is attributed to carbonates (CO_3^{2-}) which are formed inside the wear track in the case of PAG lubricant [62]. It is known that the good miscibility of CO_2 in POE is the main reason of viscosity drop of POE which in turn causes a performance deterioration of the lubricant action.

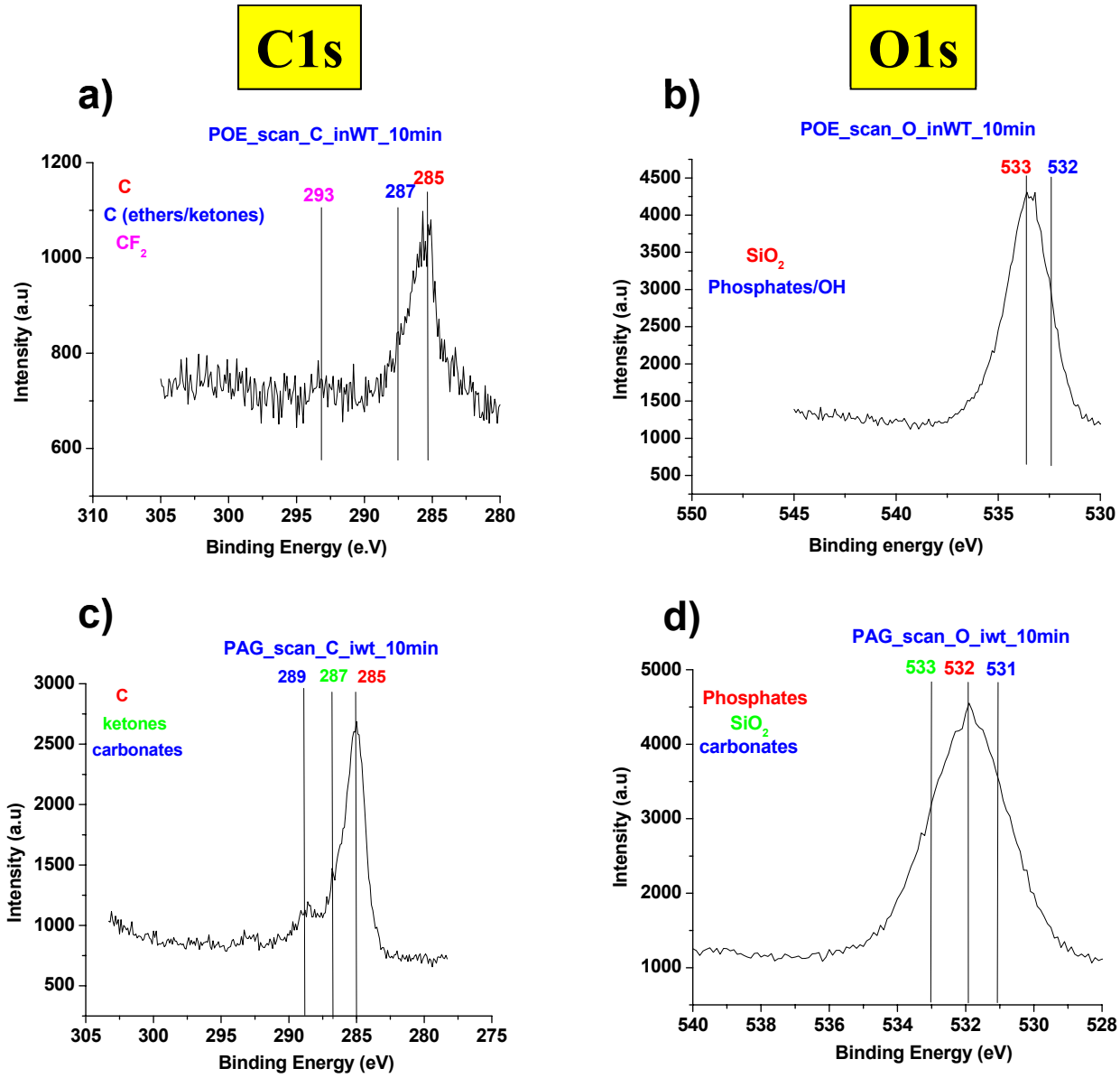

Figure 3.9─X-ray photoelectron spectra obtained from disk samples after Set 3 wear experiments; a), c) C1s spectra, b), d) O 1s spectra

Furthermore, the different chemical nature of PAG and POE molecules (as shown in Figure 3.1) has an impact on PAG and POE packing density on the surface and on PAG-CO_2 and POE-CO_2 interactions. Parameters, such as temperature, pressure, dipole moment, Lewis acid-base interaction, specific chemical interaction between quadrupole moments, or hydrogen

bonding and the nature of the interaction between the solvent and the solute greatly affect the solubility of CO_2 in PAG-CO_2 and POE-CO_2 systems [63].

Due to the different chemical structure of POE and PAG molecules, the packing of the molecules onto Al360-T6 surface is different. PAG is a straight chain (with a small fraction of side C chain) saturated molecule with ether-like linkages and one polar OH terminal group. In the presence of humidity (55% in this experiment), in the case of POE ester, hydrolysis occurs and products CO_2-philic groups ($RCOO^-$) are formed, which can explain the good solubility of POE in CO_2. In the case of PAG lubricant, in the structure of which a non-polar backbone and a polar terminal group are present, a self-arrangement in micelles is possible, which is the basis for resistance against dilution by the refrigerant during compression, even at high pressures, and thus provide improved compression efficiency [64, 65]. In the micelles, OH polar groups are directed towards lubricant-air interface. This makes OH polar groups susceptible to reaction with CO_2 towards carbonates formation.

Furthermore, it is well-established that water acts as Lewis base, an electron donor, in bonding to metal surfaces [66]. The same is valid for ether-like backbone (C-O-C groups) of PAG molecules. Therefore, there is a competitive adsorption of H_2O and PAG molecules onto the surface. Water (coming from air in the chamber) is a stronger Lewis base due to the fact that the electron density in PAG molecule is more delocalized than in a compact water molecule. Thus, water is adsorbed more strongly than PAG, making PAG-surface interaction weak (increased mobility of PAG molecules). In the case of PAG the weak adsorption takes place through ether oxygen in the backbone. The bonding between the first and second layer of the lubricant is strong due to hydrogen bonds between OH groups. In the upper layer, the free OH groups contribute to formation of carbonates through reaction with CO_2. In the case of

hydrolyzed POE, the bonding between the first and second layer of the lubricant is very strong due to a packing of the fragments based on electrostatic interactions between COO^- groups. In the very first and upper layer of POE, COO^- groups contribute to the adsorption process and CO_2 miscibility, respectively [64, 67].

Figure 3.9b) and d) presents O 1s core level spectra. For the PAG lubricated case, a peak at 531.6 eV is observed corresponding to carbonate species [62]. In the case of POE lubricant, a peak at 532 eV is present, which corresponds to anionic species $CO_2^{\delta-}$.

3.4 Summary

Even though the desired lubrication regime for an air conditioning compressor would be full flooded lubrication, in reality many of the critical tribological interfaces (e.g., wrist pin in a piston-type compressor and crowned pin in a swash plate compressor) operate under reduced lubrication conditions. Exact replication of the conditions found inside a compressor is very difficult and in this work we performed starved lubrication experiments with step loading conditions simulating aggressive compressor operating conditions.

The findings, based on scuffing experiments at two different temperatures and also under constant load wear conditions, indicate that PAG lubricant had a scuffing resistance 234% and 140% better than POE in a CO_2 refrigerant atmosphere at 22 and 90 °C respectively. Based on microscopy images of the constant load wear experiments, it was found that the contact pair lubricated with PAG exhibits less burnishing than the one lubricated with POE. This finding was quantified using roughness indices from surface topographical measurements inside the burnished tracks. Specifically, samples lubricated with POE showed higher decrease in S_q and higher reduction in the skewness values with testing. Also, functional parameters extracted from

the bearing area curve, showed that the samples lubricated with PAG had a higher capacity to retain lubricant. Through XPS analysis it was found that in the presence of PAG, carbonates are formed inside the wear tracks, which act as a protective layer leading to improved tribological performance. These carbonate (CO_3^{2-}) layers based on the binding energy peak at 289.5 eV improve the scuffing resistance of Al390-T6. On the other hand, due to the chemical composition of POE, humidity hydrolysis of this lubricant occurs. This promotes the formation of CO_2-philic groups which leads to a high solubility of POE-CO_2. It is this fact which explains the drop in viscosity of POE during the tests and the lower performance of the samples lubricated with POE compared to PAG. The carbonate formation that was observed only in the case of PAG lubricant is attributed to the intrinsic chemical differences between the two lubricants which in turn lead to different bonding to the surface and packing density.

CHAPTER 4
COMPARATIVE SCUFFING AND WEAR PERFORMANCE OF METALLIC SURFACES FOR AIR-CONDITIONING AND REFRIGERATION COMPRESSORS IN THE PRESENCE OF CO_2 REFRIGERANT

Chapter 3 focused on the comparison of PAG and POE lubricants in the presence of CO_2. Experimental and analytical results showed that PAG performed better than POE from the scuffing and wear point of view. In this chapter, the scuffing and wear performance of three different compressor material interfaces in the presence of CO_2 were studied.

4.1 Background

In air-conditioning systems materials such as Al390-T6, gray cast iron, and Mn-Si brass (UNS C67300) are commonly used for critical tribopairs, with Al390-T6 and Mn-Si brass found in automotive air-conditioning compressors and gray cast iron in industrial scroll compressors.

The wear and scuffing performance of silicon enriched aluminum alloys such as Al390-T6 have been investigated before [27, 58, 68, 69] with the main emphasis being on the tribological performance leading to scuffing. In the case of unlubricated experiments [27], it was shown that scuffing was caused by plastic flow and propagation of voids and cracks from the subsurface leading to the removal of a transformed top layer of material. Similar conclusions were reached for boundary/mixed lubricated experiments.

Several research groups have reported on the tribological performance of gray cast iron. A positive effect of phosphorus and boron addition on the wear resistance of pearlitic gray cast iron was reported [70]. Good tribological behavior was also reported when gray cast iron was tested against gray cast iron in a CO_2 atmosphere as compared to R134a using PAG lubricant under boundary/mixed lubricated conditions [52]. An increase in the friction coefficient was

also reported with an increase in the percentage of graphite phase in gray cast iron disks (tested against linings containing steel fibers) [71]. In this case it was proposed that the friction coefficient increased due to the interaction between sharp corners of the graphite flakes and the steel fibers present in the linings.

Mn-Si brass is a high tensile brass commonly used for applications where good resistance and low friction coefficient is required as for example in automotive synchronizers in gearboxes, where the tribological performance was reported to depend on hardness and relative fraction of its α and β phases [72]. It was reported that wear originated from the detachment of hard Mn_5Si_3 particles which resulted in material weakening. In a separate study it was reported that an increase in the α phase increased the wear resistance [73].

The objective of this chapter is to perform a comparative investigation of the tribological scuffing performance of Al390-T6, gray cast iron, and Mn-Si brass in CO_2 refrigerant. Compressor conditions were simulated using a specialized high pressure tribometer [74] under boundary/mixed lubrication conditions using PAG lubricant. The scuffed surfaces were analyzed using scanning electron microscopy (SEM), electron dispersive spectroscopy (EDS), and X-ray photoelectron spectroscopy (XPS) to identify the chemical nature of the formed tribolayers and their lubricity effect.

4.2 Controlled tribological experiments

Using a specialized high pressure tribometer [74] in a sliding configuration, two set of experiments were performed. In the first set the scuffing resistance was determined while in the second set of the wear resistance of the different metallic interfaces was investigated. The scuffing resistance was determined using the same protocol described in Chapter 3. The PAG

lubricant (Idemitsu Kosan Co., Ltd. PZ 68ZL) employed had the same characteristics as the one used in the tests carried out in chapter 3.

During set one experiments were performed on Al390-T6, gray cast iron, and Mn-Si brass disks tested against swash plate compressor 52100 steel shoes (shown in Figure 2.6d)). This set was performed at room temperature (22 °C) to minimize viscosity changes with temperature. In addition a small amount of 40 mg of PAG lubricant (approximately 2 drops) was applied onto the surface of the shoes. The normal load was increased in steps of 67 N every 15 seconds up to the point of scuffing. A rotational speed of 1000 rpm, corresponding to a linear speed of 2.4 m/s was used and the CO_2 chamber pressure was kept constant at 0.17 MPa.

The chamber pressure used during the experiments is lower than typical pressures experienced by CO_2 compressors, which are around 3.0 MPa and 12.0 MPa for the compressor low and high pressure sides respectively. The reason for using lower chamber pressures, other than the fact that is convenient, is justified since during boundary/mixed lubrication experiments using CO_2 refrigerant and PAG lubricant, the effect of CO_2 pressure on viscosity is relatively small. This can be explained by the partial solubility between PAG lubricant and CO_2 [75]. Such measurements show that the amount of CO_2 that can be dissolved in PAG lubricant is limited and the viscosity of PAG lubricant does not decrease significantly as a function of the CO_2 pressure (keeping the temperature approximately constant). Furthermore, the selection of low chamber pressure can be justified based on earlier tribological studies [7] at high CO_2 working pressures (boundary/mixed lubrication conditions in the presence of PAG) where no significant differences were found in terms of friction coefficient and wear after testing at CO_2 chamber pressures of 1.4, 4.1, and 6.9 MPa.

In past experiments under similar operating conditions [51], measurements of near contact temperature (subsurface temperature measured 2 mm below the sliding interface) showed that the temperature remained steady after the running-in period and only showed a sudden increase at the onset of scuffing. This suggests that after the running-in period, the lubricant film and CO_2 lubricity become stable thus significantly reducing asperity interactions and thus high flash temperatures, which could affect the lubricant viscosity.

During set two of experiments, a constant normal load of 1340 N (300 lbs) for 20 minutes was used and the interfaces were submerged in a pool of PAG lubricant. The CO_2 pressure was kept constant at 1.4 MPa (200 psi) and the temperature at 90 °C while the rotational speed was 1000 rpm (which corresponds to a linear speed of 2.4 m/s). The chamber temperature of 90 °C was selected to simulate the behavior of compressors under idle conditions. Experimental conditions of set one and two are summarized in Table 4.1.

Before initiating a test, the samples were immersed in a pool of acetone and ultrasonically cleaned, then rinsed with alcohol and dried using warm air. In order to ensure repeatability each experiment was performed twice. In the contact geometry used for these experiments, the shoe was the lower stationary part, and the disk was the upper rotating part. Photographs of typical tested samples are shown in Figure 2.6e). It should be noted that the 52100 steel shoes are curved or "crowned" with a radius of curvature of 0.3 m and also have a dimpled geometry that helps retain lubricant during sliding [28].

To obtain similar surface roughness, all disks were machined and polished using the same technique, namely lapping. The root-mean square roughness of the samples was determined using 5 mm and 1 mm long profilometric scans for the disks and shoes respectively, profilometric scans of the disks before testing can be observed in Figure 4.1 to Figure 4.3 while

Figure 4.4 show a scan of the surface of the shoe. After testing, cross sections of Al390-T6, gray cast iron, and Mn-Si brass were prepared by cutting the samples exposing the cross section of the wear tracks, then polishing using different grit emery papers ranging in ANSI standard grit size from 320 to 4000. Final mirror polishing was performed using an emery cloth. The samples were used to take SEM cross section images.

Table 4.1–Summary of experimental conditions in the two set of tests

Conditions	**Set 1**	**Set 2**
Type of experiment	Scuffing	Constant Load
CO_2 Pressure: psi, (MPa)	25 (0.17)	200 (1.4)
Temperature (°C)	22	90
Step Loading Conditions: N/s	67/15	-
Constant load: N	-	1340
Time (s)	-	1200
Lubricant Amount (mg)	40	Submerged
Linear Speed (m/s)	2.4	2.4

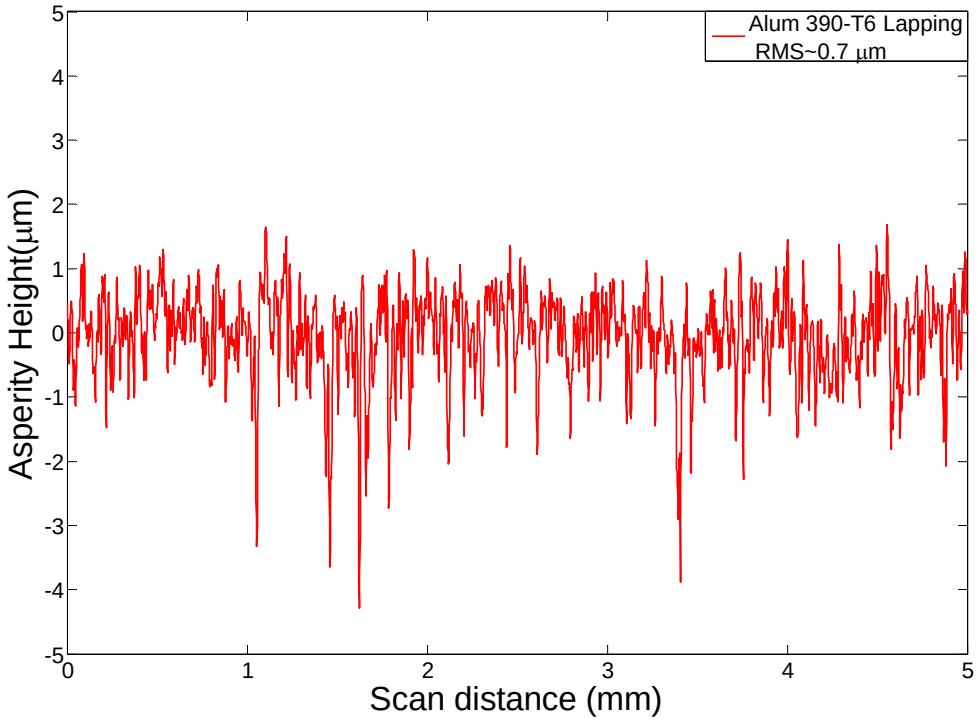

Figure 4.1—Profilometric scan of the untested surface of Al390-T6 disk

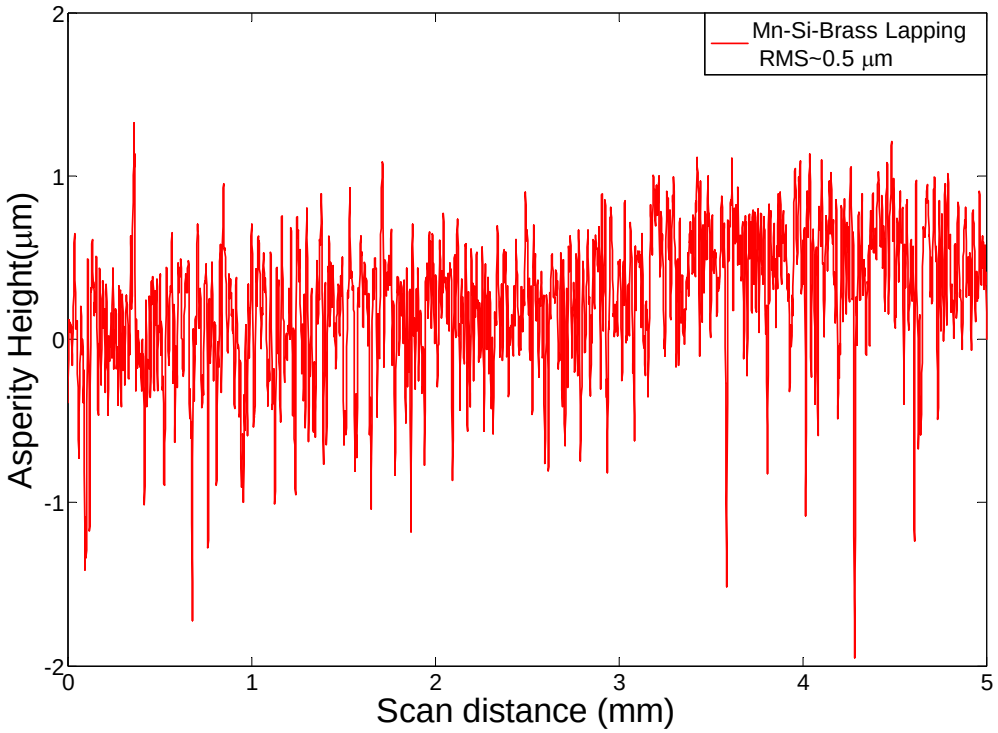

Figure 4.2—Profilometric scan of the untested surface of Mn-Si brass disk

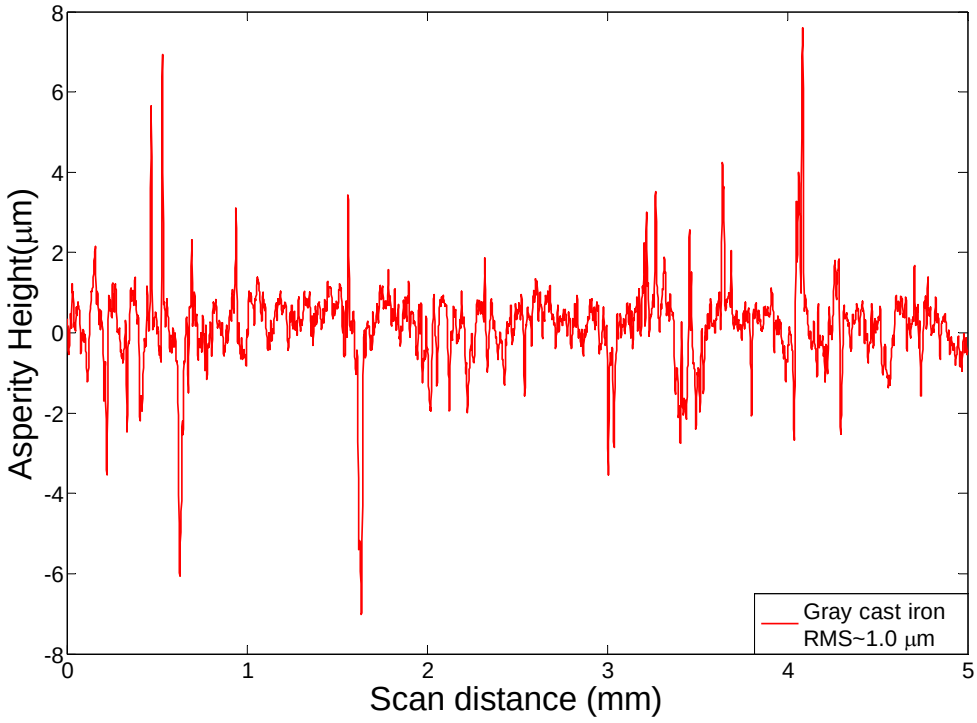

Figure 4.3─Profilometric scan of the untested surface of Gray cast iron disk

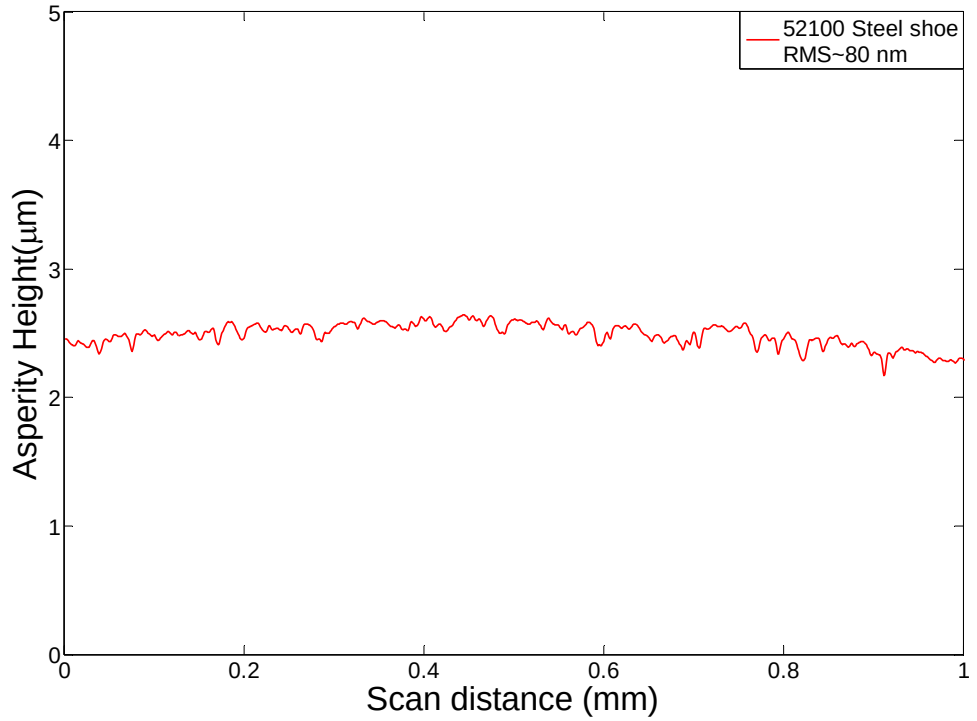

Figure 4.4─Profilometric scan of the untested surface of 52100 steel shoe

4.3 EDS

EDS experiments were conducted on a high resolution, field emission JEOL 7000F SEM. The electron source is a Schottky field emission gun with probe current of 1 pA to 200 nA and accelerating voltage from 0.5 to 30 kV. EDS studies were performed inside the wear tracks to analyze chemical composition.

4.4 XRF

XRF experiments were performed in a Kevex analyst chamber/spectrometer with a X-ray tube as primary excitation mode. The target current varies from 0-3.3 mA and the voltage from 0-60 kV. XRF was performed in the lubricant with the objective to investigate its chemical changes after constant load tests. During this analysis, Ti and Rh were used as primary excitation elements to obtain the spectrum.

4.5 Experimental results

4.5.1 Controlled tribological scuffing experiments

Typical experimental results of set one of tests are shown from Figure 4.5 to Figure 4.7, where the in-situ normal load and friction coefficient are shown for the three different material pairs. Before the experiments, the surface roughness were measured and found to be 0.5-1.0 μm and 80 nm for the disks and shoes, respectively. As seen in Figure. 4.5, the scuffing resistance (maximum normal load to cause scuffing) of Al390-T6 was approximately 500 N. For gray cast iron and Mn-Si brass, the scuffing resistance was higher at 850 N as shown in Figure. 4.6 and Figure 4.7 respectively. The tribological behavior of Mn-Si brass near scuffing was different compared to Al390-T6 and gray cast iron, as it failed gradually. This phenomenon can be

attributed to the presence of Pb in Mn-Si brass, which has a low melting point. It has been reported that friction coefficient and temperature increase abruptly during scuffing [59] and the increase in temperature can cause melting of Pb at the onset of scuffing allowing the Pb to act as a lubricant. It is believed that this is the reason why under the presence of a sudden transient load Mn-Si brass can resist catastrophic failure as can be seen in Figure. 4.7. This lubricity effect will also be demonstrated in section 4.7 where using EDS the presence of melted lead in the region near to the sliding interface will be shown.

The friction coefficient values were similar in all cases with Al390-T6 being somewhat higher (~0.18) compared to gray cast iron and Mn-Si brass (~0.14). Despite the fact that these experiments are short in duration, they provide information about the maximum load sustained before failure (scuffing). From these experiments it is evident that gray cast iron and Mn-Si brass perform better than Al390-T6 in terms of both scuffing resistance and lower friction coefficient values. Also, it should be noted that in these experiments the friction coefficient was unsteady at the beginning of the tests due to run-in, which was similar for the three materials as the same surface preparation was used to prepare the samples.

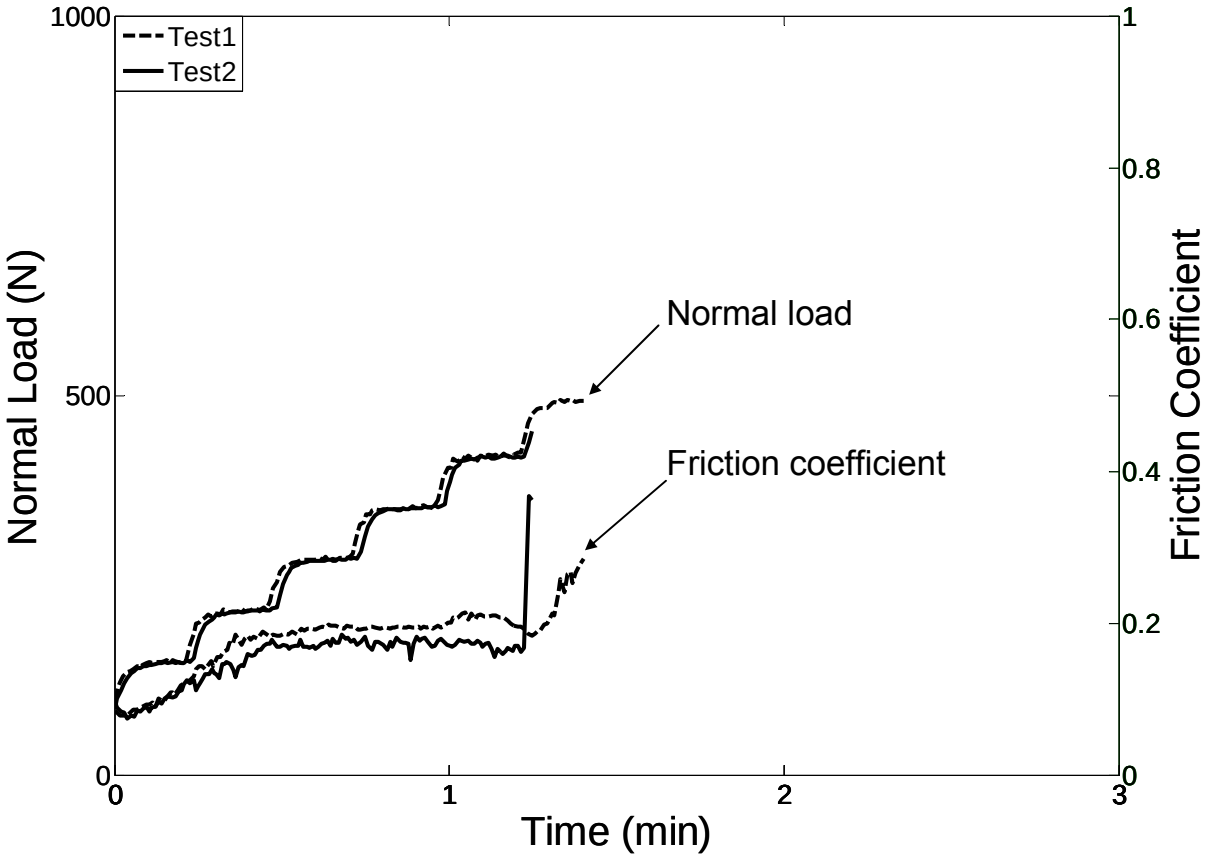

Figure 4.5─Typical scuffing experiments: Normal load and friction coefficient for Al390-T6

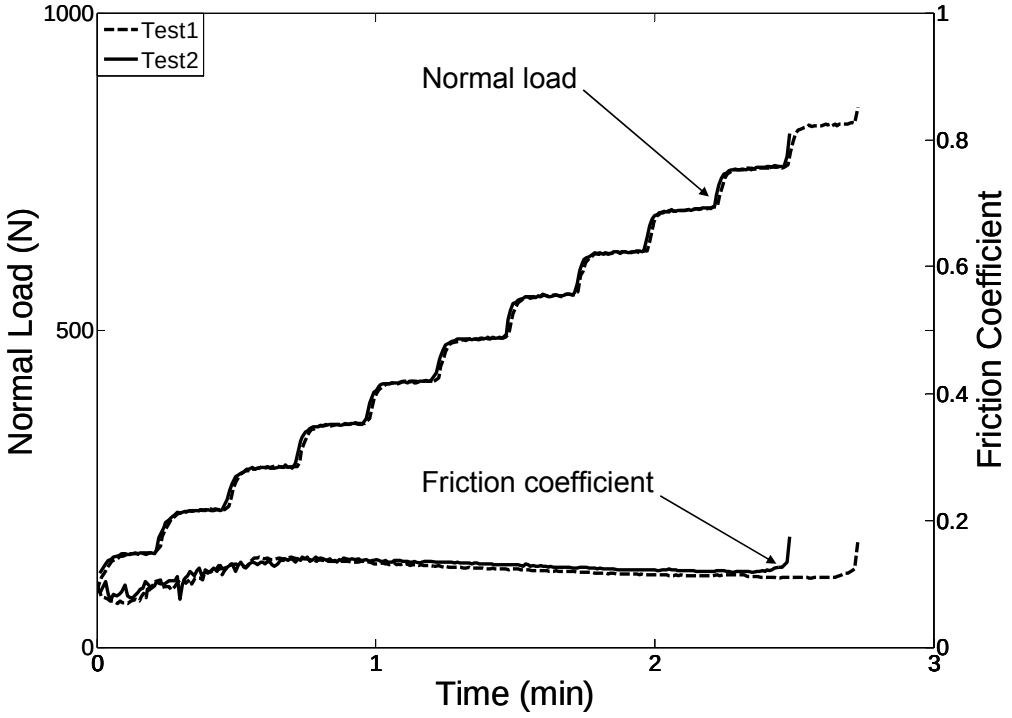

Figure 4.6—Typical scuffing experiments: Normal load and friction coefficient for Gray cast iron

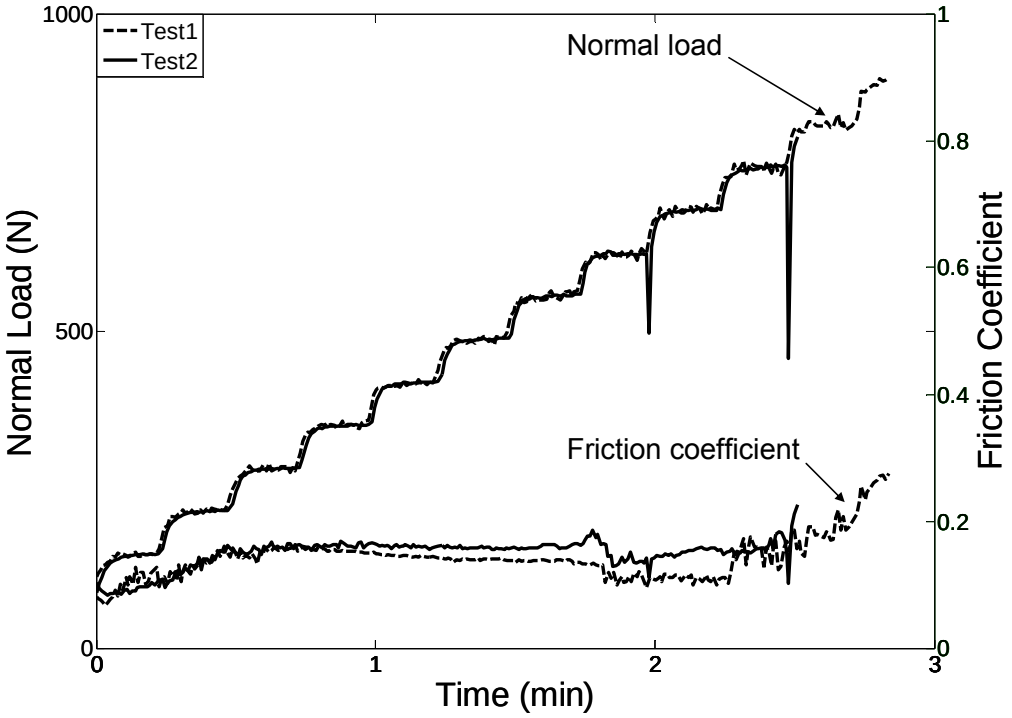

Figure 4.7—Typical scuffing experiments: Normal load and friction coefficient for Mn-Si brass

Experimental results for set 2 of experiments are shown in Figure 4.8a) and b). As can seen in Figure 4.8b) friction coefficient for Al390-T6 started at approximately 0.1 and reached a steady state value of approximately 0.03. The peak at about 10 minutes in the friction coefficient during Test 1 in Figure 4.8d) might be caused by the wear debris particles generated during the testing. In the case of the gray cast iron sample the friction coefficient started at approximately 0.1 and reached a steady state of approximately 0.08 as seen in Figure 4.8e). For the case of the Mn-Si brass sample friction coefficient also started at approximately 0.1 and reached a steady value of approximately 0.05 (Figure 4.8f)).

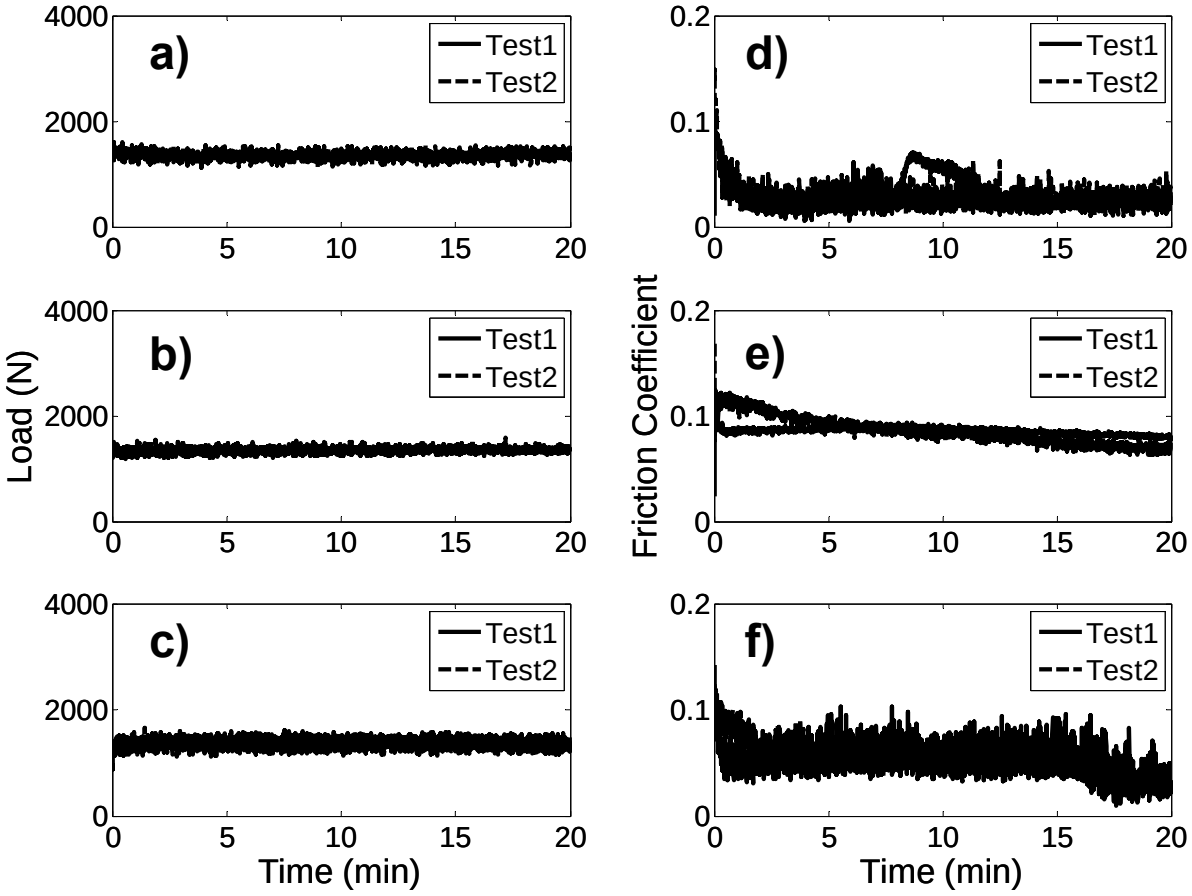

Figure 4.8─Submerged experiments for a) Al390-T6, b) gray cast iron, and c) Mn-Si brass at high temperature (90 °C)

Single line profilometric scans were performed after the tests for every material as seen in Figure 4.9. Figure 4.9a) shows typical wear scan for the Al390-T6 sample which showed the highest wear (~0.6 μm) compared to the case of gray cast iron (Figure 4.9b)), and Mn-Si brass samples (Figure 4.9c)), where the wear depth was approximately 0.1 μm and 0.3 μm, respectively. These results can be explained if we consider the hardness of the three materials. Al390-T6 was the softest material with a hardness of 1.3 GPa, followed by Mn-Si brass (1.4 GPa), and the gray cast iron (2.3 GPa) which had the highest hardness. Despite the fact that Mn-Si brass and Al390-T6 showed similar hardness values, the wear of Al390-T6 was higher. This behavior can be explained based on the high percentage of silicon (16-18%) in Al390-T6. As will be explained through XRF analysis, during submerged lubrication some of the eutectic silicon particles (small particles) present in the Al390-T6 at the surface roughness level (a few microns below the surface) are being depleted out of the matrix. The small eutectic silicon particles are harder than 52100 steel shoes; therefore, they are abrasive. As a consequence, Al390-T6 weakens at the surface roughness level which leads to increased wear compared to Mn-Si brass. Unlike the case of Al390-T6, the Mn_5Si_3 particles (which provide additional strength) in the case of Mn-Si brass are present in smaller quantities and do not contribute significantly to the overall hardness of this alloy.

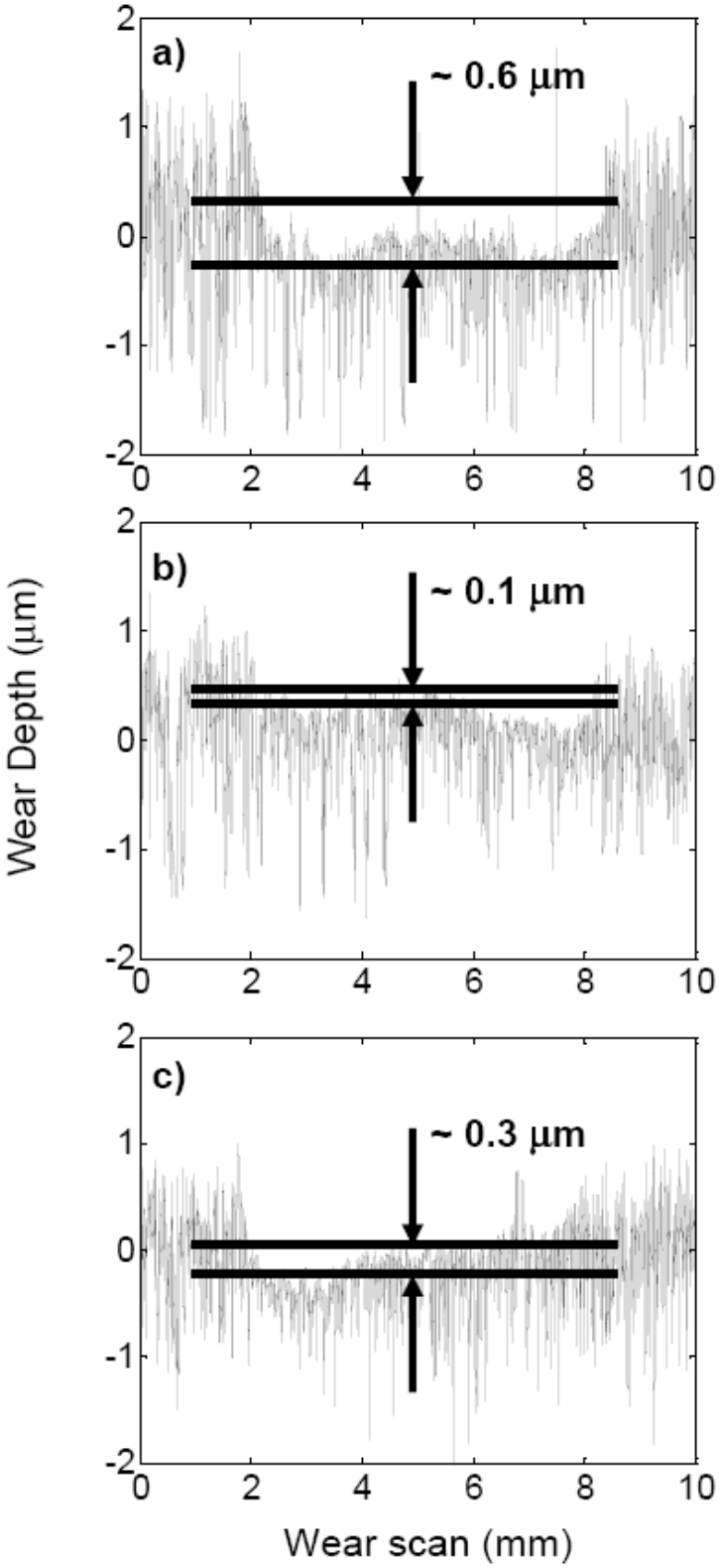

Figure 4.9─Profilometric line scans of the samples tested under submerged experiments for a) Al390-T6, b) gray cast iron, and c) Mn-Si brass.

4.6 SEM studies of scuffed disks

SEM images of the wear tracks are shown in Figure 4.10. Referring to Figure 4.10a), Al390-T6 shows large delaminated regions in the scuffed surface, while Figure 4.10b) shows typical galling behavior. Failure of the lubricant film causes the destruction of the protective tribolayer [27], thus causing scuffing.

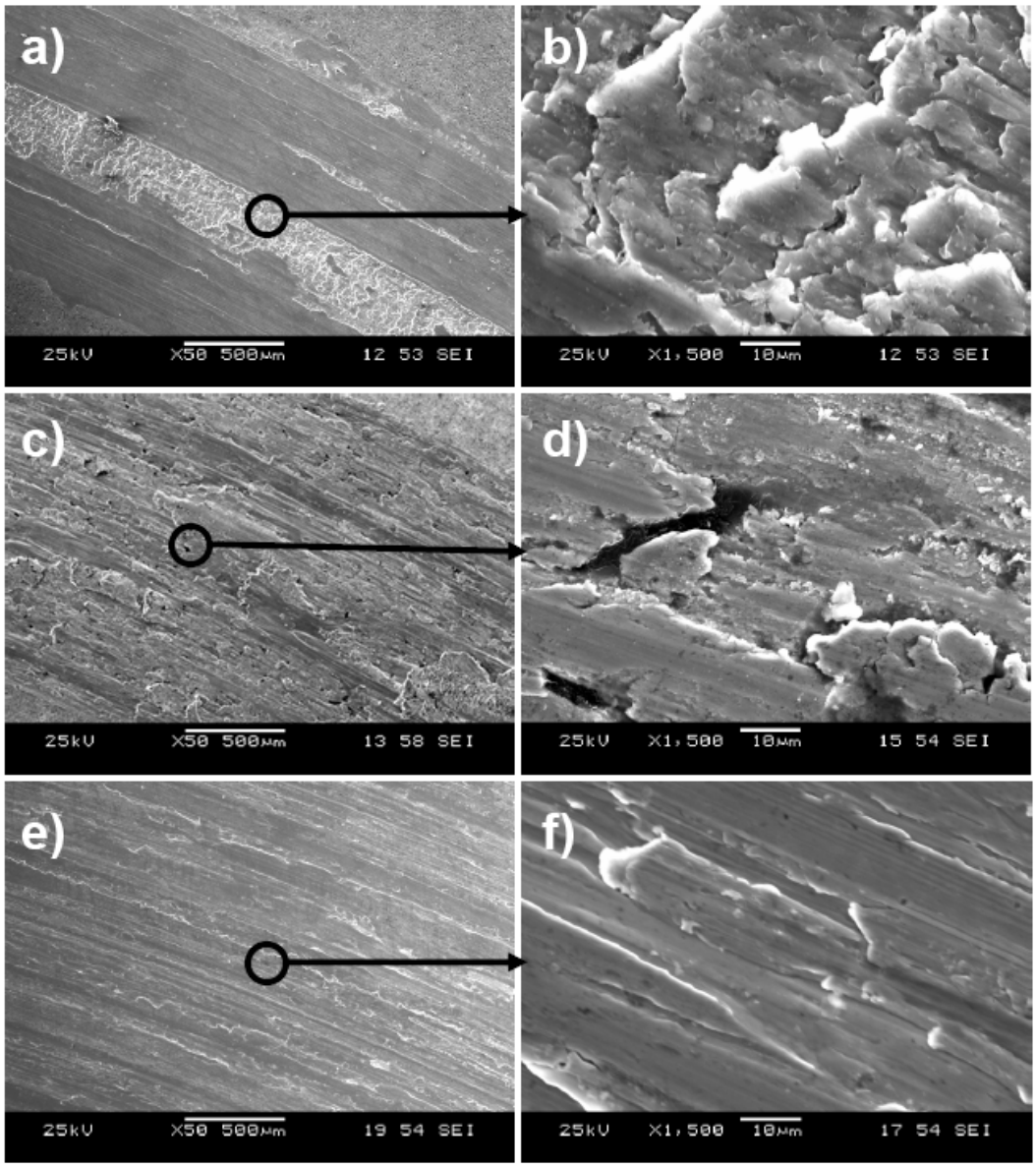

Figure 4.10─SEM surface images inside the wear track of (a) and (b) Al390-T6 (c) and (d) gray cast iron (e) and (f) Mn-Si brass after scuffing experiments.

With scuffing, fracture of subsurface primary silicon particles is evident, as shown in Figure 4.11, thus exposing hard and abrasive silicon particles at the interface. Eventually, severe adhesion takes place leading to the plastic shearing of the bulk of the material (seizure). This explains the large delamination bands present in the Al390-T6 sample after scuffing.

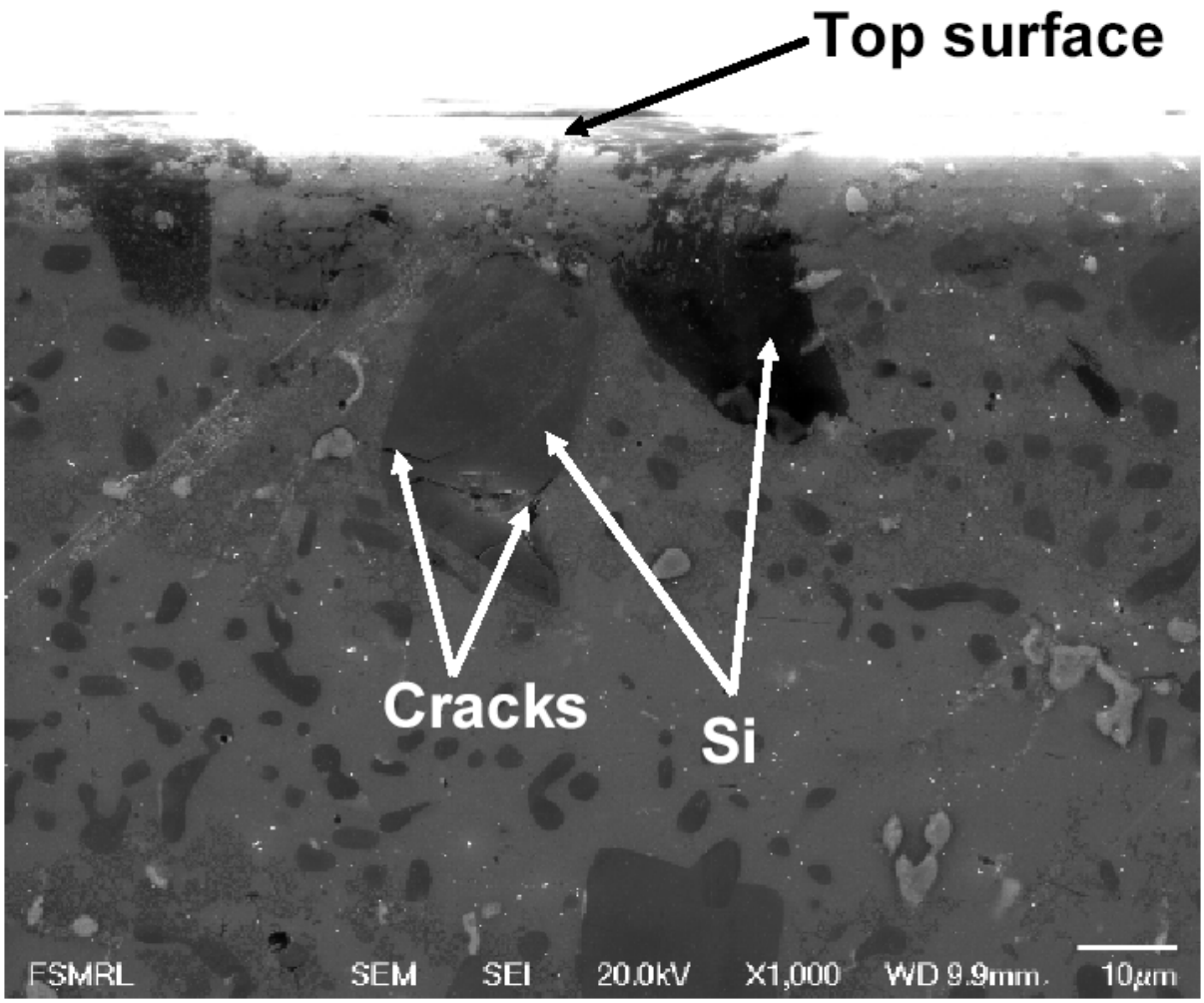

Figure 4.11—Surface cross section SEM image of Al390-T6 showing cracks on a primary silicon particle below the surface during scuffing.

In the case of gray cast iron shown in Figure 4.13c) and Figure 4.13d) less adhesive wear compared to Al390-T6 was observed. Due to the presence of graphite flakes, a sudden failure can be expected during scuffing because the tips of the graphite flakes are sharp thus acting as stress concentration sites, as also shown in Figure 4.13a) and Figure 4.13b). Mn-Si brass shown in Figure 4.10e) and Figure 4.10f) shows minor adhesive wear with plastic deformation during scuffing. Large plastic deformation during scuffing in the case of Mn-Si brass can be explained by the detachment and fracture of hard Mn_5Si_3 particles during sliding, as shown in Figure 4.12. Since the size and percent by volume of Mn_5Si_3 particles is small, it is believed that after fracture, depletion of these particles leads to a decrease in strength and fatigue resistance leaving a softer matrix that can more readily flow plastically, as seen in Figure 4.10f).

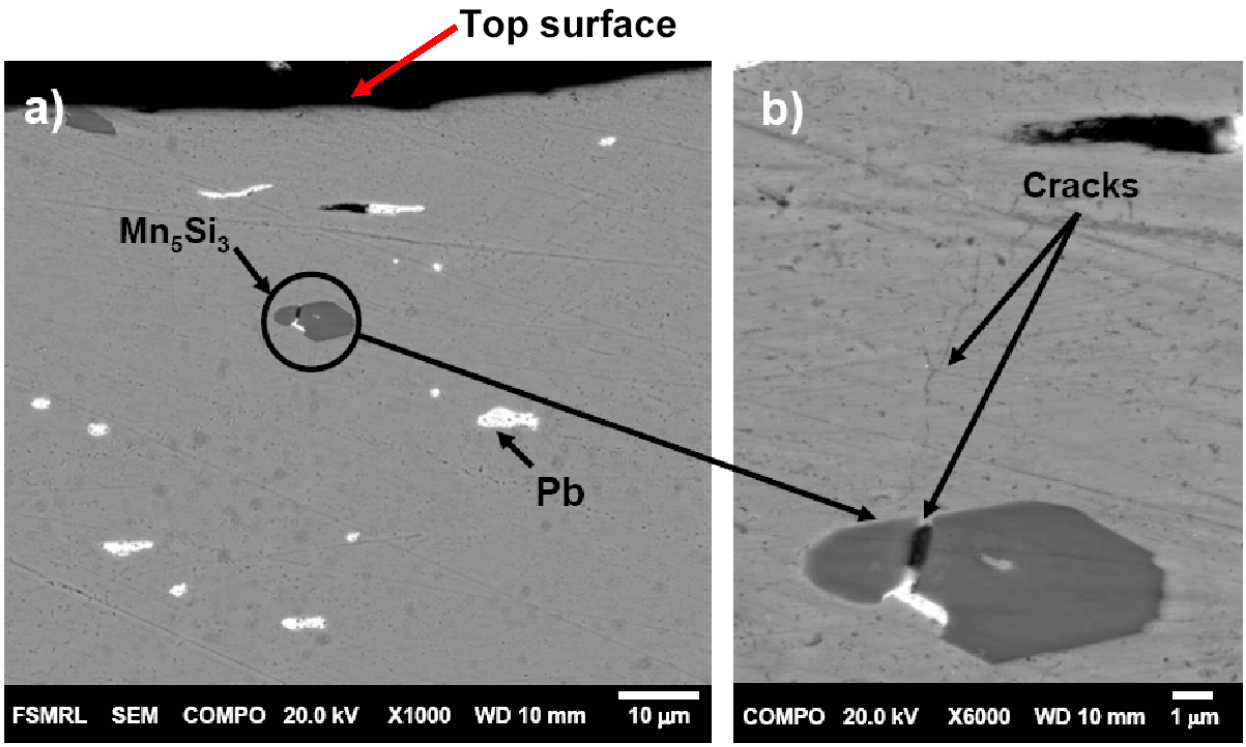

Figure 4.12—Surface cross section SEM image of Mn-Si brass in SE mode showing a fractured Mn_5Si_3 particle and cracks propagating from this particle during scuffing.

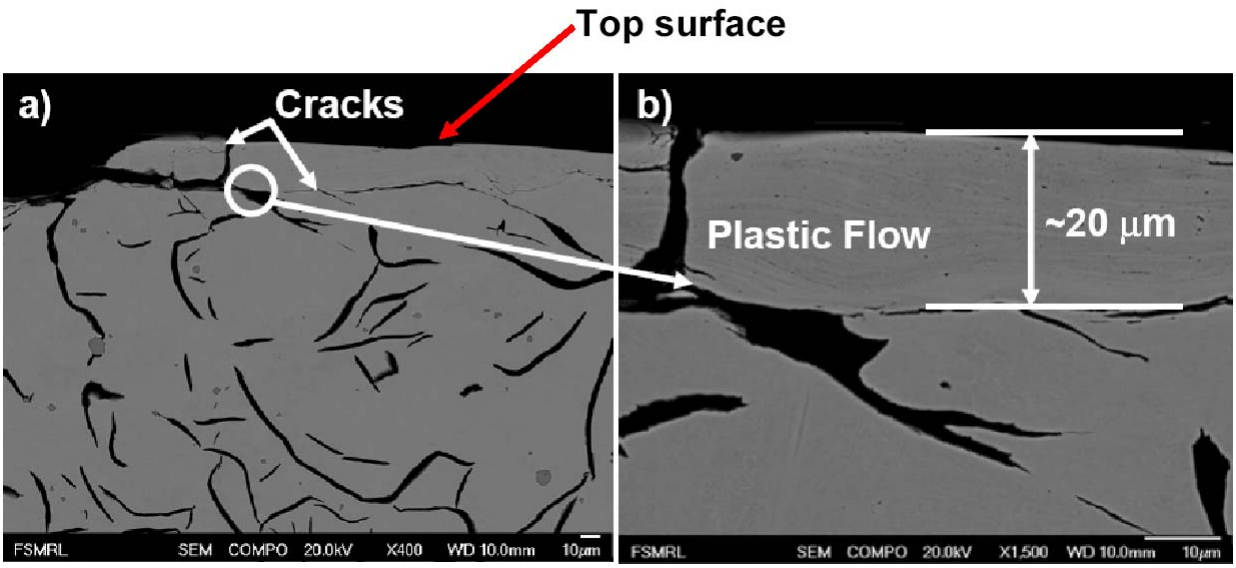

Figure 4.13─Surface cross section SEM image of gray cast iron in SE mode showing plastic flow and propagation of cracks originated from graphite flakes below the surface during scuffing.

4.7 EDS studies

EDS analysis of scuffed Mn-Si brass is depicted in Figure 4.14 where the spectra and the chemical elements at each point inside the wear track are presented in Figure 4.14 and Figure 4.14. Fracture of Mn_5Si_3 particles and propagation of cracks resulted in surface failure. Spectral analysis reveals the presence of lead inside the broken Mn_5Si_3 particles (spectrums 2 and 4 in Figure 4.15 and Figure 4.16 respectively). This finding supports the observation made previously that Pb melts during scuffing of Mn-Si brass leading to a gradual failure. The local melting of Pb and thus its lubricity effect is due to an increase in temperature at the onset of scuffing.

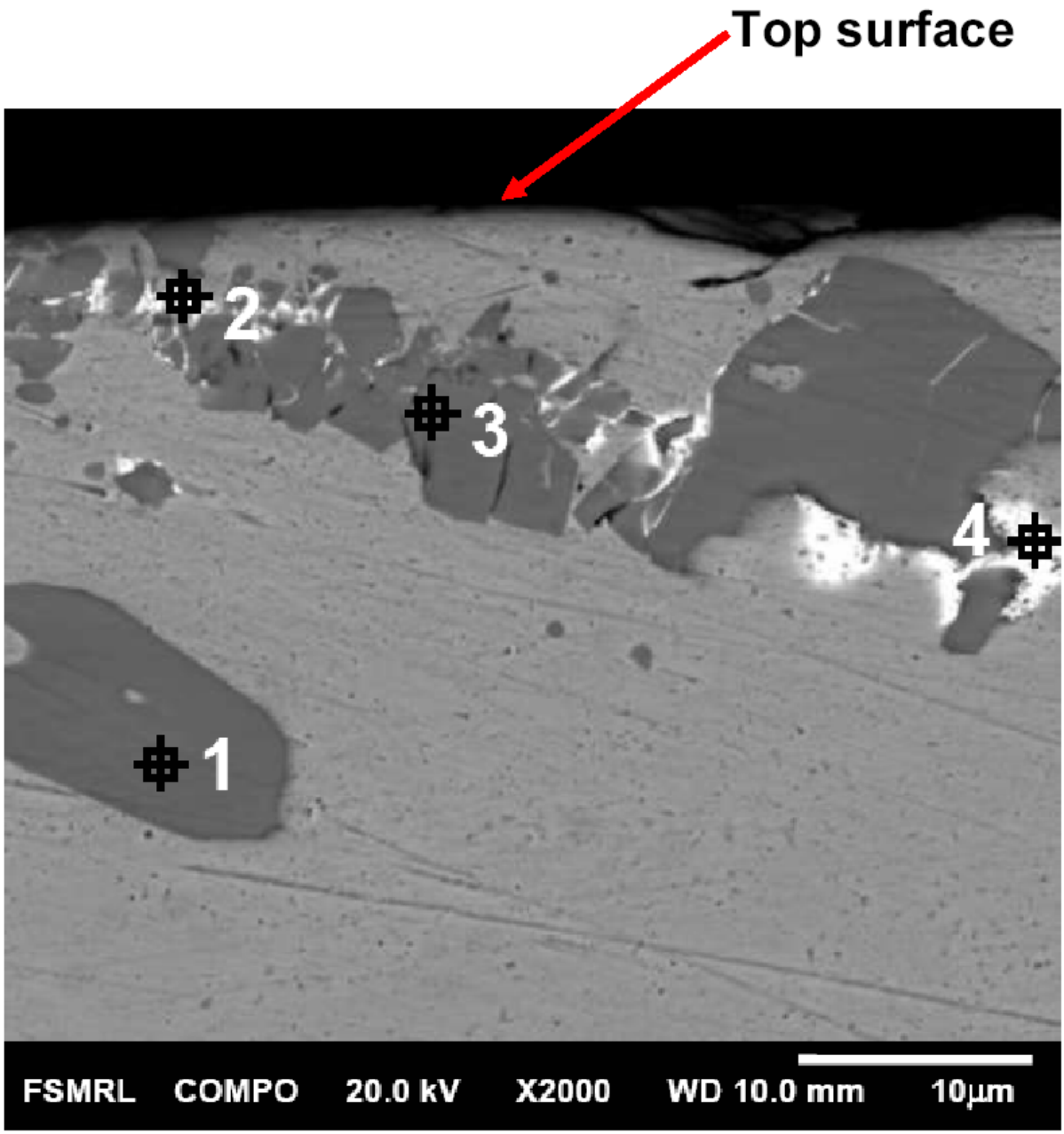

Figure 4.14─Surface cross section SEM inside the wear track of Mn-Si brass in SE mode and EDS mapping in different locations (see numbers).

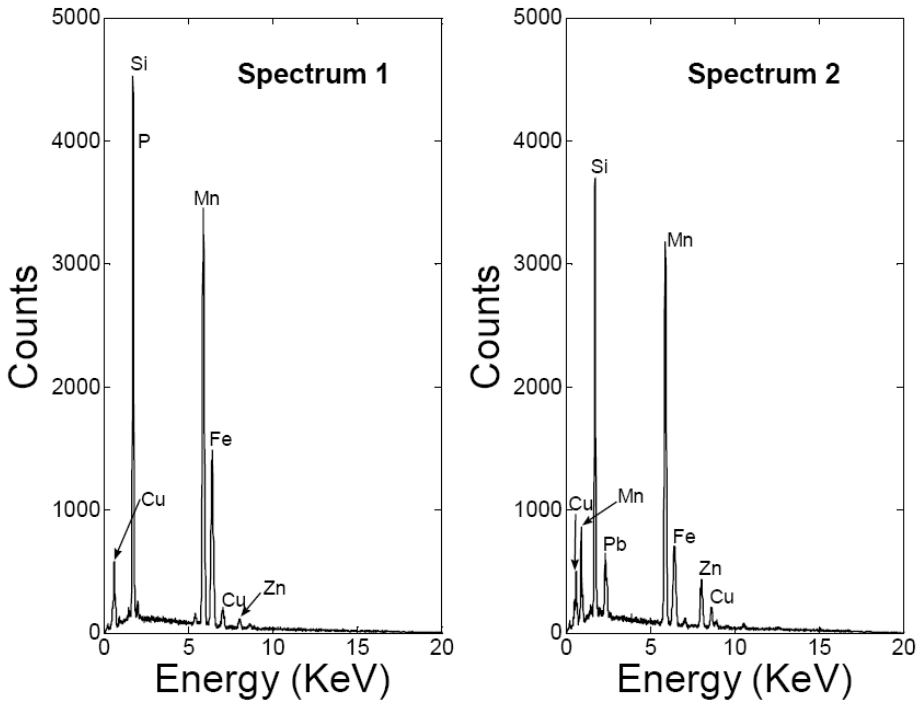

Figure 4.15─Spectrum 1 and 2 displaying the chemical composition during cross section EDS of Mn-Si brass (see Figure 4.8)

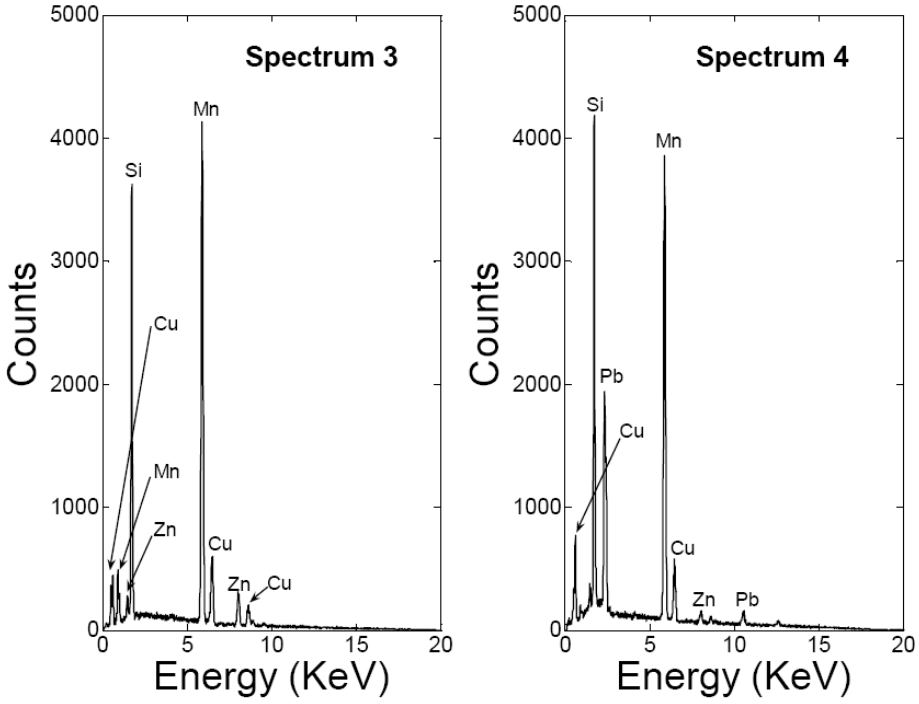

Figure 4.16─Spectrum 3 and 4 displaying the chemical composition during cross section EDS of Mn-Si brass (see Figure 4.8)

4.8 Surface topographical measurements

Since the wear was not significant (less than 1 μm) and there was only mild-burnishing of the asperities during constant load experiments (Figure 4.8), Birmingham-14 parameters were calculated with a focus on fluid retention parameters (similar to the analysis performed on Chapter 3) using the bearing area curve (Figure 2.10). These parameters are obtained using a Matlab code called GUI program which interface is shown in Figures 4.18 and 4.19. These showed clear differences between the three different surfaces tested. From these data, root-mean square (S_q) and skewness (S_{sk}) values were extracted and summarized in Table 4.2.

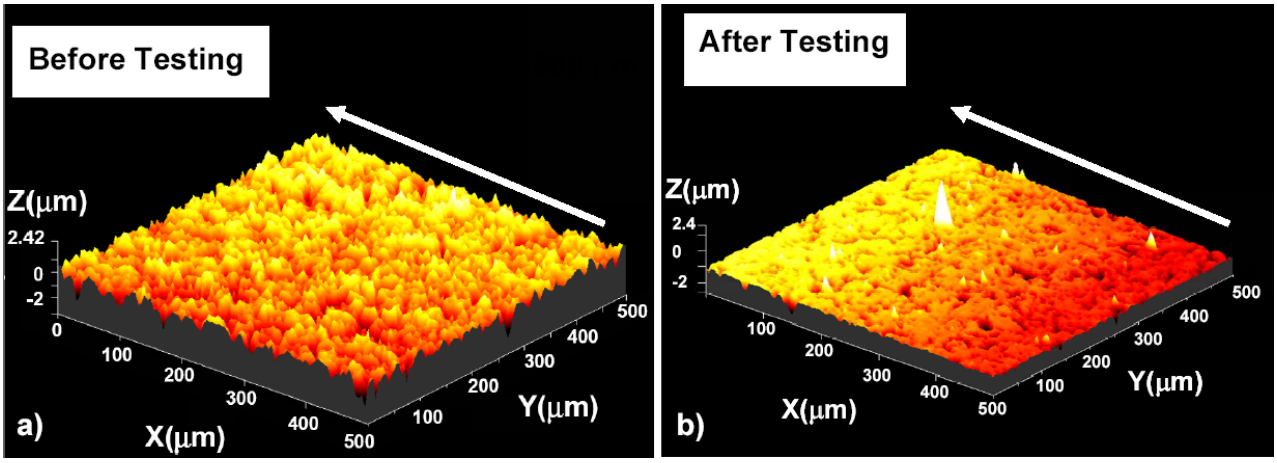

Figure 4.17─Typical 2D roughness measurements for Set 2 (wear experiments); a) before testing, b) after testing.

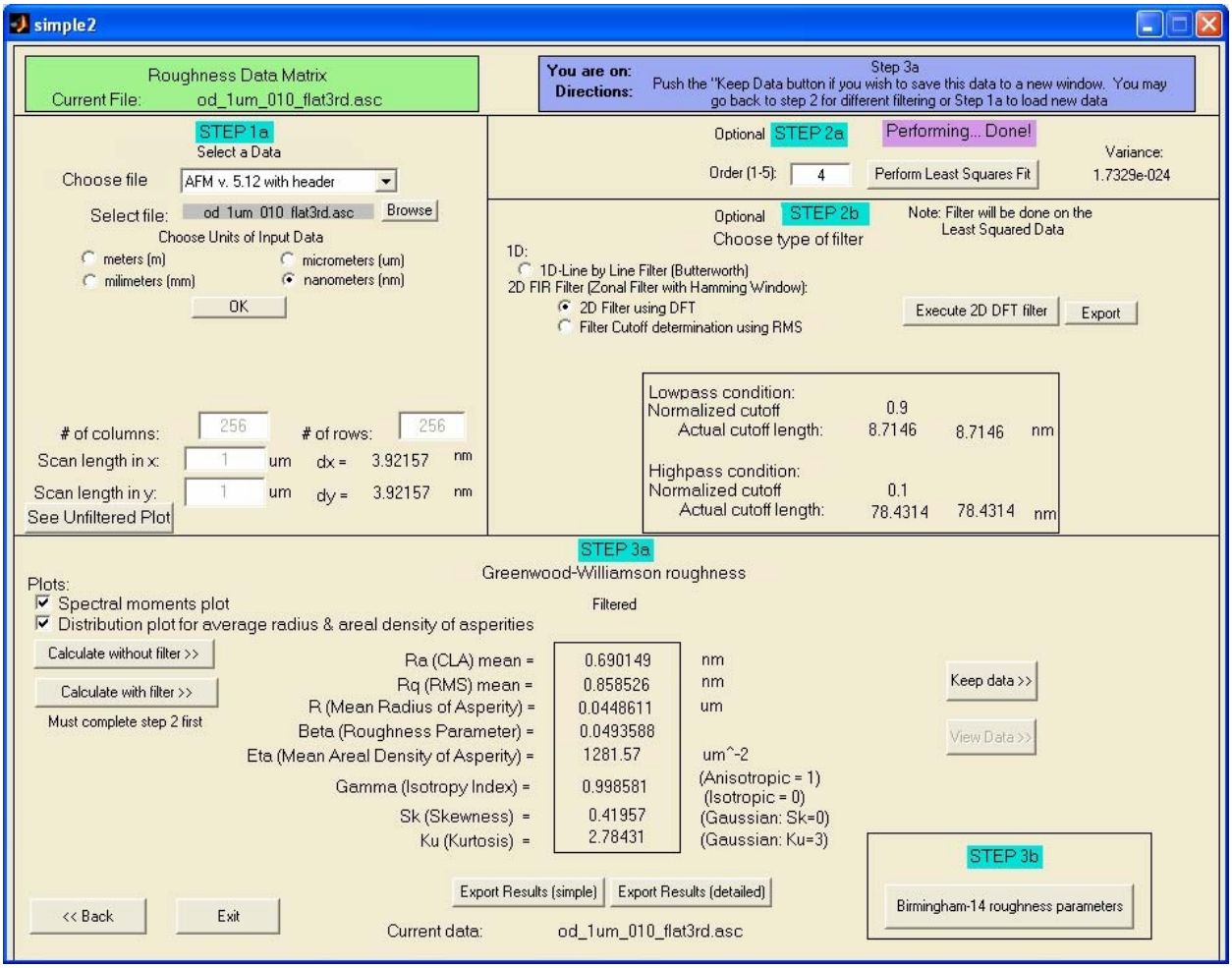

Figure 4.18─Printscreen of the GUI program to extract Birmingham 14 parameters.

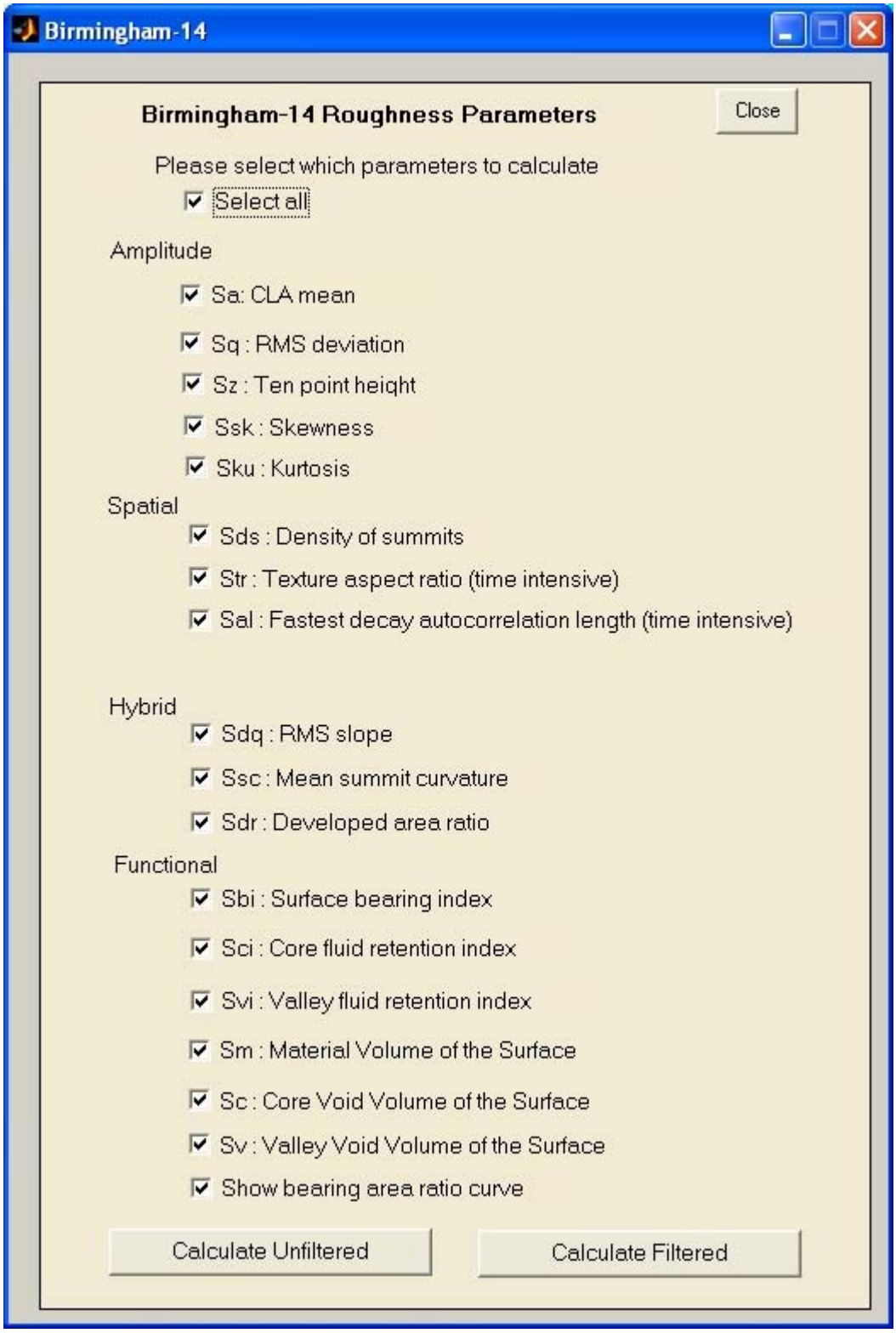

Figure 4.19─Birmingham 14 parameters in the GUI program.

After testing, the value of S_q of the Al390-T6 disk decreased by 58% while the reduction of S_q for the gray cast iron and Mn-Si brass was 16% and 30% respectively. Moreover, skewness decreased by 80% for Al390-T6, while a decrease in 3% and 30% was found for gray cast iron and Mn-Si brass respectively. The larger changes of the Sq and Ssk values for the case Al390-T6 indicate a higher degree of burnishing, compare to gray cast iron and Mn-Si brass.

In addition, functional volume parameters provide information related to the material and fluid retention properties of the surfaces. These parameters were also extracted to evaluate the functional performance of the three surfaces. From these parameters, the core void volume (Sc) decreased by 69% for the Al390-T6 disk and approximately in 30% and 41% for gray cast iron and Mn-Si brass respectively. Also, the material volume of the surface for the Al390-T6 disk decreased by 52.5% compared to gray cast iron and Mn-Si brass where this parameter reduced in approximately 20 and 31% respectively. The reduction of material volume can be explained by a decrease in mass and volume as the asperities get burnished. Moreover, the valley void volume of the surface (defined between 80-100% of the bearing area curve) decreased by 52% for Al390-T6 and approximately 21% and 35% for gray cast iron and Mn-Si brass respectively. Clearly, Al390-T6 experiences more burnishing compared to gray cast iron and Mn-Si brass supporting the wear profilometric measurements shown in Figure 4.9.

Table 4.2–Surface roughness parameters of the disks tested on set 2 of tests. The units of S_c, S_m, and S_v are in nm^3/nm^2

Parameter	**Al390-T6**			**Gray cast iron**			**Mn-Si brass**		
	Virgin	**Wear Track**	**%**	**Virgin**	**Wear Track**	**%**	**Virgin**	**Wear Track**	**%**
S_q (μm)	777	324	58	653	548	16	735	510	30
S_{sk}	-1.76	-3.16	80	-1.35	-1.39	3	-0.30	-0.39	30
S_c	668	207	69	723	505	30	870	509	41
S_m	23	11	52.5	18	15	20	25	17	31
S_v	141	67	52	118	94	21	89	58	35

4.9 XPS studies

The XPS C1s and O 1s core level spectra for the worn surfaces of Al390-T6, gray cast iron, and Mn-Si brass are presented in Figure 4.20 and Figure 4.21, respectively. C 1s XPS peak in the case of Al390-T6 consists of a symmetric peak, whereas in the case of Mn-Si brass and gray cast iron more carbon components can be seen. The peak at 284.6 eV corresponds to the C contamination, which is always present [76, 77]. The C 1s peak at 287.1 corresponds to -(C-O-R or C=O) entities, the origin of which could be from the fragmentation of the PAG lubricant used in the experiments [76, 77]. Due to polar oxygen species, this layer exhibits increased adhesion to the metallic surface. It is suggested that the good chemical affinity (improved adhesion) of this transfer layer with Mn-Si brass and gray cast iron might be the reason of their better performance, unlike the case for Al390-T6 alloy, in which case this transfer layer seems not to be XPS detectable. In the case of Al390-T6, the XPS investigation inside the wear track showed the

presence of fluorine (which is probably a lubricant additive) something that at a first sight seems to be opposite to the previous findings, though this could imply that indeed a transfer layer exists in the case of Al390-T6 alloy, but the chemical composition of this layer is different due to different interaction of the lubricant/additives with the metal aluminum surface. This different chemical identity of the transfer layer could lead to different wear mechanisms. No fluorine was detected in the cases of gray cast iron and Mn-Si brass materials.

Figure 4.21 presents the O 1s core level spectra. In the case of Al390-T6, a small broad peak centered at 531.1 eV is seen, which corresponds to O^- adsorbed on the surface (most probably coming from CO_2). In the case of gray cast iron a peak at 528.9 eV corresponding to metal oxide formed (most probable iron oxide due to the iron abundance in the alloy), a peak at 530.5 eV which corresponds to O^- adsorbed on the surface and a shoulder at 532.6 eV which corresponds to C-O-C (ether-type oxygen species) coming from the lubricant used [76, 77]. In the case of Mn-Si brass the O 1s peak appears at 531.1 eV and corresponds to adsorbed oxygen, whereas the contribution coming from a metal oxide at 529.3 eV appears as a shoulder in this case. The oxide in this case could be copper oxide due to the abundance of copper in this alloy. In the case of gray cast iron, the peak at 531.1 eV present lower intensity and also another component at 528.9 eV appeared, which corresponds to metal oxide. It is known that graphite has a layered structure with carbon atoms bond to each other in the layer by strong covalent bonds. Under applied tribological conditions breakdown of graphite structure can occur leading to species formation which contribute to the peak at 531.1 eV. The fragmentation of graphite leads to the formation of exposed covalent bonds and wear debris, entities having strong adsorption tendency (chemical affinity) to the oxygen (present in air) and H_2O-originating

groups (such as OH) (present in a humid environment) leading thus to species corresponding to the peak at 531.1 eV as previously mentioned [78].

In the above cases of oxides formed inside the wear track of cast iron and Mn-Si brass alloys the possibility of binary oxides formation cannot be excluded. The different metal cations in the two alloys could lead to a totally different combination of oxides which seems to be beneficial in the case of Mn-Si brass in addition to the previously discussed Pb melting positive effect. This could be attributed to the fact that Mn-Si brass mainly contains Cu (major element), the oxide of which has been reported to exhibit lubricious behavior, in comparison with iron oxide (oxide formed in the case of cast iron) [79]. Also in the case of Mn-Si brass, Cu_2O and CuO have been found according to our XPS studies. Based on the crystal chemistry approach introduced by Erdemir and co-workers [79, 80], in the case of binary oxides as the difference in ionic potential between the two metal cation centers increases, the formed oxides (under tribo-testing conditions) exhibit an increased tendency of forming shearable species [80]. This has the consequence of lowering the hardness and shear strength at high temperatures. According to this approach, a better screening of cations by the anions, which potentially leads to less interaction between the former and in turn leads to lower friction, can also explain the better performance of gray cast iron and Mn-Si brass compared to Al390-T6, based dominantly on the nature of different oxides formed in the contact zone under tribological conditions applied.

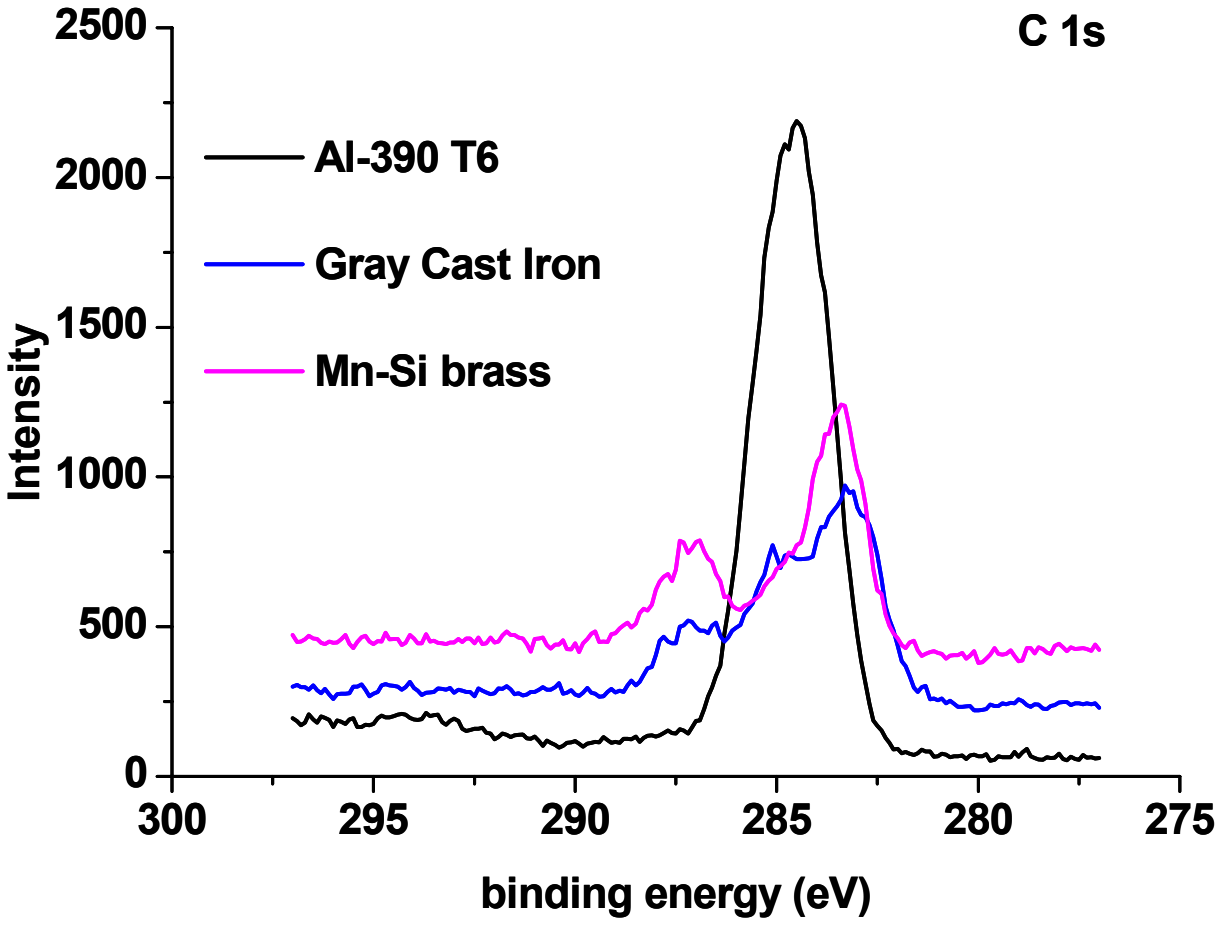

Figure 4.20─C 1s XPS core level spectra obtained inside the wear track of Al390-T6, Gray cast iron, and Mn-Si brass.

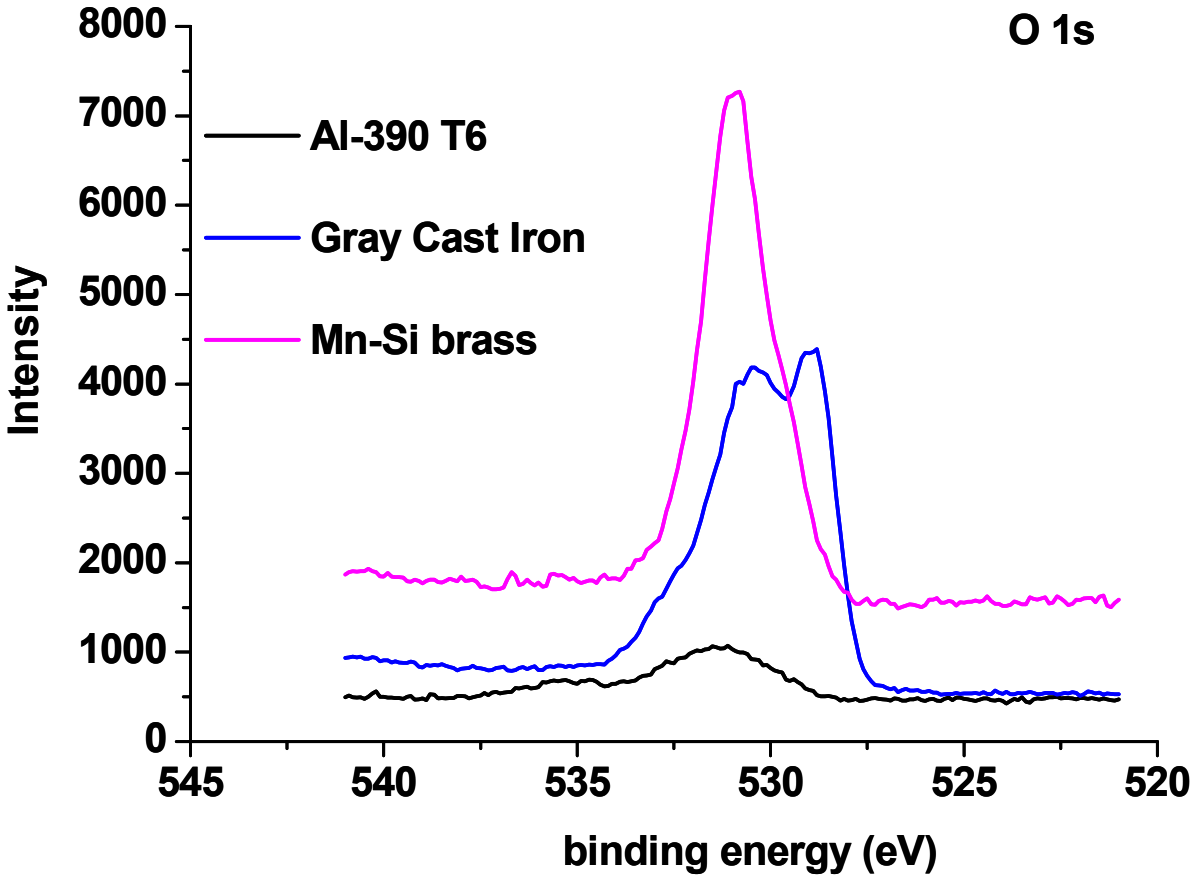

Figure 4.21—O 1s XPS core level spectra obtained inside the wear track of Al390-T6, Gray cast iron, and Mn-Si brass.

4.10 XRF studies of the PAG lubricant

After visual inspection of the lubricant after testing, it was noticed a change in color specially after the testing of Al390-T6 where in this case the lubricant turned dark. That was not the case after testing of gray cast iron and Mn-Si brass. The spectrum of XRF for the PAG lubricant before testing is shown in Figure 4.15a), while the spectrum of the same lubricant after testing with Al390-T6 is shown in Figure 4.15b). It should be noted the presence of Si (showed with an arrow) in Figure 4.15b) when compared to Figure 4.15a). Presence of Si was due to the depletion of eutectic silicon particles and is what explains the change in color of the lubricant

and the weakening of Al390-T6 at the asperity level during the wear tests. Presence of other elements such as Ca, and K can be attributed to contamination, while P it is believed to be related to the additives present in the chemical structure of PAG. Traces of other elements such as Al and Fe can be related to the chemical structure of Al390-T6. Also, it should be noted in Figure 4.15 that the La1, La2, Lb1, Lb2, Ka1, and Kb1 that followed each chemical element in the spectrum refer to electron transition in the shell being this transition characteristic for each chemical element.

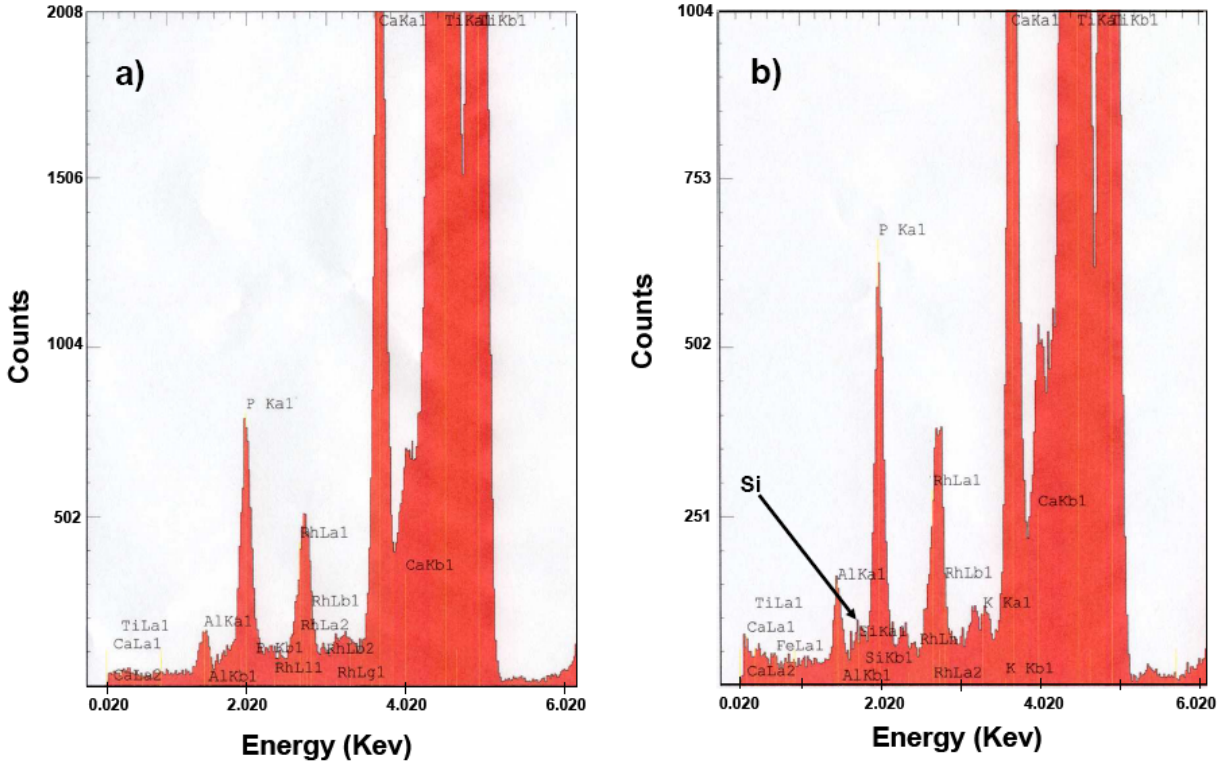

Figure 4.22─XRF spectrum of PAG lubricant tested with Al390-T6; a) before testing and b) after set 2 of experiments (constant load). The arrow indicates the presence of eutectic silicon particles in the lubricant

4.11 Summary

A comparative tribological performance of three different materials used in air-conditioning compressors and in the presence of the environmentally friendly refrigerant CO_2 was carried out. Results showed that the scuffing performance of gray cast iron and Mn-Si brass was similar and both materials performed better than Al390-T6. Unlike cast iron and Al390-T6 that exhibited abrupt scuffing failures, Mn-Si brass exhibited gradual failure, which could be advantageous in actual applications. This is an interesting finding taking into account that gray cast iron has a higher strength compared to Mn-Si brass. Based on EDS surface analysis, retardation of scuffing in the case of Mn-Si was attributed partly to the presence of lead in the matrix which melted during the onset of scuffing providing additional lubricity. Through SEM it was found that in gray cast iron cracks nucleated and propagated in the sharp corners of graphite flakes at the onset of scuffing. Also, using SEM it was shown that subsurface failure in Mn-Si brass was from fragmentation of Mn_5Si_3 particles, which was caused by stress raisers in the sharp corners of these particles leading to material failure. In the case of Al390-T6 subsurface failure was initiated in the sharp corners of primary Si particles leading to its depletion to the surface and thus weakening of this alloy. XPS showed that there is a correlation between different species coming from the fragmentation of the PAG lubricant and the scuffing behavior of the different materials tested. Also, different metal oxides formed on the surfaces could have a beneficial lubricious effect contributing to an increased scuffing resistance, as seen with Mn-Si brass. In addition, profilometric measurements and 2D roughness performed through the wear tracks of the three different materials in set two of experiments showed that gray cast iron had the lowest wear and highest material and fluid retention capacity compared to the other two materials and this was in agreement with hardness measurements. Through XRF, it was

confirmed that the dark appearance of the oil after testing in the case of Al390-T6 was due to the depletion of eutectic silicon particles. Depletion of these particles during testing was responsible for the decrease in hardness in Al390-T6 through out the wear experiments and therefore this material showed more wear compared to Mn-Si brass.

CHAPTER 5
LUBRICITY EFFECT OF CARBON DIOXIDE EVALUATED AT DIFFERENT REGIONS OF THE PRESSURE-TEMPERATURE PHASE DIAGRAM

The friction and wear performance of different lubricants and material interfaces suitable for CO_2 air-conditioning and refrigeration compressors was evaluated in chapters 3 and 4. However, those studies were performed at low chamber pressures using the HPT. This chapter studies the friction and wear performance of typical air-conditioning and refrigeration compressor interfaces at representative (high) CO_2 pressures using the UHPT, which represent realistic CO_2 compressor operating conditions.

5.1 Background

Gray cast iron is a typical sliding interface in air-conditioning and refrigeration compressors due to its high wear resistance and low cost compared to other metallic materials [81]. Gray cast irons are ferrous-based alloys with carbon and silicon percentages by volume between 3.0-4.0% and 1.0-3.0%, respectively. Note that the addition of silicon promotes the formation of graphite [81]. Graphite which constitutes one of the polymorphs of carbon is anisotropic and lamellar in nature with hexagonal crystallographic structure. It is characterized by atoms with a strong covalent type of bonding in the parallel plane and weak van der Waals bonding in the basal or perpendicular plane [82]. The weak bonding in the basal plane provides an easy cleavage and lubricity properties under sliding conditions. These lubricity properties of graphite have been the subject of investigation, e.g., studying the effect of different atmospheres on the friction and wear behavior of graphite brushes [83]. It was found that the presence of CO_2 inhibited rapid wear of graphite compared to other gases such as air, helium, and nitrogen. By

investigating the friction and wear behavior of graphite in different atmospheres it was shown that in the presence of humid environments, graphite exhibits low friction and wear compared to when tested in vacuum [84]. In a similar study the same researchers also showed that significant decrease of friction could be obtained by the introduction of inert gases (such as Ar and He) which behaved as foreign bodies aligning the surface of graphite parallel to the sliding direction [85]. Low wear was measured when gray cast iron disks were tested against gray cast iron pins in CO_2 gas environment under unlubricated conditions (similar results were also obtained in R-134a refrigerant) [52]. The wear in both CO_2 and R-134a was lower compared to the wear measured in air. In addition, an increase in hardness in the 200 nm top layer was measured during the initial stages of testing and the hardness of this layer decreased during the onset of scuffing [22]. This layer was composed of oxides due to the interaction with CO_2. Similarly, it was found that CO_2 offers an advantage over R-410a refrigerant [86]. By using Auger Electron Spectroscopy (AES) an oxygen enriched layer up to 100 nm below the surface on the sample tested in CO_2 was found, and it was claimed that this layer increased the strength of the sliding surface, thus reducing wear [86]. Improved tribological performance of gray cast iron compared to other metallic interfaces commonly used in air-conditioning compressors such as Al390-T6 and Mn-Si brass was also reported [81]. This superior behavior of gray cast iron was partially attributed to its ability to form metal oxides on the sliding surfaces providing a lubricity effect and an increased scuffing behavior [81]. The tribological behavior of 52100 steel disks against 440C bearing steel balls in the presence of CO_2 was also reported [87]. It was found that the presence of tribochemical layers of iron carbonates on the sliding surface exhibit a beneficial effect in reducing friction and wear. Based on the CO_2 refrigerant -related studies, it is important to study the impact of pressure and mass of CO_2 on the friction and wear behavior of different

materials. The motivation of this chapter is to understand the effect of CO_2 pressure and mass on the tribological performance of gray cast iron and 440C stainless steel as a representative contact tribopairs used in air-conditioning and refrigeration compressors. In particular, different regions of the CO_2 P-T phase diagram were studied by controlling the pressure and temperature conditions during testing. X-ray Photoelectron Spectroscopy (XPS) was performed outside and inside the wear tracks to quantify changes in the chemical/bonding environment after tribological testing as a function of CO_2 pressure. Focused Ion Beam (FIB) was also employed to measure the thickness of the tribolayers being formed due to the interaction of CO_2 with the sliding surfaces under study.

5.2 Controlled tribological experiments

Tribological experiments were performed using a stationary self-aligned pin in contact with an upper rotating disk; both made of gray cast iron. The chemical percentage by weight of the gray cast iron samples was Iron (balanced), Carbon (3.2-3.7%), Manganese (0.70-0.80%), and Silicon (2.2-2.55%). The geometry of the samples used is shown in Figure 5.1. The lower stationary pin and the upper rotating disk were mounted on the UHPT which is a specialized custom-designed machine for testing at high chamber pressures up to 2000 psi and temperature control up to 120 ^{o}C. Four different sets of unlubricated wear type of experiments were performed. Unlubricated experiments are useful in situations where the impact of the atmosphere (in this case CO_2) on the tribological performance of tribopairs needs to be evaluated. During this study the effect of CO_2 pressure and mass on the friction and wear behavior of gray cast iron was of interest.

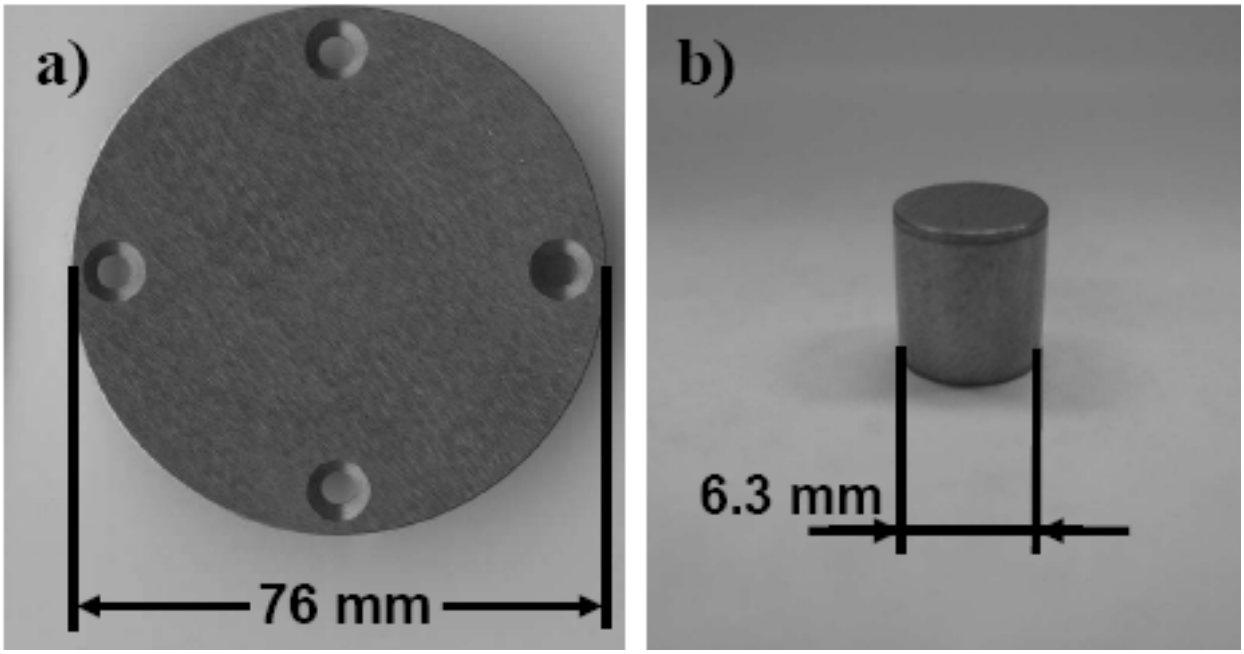

Figure 5.1─Gray cast iron samples used for tribological testing; a) disk and b) pin.

The experimental parameters of normal load, linear speed, CO_2 chamber temperature, mass, and pressure are summarized in Table 5.1 and using a combination of these parameters different regions of the CO_2 phase diagram were studied as shown in Figure 5.2. Since the volume of the chamber of the tribometer was constant (~$2x10^{-3}$ m^3), the desired CO_2 pressure during experimental sets 1, 2, and 3 was achieved by increasing the number of CO_2 molecules. To decouple the effect of pressure from the effect of mass (molecules) of CO_2 on the tribological behavior, the last set of experiments (set 4) was performed under constant CO_2 mass and the desired pressure was reached by introducing Argon molecules in the chamber. This set was also verified using Helium gas. During set 4, the amount of CO_2 mass fed into the chamber was 100, 50, 10, and 5g and the desired total pressure was increased by introducing Argon or Helium (inert gases) inside the chamber. It should be mentioned that the region of interest at the high pressure side of an air-conditioning compressor is the one corresponding to set 3 where CO_2

above the critical point is called supercritical fluid. Under the supercritical condition, CO_2 can no longer be considered a fluid composed of two separate phases (gas-liquid). Due to its specific location in the phase diagram, supercritical fluids possess distinctive properties. Depending on the pressure and temperature (P-T) values on the phase diagram, the density of CO_2 will be closer to the liquid or the gas phase. As can be seen in Fig. 5.3, above the critical point the isothermal lines have a negative slope which means that the fluid can be isothermally compressed and can be in equilibrium [88]. However, when the critical point is reached the isothermal becomes horizontal and the compressibility of the fluid becomes infinite. Although at temperatures above the critical point CO_2 has a combined density of gas and liquid, it has been proven that the higher the temperature the closer the behavior to an ideal gas [89]. Fig. 5.4 shows a compressibility chart for different gases including CO_2. On this diagram, T_R and P_R are the reduced temperature and pressure respectively. These parameters represent the ratios of the temperature and pressure of the gas of interest over their critical temperature (T_c) and critical pressure (P_c) respectively and are plotted against the compressibility factor (Z) [89], which is a function of the ideal gas parameters (see equation 5.3). The previous relationships can be expressed as:

$$T_R = \frac{T}{T_c} \tag{5.1}$$

$$P_R = \frac{P}{P_c} \tag{5.2}$$

$$Z = \frac{PV}{RT} \tag{5.3}$$

For instance as shown in Fig. 5.4 for CO_2 under supercritical conditions (P=8.27 MPa, T=70 °C) T_R=2.25 and P_C=1.16 and Z~0.80 and CO_2 resembles the behavior of an ideal gas in which case

Z=1.0. However, at the critical condition Z=0.1 and CO_2 deviates significantly from an ideal gas behavior.

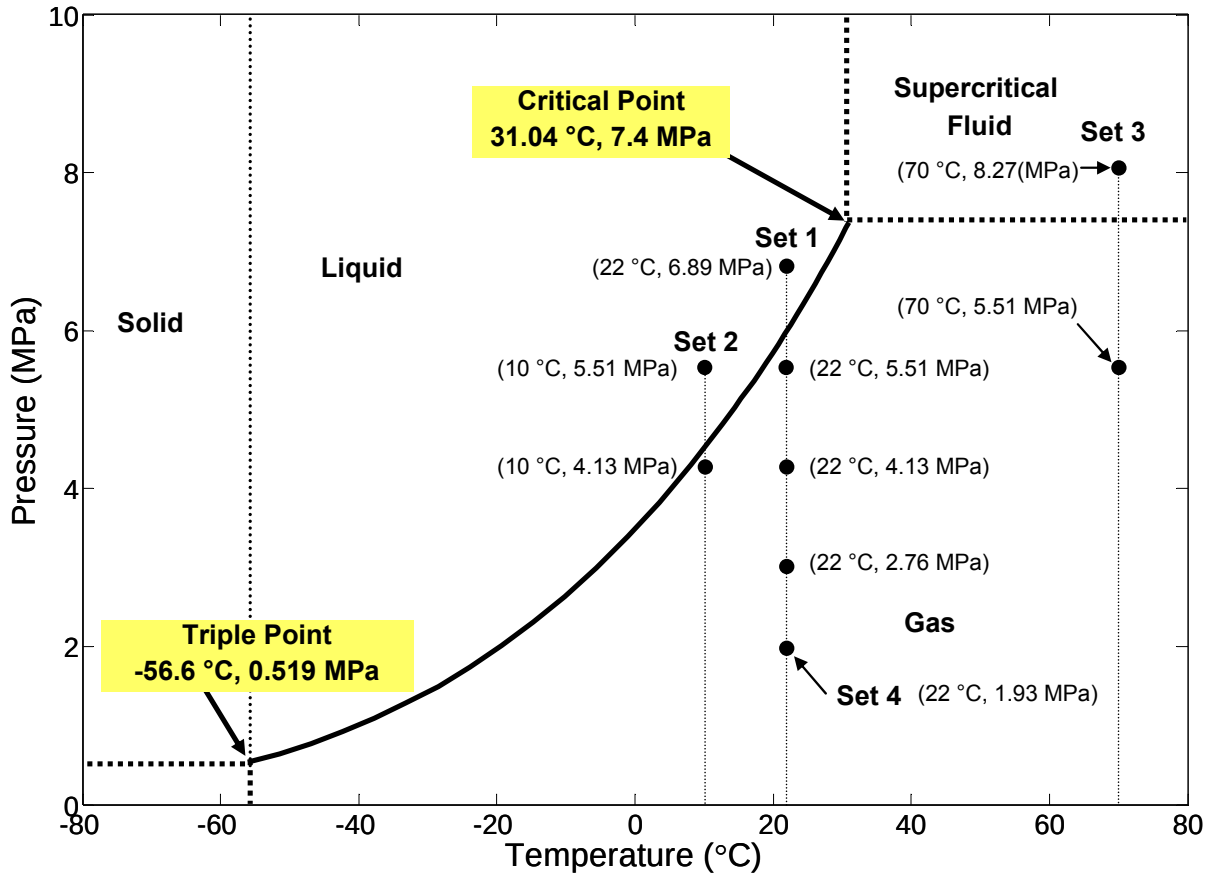

Figure 5.2—CO_2 phase diagram indicating the 4 sets of experiments: sets 1 and 4 were performed at identical temperature and pressure conditions with the difference being that in set 1 the CO_2 mass was increased with pressure whereas in set 4 the CO_2 mass was kept constant and pressure was increased by introducing Argon and Helium molecules.

An extra set of experiments using 440C steel disk in contact with a 52100 steel shoe (configuration of this geometry can be found in [81]) was performed at identical conditions as in set 3 (8.27 MPa, 70 °C) to verify that the findings were not only relevant to gray cast iron.

Chemical percentage by weight of 440C stainless steel was Iron (79.15%), Carbon (1.10%), Manganese (1%), Silicon (1%), Chromium (17%), and Molybdenum (0.75%).

Table 5.1—Experimental conditions used in the different sets of experiments.

Note that all experiments were conducted at a constant normal load of 89 N, a linear speed of 2.4 m/s and a sliding distance of 2880 m. Superscript numbers 1^* and 2^* refer to the transcritical and supercritical gas phases of CO_2 respectively.

Set of Experiments	**Pressure of CO_2 (MPa)**	**Chamber Temperature (°C)**	**CO_2 Mass (g)**	**Phase**
Set 1	2.75	22	72	Gas
	4.13	22	108	Gas
	5.51	22	143	Gas
	6.89	22	180	Liquid
Set 2	4.13	10	108	Gas
	5.51	10	143	Liquid
Set 3	5.51	70	143	Gas^{1*}
	8.27	70	215	Gas^{2*}
Set 4	4.13	22	50	Gas
	5.51	22	50	Gas
	6.89	22	50	Gas

As mentioned in Chapter 1, the operating pressure conditions in CO_2 systems are approximately 3.5 MPa and 30 °C at the low pressure side of the compressor and 13.5 MPa and 160 °C at the high pressure side (see Figure 1.1). The root-mean square roughness (R_q) of the samples before testing was approximately ~0.50-0.80 μm (using 1 mm-long profilometric scans).

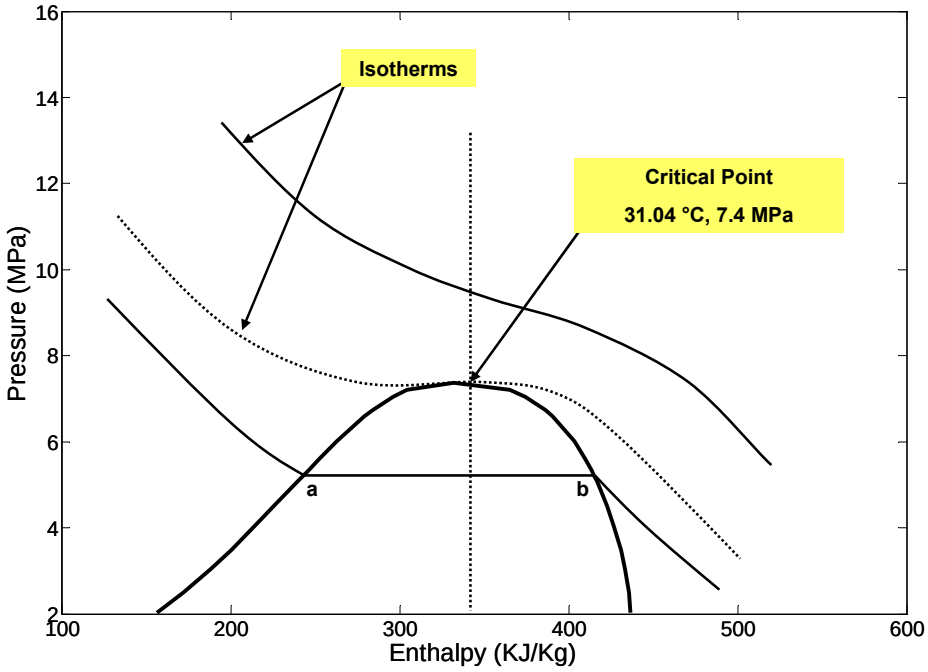

Figure 5.3—Pressure-Enthalpy diagram for CO_2 showing isotherm lines.

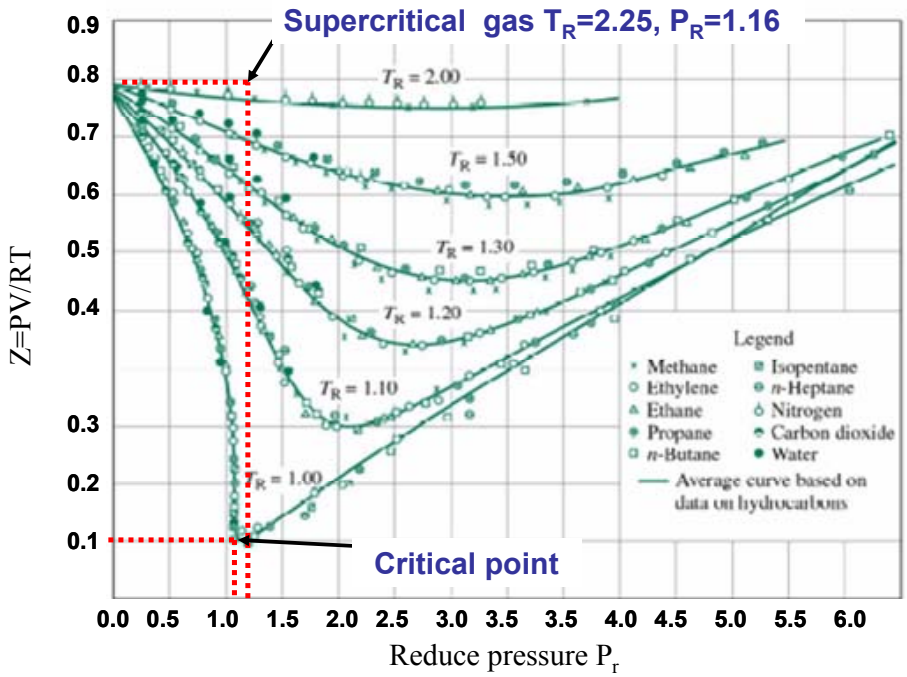

Figure 5.4—Compressibility chart for different gases; Z represents the compressibility factor and T_R and P_R the reduced temperature and pressure respectively.

5.3 Experimental results

Representative experimental results from set 1 are depicted in Figure 5.5. For the cases of 2.75, 4.13, and 5.51 MPa CO_2 pressure, the friction coefficient behavior was similar with average values ranging from 0.11 to 0.17. Note that these values are similar to boundary lubricated experiments at 0.17 MPa CO_2 pressure, where the friction coefficient was 0.14 [81]. Interestingly, when the CO_2 pressure was raised to 6.89 MPa, the friction coefficient was significantly reduced to approximately ~0.07 displaying a positive lubricity or "superlubricity" effect. This lubricity effect can be explained from two different perspectives; the first one has to do with triggering of the anti-frictional effect of the graphite (which is present in gray cast iron) at the onset of transition from gas to liquid phase (see Figure 5.2). The second possible explanation for the low friction with increased CO_2 pressure is related to the formation of dangling bonds. Dangling bonds are those that have been broken because of sliding and are available for species to react with. CO_2 is a reactive gas which leads to the passivation of dangling bonds during sliding, resulting in a decrease in friction [85]. This passivation results in the formation of iron oxides and iron carbonates that have been reported to have a positive tribological effect [87]. Also, this decrease in friction has been reported in the past, where it was found that a decrease in friction was observed when cast iron was tested in air [90]. They attributed this friction decrease to the adsorption of water molecules present in the humid air. The near contact temperature shown in Figure 5.5b) was stable throughout the duration of the tests with an average value from 22-31 °C. Similar behavior was observed in earlier studies [52], where the near contact temperature only increased significantly at the onset of adhesive failure (scuffing). For repeatability purposes two set of experiments performed at room temperature and

5.51 MPa are shown in Fig 5.6 where it can be observed that friction coefficient has similar trend for the two experiments.

Experimental results from set 2 are shown in Figures 5.7. During this set of experiments as well as sets 3 and 4, only the variation of friction coefficient is shown because there were no significant changes in the near contact temperature. As shown in Figure 5.7, at 10 °C the friction coefficient was approximately 0.12 (4.13 MPa CO_2 pressure), which is similar to the experiments performed at identical pressure and room temperature conditions in set 1 (where in both cases CO_2 is in gas phase). Note that at 5.51 MPa and 10 ^oC, the friction coefficient was 0.07, which is lower compared to the 5.51 MPa and 22 ^oC case. It should be clarified that at 5.51 MPa and 10 °C, CO_2 is in the liquid phase (see phase diagram in Figure 5.2) and the explanation for the decrease in friction is similar to the one given for the case of 6.89 MPa at 22 °C, set 1.

Results from set 3 are shown in Figure 5.8, where at 5.51 MPa and 70 °C (CO_2 behaves like a transcritical gas) the friction coefficient starts at 0.07 reaches a peak of 0.11 (at 390 m sliding distance) and decreases again to 0.07 at ~1990 m where it reaches steady-state until the end of the experiment. At 8.27 MPa and 70 °C, CO_2 is a supercritical fluid (see Figure 5.2) and its behavior resembles that of an ideal gas. Under this state, CO_2 is a complex fluid where no distinction between gas and liquid phase could be made. As seen in Figure 5.8, under supercritical conditions (which is the state found at the high pressure side of CO_2 air-conditioning compressors), friction coefficient starts at 0.11 and then decreases to approximately 0.07. These transitions were also observed when 440C stainless steel was tested against 52100 steel shoes. In this particular experiment, friction coefficient started at 0.15 decreasing to ~0.07 at the end of the experiment. As will be explained in the XPS section, this evolution toward lower friction values can be attributed to the formation of tribolayers with anti-frictional

properties that improve the wear resistance and the event of asperity interaction resulting in lower friction values.

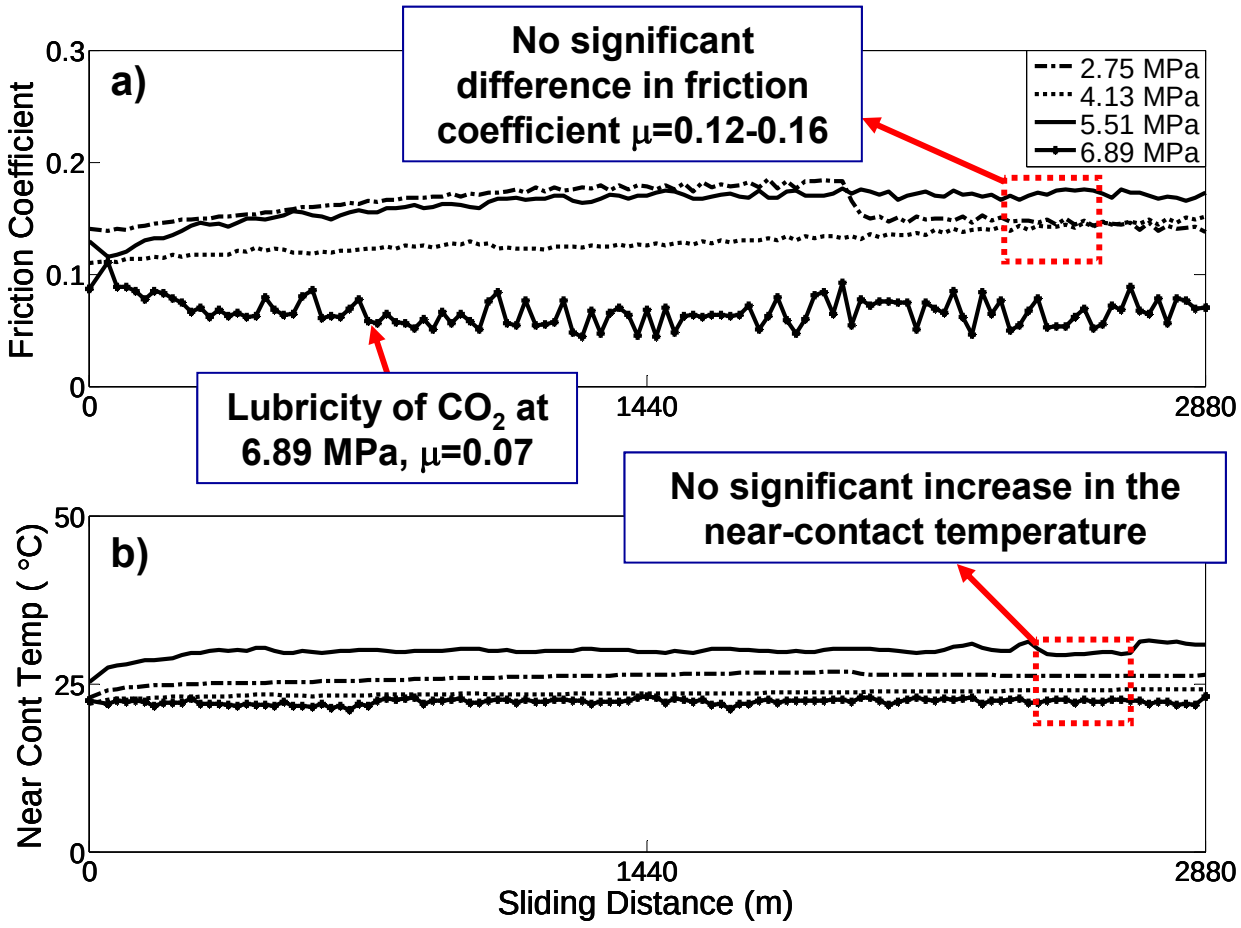

Figure 5.5—Typical experimental results from set 1 (Table 5.1); a) friction coefficient, b) near contact temperature as functions of sliding distance.

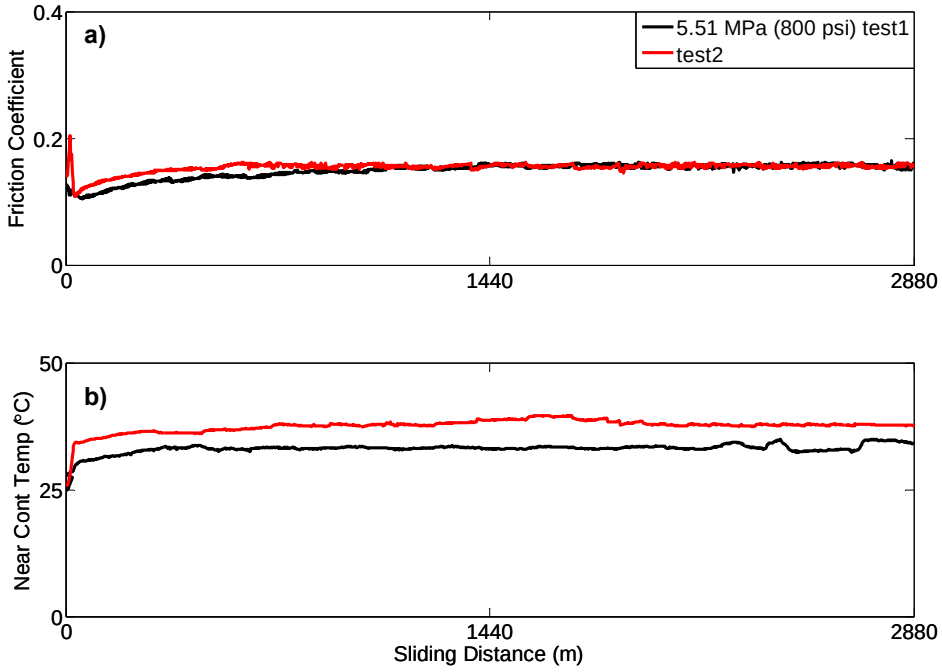

Figure 5.6─Experimental results at 5.51 MPa during set 1. It can be observed that both friction coefficient and near contact temperature trends are repeatable; a) friction coefficient, b) near contact temperature as functions of sliding distance.

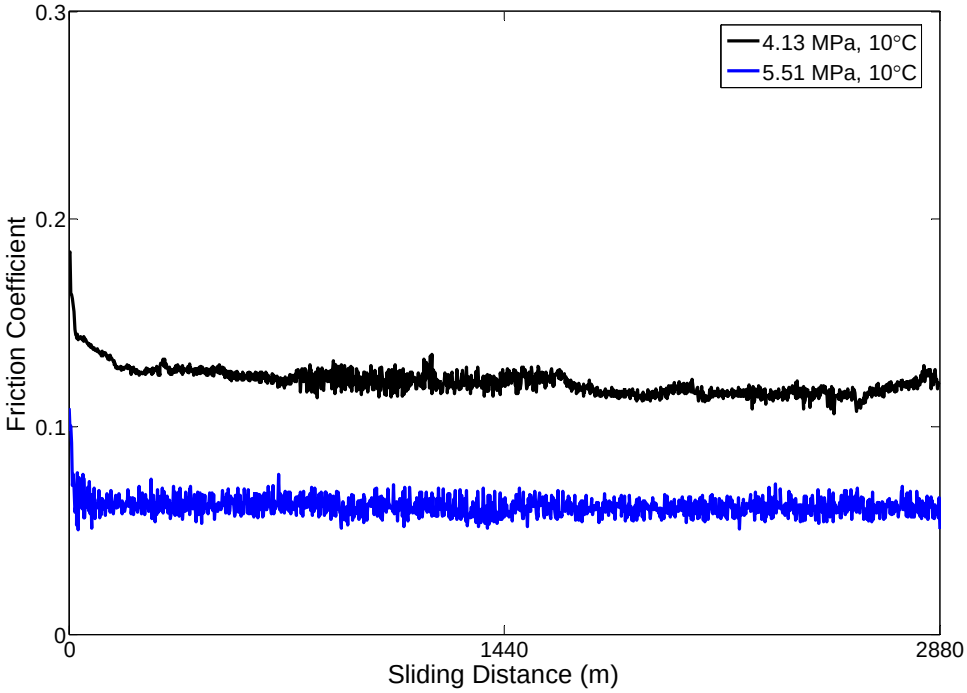

Figure 5.7─Typical experimental results for set 2. Parameters are listed in Table 5.1.

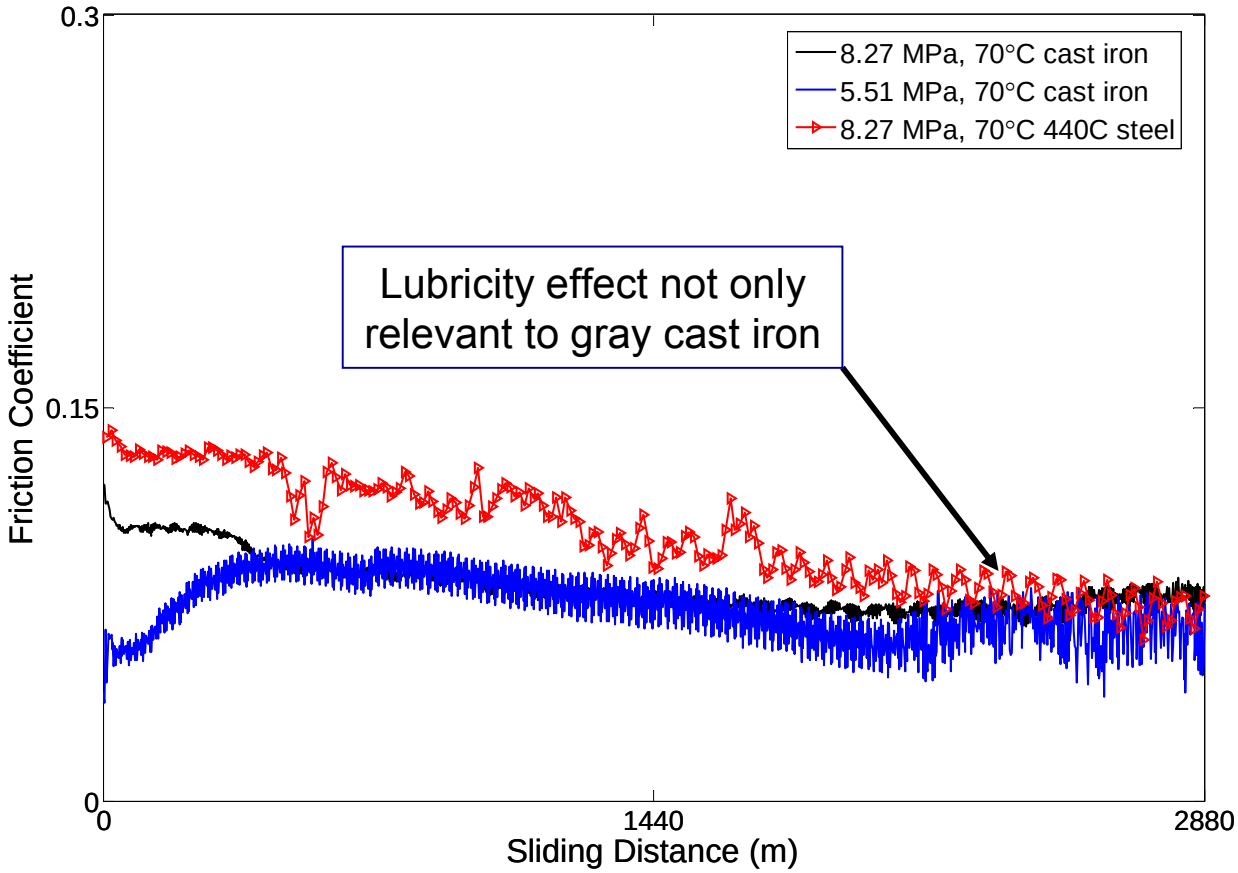

Figure 5.8—Typical experimental results for set 3. Parameters are listed in Table 5.1.

Experimental results from set 4 are shown in Figure 5.9. The objective of this set of experiments was to decouple the effects of mass and pressure on the tribological behavior. Under these testing conditions it has to be mentioned that the partial pressure of CO_2 is 1.93 MPa (280 psi) and the effect of Ar is only of compressing the CO_2 molecules on the sliding interface. Experimental results show that at 4.13 MPa, the friction coefficient reaches a maximum value of 0.14 during the running-in period and then decreases to 0.11 (similar behavior was observed at 5.51 and 6.89 MPa with subtle differences on the transitional behavior). This transitional behavior can be explained by the fact that Argon (which is an inert gas) does not have the potential to chemically react on the surface of gray cast iron during sliding. Nevertheless, it has the tendency to be inserted into the graphite lattice [85]. This insertion has the effect of causing

mobility since Ar atoms behave like foreign bodies which distort the crystal lattice, forcing recrystallization. During recrystallization, reorientation of crystallites takes place and the surface of graphite aligns parallel to the sliding direction resulting in a decrease in friction. According to different researchers, graphite displays several transitions towards a low friction coefficient in the presence of argon and these transitions can take significant time to reach steady state [85], even though in the experiments shown in Figure 5.9, it appears that steady-state friction values are reached within the test duration.

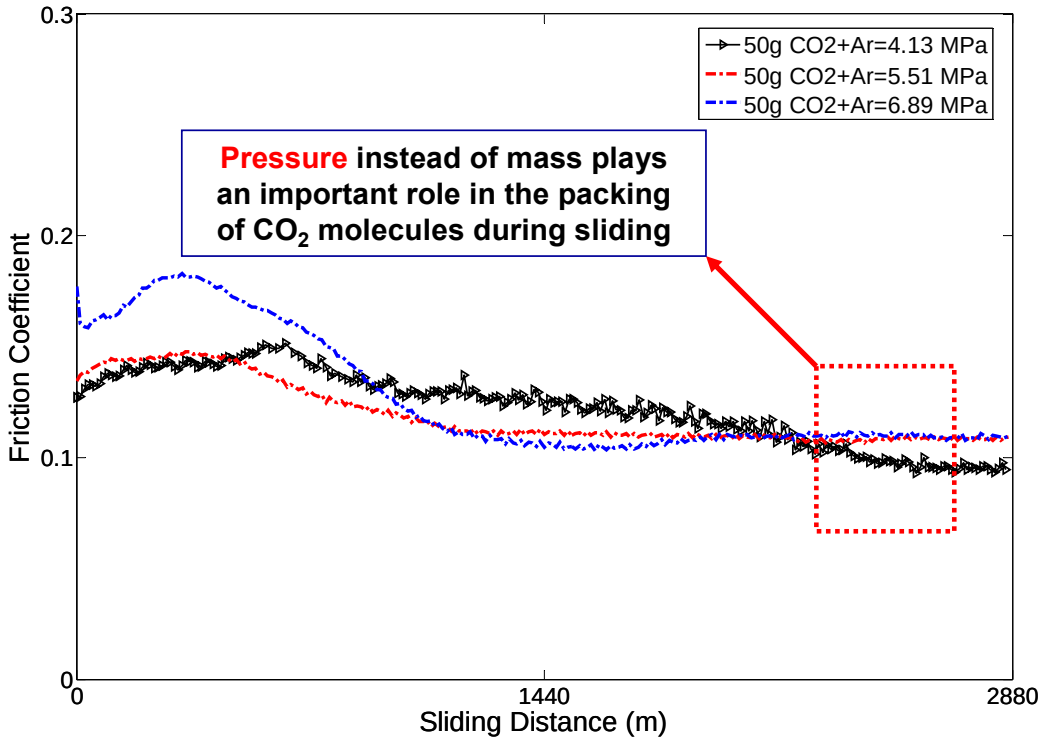

Figure 5.9—Typical experimental results for set 4. Parameters are listed in Table 5.1.

Additional experiments were performed using 5 g of CO_2 and the pressure was increased using Argon and Helium. As can be observed in Figure 5.10 by using 5 g of CO_2 mass and raising the pressure up to 400 psi (2.75 MPa) the friction coefficient was approximately ~0.15

(slightly higher compared to Figure 5.9) throughout the 2880 m of sliding distance. However, when the pressure was raised only to 100 psi (0.69 MPa) scuffing was observed. These results suggest that is the CO_2 pressure and not the mass which plays a positive role in the tribological performance of gray cast iron. It was also observed that using the same testing conditions (normal load and sliding speed), but only compressing the testing chamber with Argon the interface scuffed after few minutes of the tests reinforcing the positive role of the CO_2.

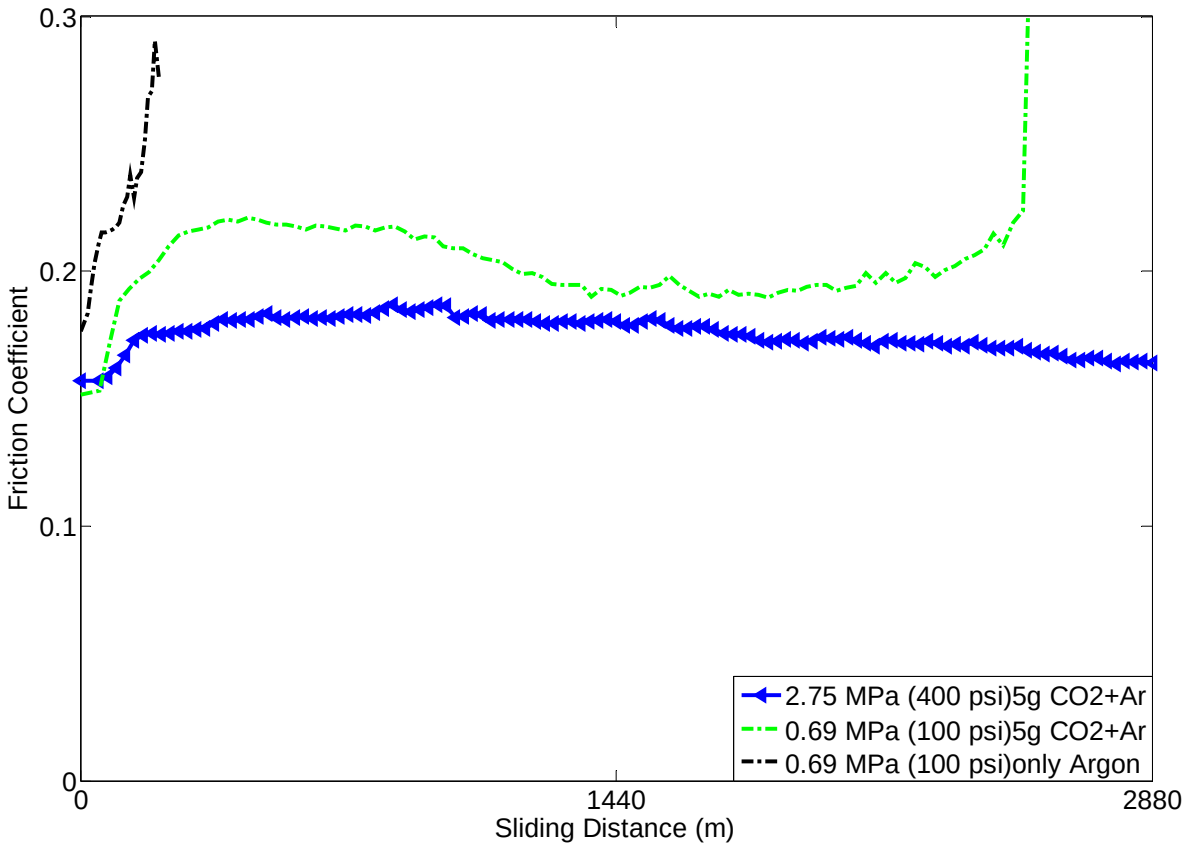

Figure 5.10─Experimental results for set 4. In this case 5 g of CO_2 were used which provide a partial pressure of approximately 0.17 MPa (25 psi). The pressure was raised to the desired value using Argon.

In addition, further tests were performed using 10 and 50 g of CO_2 and the chamber compressed using Helium (see Figure 5.11) at 2.75 MPa (400 psi). It can be observed that friction values are similar comparing 10 and 50 g of CO_2. Also, both previous friction values were similar compared to those obtained at 10 g of CO_2 and Argon.

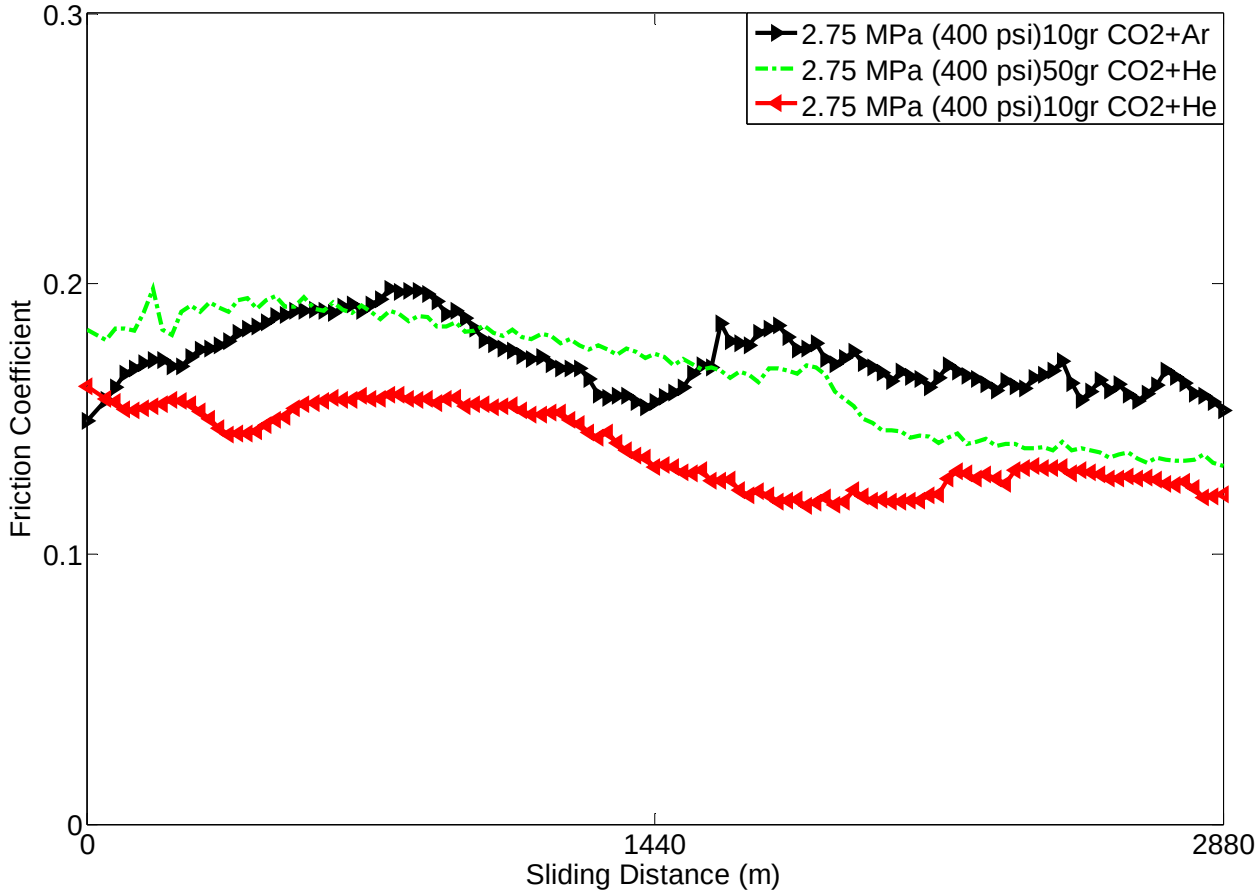

Figure 5.11—Experimental results for set 4. In this case 10 and 50 g of CO_2 were used which provide a partial pressure of approximately 0.31 MPa (45 psi) and 1.93 MPa (280 psi). The pressure was raised to the desired value using Helium and Argon.

Table 5.2 summarizes all the friction data obtained from the performed unlubricated experiments. From this table it is clear that the minimum amount of CO_2 that must be placed in the chamber to avoid scuffing is 5 g. This value corresponds to ~2.5 kg/m^3 if the empty volume of the chamber

of the UHPT is considered. It is expected that above this value of mass of CO_2 per unit volume of the chamber scuffing will not appear. Although the friction results shown here are expected to be representative of gray cast iron and steels under mild loading conditions (90 N, 2.4 m/s), they can not be used for other type of alloys such as Al390-T6 and Mn-Si brass due to the abrasive behavior of Si which could cause premature scuffing.

Table 5.2—Summary of experimental results for the different set of tests. It should be noted that in set 4 CO_2 molecules were compressed using Argon while in the additional tests Argon and Helium were employed.

Set of Experiments	**Pressure of CO_2 (MPa)**	**Chamber Temperature (°C)**	**CO_2 Mass (g)**	**Friction coefficient**
Set 1	2.75	22	72	0.14
	4.13	22	108	0.14
	5.51	22	143	0.17
	6.89	22	180	0.07
Set 2	4.13	10	108	0.12
	5.51	10	143	0.08
Set 3	5.51	70	143	0.07
	8.27	70	215	0.07
Set 4	4.13	22	50	0.09
	5.51	22	50	0.12
	6.89	22	50	0.12
Additional tests	0.17	22	5 (Argon)	0.30 (scuffed)
	2.75	22	5 (Argon)	0.15
	0.69	22	0 (only Argon)	0.30 (scuffed)
	2.75	22	10 (Argon)	0.16
	2.75	22	10 (Helium)	0.13
	2.75	22	50 (Helium)	0.12

5.4 Surface topographical measurements

Roughness measurements were performed inside and outside the wear tracks of the samples tested in set 1 under 4.13 and 6.89 MPa (since they exhibited different friction behavior, Fig. 5.5). Figure 5.12a) shows a typical surface image on the untested region (outside the wear track) while Figure 5.12b) shows the burnishing of the asperities inside the wear track (tested region). It is expected that under sliding conditions asperities will touch and deform causing wear or burnishing, depending on the normal loading conditions. It should be emphasized that despite the absence of any liquid lubricant, no significant wear was observed, further supporting the lubricity properties of CO_2.

Using the same techniques described in chapters 3 and 4, detailed parameters were obtained from the surface scans and comparisons of the root-mean square (R_q) and skewness (S_{sk}) values are shown in Table 5.3. After testing, S_q decreases by ~ 44% for the sample tested at 4.13 MPa while a reduction of ~13% was observed for the case tested at 6.89 MPa. Skewness provides information about burnishing and values are typically negative for engineering surfaces [15], becoming more negative as the surface experience burnishing. As seen in Table 5.3, S_{sk} decreased by 234%, and only 49% for the 4.13 MPa and 6.89 MPa cases, respectively. Larger changes in S_q and S_{sk} in the case of 4.13 MPa indicate higher degree of burnishing, thus confirming better lubricity properties at higher CO_2 pressures.

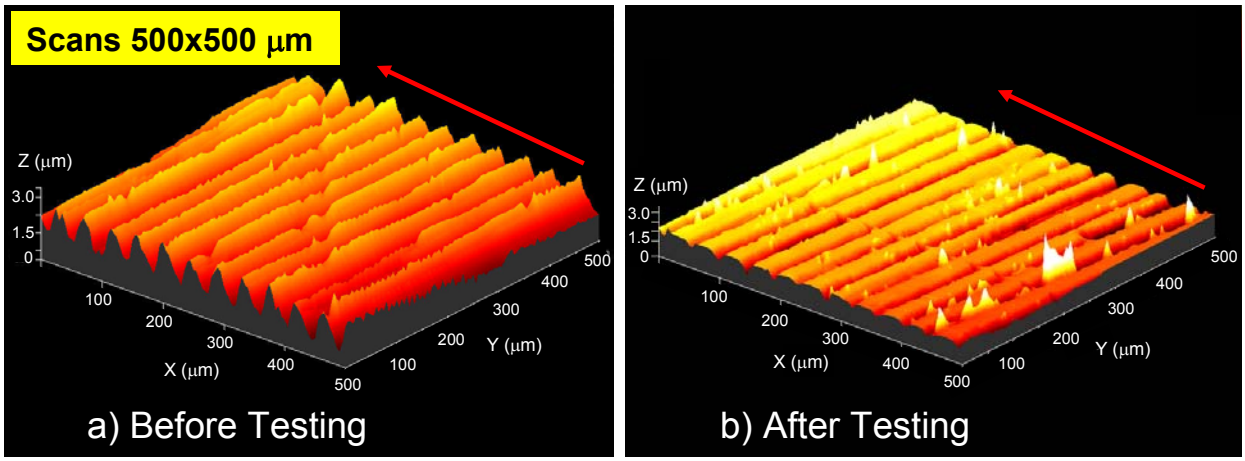

Figure 5.12—Typical surface roughness scans using a contact profilometer; a) before testing, b) after testing , set 1, 4.13 MPa.

Table 5.3—Surface roughness parameters obtained during set 1.

Parameter	**Chamber Pressure (MPa)**					
	4.13			6.89		
	Virgin	Tested	% Change	Virgin	Tested	% Change
S_q (μm)	0.78	0.42	44	0.48	0.42	13
S_{sk}	-0.19	-0.64	234	-0.37	-0.55	49
S_c (nm^3/nm^2)	961	465	52	593	398	33
S_m (nm^3/nm^2)	23	14	39	14	12	14

A set of functional volume parameters to characterize material and fluid retention properties were also obtained and given in Table 5.3. The unoccupied material volume is encompassed between the 10 and 80% of the bearing area curve and represents the empty volume within this region. As seen in Table 5.3, the core void volume of the surface (S_c) in the case of 4.13 MPa decreased by ~ 52% after testing, while in the case of 6.89 MPa decreased by

33%. The material volume (S_m) of the asperities contained at 100% of the bearing area curve decreased by 39% and 14% for the 4.13 MPa and 6.89 MPa case, respectively. Variation of these roughness indices effectively show that as the CO_2 pressure increases, less burnishing of the asperities is observed.

Using Scanning Electron Microscopy (SEM) the changes on the topography of the surface were also verified. As observed in Figure 5.13a) and c) morphological changes of the sample surface tested at 4.13 MPa are clearly seen with testing. The surface undergoes mild burnishing and this burnishing was deeper for sample tested at 4.13 MPa compared to the one tested at 6.89 MPa (shown in Figure 5.13b) and d)). The usefulness and applicability of functional parameters becomes relevant when the wear can not be characterized by loss of mass or volume changes and only mild burnishing is seen. In the present work no significant amount of wear either by mass or volume was measured which justified the usefulness of the functional parameters, and furthermore confirmed the lubricity properties of CO_2 refrigerant.

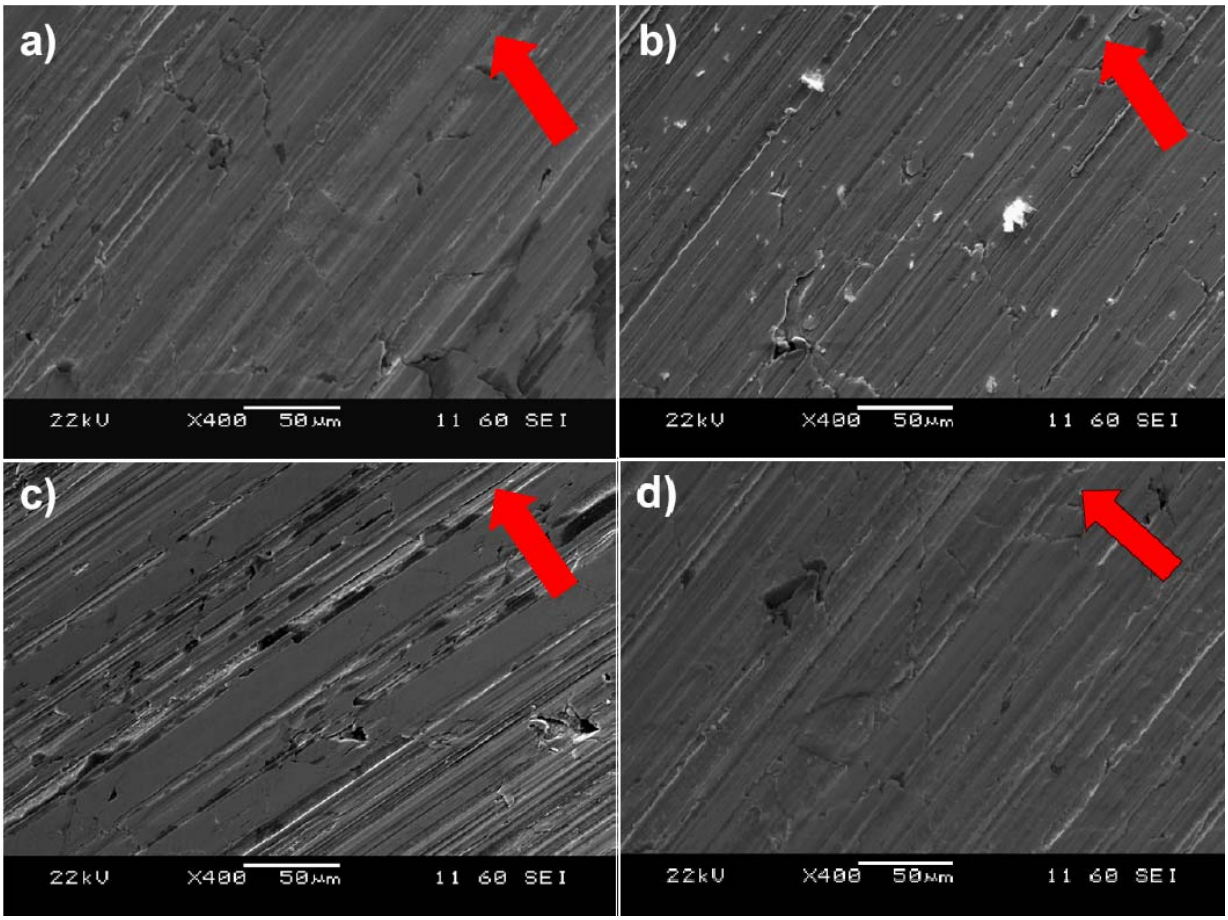

Figure 5.13─SEM microscopy images of the samples tested during set 1; a) outside and c) inside the wear track at 4.13 MPa, b) outside and d) inside the wear track at 6.89 MPa (arrows represent sliding direction).

5.5. XPS

Figure 5.14a), b), and c) present the C1s, O1s, and Fe 2p XPS core level spectra obtained from the worn surfaces of gray cast iron disks under 4.13, 5.51 (both at room temperature, set 1) and 8.27 MPa (70 °C, set 3) CO_2 pressures. Figure 5.14d), e) and f) present the C1s, O1s, and Fe 2p XPS core level spectra of the original (unworn) surfaces for comparison purposes after the experiment conducted at 5.51 MPa. The C 1s spectrum of the unworn surface presents a main peak at 285 eV and a smaller one at about 288.9 eV which can be attributed to C-C or C-O bonds originating from organic contamination. In the O 1s spectrum of the unworn surface the peaks at

529.8 and 531 eV could be attributed to oxides and hydroxides present on the surface, most likely Fe_2O_3 and $Fe(OH)_3$. The width of the O1s peak in the 531-533 eV area could be linked with hydroxides, C-O bonds and adsorbed water species, as reported in [91] and [92].

In the case of the worn surfaces, the peak in the C1s spectrum at 289.4 eV is associated with the presence of iron carbonates, $FeCO_3$ [91, 93]. This result is supported by the O 1s peak at 531.7±0.2 eV and the peak at 710.2 eV (Fe 2p spectrum) which are presented in Figure 5.14b) and c) respectively. These peaks are also shown in Figure 5.15 and 5.16 for the O1s and C1s respectively. Also the peak at 289.4 eV (C 1s) presents an increase in its intensity as CO_2 pressure increases, a supporting evidence for the greater extent of reaction towards carbonates formation (increase on tribolayer growth kinetics). In the case of Fe 2p spectrum for the specimen tested at 4.13 MPa, the two peaks at 710.2 and 711 eV, corresponding to iron carbonates and iron oxides respectively, can be clearly observed (see in more detail in Figure 5.17). The carbonate species peak is becoming more intense as CO_2 pressure is increased to 5.51 and 8.27 MPa. The aforementioned results strongly support the fact that CO_2 molecules react with the surface, under sliding conditions, towards formation of $FeCO_3$. This carbonate containing tribolayer contributes to the reduction of friction in agreement with the literature [87].

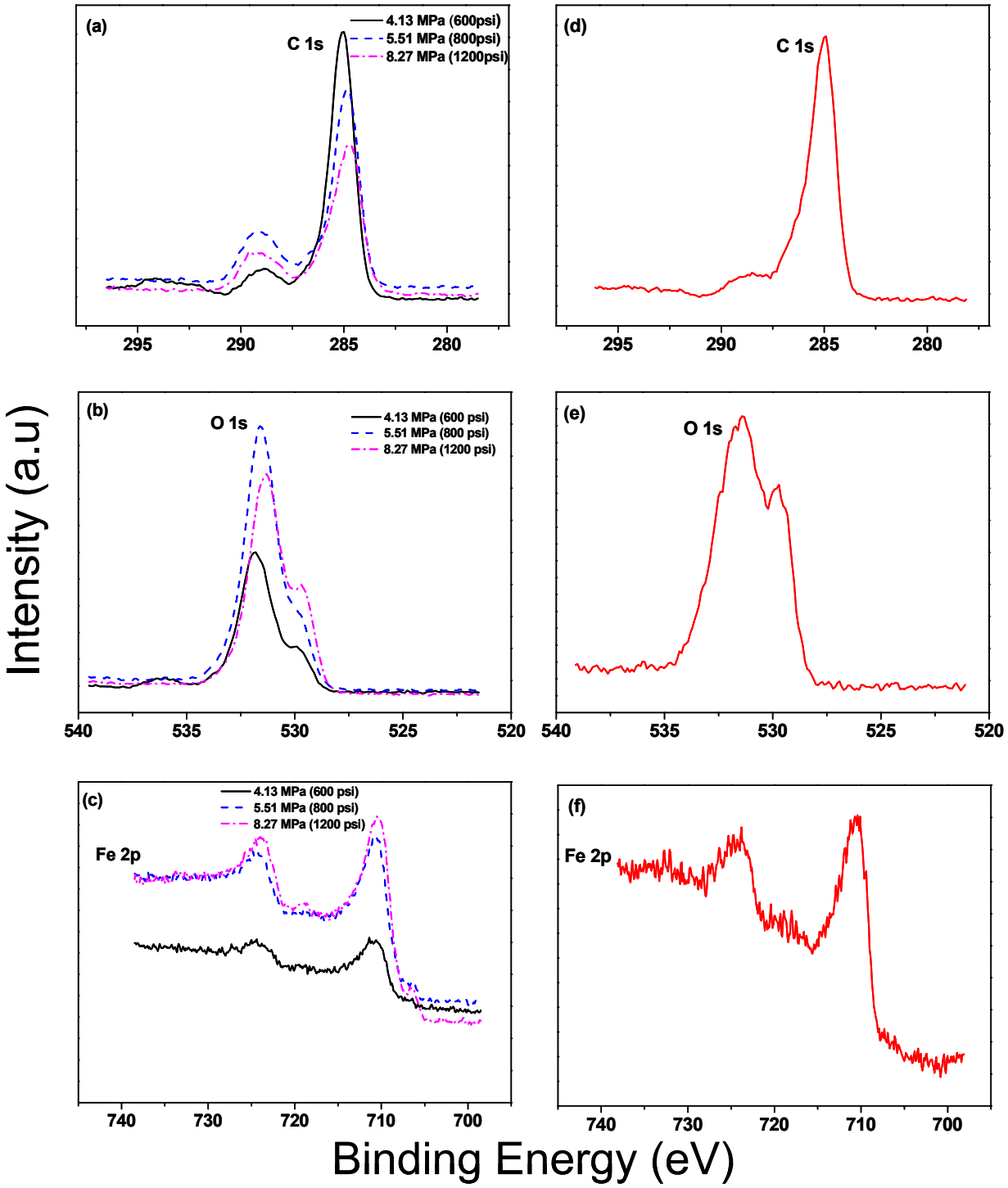

Figure 5.14─XPS core level spectra measured inside the wear track; a) C 1s, b) O 1s, c) Fe 2p for the samples tested at 4.13 and 5.51 MPa (22 °C), set 1 and at 8.27 MPa (70 °C), set 3; d), e) and f) are measurements outside the wear track (unworn) for the 5.51 MPa, set 1 case.

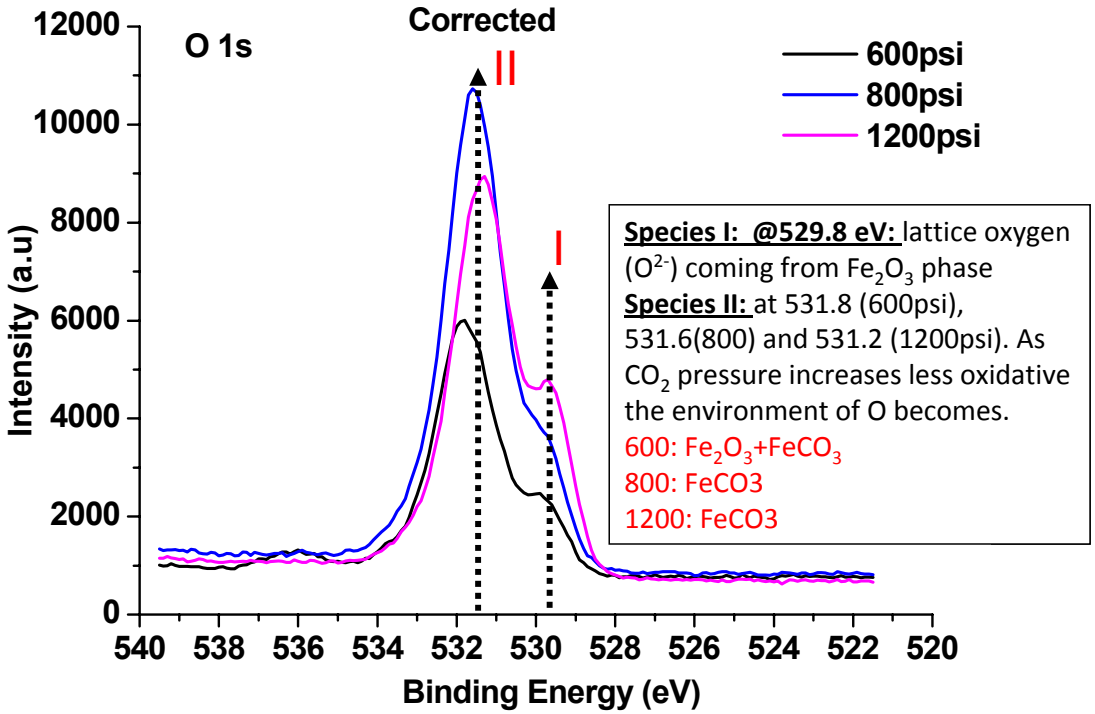

Figure 5.15—O 1s XPS core level spectra measured inside the wear track for the samples tested at 4.13 and 5.51 MPa (22 °C), set 1 and at 8.27 MPa (70 °C) set 3.

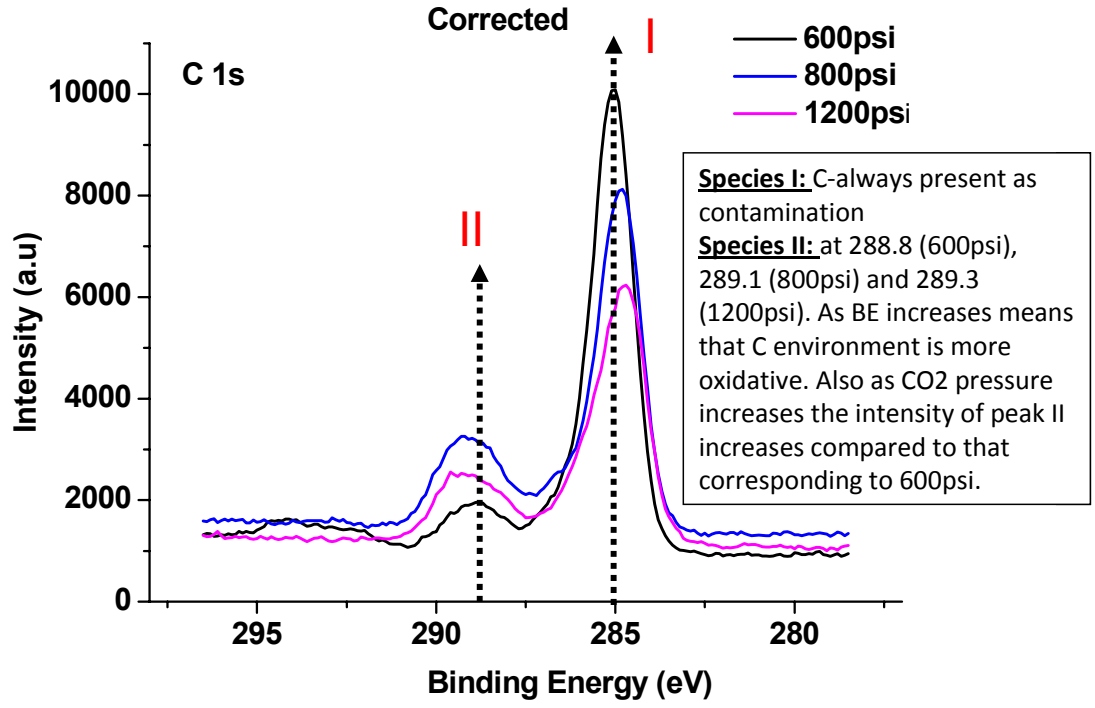

Figure 5.16—C 1s XPS core level spectra measured inside the wear track for the samples tested at 4.13 and 5.51 MPa (22 °C), set 1 and at 8.27 MPa (70 °C) set 3.

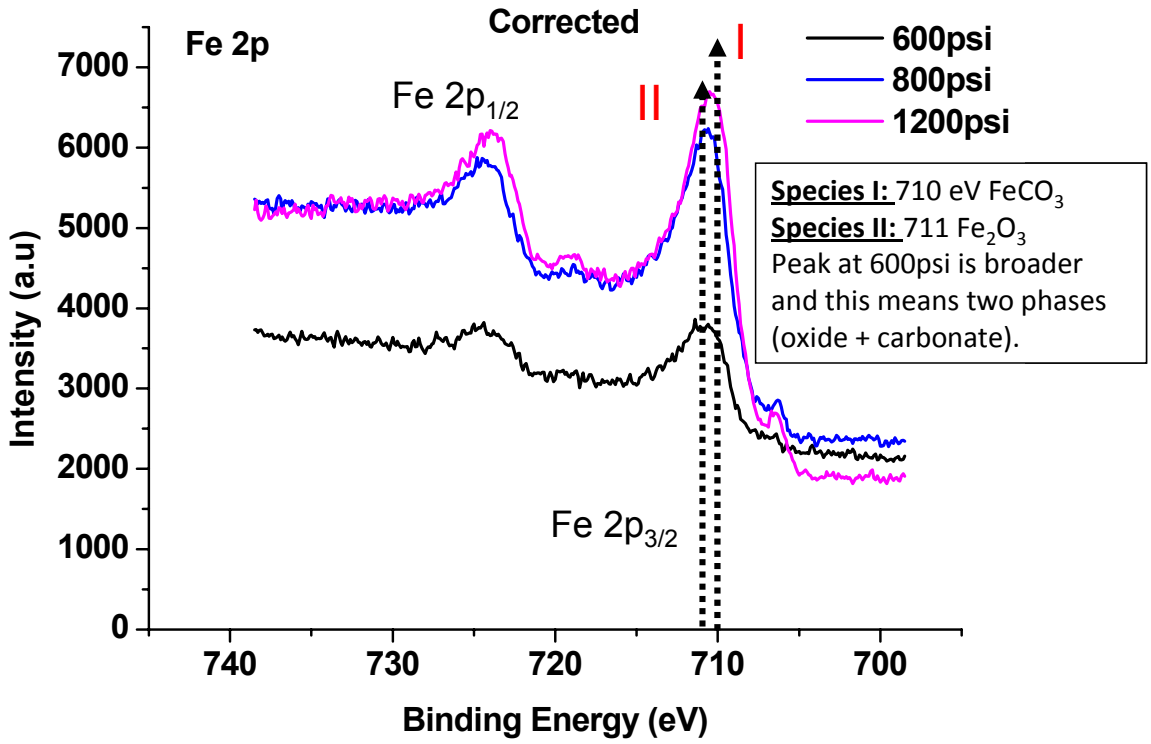

Figure 5.17—Fe 2p XPS core level spectra measured inside the wear track for the samples tested at 4.13 and 5.51 MPa (22 °C), set 1 and at 8.27 MPa (70 °C) set 3.

For a detailed analysis of the above presented data, peak fitting of XPS peaks was performed using CasaXPS tool and a Shirley type background subtraction. Figure 5.18, 5.19, and 5.20 presents the peak fitted spectra of C 1s, O 1s, and Fe 2p respectively for the specimen tested under 4.13 MPa of CO2 pressure and the quantitative results for all the tests studied (4.13, 5.51, and 8.27 MPa) are given in Table 5.4. α, β, and γ components in the C 1s peak are the peaks with maxima at 285, 286.1 and 289.3 eV corresponding to C contamination, C-O bonds and carbonates species, respectively [94]. For the O 1s peak, α, β, and γ components correspond to the peaks with maxima at 531.7, 529.9 and 533.5 eV which are associated with carbonates, lattice (oxidic) oxygen and adsorbed water, respectively [94]. For the Fe 2p spectra, the α and β

components correspond to 710.2 and 711.5 eV which are linked with carbonates (most likely iron carbonates) and oxides (most likely iron oxides), respectively [94].

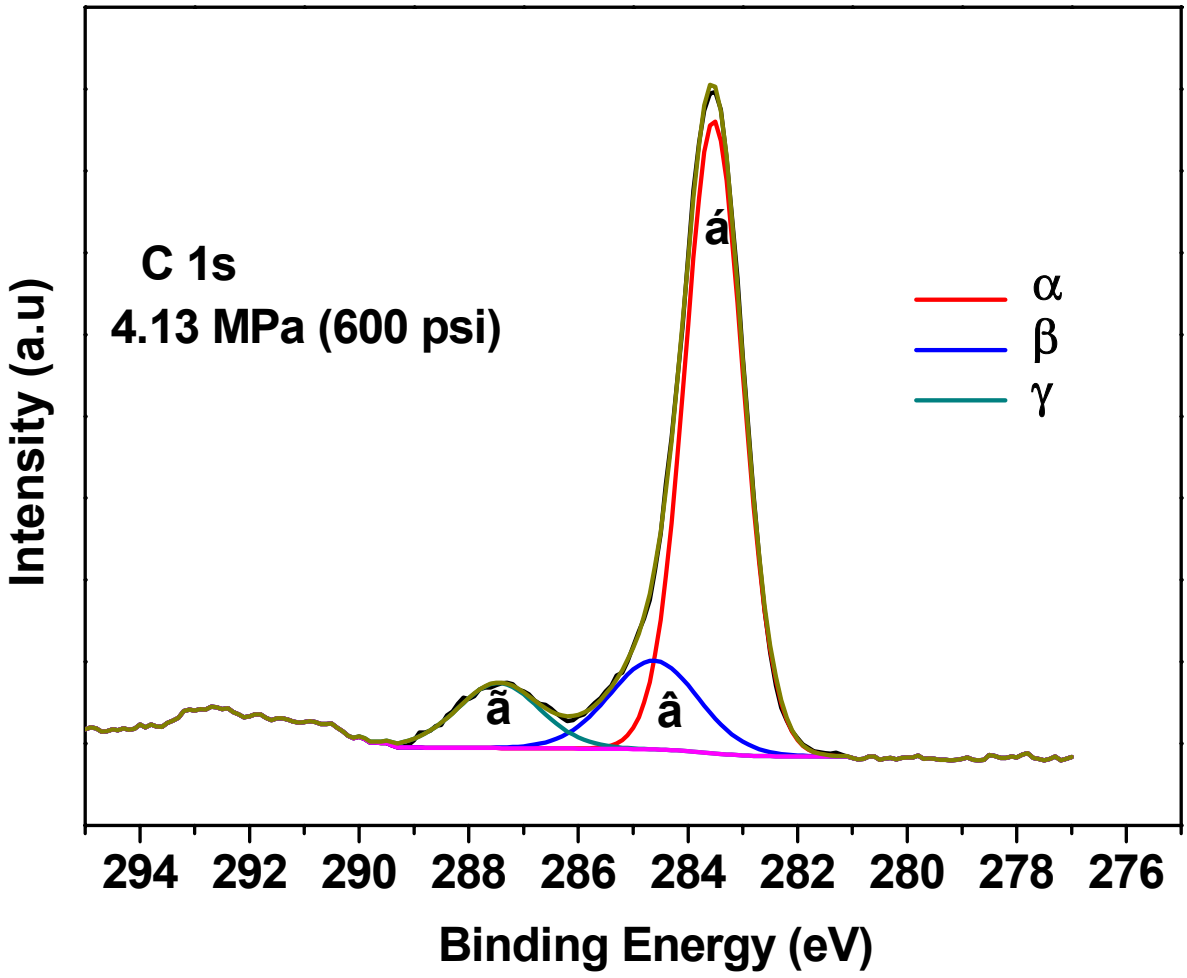

Figure 5.18─C1s XPS core level spectra measured inside the wear track (4.13 MPa, 22 °C) after peak fitting, showing components α, β, γ.

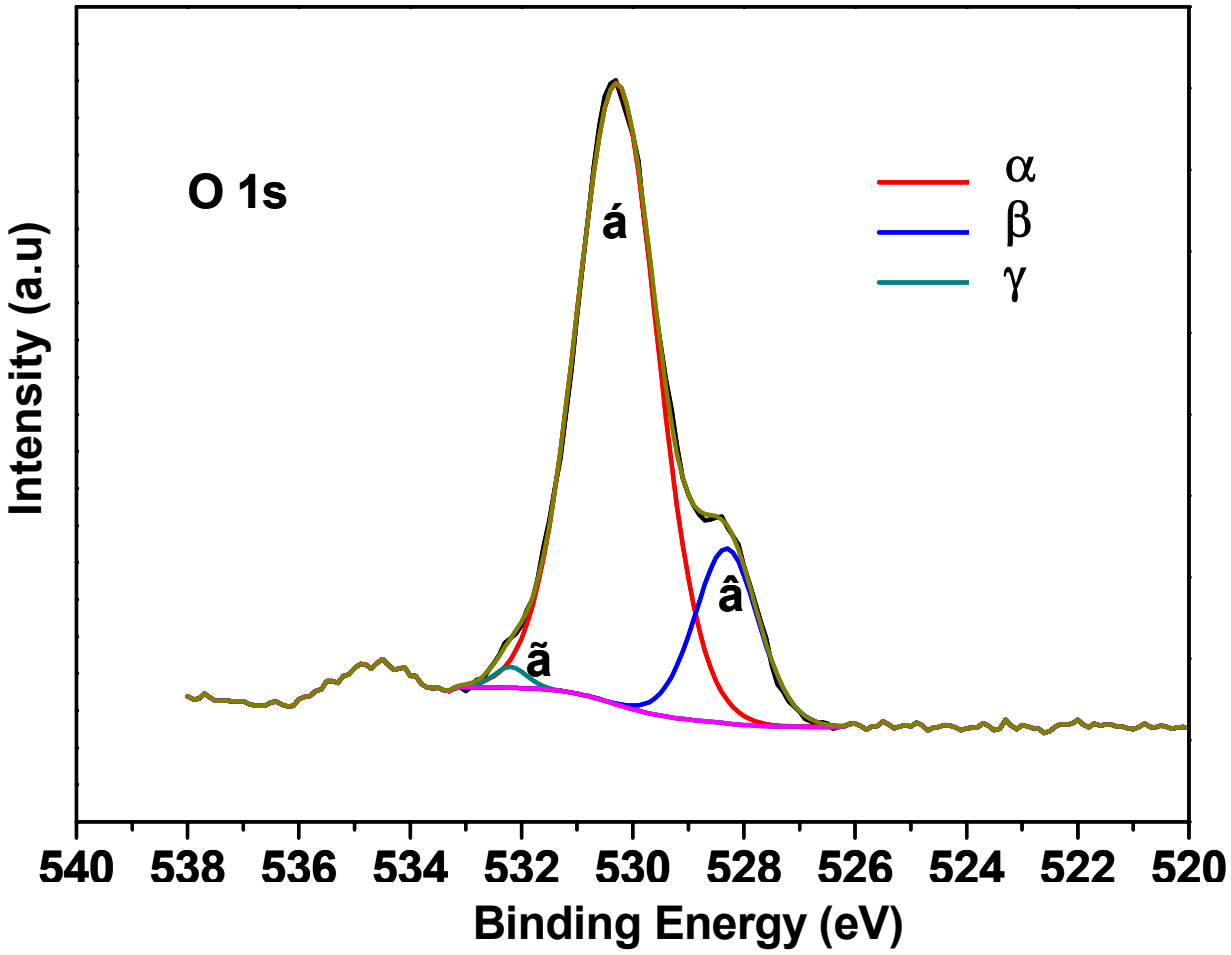

Figure 5.19─O 1s XPS core level spectra measured inside the wear track (4.13 MPa, 22 °C) after peak fitting, showing components α, β, γ.

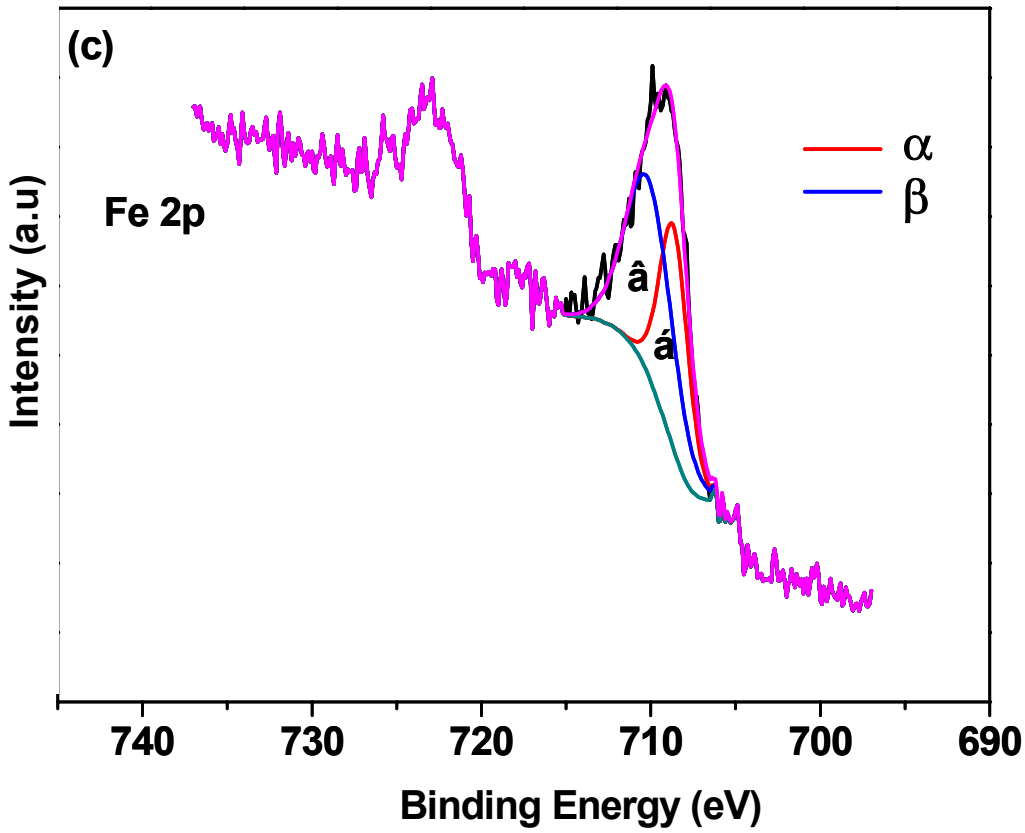

Figure 5.20─Fe 2p XPS core level spectra measured inside the wear track (4.13 MPa, 22 °C) after peak fitting, showing components α, β (Fe 2p).

In the above cases, the 1.5, 1.7, and 1.9 eV charge shifts were taken into account for the experiments run at 4.13, 5.51, and 8.27 MPa, respectively. Based on the values listed in Table 5.4: (i) as CO2 pressure increases, the Fe component linked with carbonates species increases from 41% at 4.13 MPa to 57-60% at 5.51 and 8.27 MPa. This implies that as more CO_2 molecules are place in the chamber during sliding, the higher the rate of tribochemical reactions (all the tests were performed for the same amount of time). This could be understood considering that CO_2 (an acidic molecule) is adsorbed on the surface of a metal oxide, interacting with groups having basic character, such as O_2- and OH- towards formation of carbonate species, as depicted in Figure 5.21; (ii) As CO_2 pressure increases, C-components associated with

carbonate species (γ peak at 289.3 eV) increases from ~11% to 25 % indicating that the above mentioned reaction is facilitated; (iii) The simultaneous decrease of the percentage of α component in the case of O 1s and Fe 2p corresponding to iron carbonates, after the run performed at 8.27 MPa, could be indicative of a minor chemical decomposition of the iron carbonates.

Table 5.4─Surface atomic concentrations measured by XPS after peak fitting.

Pressure (MPa)	**Temperature (°C)**	**C components (%)**	**O components (%)**	**Fe components (%)**
4.13	22	*α* (73.5) *β* (15.8) *γ* (10.7)	*α* (81.0) *β* (18.0) *γ* (1.0)	*α* (41) *β* (59)
5.51	22	*α* (57.7) *β* (17.5) *γ* (24.8)	*α* (81.7) *β* (14.4) *γ* (3.9)	*a* (59.8) *β* (40.2)
8.27	70	*α* (38.7) *β* (36.6) *γ* (24.7)	*α* (73.8) *β* (22.3) *γ* (3.9)	*α* (57.3) *β* (42.7)

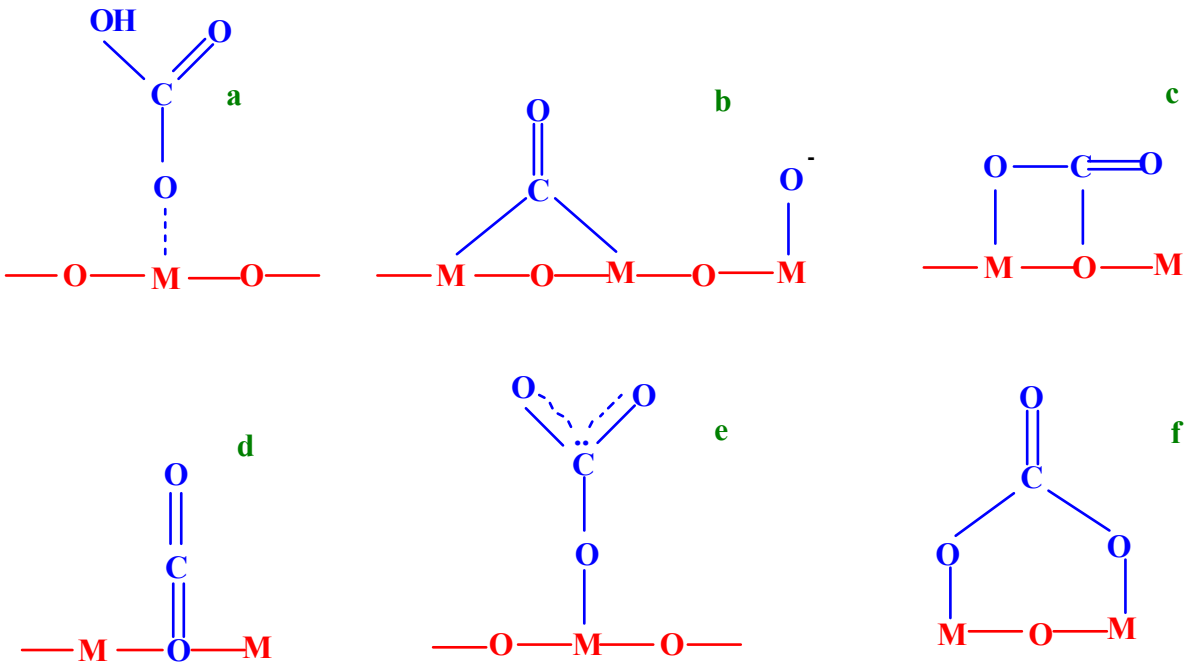

Figure 5.21—CO_2 adsorption modes onto metal oxides.

5.6 FIB

FIB measurements were performed on a dual high-resolution field emission scanning electron microscope (FE-SEM) and a scanning metal ion beam microscope. The SEM column is equipped with a Schottky thermal field emission gun that provides a resolution < 2.5 nm for accelerating voltages between 0.2 to 30 keV. Up to 30 keV ion column with a gallium metal ion source provides currents ranging from 1 pA to 40 nA. In the ion beam imaging (secondary electrons) the resolution is 7 nm at 1 pA beam current. The concurrent use of the ion and electron microscopes has a synergistic effect and significantly expands the capabilities of both.

The measurements were performed inside the wear track of the specimen tested at 8.27 MPa, 70 °C (Set 3) to measure its tribolayer thickness. This sample was exposed to the highest amount of CO_2 among all the experiments, and based on the XPS results it is expected to have a

protective layer of carbonate and iron oxides. Figure 5.22a) shows an SEM image of a deposited rectangular (30 μm by 2 μm) sacrificial layer of Platinum (Pt) on the wear track. Pt was deposited to protect the surface from sputtering during the milling process as seen in Figure 5.22b). After several steps of milling the surface was polished and the features of its microstructure were revealed using the Ion beam mode as seen in Figure 5.22c). The tribolayer which can be seen in Figure 5.22d) has an approximate thickness of 500 nm (0.5 μm). As was discussed in the XPS section, this tribolayer in the presence of CO_2 is composed of iron oxides (Fe_2O_3) and iron carbonates (siderite $FeCO_3$).

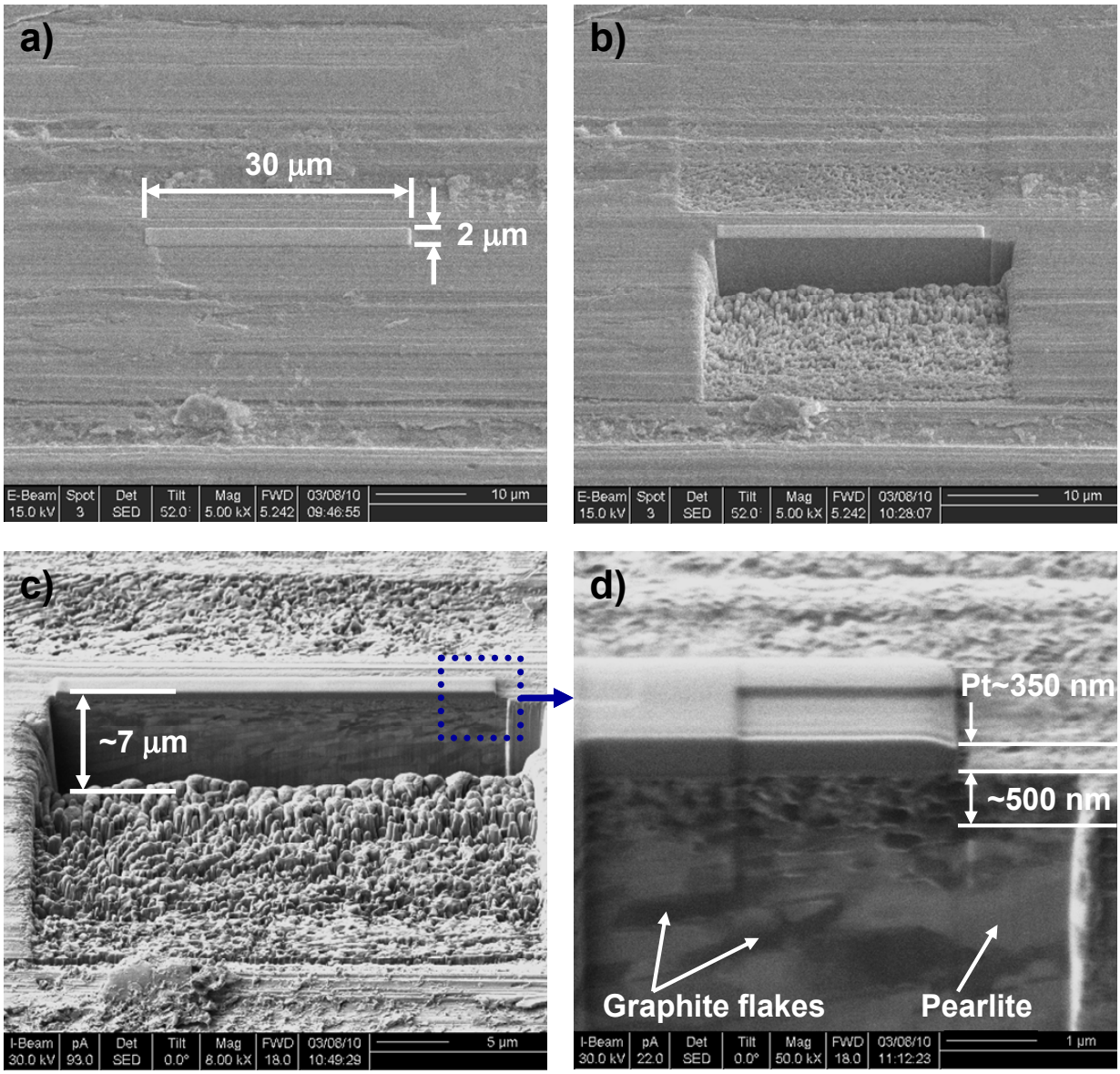

Figure 5.22─SEM microscopy images obtained from the FIB process inside the wear track of the sample tested in Set 3 (8.27 MPa, 70 °C).

5.7 Summary

In this chapter, different regions of the CO_2 P-T phase diagram were investigated (including those commonly found on the high pressure side of air-conditioning compressors). Unlubricated experiments were performed to evaluate the effect of CO_2 pressure, temperature,

and mass on the friction and wear behavior of gray cast iron. Based on the tribological and surface analysis results the following conclusions could be drawn:

a) The friction coefficient decreases to values well below 0.1, when CO_2 is on the transition from gas to liquid phase.

b) Under conditions of constant CO_2 mass (set 4) it was found that friction coefficient values were somehow different to the ones obtained under conditions of variable mass (set 1). However, based on this results and the additional tests performed, it can be stated that the determining factor for low friction is the CO_2 pressure and not the amount of CO_2 mass. Naturally there should be a minimum amount of CO_2 mass to enable superior tribological performance. Under the conditions described in this work, scuffing was observed when the CO_2 mass in the tribochamber was 5 grams. Under this amount of mass of CO_2 and it was found that the interface scuffed at low chamber pressure (0.69 MPa), but a stable friction coefficient was observed when the amount of CO_2 was kept constant the pressure was raised up to 2.75 MPa. Based on these experimental results it is not recommended to decrease the ratio mass of CO_2 to volume of the chamber to less than 2.5 kg/m^3 for tests performed under unlubricated conditions at 90 N and 2.4 m/s of normal load and sliding velocity respectively.

c) After testing, wear was minor and could not be quantified using changes in mass and volume. Therefore, mild burnishing wear was quantified using topographical functional volume parameters showed lower burnishing and

better fluid retention capacity at 6.89 MPa, compared to 4.13 MPa (set 1). These findings were verified by SEM.

d) Superlubricity effect of CO_2 was observed under supercritical conditions (8.27 MPa and 70 °C in set 3) during testing of both; gray cast iron and 440C stainless steel. This behavior means that the superlubricity effect can probably be extended to other type of materials.

e) Through XPS it was found that iron oxides and iron carbonates were formed on the tribolayer film. As CO_2 pressure in the chamber increased, iron carbonate species concentration increased at the expense of the oxides, providing anti-wear resistance. The CO_2 lubricating effect seems to be CO_2 pressure dependent and this result is most likely linked to the effect of CO_2 pressure onto the extent of CO_2 adsorption and subsequent reaction with the surface, leading to different amount of products in each case.

f) In the case of the sample tested at 8.27 MPa, 70 °C (set 3) that exhibited superlubricity, the surface tribolayer thickness was found to be 0.5 μm.

CHAPTER 6
TRIBOLOGICAL STUDY OF HIGH BEARING BLENDED POLYMER-BASED COATINGS FOR AIR-CONDITIONING AND REFRIGERATION COMPRESSORS

Chapters 2 through 5 focused on the studies of different lubricants, bare materials, and the impact of CO_2 on the friction and wear behavior respectively. This chapter will be focused on the study of advanced blended polymer based materials for air-conditioning and refrigeration compressors towards ideal situations where no lubricant is present.

6.1 Background

Tribology has emerged as one of the fields that contribute to the solution of environmental problems through the development of products and solutions less hazardous or harmful to the atmosphere. Such solutions include the development of lighter tribomaterials to decrease the energy consumption in machine components, fuel in the transportation sector and appliances, and biodegradable oils that contribute to greener environments [95]. The air-conditioning and refrigeration industry has partially addressed this issue of greener technology shifting its attention towards advanced oil-less compressors which constitute greener or cleaner technology [96]. Soft polymeric coatings are being considered a good option in situations where the absence of lubricant is desirable or in situations where abrasive particles present in the atmosphere can lead the malfunction of the liquid lubricant [49, 50, 51]. PTFE, PEEK, and Fluorocarbons are ones of the most commonly used polymer materials for high bearing blended coatings [97]. Filler particles such as MoS_2, graphite, ceramics, and boron nitride can be added to improve the friction and wear performance under unlubricated conditions. The tribological behavior of PEEK and PTFE based coatings have been studied by different researchers. For

instance, a temperature dependence on the tribological behavior of amorphous PEEK was reported [98]. On that study, the coating was composed of semi-crystalline PEEK particles (Victrex Scales Ltd, West Conshohocken, PA 19428, USA) deposited on an Aluminum substrate and turned amorphous by heating up the substrate coating up to 400 °C followed by quenching in water at room temperature. It was shown that once the temperature at the sliding interface surpasses the glass temperature (T_g) and reaches 179 °C, PEEK exhibited the largest friction coefficient and the lowest wear rate. It was shown through differential scanning calorimetry (DSC) and x-ray diffraction (XRD) that this tribological behavior was due to the crystallization of PEEK. Crystallization of the coating increases its stiffness and improves the wear behavior [98]. Regarding crystallinity of PEEK, different researchers have shown the rearrangement of polymer molecules to form crystalline grains at temperatures above T_g [99, 100]. In the case of thermoplastics materials such as PEEK, spherical crystalline regions (lamellar structures also known as spherulites) are formed due to polymer crystallization. These lamellar structures, as organized regions provide an increase in hardness and density to the disorder polymeric chains restricting their slippage and motion [101, 102]. The role of PTFE on the load carrying capacity of PEEK was examined by different authors [103, 104]. By TOF-SIMS it was shown that a film of PTFE was transferred to the counterface and its formation is governed by the degree of dispersion of PTFE into PEEK.

Even though there are some studies on the performance of commercially available PTFE and PEEK deposited coatings in the presence of refrigerant, studies dealing with their friction and wear response in the presence of lubricant (in addition to refrigerant) are missing. The objective of this chapter is to measure the friction and wear behavior of four different PEEK/PTFE (1704 PEEK®), PTFE/MoS_2 (Fluorolon 325®) , Fluorocarbon (Impleglon 218®),

and PEEK/Ceramic (1707 PEEK/Ceramic®) blend polymeric coatings under aggressive oscillatory unlubricated sliding conditions, boundary/mixed unidirectional sliding conditions, and unlubricated sliding conditions at high temperature (100 °C). Experimental findings were supported by SEM, TOF-SIMS, and XRD analysis.

6.2 Coating samples

Gray cast iron disks with an initial surface roughness (R_q) of approximately 0.2-0.4 μm before grid blasting were used as the substrate for the deposition of the coating. Grid blasting was applied on the surface of the disks to increase the surface roughness (R_q) to approximately 3.5 μm. These roughness measurements were performed using a contact profilometer (Tencor P-15). Deposition of the coatings onto the surface of the disks after blasting was performed by an authorized vendor [97]. The coatings were applied using a spray gun which deposits the coating on a previously treated substrate. The grid-blasting treatment on the surface of the disks (prior deposition of the coating) was performed by applying an 80-grit aluminum oxide abrasive which provides a stippled surface to enhanced the mechanical bonding of the deposited coating (typically during this step a blasting pressure between 40-60 psi is used). In the case of PEEK/PTFE, the PEEK particles used in the mixing are distributed by Victrex Ltd (West Conshohocken, PA 19428, USA). These particles which are grinded from the 450-G series material have an average size of ~10-12 μm and are semi-crystalline in nature [98]. Morpholine and xantham gum are used to inhibit rust and avoid sagging (formation of tears of the deposited coating) respectively. Once the coating is deposited only the main solid particles are left after curing or baking (for instance PEEK and PTFE in the case of PEEK/PTFE coating). Also, in the case of PEEK/PTFE, once the coating is deposited and cure in the oven at approximately 400 °C

the PTFE particles migrate to the top of the PEEK. In PTFE/MoS_2 the MoS_2 particles are dispersed evenly throughout the thickness of the coating to provide high load bearing properties while the PTFE component migrates to the top of the coating. In the case of Fluorocarbon, a fluorinated ethylene propylene (FEP) resin was deposited after blasting and the curing was performed at ~316 °C. In the case of PEEK/Ceramic ceramic particles are added and distributed uniformly in the thickness of the coating to improve the wear resistance at elevated temperatures. Some of the properties of these coatings are shown in Table 6.1, where the cure and in-use temperature are listed along with their hardness and typical physical color. Nanoindentation measurements were performed on a commercially nanoindenter using successive step loading (referred as pul-loading). The loading was applied employing a 90° cube corner or Berkovich tip and using a range of loads from approximately 50 to 6000 μN. Four measurements were performed for each sample and the average and plus/minus one standard deviation values are reported in Table 6.1 and shown in Figure 6.1, in this figure the hardness is plotted as a function of the contact depth.

Table 6.1—Physical properties of the polymeric coatings under study (E_r represents the reduced Young's modulus)

Property	**PEEK/PTFE**	**PTFE/MoS_2**	**Fluorocarbon**	**PEEK/Ceramic**
In-use temperature (°C)	260	260	232	260
Cure temperature (°C)	400	316	316	400
Hardness (GPa)	0.17±0.07	0.56±0.10	0.35±0.09	0.21±0.07
E_r (GPa)	6.76±0.55	7.47±0.59	4.89±1.19	8.46±1.39
Color	Dark-green	Light-blue	Black	Beige-tan

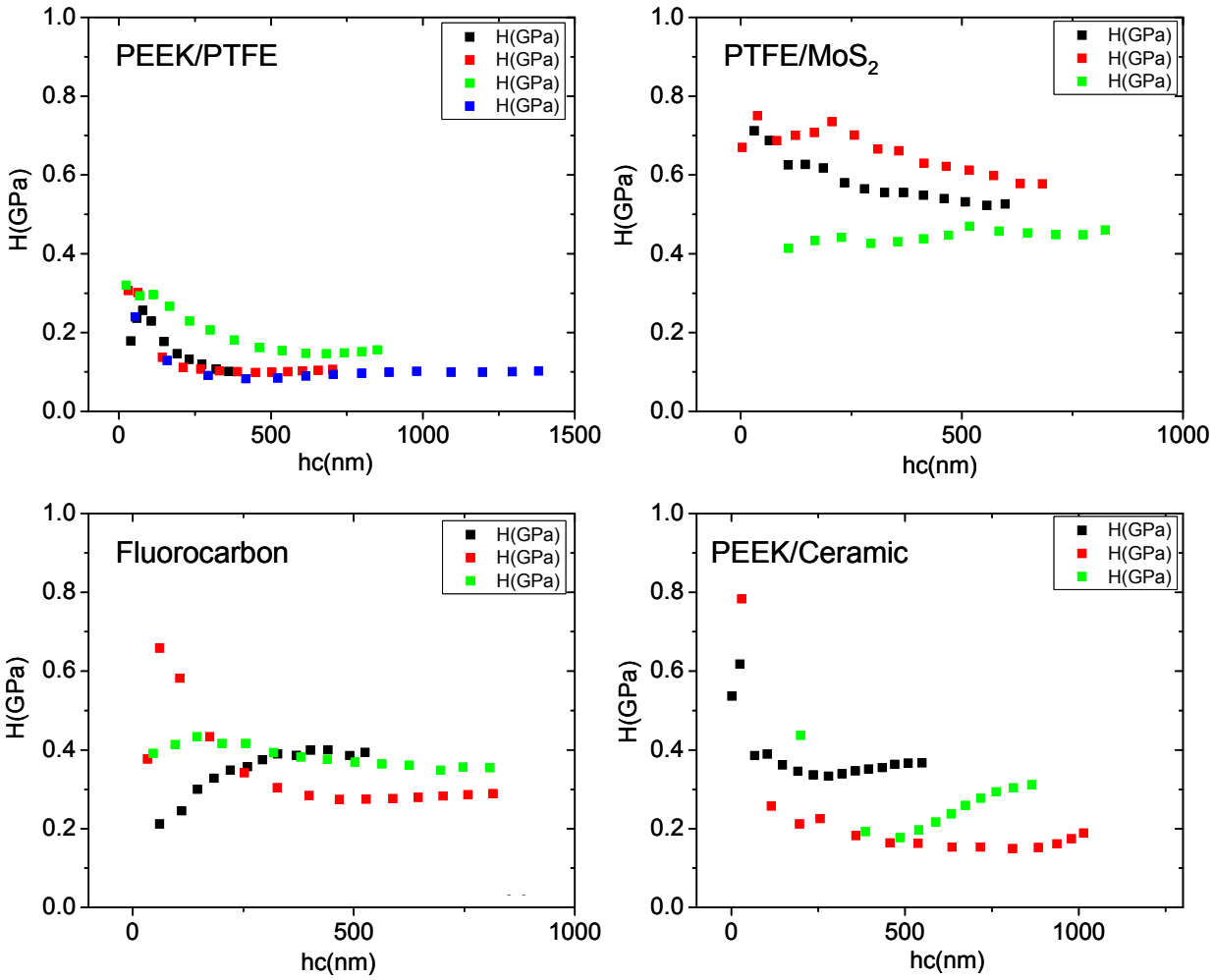

Figure 6.1—Hardness measurements of the different coatings using nanoindentation

The measured values are in agreement with the literature where a vicker micro hardness ranging from 10-16 (0.10-0.16 GPa) was measured on PEEK deposited on aluminum substrate [98, 105]. This range in hardness was obtained by changing the cooling rates after baking which provided differences in PEEK crystallinity. It should be mentioned that the nanoindentation values reported in this study did not take into account the viscoelastic nature of these polymer materials. Recommendations for future studies of the viscoelastic nature of deposited polymer coatings will be given in chapter 7.

6.3 Controlled tribological experiments

Using a sliding configuration shown in Figure 6.2, three set of experiments were performed in the HPT. During set 1, a line contact with an oscillation of ±30° and an average wear track diameter of 47.6 mm was used. The oscillation was kept constant at 4.5 Hz, generating an average and maximum velocities of 0.21 and 0.33 m/s respectively. The normal load was kept constant at 445 N (100 lbs) during 30 mins. Under these loading conditions, the line contact stress can be calculated as:

$$P_{\max} = \sqrt{\frac{E^* W}{RL\,\pi}} \tag{6.1}$$

Where E^* is the contact Young's modulus, W the contact load, R the radius of curvature of the half cylinder (shown in Figure 6.2 d)), and L is the length of the cylinder. The contact Young's modulus can be obtained as:

$$\frac{1}{E^*} = \frac{1-\upsilon_1^2}{E_1} + \frac{1-\upsilon_2^2}{E_2} \tag{6.2}$$

where in the expression 6.2, E_i and υ_i represent the Young's modulus and Poisson's ratio of the two different materials under the contact condition. Using the dimensions shown in Figure 6.2d), a maximum contact pressure of P_{max}~175 MPa was obtained. To obtain this value υ_1=0.30, E_1=200 GPa, υ_2=0.40, E_2~6 GPa as a representative Young's modulus of the polymer coatings, W=445 N, R=4x10^{-3} m, and L=8x10^{-3} m. In addition, the pressure of the chamber was kept constant at 0.17 MPa using R-134a refrigerant (Tetrafluoroethane) and the temperature in the chamber was maintained at 100 °C as this is a typical operating temperature of compressors under idle conditions. Set 2 was performed under unidirectional boundary mixed lubrication conditions. During this set the rotational speed was kept constant at 2000 rpm to provide a linear speed of 4.8 m/s and 8640 m of sliding distance during 30 minutes. The normal load was similar

compared to set 1 providing a contact pressure at the sliding interface of approximately 8 MPa (using the contact geometry shown in Figure 6.2e)). In this set, the pressure of the mixture R-134a refrigerant and PAG (Idemitsu Kosan Co., Ltd. PZ 68ZL) lubricant was maintained approximately constant at 0.17 MPa (25 psi) inside the chamber keeping the lubricant supply rate at approximately 40 mg/min. This was achieved by careful regulation of the R-134a/PAG flow in such a way that boundary/mixed lubrication conditions were obtained. The mixture R-134a/PAG was stored on a pressure vessel and sprayed at the sliding interface using a pressure nozzle. The temperature at the contact was also maintained at 100 °C similar to set 1. In set 3, the best performing coatings during set 2 were tested under unlubricated conditions keeping the same testing parameters, except the normal load that was set at ~670 N using a modified shoe (see Figure 6.2f)) to increase the contact pressure to approximately 23 MPa and generate higher amount of wear (compared to set 2), all the testing conditions are summarized in Table 6.2. Before initiating a test, the coated disks were immersed in a pool of isopropyl alcohol, while the shoes were cleaned using acetone. After this step, all the samples were ultrasonically cleaned, then rinsed with isopropyl alcohol, and finally dried using warm air. To ensure repeatability each condition was repeated at least twice.

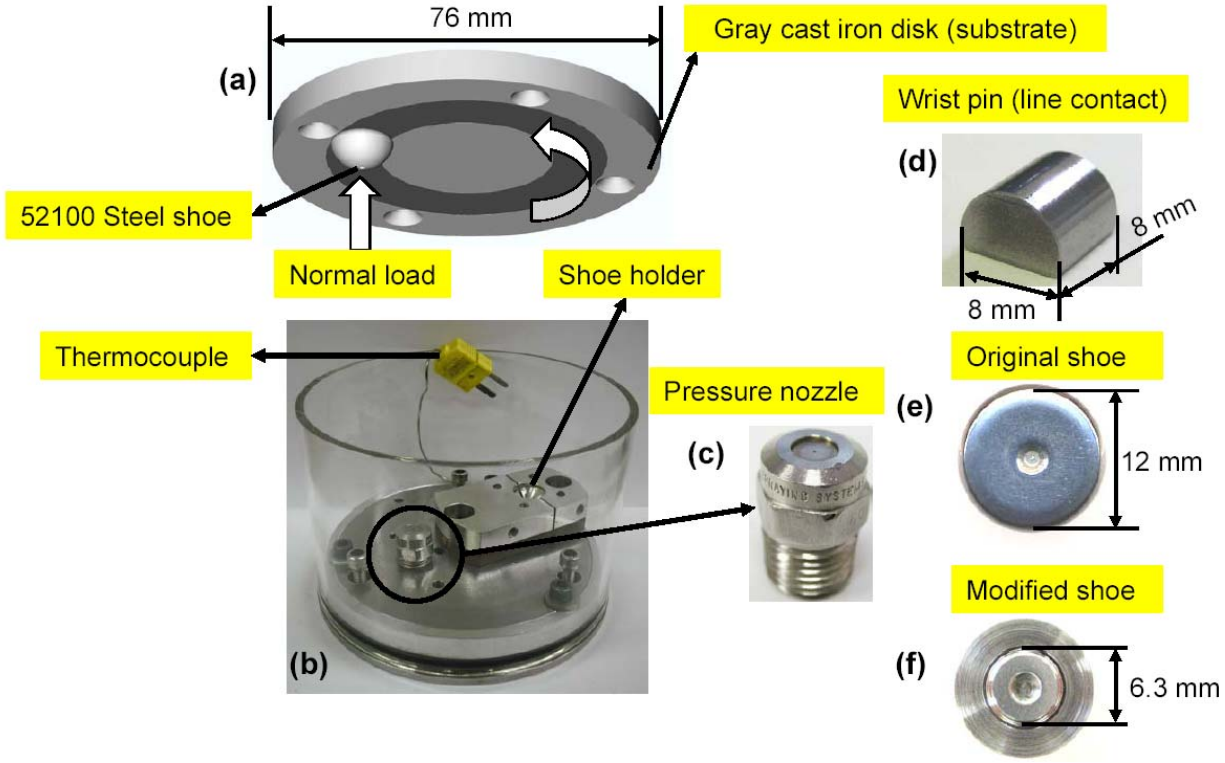

Figure 6.2─Samples and components used during the testing set up; a) upper rotating disk and shoe, b) components of the shoe holder, c) pressure nozzle to spray mixture R-134a/PAG, d) wrist pin, e) original shoe, and f) modified shoe.

Table 6.2─Summary of experimental conditions in the two set of tests

Conditions	**Set 1**	**Set 2**	**Set 3**
Type of experiment	Constant Load	Constant Load	Constant Load
CO_2 Pressure: psi, (MPa)	25 (0.17)	25 (0.17)	25 (0.17)
Temperature (°C)	100	100	100
Constant load (N)	445	445	670
Contact pressure (MPa)	175	8	23
Frequency (Hz)	4.5	-	-
Linear Speed (m/s)	0.33	4.8	4.8
Sliding Distance (m)	390	8640	8640
Lubricant Amount (mg/min)	-	20	-

6.4 Experimental Results

6.4.1 Coating thickness

The thickness of each coating was measured using cross section SEM of the cast iron samples. Cross sections of the disks were cut and prepared by polishing. Figure 6.3a) through d) show the thickness of the different coatings along with the gray cast iron substrate. It can be observed that the thickness of all the different coatings varies from 20-40 μm. In addition, the thickness of these coatings is somewhat not uniform through out the cross section (as can be observed in Figure 6.3). It is believed that this non-uniformity is due to the high surface roughness of the blasting deposited on the substrate.

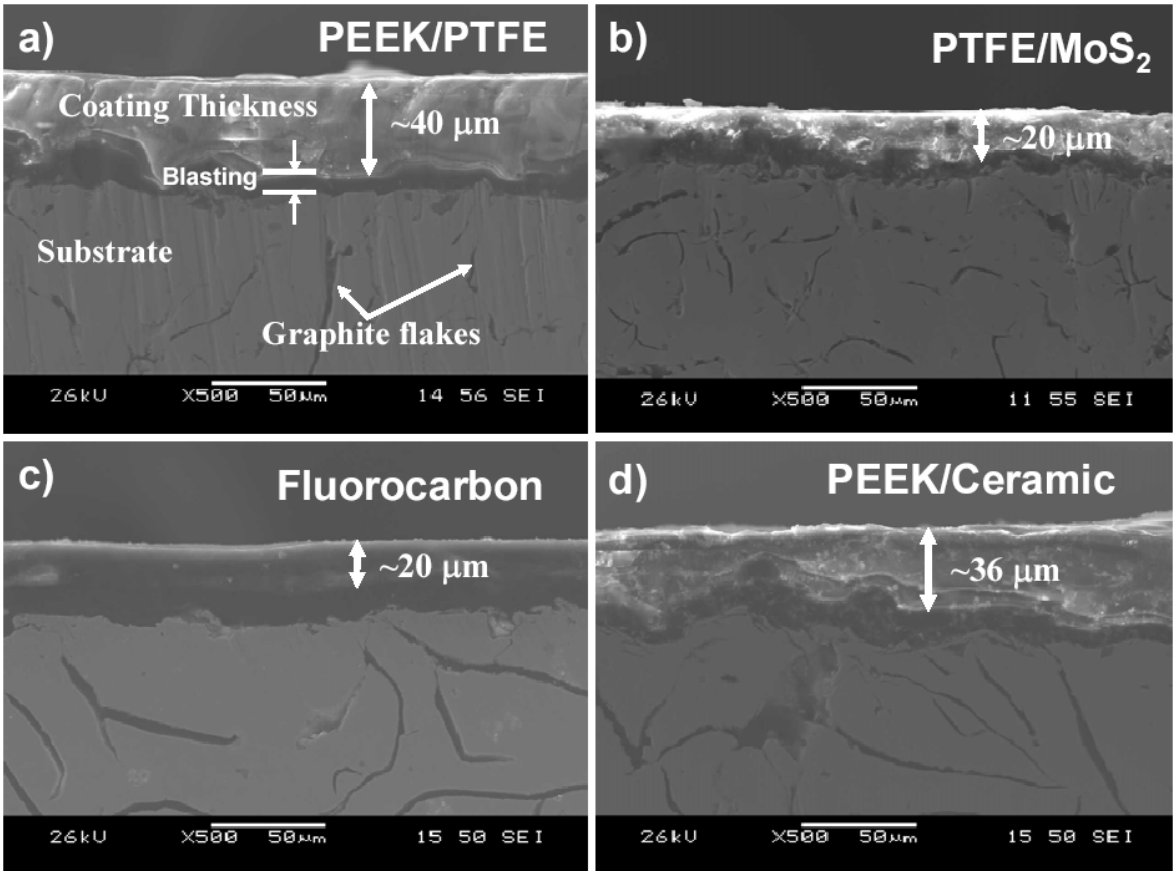

Figure 6.3─Cross section SEM images of the different polymeric coatings; a) PEEK/PTFE, b) PTFE/MoS_2, c) Fluorocarbon, d) PEEK/Ceramic.

6.4.2 Unlubricated oscillatory experiments

Figure 6.4a) shows the experimental results for PEEK/PTFE coating where it can be observed that friction coefficient builds up to 0.25 during the running-in period and then decreases and reach steady state at 0.18 until the end of the two experiments. Figure 6.4b) shows the near-contact temperature for the same coating where it can be observed that reaches a maximum of 65 °C during the running-in period following the trend of the friction coefficient. It should be noted some unsteady spiky behavior of the friction coefficient after 20 minutes of the test. As will be shown with the profilometric measurements, this behavior is related to the penetration of the coating due to the high contact stresses which exposes the asperities of the gray cast iron substrate in contact with the asperities of the 52100 steel counterpart.

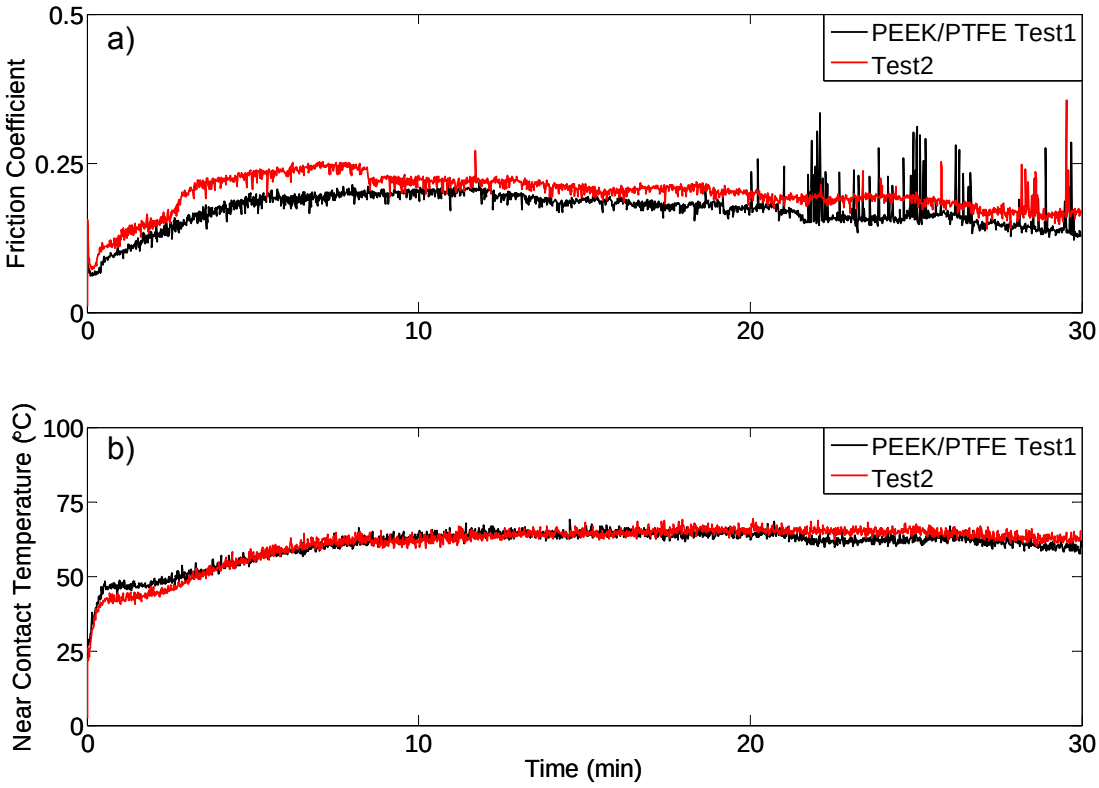

Figure 6.4—Experimental results of PEEK/PTFE during set 1; a) friction coefficient, b) near-contact temperature.

Experimental results for PTFE/MoS_2 coating are shown in Figure 6.5. As can be observed in Figure 6.5a) friction coefficient reaches a maximum of 0.20 during the running-in period and reaches a steady state value of 0.13 until the end of the test. The near contact temperature increases until 64 °C and reaches steady state at 58 °C as seen in Figure 6.5b). Although the experiments were performed under unlubricated conditions, it is interesting to observed the repeatability and the trends of both; friction coefficient and near-contact temperature which points out in the direction of the solid lubricants used to blend those coatings and the role of transfer layers.

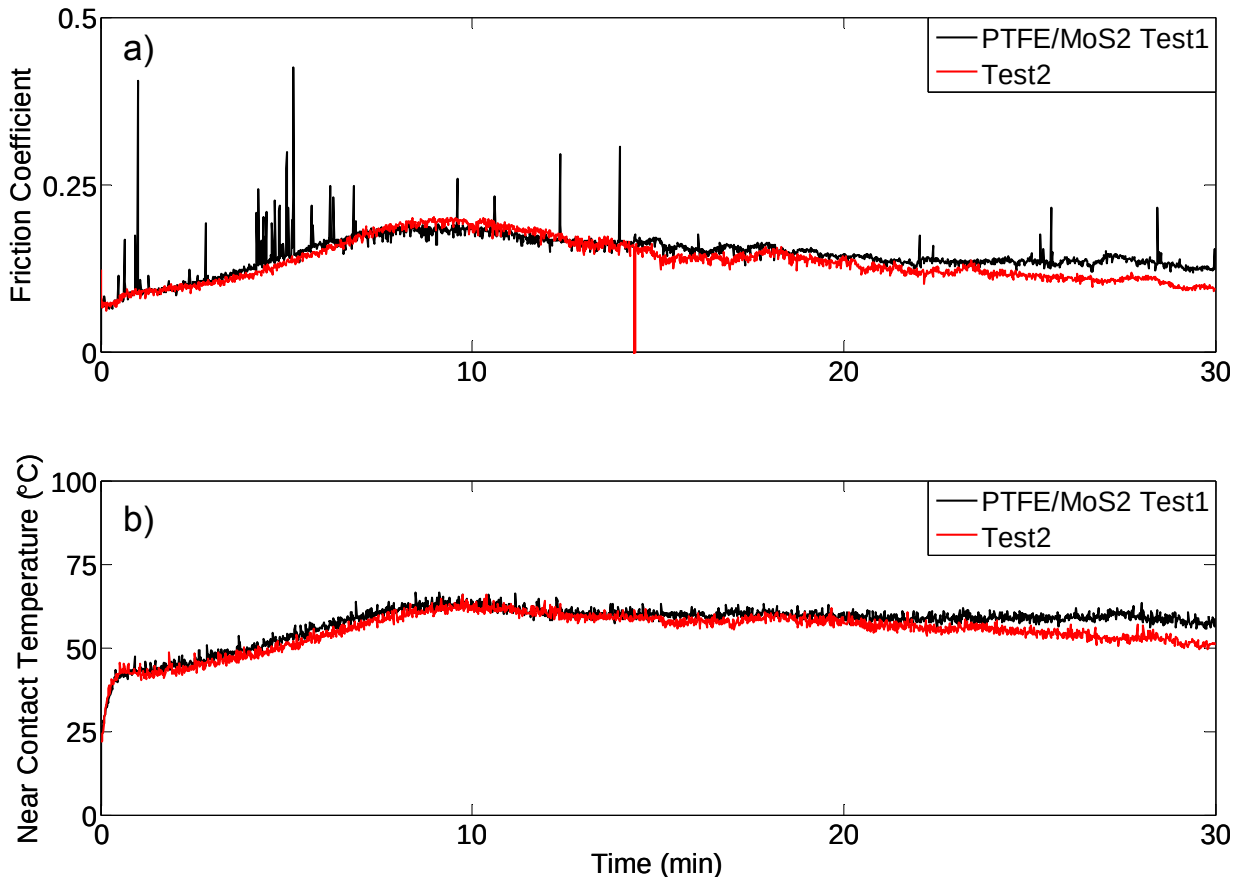

Figure 6.5—Experimental results of PTFE/MoS_2 during set 1; a) friction coefficient, b) near-contact temperature.

Friction coefficient had a maximum value of 0.20 during the running-in period and became steady state at 0.13 in the case of Fluorocarbon coating (see Figure 6.6a)). The near contact temperature had a maximum value of 64 °C and became steady at 58 °C as seen in Figure 6.6b). Similar to the previous two tested coatings the tribological experiments show similar trends and repeatability, but less spikes in the friction coefficient which probably means less interaction of the asperities of the 52100 steel pins with the gray cast iron substrate.

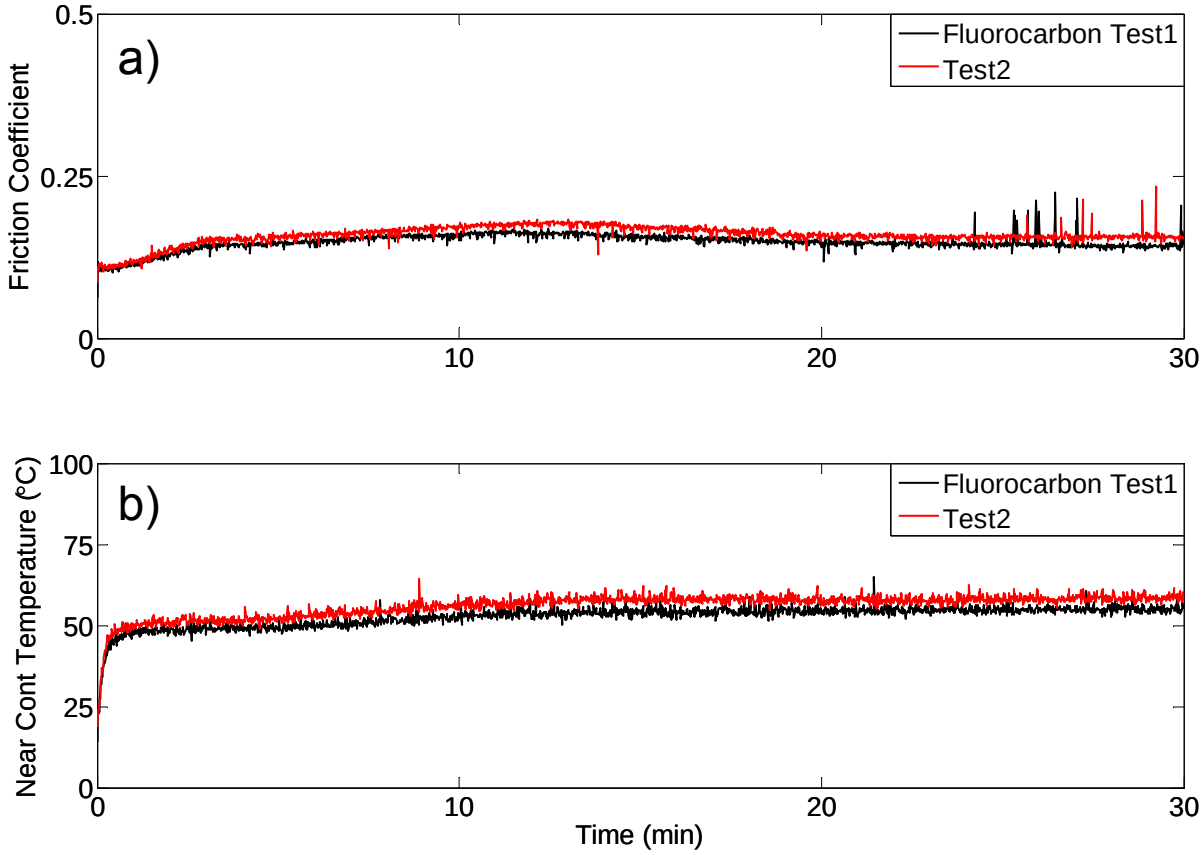

Figure 6.6—Experimental results of Fluorocarbon during set 1; a) friction coefficient, b) near-contact temperature.

PEEK/Ceramic shows a maximum friction coefficient of 0.25 during the running-in period and reaches a steady state value between 0.18-0.20 (Figure 6.7a)) until the end of the tests.

The near contact temperature reached a maximum of 75 °C being steady until the end of the tests as observed in Figure 6.7b). Although the experiments were performed under unlubricated conditions, it is interesting to observed the repeatability and the trends of both; friction coefficient and near-contact temperature which points out in the direction of the solid lubricants used to blend those coatings and the role of transfer layers.

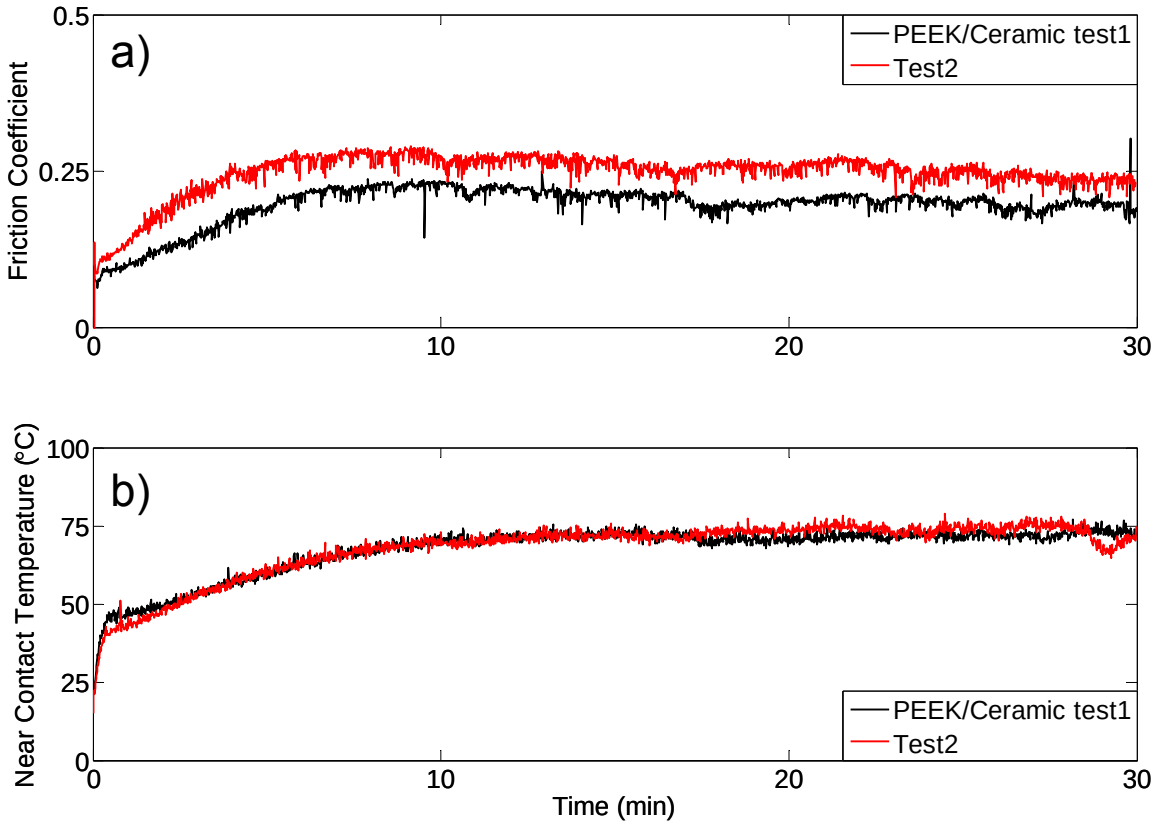

Figure 6.7─Experimental results of PEEK/Ceramic during set 1; a) friction coefficient, b) near-contact temperature.

Figure 6.8 shows profilometric measurements of the polymer coatings after the oscillatory unlubricated experiments. As can be observed for all the different cases, the wear depth was similar to the thickness of the coating (see Figure 6.3) pointing out on the role of the

wear debris. These wear debris are trapped on the surface during tribological testing preventing adhesion of the gray cast iron substrate to the 52100 steel pin counterpart [50].

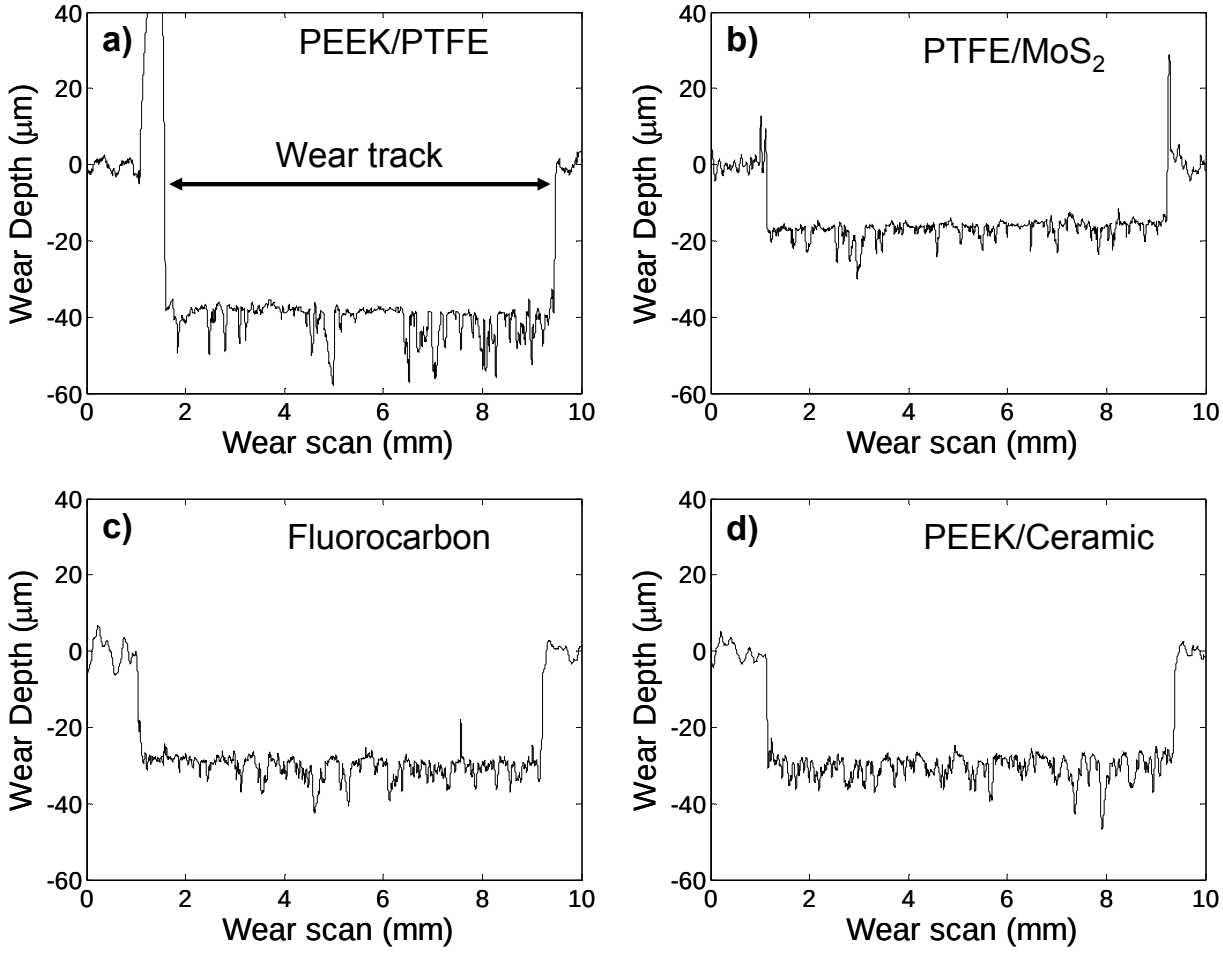

Figure 6.8—Wear profilometric measurements of tests performed under oscillatory unlubricated conditions; a) PEEK/PTFE, b) PTFE/MoS_2, c) Fluorocarbon, d) PEEK/Ceramic.

Figure 6.9 shows the wear microscopy images of the different coated disks after testing. PEEK/PTFE and PEEK/Ceramic showed voids and signs of fatigue demarcated with 1 on Figure 6.9a) and d). Interestingly, these signs are consistent with the friction data showed on Figure 6.4 where there the spikes on the friction coefficient of PEEK/PTFE suggest signs of adhesion of the

52100 steel pin with the gray cast iron substrate. Also, Figures 6.8b) and c) show the powder like morphology of the wear debris due to the oscillatory nature of the experiment. Some of these wear debris (which is powder like), is piled up on the boundary of the wear path and other is trapped at the interface of the 52100 pin and the coated disks.

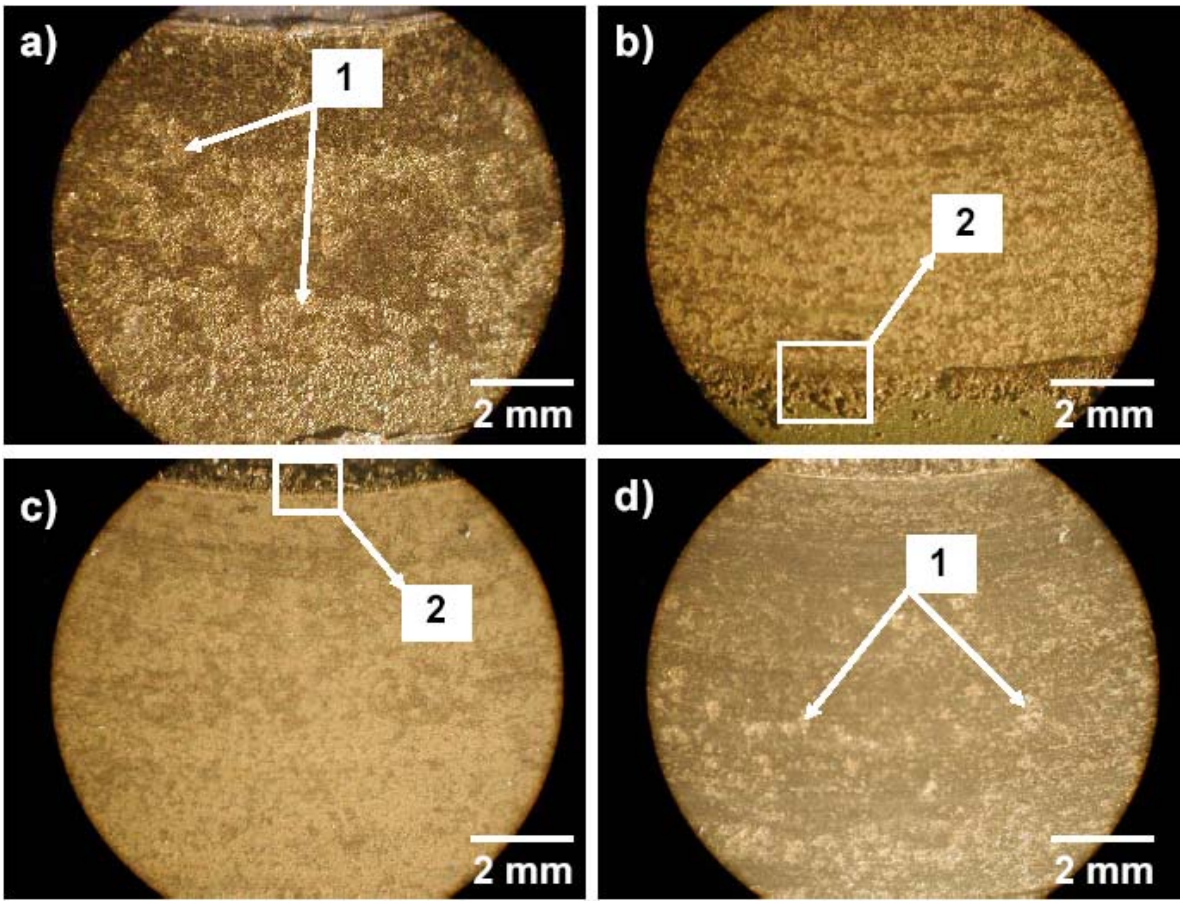

Figure 6.9─Microscopy images after oscillatory unlubricated testing; a) PEEK/PTFE, b) PTFE/MoS_2, c) Fluorocarbon, d) PEEK/Ceramic.

Table 6.3 summarizes the experimental results under oscillatory unlubricated conditions for the four different polymer coatings. According to table 6.3, the PTFE/MoS2 shows the lower

friction and wear rates compared to the other three coatings under oscillatory unlubricated conditions.

Table 6.3—Summary of experimental results of oscillatory unlubricated experiments; the sliding speed and distance were 0.21m/s and 390 m respectively.

Coating	**Friction coefficient**	**Near contact temperature (°C)**	**Wear depth (μm)**	**Wear rate (10^{-6} mm^3/N.m)**
PEEK/PTFE	0.18	65	40	7.72
PTFE/MoS_2	0.13	58	18	3.47
Fluorocarbon	0.13	58	30	5.8
PEEK/Ceramic	~0.20	75	30	5.8

6.4.3 Boundary/mixed lubricated experiments

Friction coefficient and near-contact temperature profiles were obtained during testing. Two typical experiments of PEEK/PTFE coating are depicted in Figure 6.10. In this Figure, it can be observed that the steady state value of the friction coefficient for the case of PEEK/PTFE coated disk was ~0.07 (note that two experiments are shown to prove good repeatability). It should be noted that these friction coefficient values are lower compared to those obtained under boundary/ mixed lubrication conditions using bare materials whose values oscillate between 0.12-0.16 [81]. It is conjectured that these low friction coefficient values in the case of deposited PEEK/PTFE coatings can be attributed to the transfer film from the soft coating to the hard 52100 steel shoe counterpart. This transfer film (which takes place during the running-in period) is trapped at the sliding interface as a third body. As will be explained through SEM, the

mechanism of deposition and compactness of the transfer film is through the plastic deformation caused by shear stress and normal load during sliding respectively.

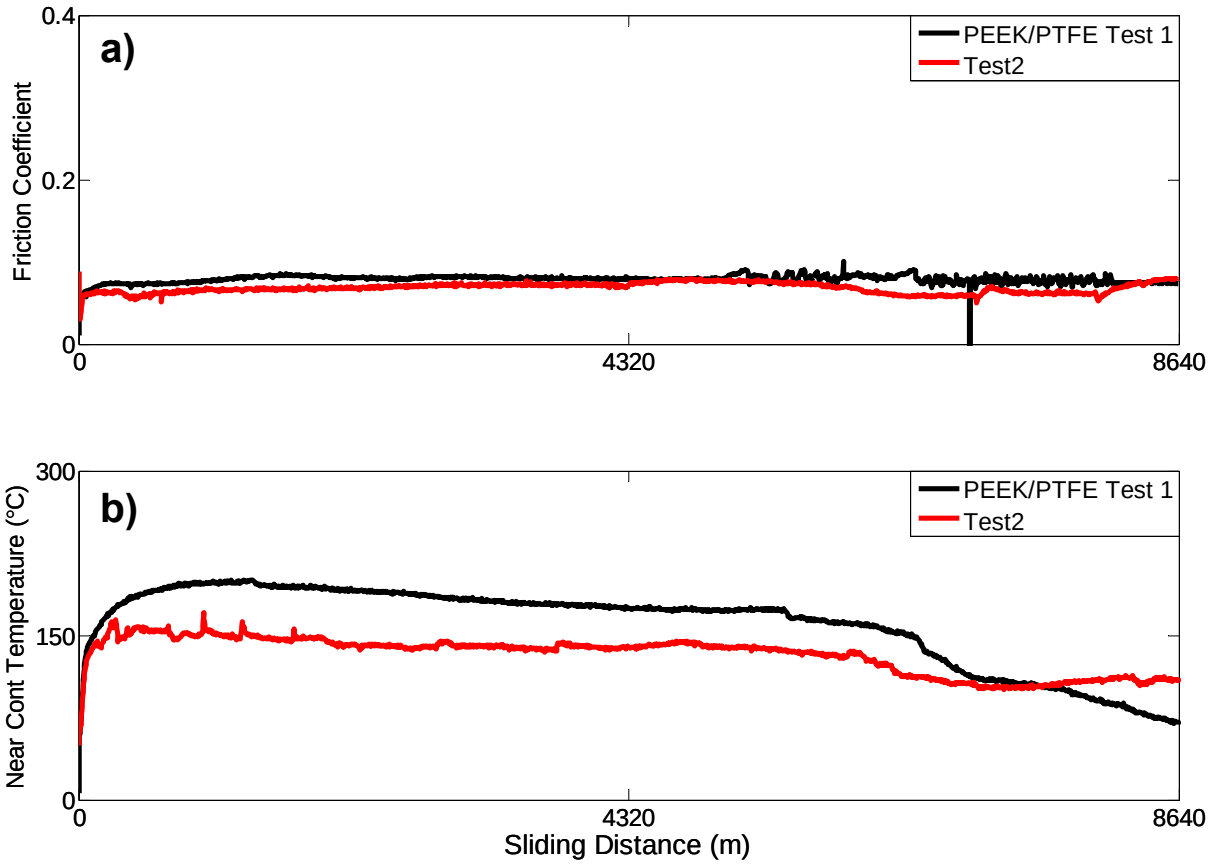

Figure 6.10─Experimental results of PEEK/PTFE during set 2; a) friction coefficient, b) near-contact temperature.

Under similar testing conditions, friction coefficient was ~0.09 in the case of PTFE/MoS_2 which is slightly higher compared to PEEK/PTFE case (as shown Figure 6.11). In the case of the Fluorocarbon (see Figure 6.11), the interface scuffed (this point was characterized by a sudden increase in friction coefficient) after approximately 2874 m of sliding distance due to penetration of the coating. Friction coefficient during testing of PEEK/Ceramic was

approximately 0.06 being slightly similar compared to the PEEK/PTFE and PTFE/MoS_2 cases (see Figure 6.12).

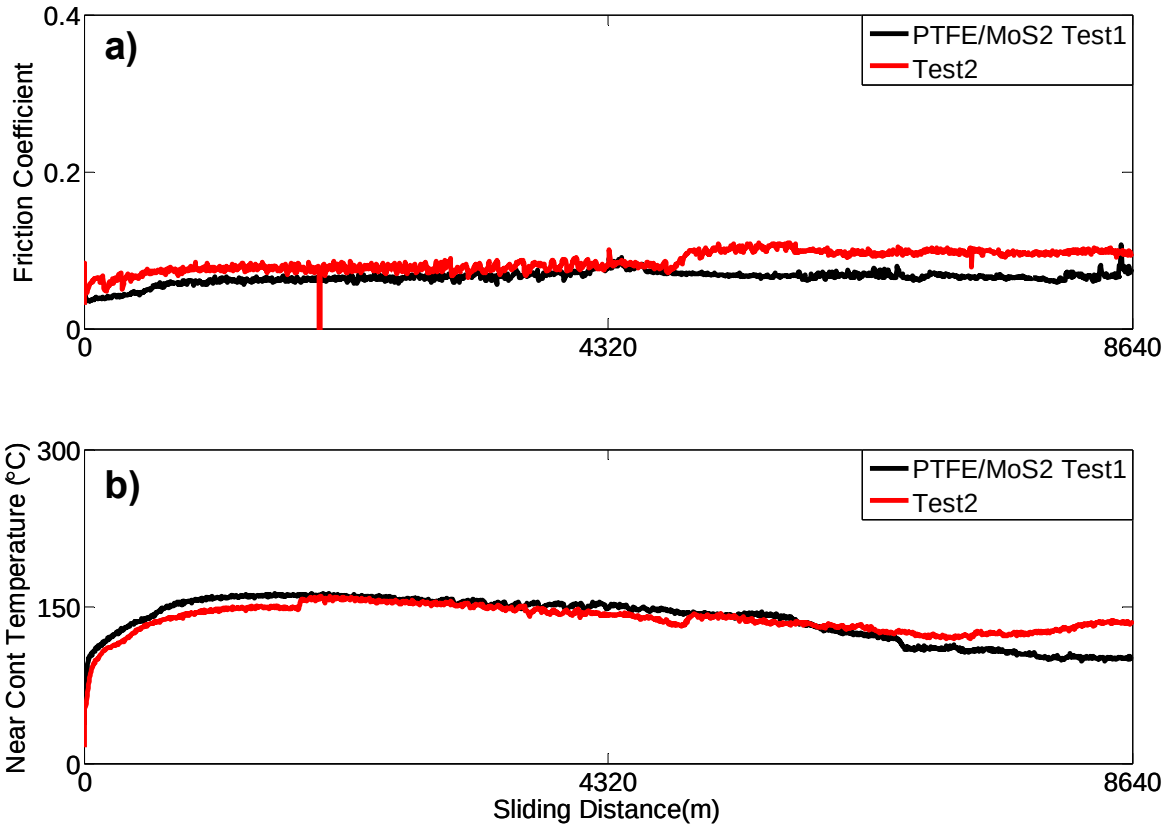

Figure 6.11—Experimental results of PTFE/MoS_2 during set 2; a) friction coefficient, b) near-contact temperature.

In all the coatings, except for FC, the near contact temperature increased during the running-in period, and then experience a decreasing trend until the of the test (as seen in Figure 6.10, 6.11 and 6.13). As will be shown in the SEM section, this decrease in the near-contact temperature can be attributed to the transfer films from the polymeric coatings to the hard 52100 steel counterface. It is believed that the transfer film is composed of polymeric coating, and

refrigerant/lubricant mix. Once the transfer layer is attached to the surface of the counterpart, it thermally isolates the surface beneath the sliding interface. Since the near-contact temperature is captured 2 mm below the sliding interface, lower temperature will be sensed by the thermocouple once the transfer film build up. In all three successful cases the maximum peak of the near contact temperature was ~190 °C which is lower compared to the in-use temperature of the coatings listed in Table 6.1. However, in the case of Fluorocarbon coating the near contact temperature reached a maximum peak of approximately 230 °C, which is close to the maximum in-use temperature of this coating during scuffing.

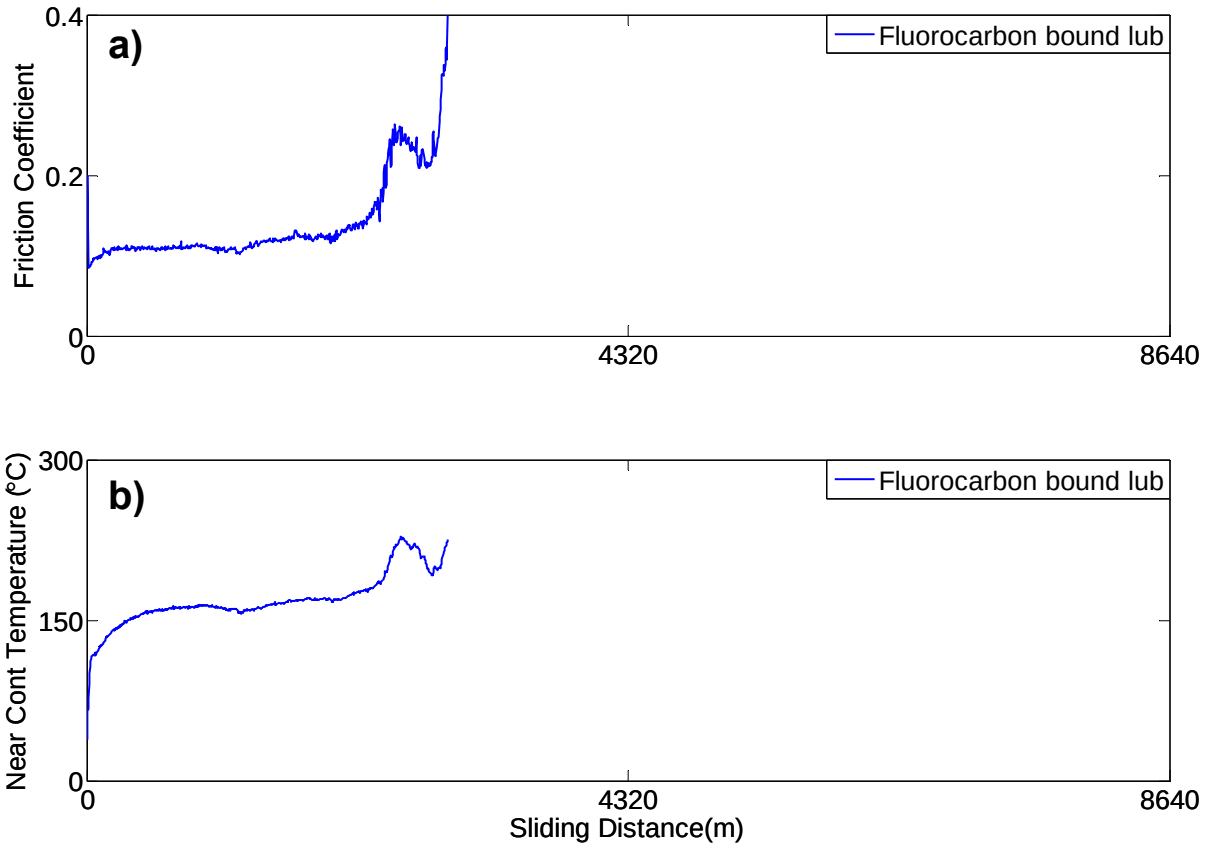

Figure 6.12—Experimental results of Fluorocarbon during set 2; a) friction coefficient, b) near-contact temperature.

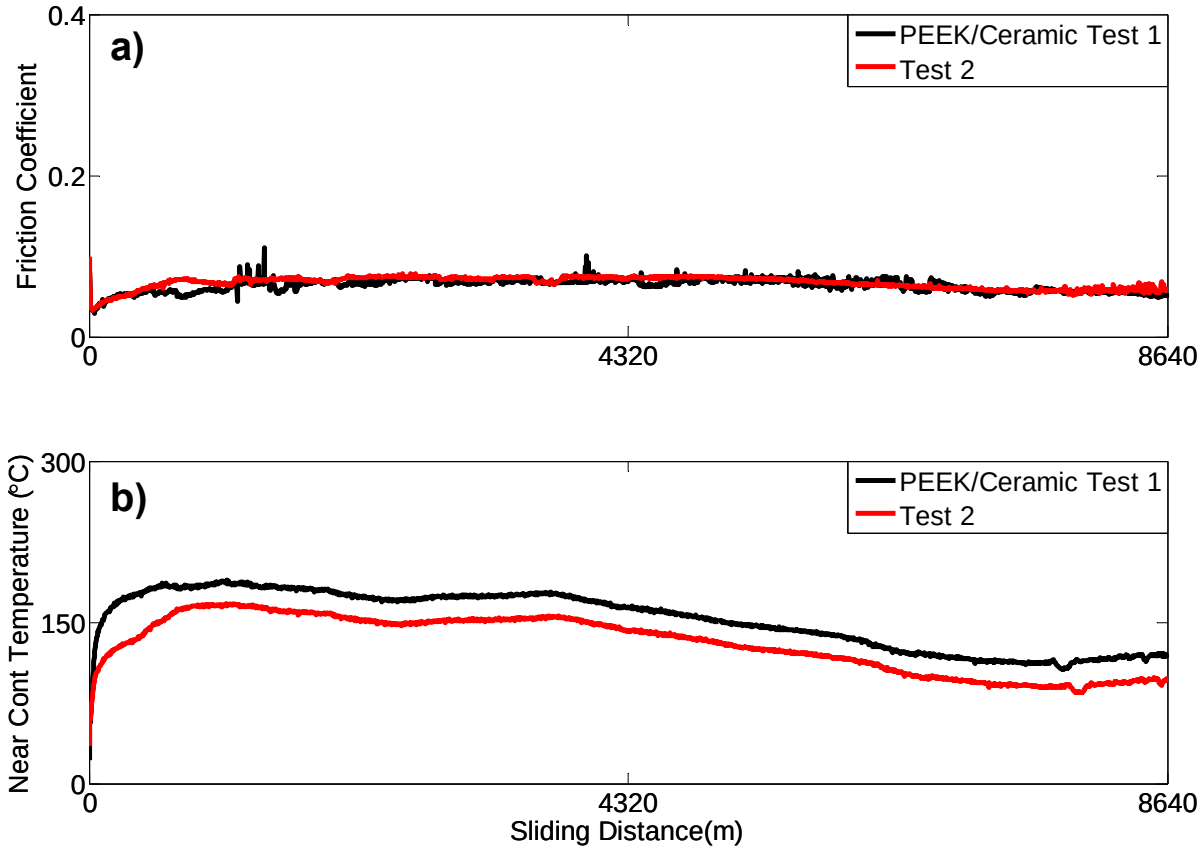

Figure 6.13─Experimental results of PEEK/Ceramic during set 2; a) friction coefficient, b) near-contact temperature.

Unlike bare metals where the relative loss of heat by conduction (sliding tribopairs and adjacent components) and convection (refrigerant and lubricant films) can be obtained as a function of physical properties (i.e., thermal conductivity and specific heat of the lubricant) and other parameters such as the thickness of the lubricant film, linear speed, sliding distance, and the gradient of temperature, polymeric coatings under the current study behave as thermal insulators. It is predicted that thermal insulation provides an advantage because the viscosity of the lubricant will be less affected. Likewise, during the aforementioned experiments, convection will be enhanced because the frictional heating will be carried away at high sliding speed (4.8 m/s).

6.4.4 Unlubricated testing

After testing under boundary/mixed lubrication conditions (set 2), the three best performing coatings were further tested under aggressive unidirectional unlubricated conditions (set 3). Experimental results for this set of experiments are shown in Figure 6.14. As can be observed in Figure 6.14a), while PTFE/MoS_2 and PEEK/Ceramic coatings showed a sharp increase in friction coefficient (in both cases the interface scuffed), PEEK/PTFE was stable and showed a low friction coefficient of 0.03 throughout the test. Interestingly, this friction coefficient was lower compared to the boundary/mixed lubrication case (0.07). This behavior has to do with the higher fragmentation of PTFE under unlubricated unidirectional conditions. Under these conditions along with higher contact stresses (reduced contact geometry as seen in Figure 6.2f), the load will be carried by the coating material and the asperities of the counterpart. As a result, the PTFE component of the coating will shear easier and will be plastically deformed under high normal load and sliding speeds. Contrarily, friction coefficient under boundary/mixed lubrication conditions is expected to be higher due to the extra tangential forces associated with the hydrodynamic shearing of the lubricant film. Due to the adverse thermodynamical effects of the circulation of the lubricant in air-conditioning and refrigeration systems, the low friction and low wear rates shown by the PEEK/PTFE coating under unlubricated conditions make it attractive for oil-less compressors. As will be explained in the TOF-SIMS section, this behavior is related to the fragmentation of PTFE polymer ions during testing.

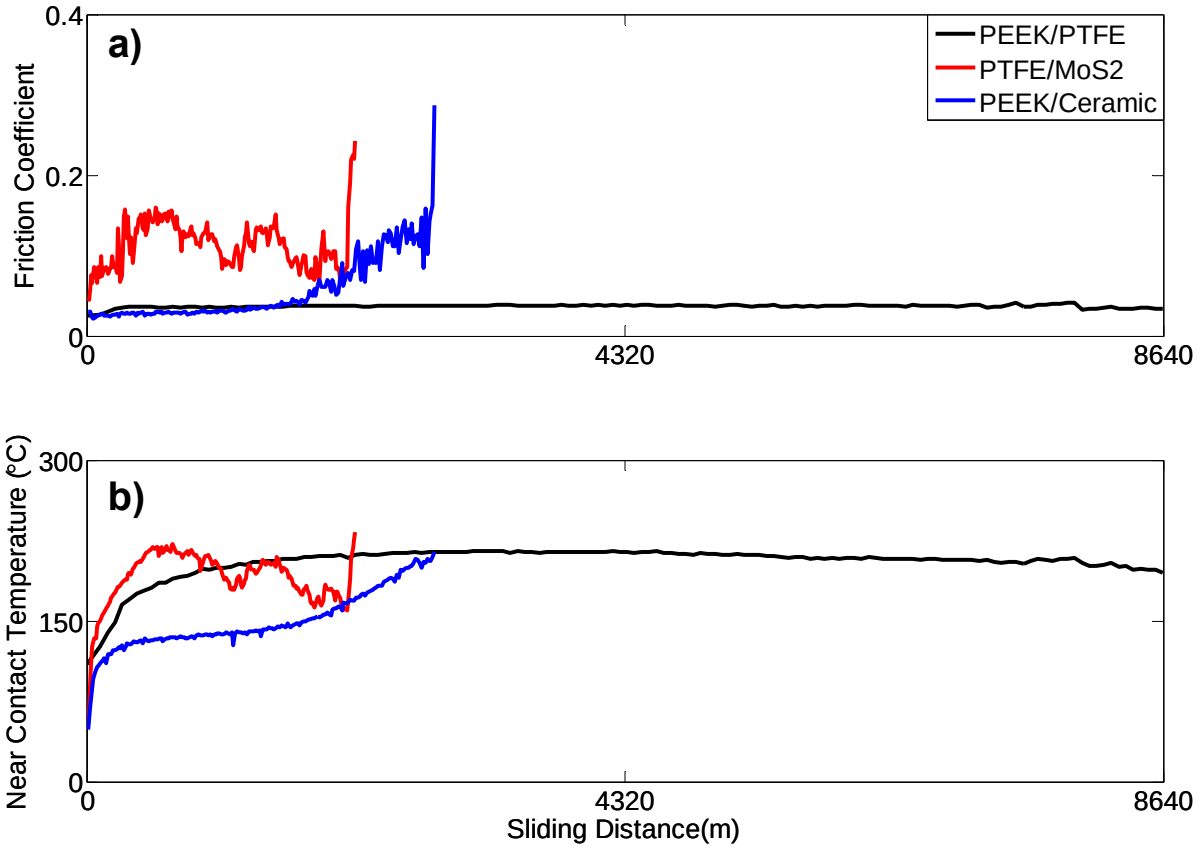

Figure 6.14– Experimental results of PEEK/PTFE, PTFE/MoS_2, and PEEK/Ceramic under unlubricated unidirectional conditions; a) friction coefficient, b) near-contact temperature.

In addition, the near contact temperature was higher under unlubricated conditions compared to boundary/mixed lubrication. As will be explained in the SEM section, transfer films (third bodies mainly composed of the mixture coating/lubricant/refrigerant) were observed on the surface of the shoes under boundary/mixed lubrication conditions. Moreover, since there is no lubricant film it is more difficult to carry away the frictional heat being generated by convection which partially explains the higher temperature under unlubricated conditions.

Wear profilometric measurements and wear rates of the different coatings tested under boundary/mixed lubricated conditions are shown in Figures 6.15 and 6.16 respectively. The

wear scan length was set to 12 mm to capture the variation in surface height from the untested to the tested region. As can be observed in Figure 6.15a) in the case of PEEK/PTFE coating only mild burnishing was caused. In PTFE/MoS_2 a wear depth of ~3 μm was observed along with some isolated wear "scars" ~8 μm deep as seen in Figure 6.15b). Fluorocarbon (which was the only coating that scuffed during set 2 of experiments) showed an average wear depth of ~30 μm and deep wear scars of ~50 μm (see Figure 6.15c)). It is evident in this case that penetration of the coating occurred and this is one of the reasons why scuffing appeared. PEEK/Ceramic showed a wear depth of ~10 μm and wear scars ~40 μm deep (Figure 6.15d)). Despite the fact these wear scars are deeper than the thickness of the coating, no sign of scuffing was observed which points out in the direction of the role of wear debris. Figure 6.16 shows a plot of the wear rate as a function of friction coefficient for the tested coatings (except Fluorocarbon which is not shown due to scuffing). Although the contact stresses were higher during testing under unlubricated conditions compared to the boundary/mixed lubrication case, the wear rate measured after unlubricated testing of PEEK/PTFE was 1.11×10^{-6} $mm^3.N^{-1}.m^{-1}$ and slightly similar compared to the wear rate obtained under boundary/mixed lubrication (1.15×10^{-6} $mm^3.N^{-1}.m^{-1}$) for the same coating. It should also be recalled that PEEK fragmentation can lead to dangling σ-bonds terminated with oxygen species in a ketonic environment (C=O). It has been reported that these species reduce friction in the case of DLC films [106]. An analogous case could be effective here, where C=O species might be exposed as sliding goes on and the PTFE fragmentation is facilitated. By comparison with starved lubricated conditions, where PAG lubricant was used, it could be stated that oxygen species can be originated from PAG as well, since O-H groups are present (hydroxylic environment). The oxygen in ketonic and hydroxylic

environment, as terminated group, can lead to different extent of adhesive interactions [106, 107, 108].

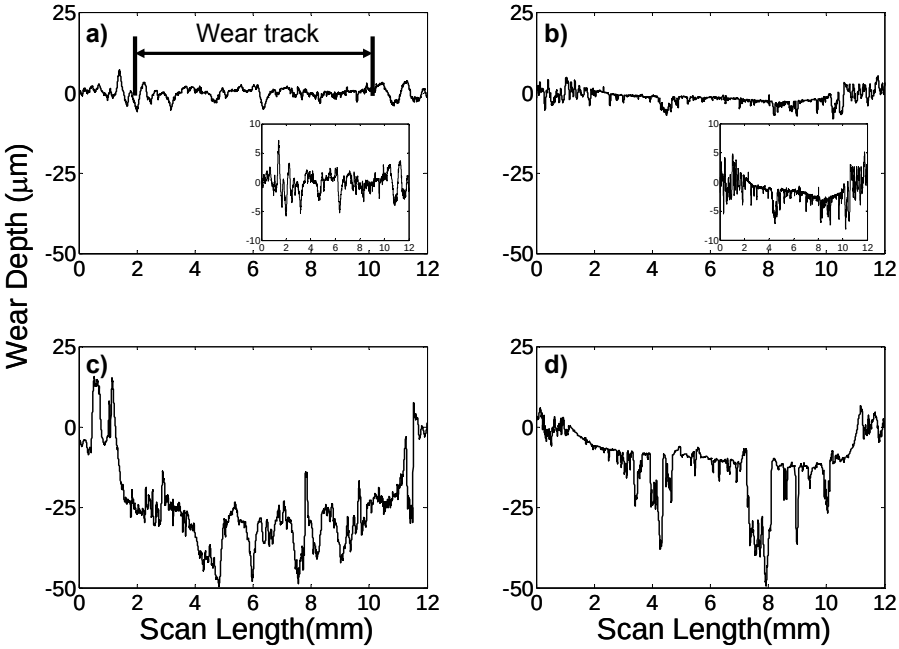

Figure 6.15—Wear profilometric measurements of the coatings under boundary/mixed lubricated conditions; a) PEEK/PTFE, b) PTFE/MoS_2, c) Fluorocarbon, d) PEEK/Ceramic.

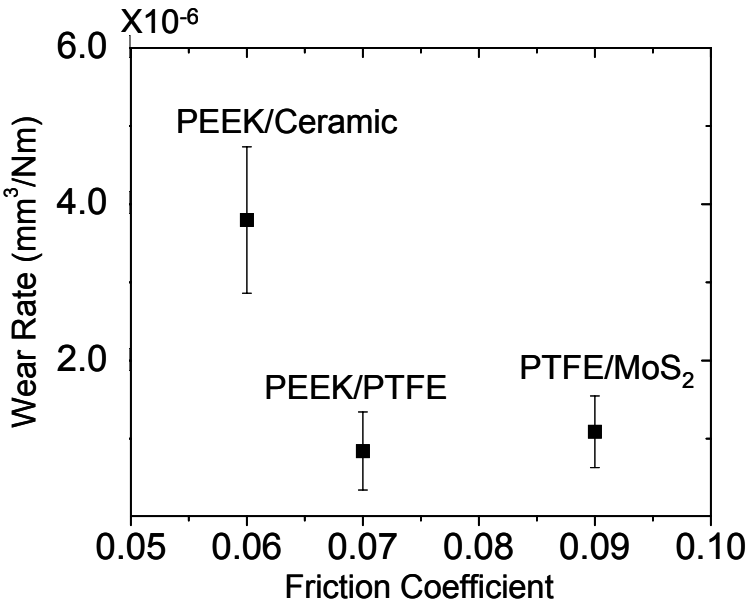

Figure 6.16—Wear rate vs. friction coefficient of coatings under boundary/mixed lubrication. Error bars designate plus and minus one standard deviation.

6.4.5 SEM analysis

Figure 6.17 shows SEM microscopy images of the coated disks tested during set 2. Figure 6.17a) shows very minor burnishing inside the wear track of the PEEK/PTFE coated disk which is consistent with the wear profilometric measurements shown in Figure 6.15a). In these measurements no significant difference in topography was observed when the tested and untested regions were compared. Burnishing and plastic deformation inside the tested area of PTFE/MoS_2 can be observed on Figure 6.17b). This change in morphology (labeled with 1 on Figure 6.17b)) on the tested area of PTFE/MoS_2 is consistent with the wear scars observed on the profilometric measurements (see Figure 6.15b)). The disk coated with Fluorocarbon showed signs of severe adhesion with the 52100 steel shoe (these adhesion signs were labeled with 2 in Figure 6.17c)) while piled up of the polymeric coating was labeled with 3 in Figure 6.17c). The morphology of the piled up shown in Figure 6.17c) resembles loosen debris wear particles with a texture similar to the original coating suggesting weak adhesion with the substrate. In the case of PEEK/Ceramic an irregular topography with higher plastic deformation component can be observed on the SEM microscopy image (Figure 6.18d)). For instance, three different regions with different morphology are labeled with 4 in Figure 6.17d), this change in morphology is also consistent with the deep wear scars observed in the profilometric scans in Figure 6.15d).

SEM images of the surface of the shoes (counter-surface) tested on set 2 are shown in Figure 6.18. It can be observed that all the microscopy images show transfer films, except in the Fluorocarbon case (Figure 6.18c)), where signs of severe adhesive wear were present. Effectively, as pointed out before, transfer films from the soft polymeric coating to the hard surface of the 52100 steel shoes provide temperature isolation and help in the transportation of the frictional heat through convection by the less temperature affected lubricant film. As can be

observed on Figure 6.18b), wear debris from the PTFE/MoS_2 coating is transfer to the dimple of the shoes. Due to the fact that the thermocouple is inserted 2 mm below the surface of the shoe (located right below the center of the dimple), the wear debris trapped on the dimple serves as thermal insulator as explained before. This trapped wear debris can also be observed on the profilometric measurement (see Figure 6.19) on the surface of the shoe (PEEK/PTFE test). In the same figure, a profile of a typical untested shoe is also shown, where the dimple region can be clearly identified. Also, notice the crown geometry of the original shoe as well as its smooth surface. After testing, flattening of the crown shape is observed as well as significant roughening, it is believed that both effects are most likely caused by the transfer films from the coated counter-surface.

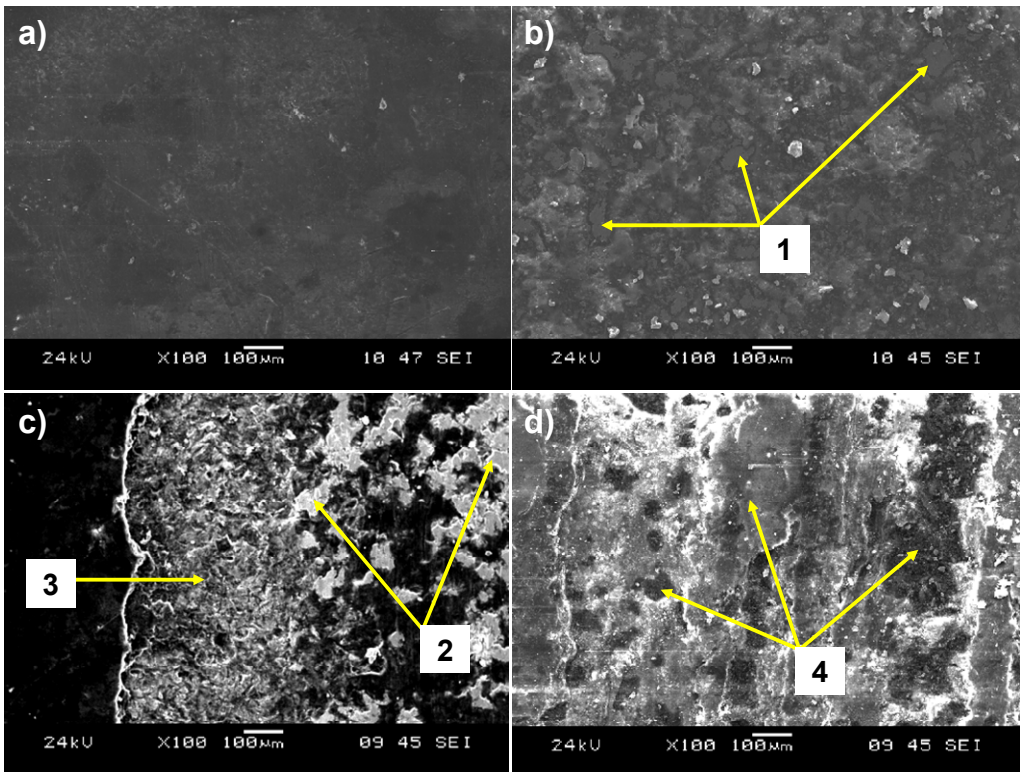

Figure 6.17─SEM microscopy images inside the wear tracks of the coated disks under boundary/mixed lubricated conditions; a) PEEK/PTFE, b) PTFE/MoS_2, c) Fluorocarbon, d) PEEK/Ceramic.

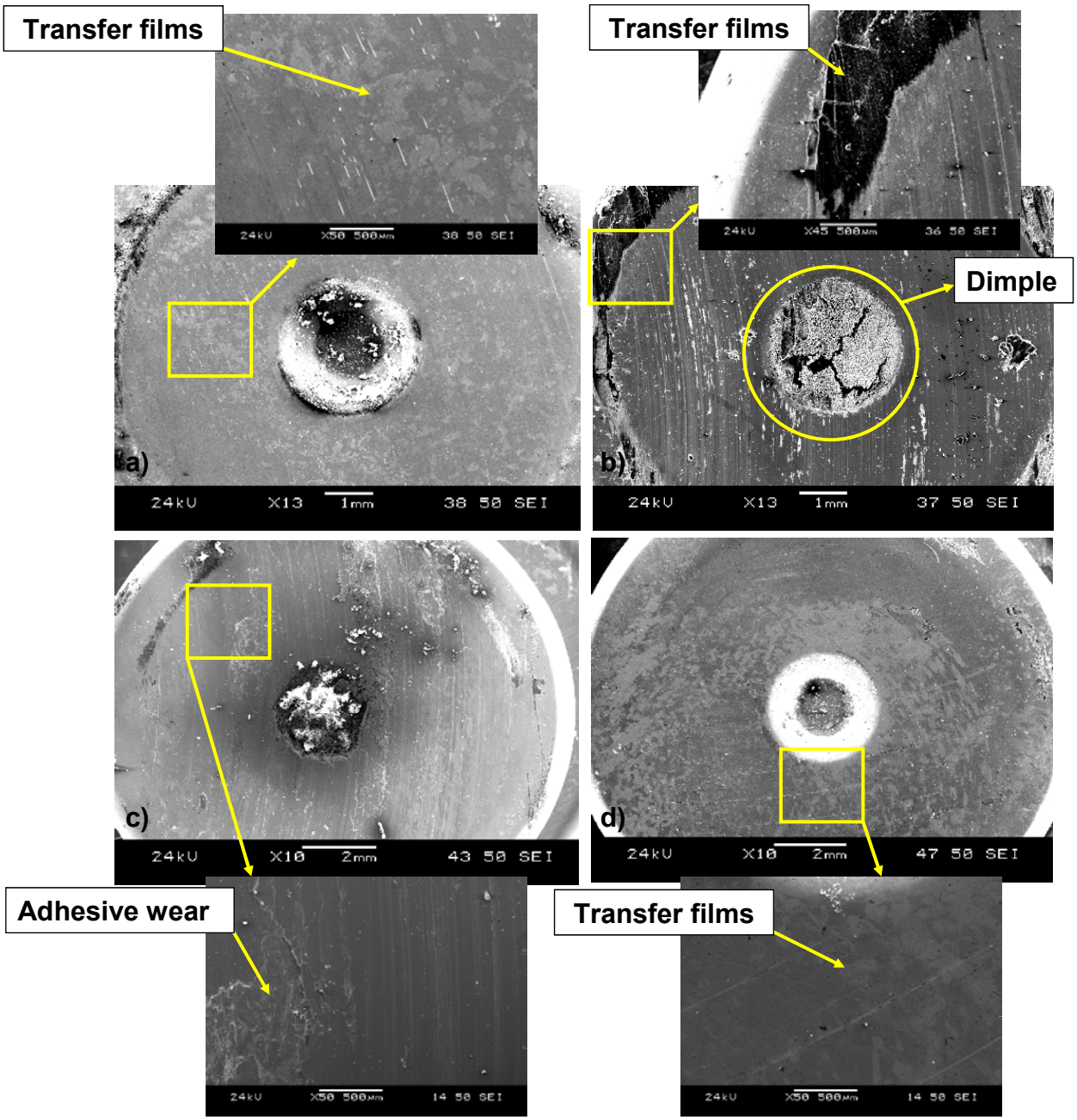

Figure 6.18─SEM microscopy images of the shoes tested under boundary/mixed lubricated conditions; a) PEEK/PTFE, b) PTFE/MoS_2, c) Fluorocarbon, d) PEEK/Ceramic.

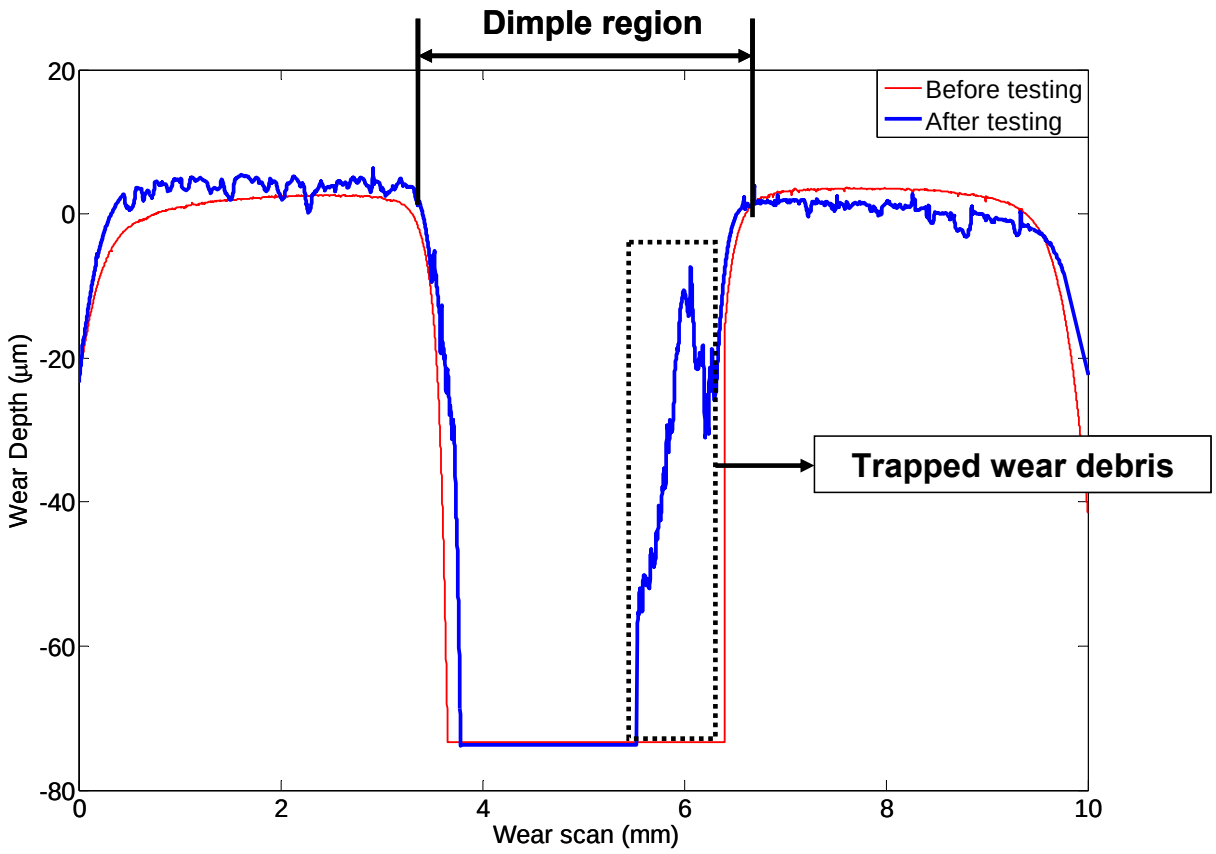

Figure 6.19─Profilometric measurement on the surface of the shoe tested against PTFE/MoS_2 coating.

6.4.6 Morphology of wear debris and wear track

The morphology of the wear debris generated after testing under oscillatory and unidirectional unlubricated conditions was analyzed using SEM. Figure 6.20a) and c) show the wear debris of PEEK/PTFE coating while Figure 6.20b) and d) show the wear debris of PEEK/Ceramic coating tested under oscillatory conditions respectively. The wear debris particles wear collected after testing and placed on double-side carbon tape. As can be observed on Figure 6.20a), the wear particles in the case of PEEK/PTFE have a granular like shape while in the case of PEEK/Ceramic (Figure 6.20b)) the wear debris is more sheet-like in form. The

morphology of the wear debris in PEEK/PTFE can be attributed to the abrasive effect of the harder asperities of the 52100 steel pins under high contact stresses (~175 MPa) which plough the polymer coating. This ploughing effect of the hard asperities generates a microcutting of the PEEK/PTFE particles [109, 110]. The sheet-like morphology of the PEEK/Ceramic coating can be attributed to delamination fatigue [111, 112], generated during the oscillatory experiments. In this case the wear debris adopts this shape due to subsurface-crack nucleation and generation of thin sheets induced by the ploughing and traction of the asperities of the harder counterpart (52100 steel pin).

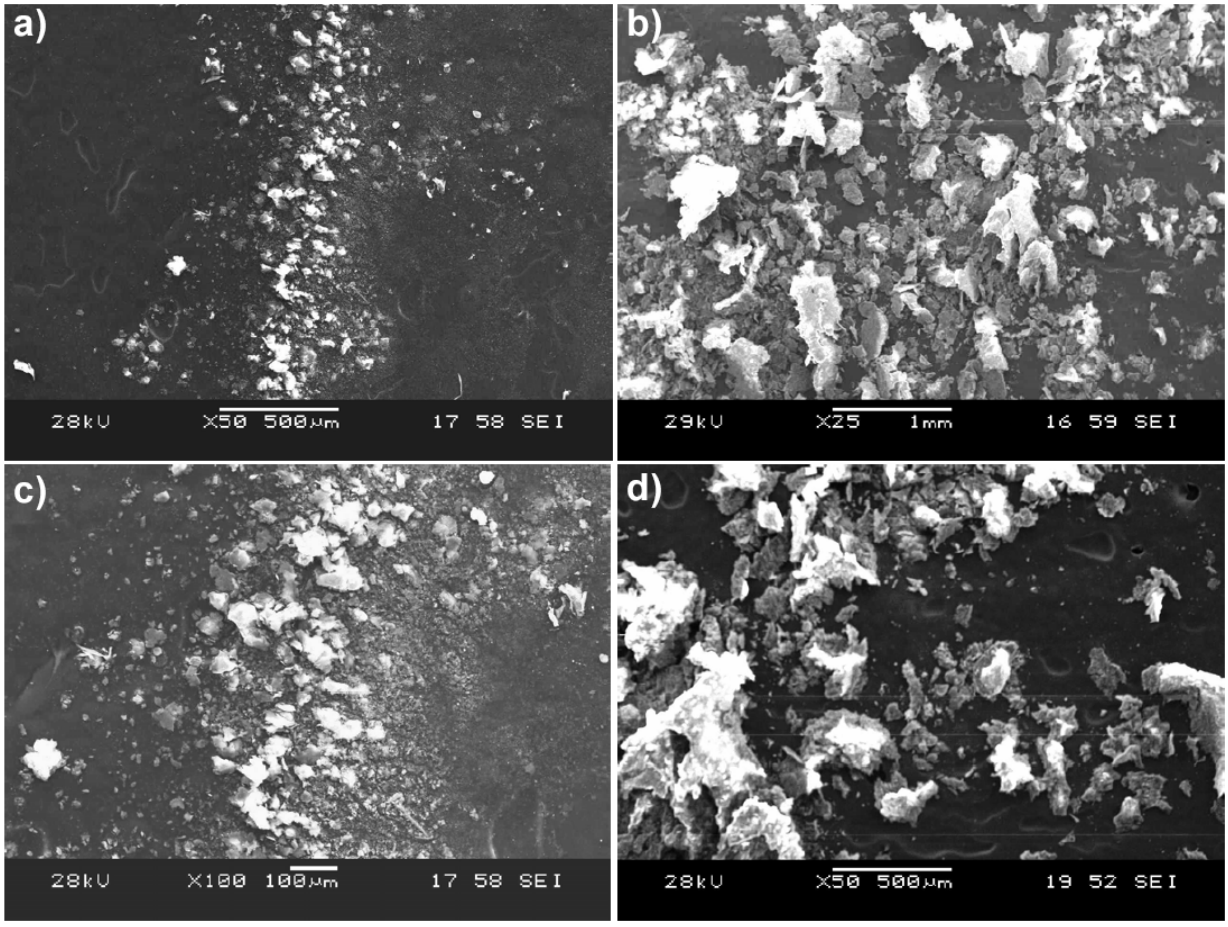

Figure 6.20─Morphology of the wear debris during oscillatory experiments; a) and c) PEEK/PTFE coating, b) and d) PEEK/Ceramic.

Figure 6.21a) and b) shows microscopy images of the PEEK/PTFE coating testing under unidirectional unlubricated conditions. As can be seen in Figure 6.21a) before testing there is a waxy, smooth, and clear PTFE layer on the top of the coating. Once sliding takes place the PTFE layer is transfer to the hard 52100 steel counterpart and the morphology of PEEK is revealed as seen in Figure 6.21b). Also in Figure 6.21b) it can be observed long delaminated sheet-like wear debris (marked as 1 in Figure 6.21b)). It is believed this wear debris adopt this shape due to the fatigue caused by the repeated number of sliding cycles during testing. Another evidence of the effect of fatigue is related to the formation of voids on the surface of PEEK marked as 1 in Figure 6.21b).

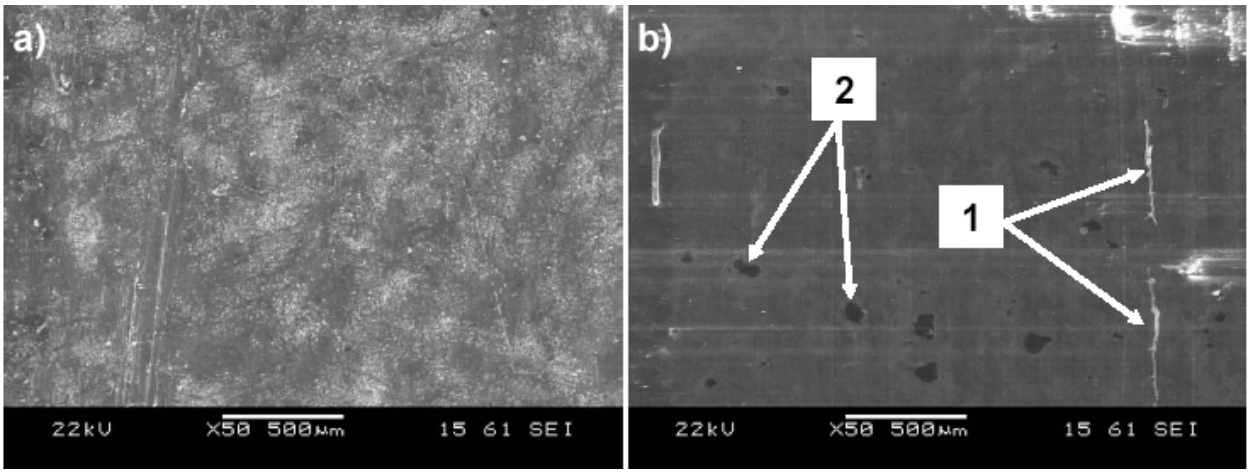

Figure 6.21─Morphology of the wear track and wear debris during unidirectional unlubricated experiments of PEEK/PTFE; a) before testing, b) after testing.

6.4.7 TOF-SIMS

To investigate the chemical compositions of the coating surfaces and their changes with sliding contacts, TOF-SIMS (PHI TRIFT III, Physical Electronics) was utilized as a valuable analytical technique probing the surface molecular structures. The static mode TOF-SIMS was used in this work with 22 KeV-pulsed Au^+ as a primary ion beam bombarding the sample

surfaces. Measurements were performed outside of the wear track (unworn coating surface) and inside the wear track, for each coating sample to quantitatively compare the chemical composition difference before and after testing. The analysis size for each sample was 500 × 500 μm^2, and the ion capturing time was 5 min for each measurement.

The four samples tested under boundary/mixed lubricated conditions and the PEEK/PTFE coating tested under unlubricated conditions, were analyzed using TOF-SIMS to study the chemical compounds present before and after testing. A representative chemical image and mass spectra of the PEEK/Ceramic coating tested under boundary/mixed lubrication can be seen in Figure 6.22. The optical image (Figure 6.22a)) clearly shows the contrast between the bright tested area (inside the wear track) and the dark untested area (outside the wear track). The explanation for a brighter contrast inside the wear track during the TOF-SIMS chemical image compared to outside it is due to a lot more chemical species detected on the untested area. For both unworn (marked with 1 in Figure 6.22b)) and worn area (marked with 2 in Figure 6.22b)), mass spectra were analyzed as seen in Figure 6.22c) and Figure 6.22d), respectively. It is shown that the major fragment ions detected on the outside wear track are carbon-fluorine based compounds such as CF^+ (31 m/z), CF_3^+ (69 m/z) and $C_3F_5^+$ (131 m/z) which are mainly attributed to PTFE polymer inside the coating. Interestingly, after testing a significant reduction of the counts corresponding to these chemical species was observed inside the wear track as seen in Figure 6.22d).

It should be pointed out that positive and negative ions mass were analyzed, but only significant counts were obtained in the case of positive ions due to the chemical nature of the found species. For direct comparison of the chemical composition among different coatings and to minimize variation of the absolute number of counts from measurement-to-measurement, the

normalized percentage intensity of each chemical species of significance was calculated for all the surfaces and depicted in Figure 6.23.

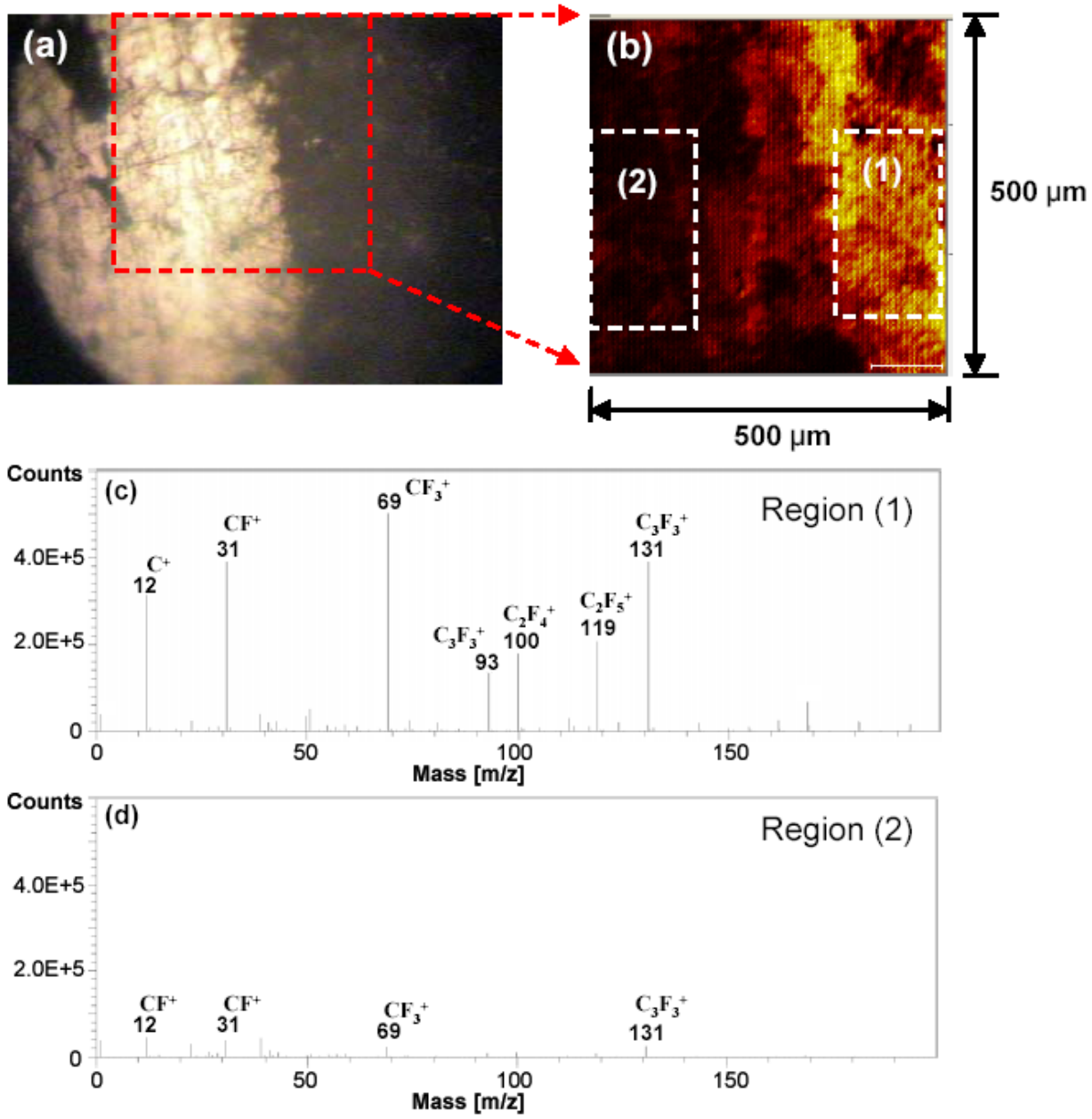

Figure 6.22─a) Optical image and b) TOF-SIMS chemical image of PEEK/Ceramic coating surface under boundary/mixed lubricated conditions. c) Positive Ions Mass spectra outside the wear track region 1), and d) Positive Ions Mass spectra inside the wear track (region 2 of chemical image shown in b).

It should be clarified that a minimum threshold of 1% of normalized intensity was set and this is the reason why other chemical species are not included in the counts since their contribution can be neglected. By comparison of the specific counts compound inside and outside the wear track (see Figure 6.23), it has to be pointed out that higher intensity or height of the peak does not necessarily mean more amount of chemical species compared to lower intensity. This is because the intensity is a normalized value based on each examined surface.

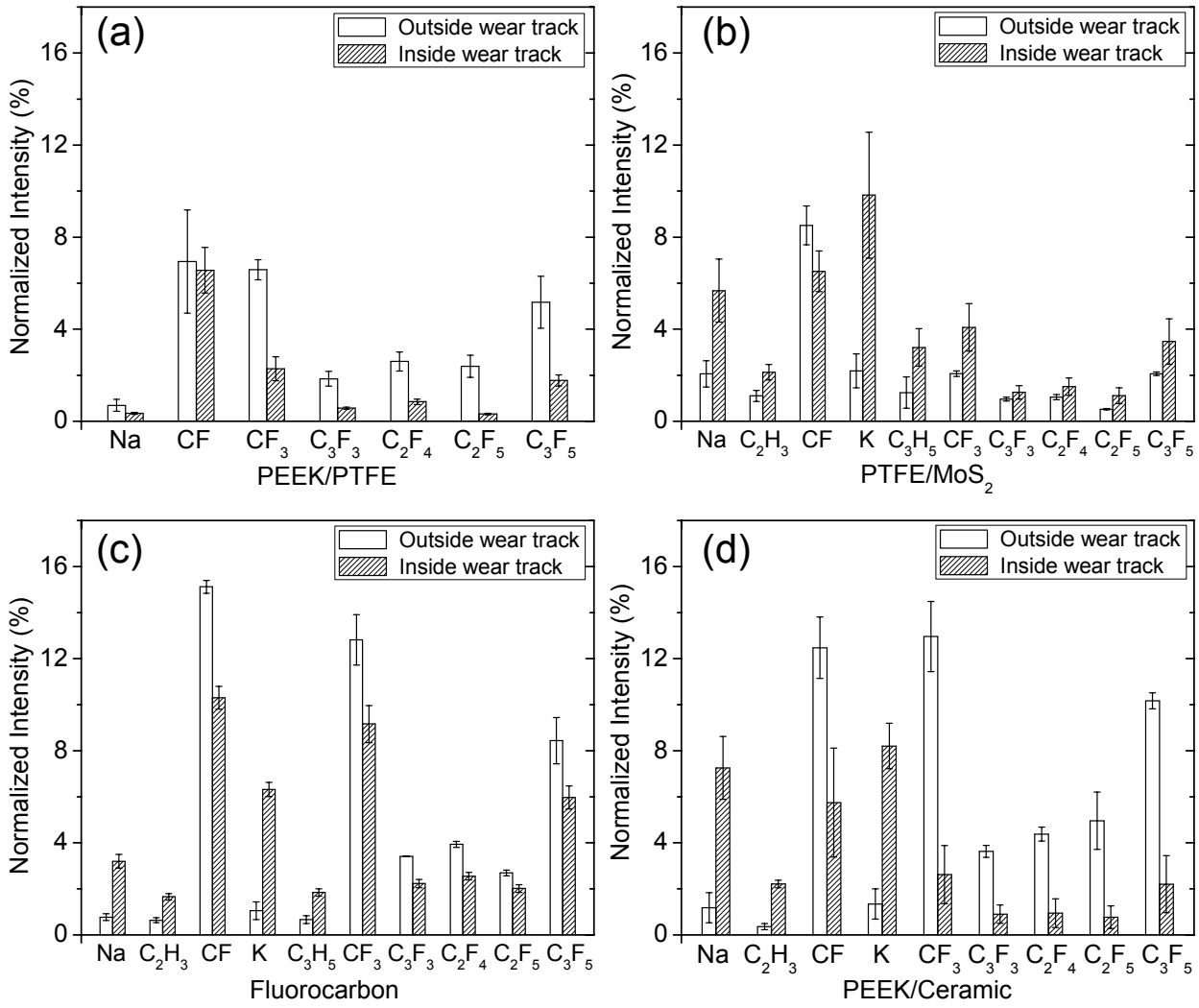

Figure 6.23─TOF-SIMS normalized values of intensity as extracted by TOF-SIMS spectra of coatings tested under boundary/mixed lubricated conditions (set 2).

Furthermore, the intensities of TOF SIMS spectra are always strongly dependent on the matrix composition and for each of the system investigated here a different pathway of ions formation (fragmentation) could be adopted. In all the cases presented here, namely PEEK/PTFE, PTFE/MoS_2, Fluorocarbon, and PEEK/ceramic, the arrangement and orientation of polymer macromolecules (e.g. PEEK, PTFE) can be different (even for the case where the same polymer is used, e.g PEEK) giving rise to chemically different interface in each case. Therefore, the normalized intensity (or relative chemical composition) changes as the surface experiences wear are plotted and shown in Figures 6.23 through Figure 6.24. The relative percentage was obtained dividing the number of counts of the each chemical species by the total number of counts of all the species present.

Even though the C-F compounds were found as the main chemical species for all coatings, their abundance was different depending on the type of coating tested (Figure 6.23). As observed on Figure 6.23, one of the main polymer fragment ions from PTFE is CF^+ (31 m/z) which showed the largest value of normalized intensity outside of wear track for all coatings. Interestingly, the percentage variation in intensity of the CF^+ peak was lower in the PEEK/PTFE and PTFE/MoS_2 cases compared to Fluorocarbon and PEEK/Ceramic (Figure 6.23a)). These lower changes in percentage variation agree and provide evidence of the higher wear resistance of PEEK/PTFE and PTFE/MoS_2 coatings when compared to Fluorocarbon and PEEK/Ceramic (as directly correlated with the wear rates shown in Figure 6.16). In addition, the intensity of the CF^+ and CF_3^+ component was higher for Fluorocarbon and PEEK/Ceramic coatings outside the wear track as seen in Figure 6.23c) and Figure 6.23d) and its intensity decreased significantly after sliding contact. It is believed that this higher intensity contributed to the lower friction coefficient behavior of PEEK/Ceramic coating compared to PEEK/PTFE and PTFE/MoS_2, but at

the same time the higher change in intensity after testing contributes to higher wear rates. This finding is supported by direct comparison of the intensity of the C_iF_j chemical compounds in the tested regions between the unlubricated and lubricated samples of PEEK/PTFE (see Figure 6.24a)). As pointed out before (section 6.4.4) under unlubricated conditions PEEK/PTFE exhibits both; a lower friction coefficient of 0.03 and a higher intensity of the C_iF_j chemical compounds compared to the boundary/mixed lubricated case. These results support the hypothesis of lower friction at higher intensity of the C_iF_j chemical compounds. For the purpose of comparison, the different polymer C_iF_j fragment ions for the tested coatings were summed up and are shown in Figure 6.25a)).

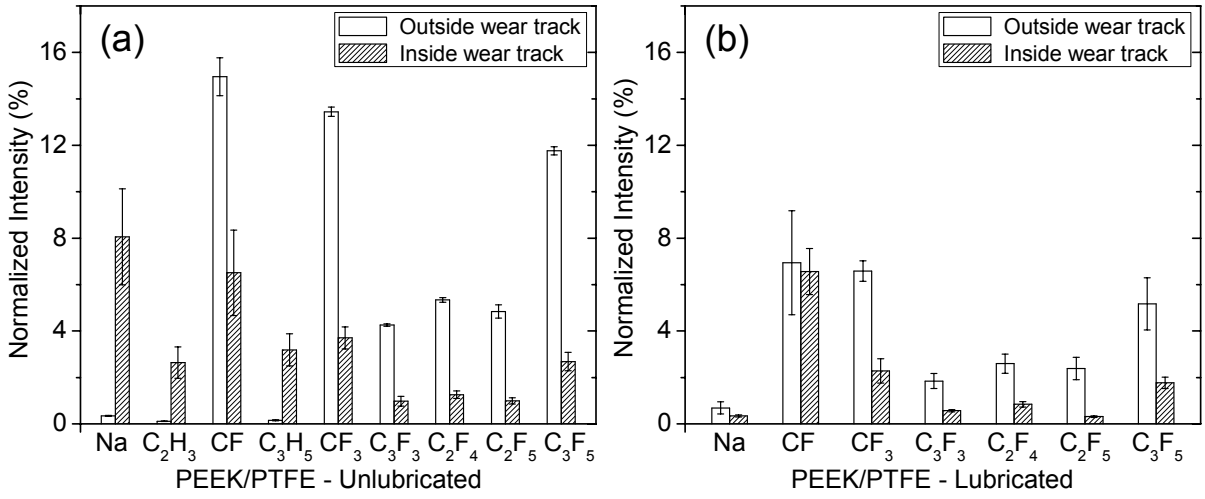

Figure 6.24─TOF-SIMS normalized values of intensity as extracted by TOF-SIMS spectra of the PEEK/PTFE coating tested under unlubricated a) (see Figure 6.14) and boundary/mixed lubrication conditions b).

These fragment ions were composed of CF^+ (31 m/z), CF_3^+ (69 m/z), $C_3F_3^+$ (93 m/z) and $C_3F_5^+$ (131 m/z). It can be observed that the intensity of ΣC_iF_j is higher in the case of PEEK/PTFE (unlubricated), PEEK/Ceramic, and Fluorocarbon compared to PEEK/PTFE (lubricated) and PTFE/MoS_2. This finding (see Figure 6.25 a)) strengthens the idea of lower

friction at higher C_iF_j intensity and lower wear in the case of PEEK/PTFE and PTFE/MoS_2 due to a rather homogeneous transfer film (by smaller change in relative intensity). Also it should be mentioned here that the different C_iF_j chemical species present different polarities (electronegativities) giving rise to different extent of transfer film adhesion onto the counterpart during the whole sliding experiment. Similar conclusions can be drawn from Figure 6.25b) where only the CF^+ fragment ion intensity is observed for all the different coatings which is in agreement with the literature [103, 104]. It is believed that the main reason why C_iF_j species are mainly found has to do with the sensitivity of the TOF-SIMS technique which is only on the range of 2 to 3 nm on the surface. This mainly exposes the PTFE and Fluorocarbon fragments on the surface of the coatings.

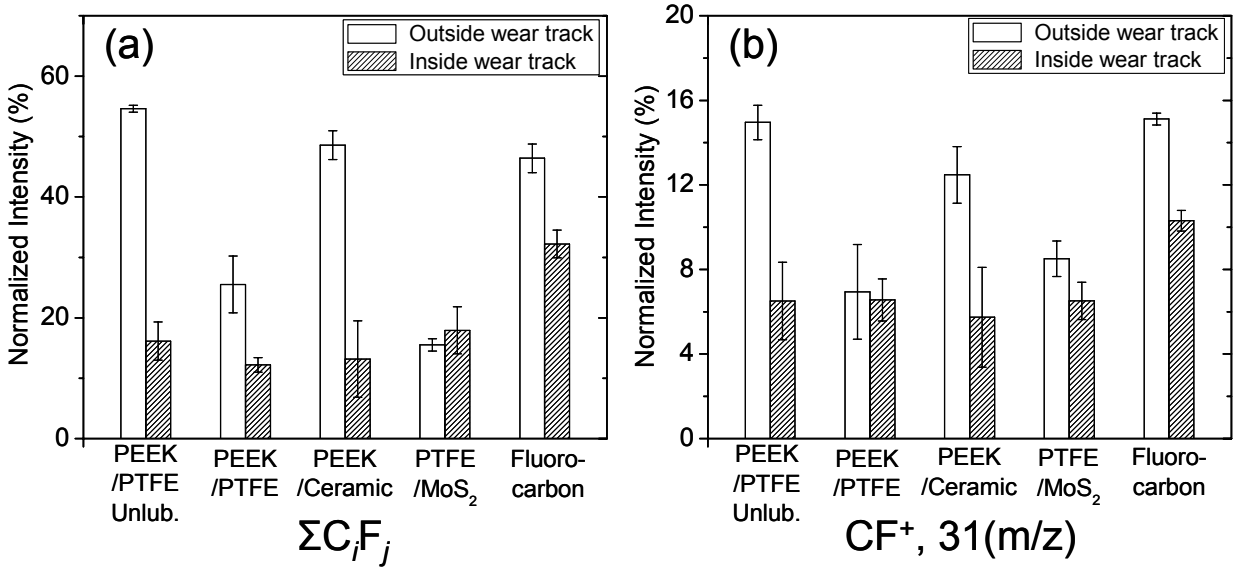

Figure 6.25—TOF-SIMS normalized values of intensity as extracted by TOF-SIMS spectra of (a) ΣC_iF_j fragment ions of the different coatings tested under unlubricated and starved lubricated conditions, (b) CF+ fragment ions.

6.4.8 XRD

XRD was used to examine the changes in crystalline structure of the coating before and after testing. Examination of the coatings was performed on a Phillips X'pert system which has a multi modular primary and secondary optics in order to account for the various requirements of primary x-ray beam divergence and detector angular acceptance. The 2 theta angle region ranged from 0 to 50° was scanned, with a rate of 0.023° s^{-1} using Copper K-alpha radiation with a wavelength of 0.15418 nm.

The XRD analysis was performed on the surface of the virgin and worn PEEK/PTFE coating testing under unlubricated conditions (set 3). Figure 6.26 shows the counts per second (CPS) as a function of the characteristic diffraction angle (2θ) of PEEK, PTFE, and gray cast iron (substrate). From this figure it can be observed a change in intensity for the diffraction angle corresponding to the PEEK component after testing. This change in intensity (counts) can be attributed to an increase in crystallization of the PEEK component of the coating. It is believed that the mechanism governing this increase in crystallization is related to the formation of lamellar structures (spherical crystalline regions). The formation of these structures is enhanced once the sliding temperature exceeds T_g of the polymer. At this point, the more organized structure of PEEK (obtained by running the experiment at 170 °C) provides an increase in hardness and due to its higher density slippage is more difficult to occur. Through nanoindentation measurements inside of the wear track after testing, it was found that hardness increased to 0.34±0.03 GPa which is higher compared to the 0.17±0.07 GPa measured before testing as can be observed in Figure 6.27. This increase in hardness provides further evidence of the increase in crystallization of PEEK which enhance its resistance to wear and plastic deformation. Also, these findings are in agreement with the literature, where an increase in

hardness and stiffness with crystallinity was measured [98, 113]. It should be mentioned that the XRD data provided here is not normalized and that to further understand the crystallization of PEEK during tribological testing, techniques like differential scanning calorimetry (DSC) should be used.

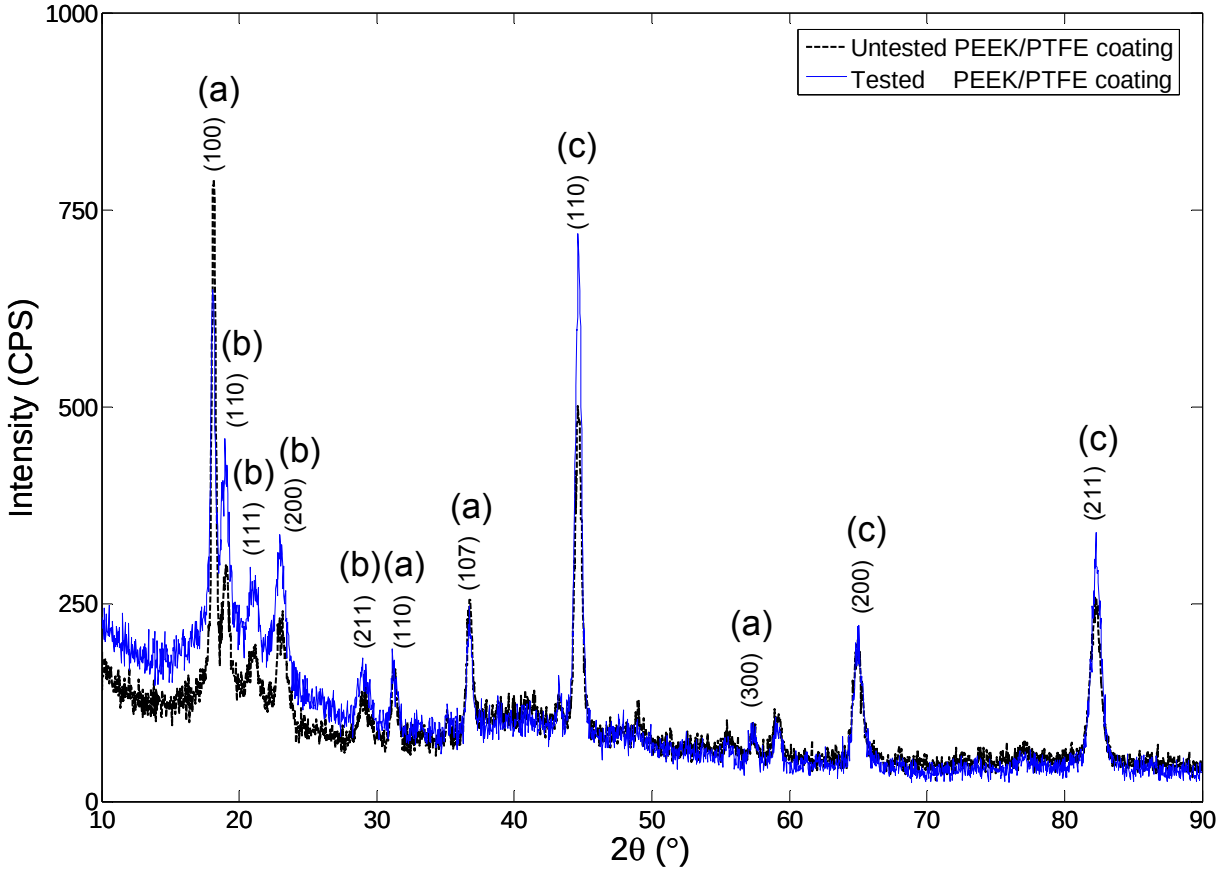

Figure 6.26—XRD profiles of PEEK/PTFE coating. The different diffraction angles characteristic of PTFE, PEEK, and gray cast iron (substrate) are denoted by (a), (b), and (c) respectively.

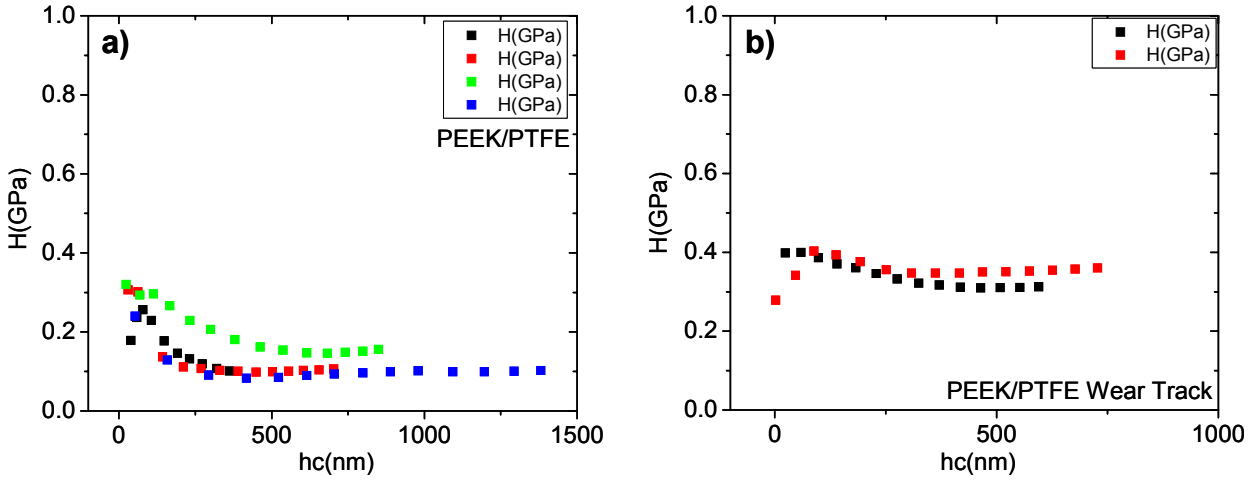

Figure 6.27─Hardness measurements of PEEK/PTFE coating; a) before testing, b) after unlubricated unidirectional testing.

6.5 Summary

In this chapter, different high bearing based polymeric coatings based on PEEK, PTFE, and Fluorocarbon were investigated under boundary/mixed and unlubricated conditions (oscillatory and unidirectional). Based on the coatings tribological performance, and comparative studies of the surfaces before and after the sliding tests, by using SEM and TOF-SIMS for imaging and chemical analysis, the following conclusions could be drawn:

a) Under unlubricated oscillatory conditions, PTFE/MoS_2 showed the lowest wear rate from all the tested coating. By analysis of the wear debris of PEEK/PTFE and PTFE/Ceramic after testing, it was observed that the wear mechanisms were mainly abrasive and fatigue.

b) PEEK/PTFE coating performed better compared to PTFE/MoS_2, Fluorocarbon, and PEEK/Ceramic in terms of wear under both; unidirectional boundary/mixed and unidirectional unlubricated sliding conditions.

c) The morphology of the wear debris of the polymer coatings suggested that the main wear mechanisms present under oscillatory and unidirectional conditions were abrasive and fatigue type respectively.

d) The near-contact temperature decreases under testing at boundary/mixed lubrication conditions. Through SEM microscopy images it was shown that this behavior is due to transfer films that seem to provide a stable interface along with thermal insulation.

e) PEEK/PTFE coating was the only from the four coatings tested that was able to perform well under unlubricated conditions and high contact pressure. Also the friction coefficient of this coating under unlubricated conditions was lower compared to boundary/mixed lubrication. The wear rate was similar under unlubricated and boundary/mixed lubrication conditions. This could be attributed to the arrangement of the two constituents polymers, where during preparation of the PEEK/PTFE coating intentionally the PTFE particles migrate to the top of the coating. PEEK, sitting below PTFE, provide strength and wear resistance and can be considered responsible for a good adhesion with the cast iron substrate.

f) TOF-SIMS analysis showed higher relative intensity of the C_iF_j fragment ions in the case of Fluorocarbon and PEEK/Ceramic. Higher intensity contributed to lower friction (PEEK/Ceramic), but higher wear rates compared to PEEK/PTFE and PTFE/MoS_2. Also the relative change in intensity of the CF^+ fragment ion (from PTFE) was lower in the case of PEEK/PTFE and PTFE/MoS_2 compared to Fluorocarbon and PEEK/Ceramic from outside to inside of the wear track. This explains the lower wear rate of these coatings under boundary/mixed lubrication conditions and can be attributed to a rather

homogeneous transfer film sustained in the cases of PEEK/PTFE and PTFE/MoS_2 coatings.

g) Evidence of the superior performance of PEEK/PTFE coating was also verified through XRD where an increase in crystallinity was observed after unlubricated testing. This increase in crystallinity improves the wear resistance of the coating through an increase in hardness. These findings make PEEK/PTFE coatings promising and attractive towards oil-less compressors applications contributing to greener environments.

CHAPTER 7
CONCLUSIONS

7.1 Contributions

By using specialized tribometers (HPT, UHPT) different studies were performed to understand the role of lubricants, materials, and refrigerants applicable to air-conditioning and refrigeration systems.

The performance of PAG and POE lubricants in the presence of CO_2 was studied under boundary/mixed lubrication conditions from the scuffing and wear point of view using the HPT. By using an Al390-T6 and 52100 steel shoe interface, it was found that PAG performed better than POE in terms of scuffing resistance and wear. Wear indexes obtained using 3D scans measurements inside the burnished tracks of the disks showed that the disks lubricated with PAG lubricant had a lower decreased in the fluid retention capabilities. The overall superior performance of PAG was confirmed using XPS where it was found the formation of carbonate species (CO_3^{2-}) after testing leading to a higher scuffing and wear resistance compared to the disk lubricate with POE. The lower performance of POE was attributed to the effect of hydrolysis caused by the chemical structure of this lubricant. Hydrolysis promoted the formation of CO_2-philic groups leading to a higher solubility of POE-CO_2. This results in a drop of viscosity in the case of POE lowering its lubricity properties.

Once the performance of lubricants in CO_2 environment was studied, different material interfaces were examined using boundary/mixed and submerged lubricated conditions using PAG. Al390-T6, gray cast iron, and Mn-Si brass were tested against 52100 steel shoes to evaluate their scuffing ad wear resistance. It was found that the scuffing resistance of gray cast iron and Mn-Si brass was higher compared to Al390-T6. Moreover, the approach to scuffing in

the case of Mn-Si brass was not abrupt compared to gray cast iron and Al390-T6. By EDS it was shown that this behaviour was attributed to the melting of Pb in the onset of scuffing which provides additional lubricity properties. XPS analysis showed that there is a correlation between different species coming from the fragmentation of the PAG lubricant and the scuffing behavior of the different materials tested. Mainly in gray cast iron and Mn-Si brass, metal oxides formed on the surfaces of the tribopairs during sliding are believed to increase the scuffing resistance. Under submerged conditions gray cast iron performed better in terms of wear compared to Mn-Si brass and Al390-T6. The wear behavior was correlated with hardness measurements where it was found that even though the hardness of Mn-Si brass was similar compared to Al390-T6; this latter material depletes Si during testing losing hardness.

Although the aforementioned studies dealt with the performance of lubricants and bare materials in the presence of CO_2, these experiments were performed at low CO_2 pressures. With the upgrade of the UHPT it was possible to perform experiments at realistic pressures of CO_2 air-conditioning and refrigeration systems. Unlubricated experiments at different regions of the CO_2 phase diagram showed that once the transition from gas to liquid phase is over passed the friction coefficient decreases below 0.10. Under conditions of variable mass and constant mass of CO_2 during testing it was shown that the dominant factor in the friction behavior was the pressure of the gas, not the mass. The minimum amount of mass was found to be 5 g of CO_2 to avoid scuffing under the testing conditions used in this study. The lubricity effect of CO_2 was also observed under supercritical conditions, where it was shown that this lubricity effect was present in other material interfaces. Using XPS it was shown that iron oxides present on the surface before testing react with CO_2 forming iron carbonates which are know to provide wear resistance during tribotesting. This reaction was proven to be facilitated at pressures higher than 6.89 MPa

by observation of the O1s, C1s, and Fe2p XPS spectrums. Using FIB a tribolayer of ~500 mm in thickness was observed and it is believed this tribolayer is composed of iron oxides and iron carbonates. The overall experimental results show that CO_2 has advantages from the tribological point of view when it is employed as a refrigerant. These tribological benefits are enhanced when CO_2 is operated at conditions similar to those found in air-conditioning and refrigeration systems. These results point out in the direction of evaluating the possibility of using CO_2 as a lubricant in areas different than air-conditioning and refrigeration systems. For instance, by taking advantage of the thermodynamical behavior of CO_2 under the liquid and supercritical phases, it could be possible to employ it as cheap lubricant to reduce energy consumption in cutting processes. Also, taking advantage of the lubricity effect of CO_2, another possibility that could be explored is to compress CO_2 in closed systems where friction needs to be reduced. Certainly, those applications do not contribute directly to greener environments, but help to recycle and postpone the CO_2 emissions.

The air-conditioning and refrigeration industry has been shifting its attention towards the development of cleaner technology that can contribute to greener environments. Greener environments, not only includes the implementation of environmentally friendly refrigerants, but the reduction of oil usage. To address the issue of less oil use towards oil-less compressors, advance materials are needed to be developed in situations where the presence of lubricant is cumbersome. In Chapter 6, the friction and wear performance of PEEK/PTFE, PTFE/MoS_2, Fluorocarbon (FEP) and PEEK/Ceramic high bearing blended polymeric coatings was studied under boundary/mixed and unlubricated conditions. These coatings were deposited on gray cast iron (a bare material commonly found in air-conditioning and refrigeration compressors). Under oscillatory conditions it was shown that even though the thickness of the coatings was

penetrated, the interface did not scuff due to the effect of the wear debris that behaved as a third body protecting the interface against adhesive wear. The morphology of the wear debris after testing, suggested fatigue and abrasive wear as the main wear mechanisms of these coatings. PEEK/PTFE and PTFE/MoS_2 performed better in terms of wear compared to PEEK/Ceramic coating. A decreased in the near-contact temperature was also observed during the experiments and it was attributed to the transfer films from the polymer coatings to the 52100 steel counterpart. These transfer films behave as thermal insulators and once they are transfer to the counterpart no further increase in wear is observed. By using TOF-SIMS it was found a smaller change in the normalized intensity of CF^+ species before and after testing in the case of PEEK/PTFE and PTFE/MoS_2 compared to PEEK/Ceramic and Fluorocarbon. This small change in the normalized intensity after testing was attributed to the fact that under boundary/mixed lubricated conditions most of the load is taken by the lubricant which implies that a small percentage of the PTFE component sitting on the top of the coatings is being transferred to the hard 52100 steel counterpart. On the other hard in the case of PEEK/PTFE and Fluorocarbon, these relative changes in normalized intensity were larger. In addition, TOF-SIMS results of PEEK/PTFE tested under unlubricated unidirectional conditions showed a larger decreased in the CF^+ component after testing compared to the same coating tested under boundary/mixed lubrication which means that a larger component of the PTFE was transferred to the counterpart. This also explains the lower friction coefficient of PEEK/PTFE under unlubricated conditions compared to boundary/mixed lubrication. Furthermore, using nanoindentation, an increase in hardness was observed after testing under unlubricated conditions in which case a PTFE layer is transferred to the 52100 steel counterpart and the hard PEEK component of the coating is exposed. The increase in hardness was also explained based on XRD which suggested

crystallization of the PEEK component of in PEEK/PTFE at the sliding temperature conditions. This temperature at the sliding interface was higher compared to Tg resulting in a higher molecular density and an increase in the stiffness and resistance against slippage of the PEEK/PTFE coating. These results are promising, since the possibility of operation under less oil use seems achievable even under extreme conditions, thus contributing to cleaner environments.

7.2 Recommendations for future work

The performance of different materials and lubricants were evaluated under boundary/mixed lubricated conditions in chapters three and four. It is recommended to perform boundary/mixed lubricated experiments at high CO_2 pressures to better understand the role of the miscibility between lubricant and CO_2 refrigerant at high pressures (similar to those studied in chapter 5) and its ultimate impact in the friction and wear behavior. Due to the extraordinary behavior of CO_2 at high pressures and its tendency to form tribolayers, it is recommended to study and consider this refrigerant in processes where there is a need to reduce friction.

Through different experimental conditions, it was shown that polymeric coatings are promising for oil-less applications compressors systems, thus contributing to greener environments. However, more studies at high temperature are needed to understand the behavior of these coatings at conditions above their glass temperature (Tg). These experiments will not only provide answers of the friction and wear behavior of these coatings under adverse sliding conditions, but will also shed light on the different wear mechanisms of these coatings at high temperature. The future towards greener environments by application of cleaner technology looks promising due to the technological advances in engineering materials and deposition

techniques. The advent of these technological advances coupled with the use of environmentally-friendly refrigerants would not only impact our environment, but would also limit the use of oil, contributing to greener environments in the upcoming years.

In addition, to better understand friction and wear under starved lubricated conditions, it is suggested to improve the lubricant supply system showed in Figure 2.3 which is appropriate for long duration experiments. Experimental evaluation of the tribological behavior of the new refrigerant HFO-1234yf needs to be carried out. In this direction it is recommended to study the following aspects:

a) Compare the friction and wear behavior of the HFO-1234yf refrigerant against CO_2 and R-134a using the same protocol employed by Demas et al [52]. These experiments will provide answers on the impact of HFO-1234yf on bare materials under unlubricated conditions.

b) After testing under unlubricated conditions, a new set of experiments performed under starved lubricated conditions should be performed. Since the thermodynamical properties and chemical structure of HFO-1234yf are similar to R-134a, *PV* curves can be obtained under different lubricant supply rates and sliding speeds on both refrigerants using the spray system. The experimental results will show direct comparison of the load bearing capacity of both refrigerants in the presence of synthetic lubricants (i.e., PAG, POE). Chemical analysis of the surface using TOF-SIMS and XPS will also be necessary for the understanding of the role of tribochemistry.

c) Similar studies as the ones suggested in chapter 6 can be applied in the presence of HFO-1234yf refrigerant under starved lubricated conditions using polymer coatings, especially

to understand the interaction of refrigerant, lubricant, and polymer coating under starved lubricated conditions.

d) The viscoelastic properties of the deposited polymer coatings should be studied to further understand the behavior of these materials. It is suggested to deposit a thicker coating (according to the commercial vendor thicknesses up to 750 μm can be obtained by different spray passes and baking steps) and peel it. After, small samples can be obtained to perform microtensile testing at different strain rates.

APPENDIX A

A.1. Instructions of operations of the UHPT

The upgraded Ultra High Pressure Tribometer (UHPT) is a very delicate equipment which has to be operated with extreme care in order to avoid collision and damage of its components. The following steps must be followed for appropriate operation:

1) To start up the machine turn the knob located below system power to the right position (see Figure A.1).

Figure A.1─Front panel of the UHPT.

2) Wait 30 s while the self-calibration and system check takes place (see Figure A.2), then press ok. Push the Red button (Figure A.1)

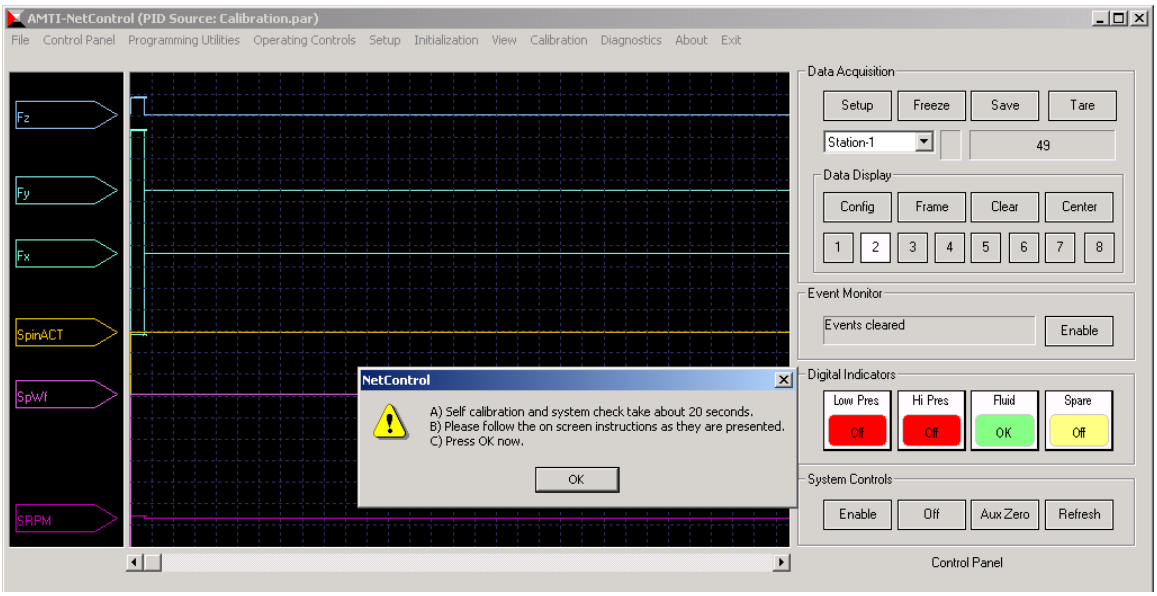

Figure A.2—Self calibration and system check.

3) A system check window will open, on this window check that the **On line** option is enabled with **Yes**, then press ok. The Fz, Fx, and Fy components of the transducer will start to acquire data

4) **Self calibration complete** will pop up. Click ok.

5) A new window **Net control** window will pop up as seen in Figure A.3. Turn the key placed on the red button to the reset position (see Figure A.1), then move the black knob located on the actuator power to the **START** position. Sometimes once the machines start, the actuator moves and the pin-holder and the upper disk might crash. To avoid this problem, before moving the knob to the START position click on the control panel tab (upper left in Figure A.3) and select the **General Purpose Mode** option, then a window

similar to the one shown in Figure A.4 will pop up, click on the minus sign of the **Jog** to return the actuator to the initial position.

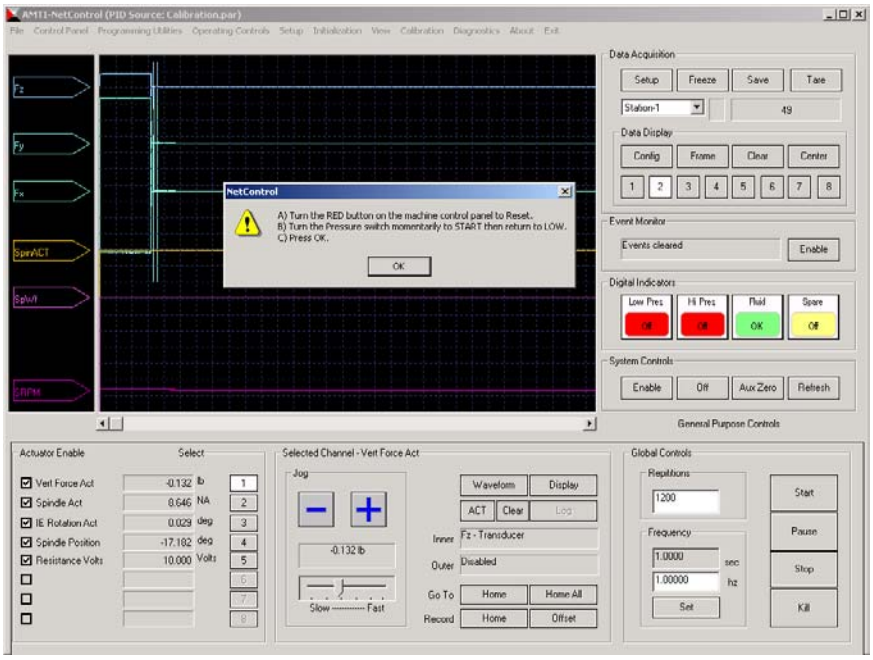

Figure A.3─Net control window.

Figure A.4─In-situ normal and friction forces captured on the UHPT.

Once the machine starts running, an unstable noise coming from the pump and the circulation of the hydraulic fluid will be noticeable in the first minutes. After some point the noise will be uniform at which point the black knob in the actuator power (see Figure A.1) can be switch to **High**. The machine must be operated in the High mode especially when the experiments are going to be performed at chamber pressures higher than 200 psi. Also in this mode the hydraulic pressure shown the by pressure gage on Figure A.1 should increase to around 800 psi.

Two different transducers are used to control and measure the normal and the friction forces. The first one is a 250 lbs Aluminum transducer that must be used for experiments performed at low normal loads (<50 lbs for safety purposes). The second transducer (stainless steel based) has a maximum capability of 1000 lbs in the normal direction and should be used in situations where the range of load is higher than 50 lbs (scuffing, wear, and submerged experiments). The correct calibration parameters have to be uploaded for each transducer. To upload the calibration parameters go to the **Setup** option on the menu and select the **Load** option, then select the calibration file corresponding to the chosen transducer as seen in Figures A.5 and A.6.

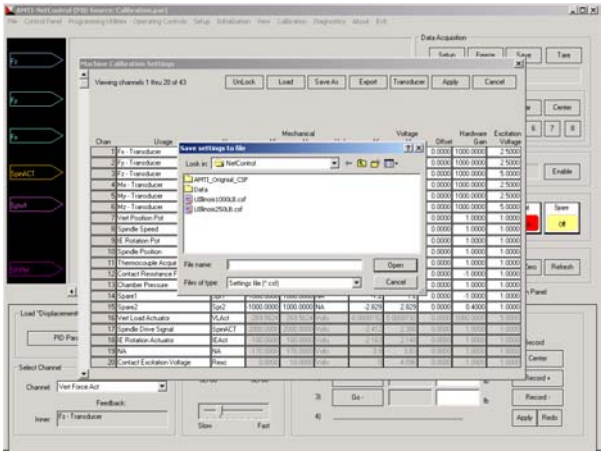

Figure A.5─Different calibration files of the force transducers used in the UHPT.

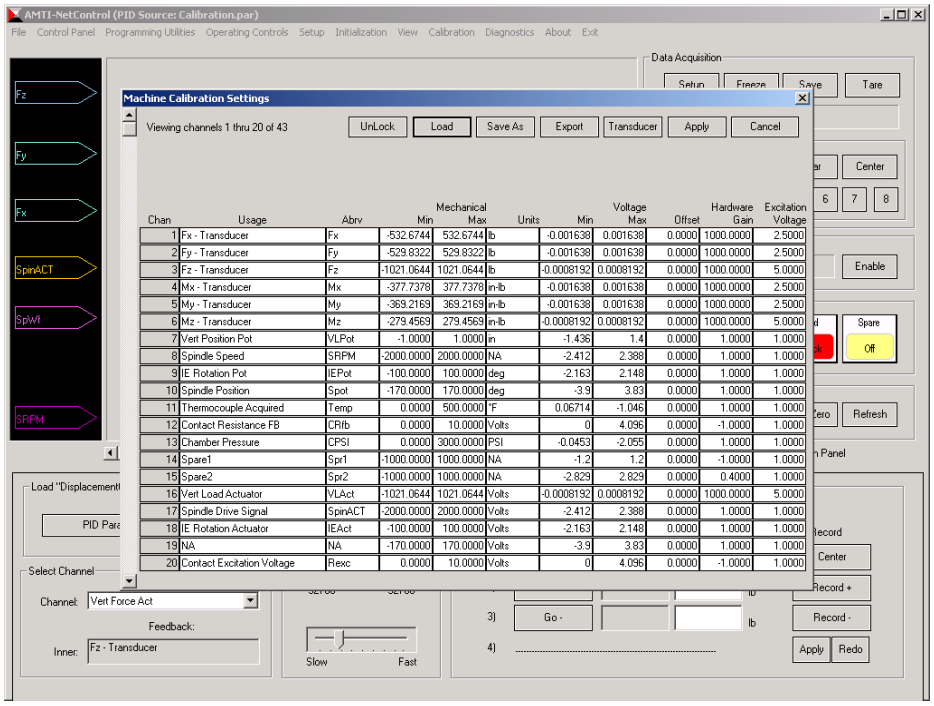

Figure A.6─Calibration parameters of the 1000 lbs transducer.

In addition, the upgraded UHPT can be set up in such a way that some limits in the normal and tangential forces can be applied to avoid damage of the transducers. These limits can be applied in the **Operating controls** choosing the option **Event Monitor Program**. As seen in Figure A.7 limits in the F_z, F_x, and F_y directions can by applied by typing the maximum values in the **Upper Threshold**. In the event the threshold is crossed in any of the axis, the actuator will disengage the contact avoiding damage of the transducer.

Before initiating a test some PID parameters have to be used in order to guarantee that the normal load is kept constant during the experiments. As can be seen in Figure A.8, there are three PID parameters; namely K_p, T_i, and T_d need to be set for the hydraulic actuator to keep the normal load constant at high pressure during the experiments. From these parameters, K_p values should be used between 0.4-0.5 in such way that the waveform of the normal load follows the

desired wave. T_i should set at 30000 when the machine is used in the High pressure mode (see Figure A.1) and set at 1 in the low pressure mode. Td should be set at zero all the time.

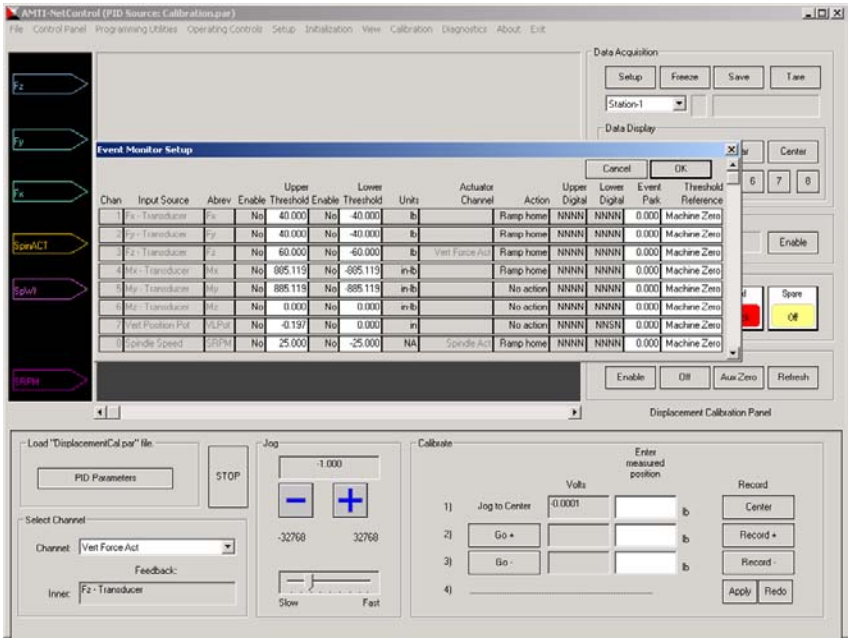

Figure A.7─Set up of the threshold forces to avoid damage of the transducer.

Figure A.8─Set up of the PID parameters K_p, T_i, and T_d of the UHPT.

Once the PID parameters are set, the next step is to set up the testing conditions. To upload the waveforms for normal force and revolutions per minute, click on the option waveform shown in Figure A.4. A new window similar to Figure A.9 will be shown, on this window click on the row label with **Vert Force Act** to set up the parameters of normal force. After, click on the **Edit Wave** option and select the **Sine Wave** option on the **Create/Load Waveform Data**. A sine wave similar to the one shown in Figure A.9 will be displayed, now click on the **Max** and **Min** windows below the **Edit Waveform Data** and after typing zero in both windows click apply. Now click on the **Offset** option and type the desire value of the normal load in lbs, then click apply. Repeat the same procedure for the **Spindle Act** to set up the RPM in unidirectional experiments. Click **Apply** to save these changes, also click on the **ACT** option below the waveform to activate the PID parameters. This is useful to keep the normal load constant, especially when the pressure inside the chamber fluctuates.

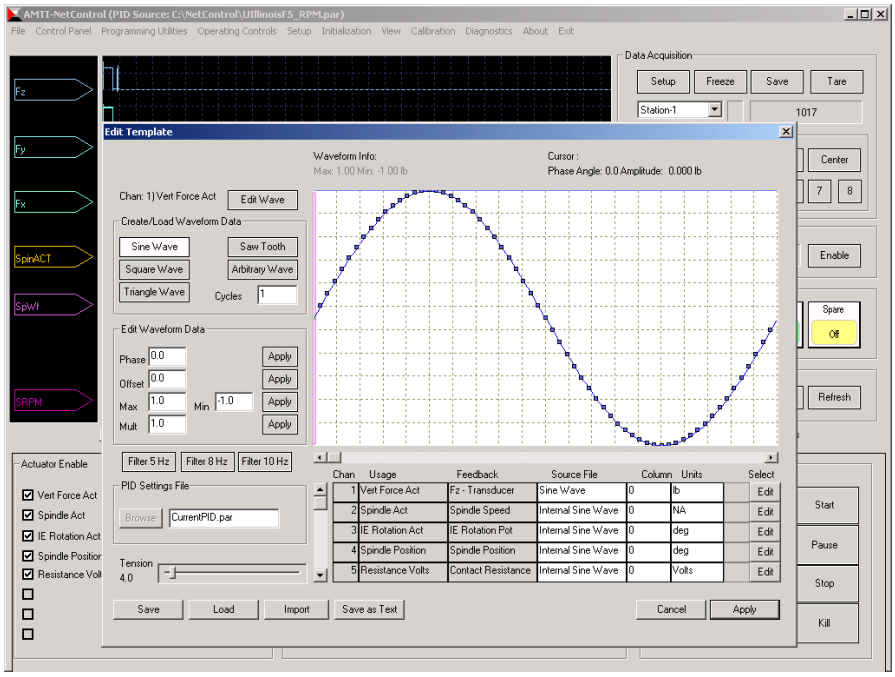

Figure A.9—Set up of the testing parameters or waveforms.

To perform unidirectional experiments the knob shown in the upper right corner of Figure A.1 should be placed on the **Vel** mode. Also the correct PID file must be selected for unidirectional experiments; this can be done by making a click on the **Operating Controls** on the top menu and then selecting the option **PID configuration**. The PID file for unidirectional (IllinoisF5_RPM.par) or oscillatory (IllinoisF5_POT.par) experiments can be selected on the **Load Settings** option (see Figure A.10). Once the file is loaded, click on the **Apply** option.

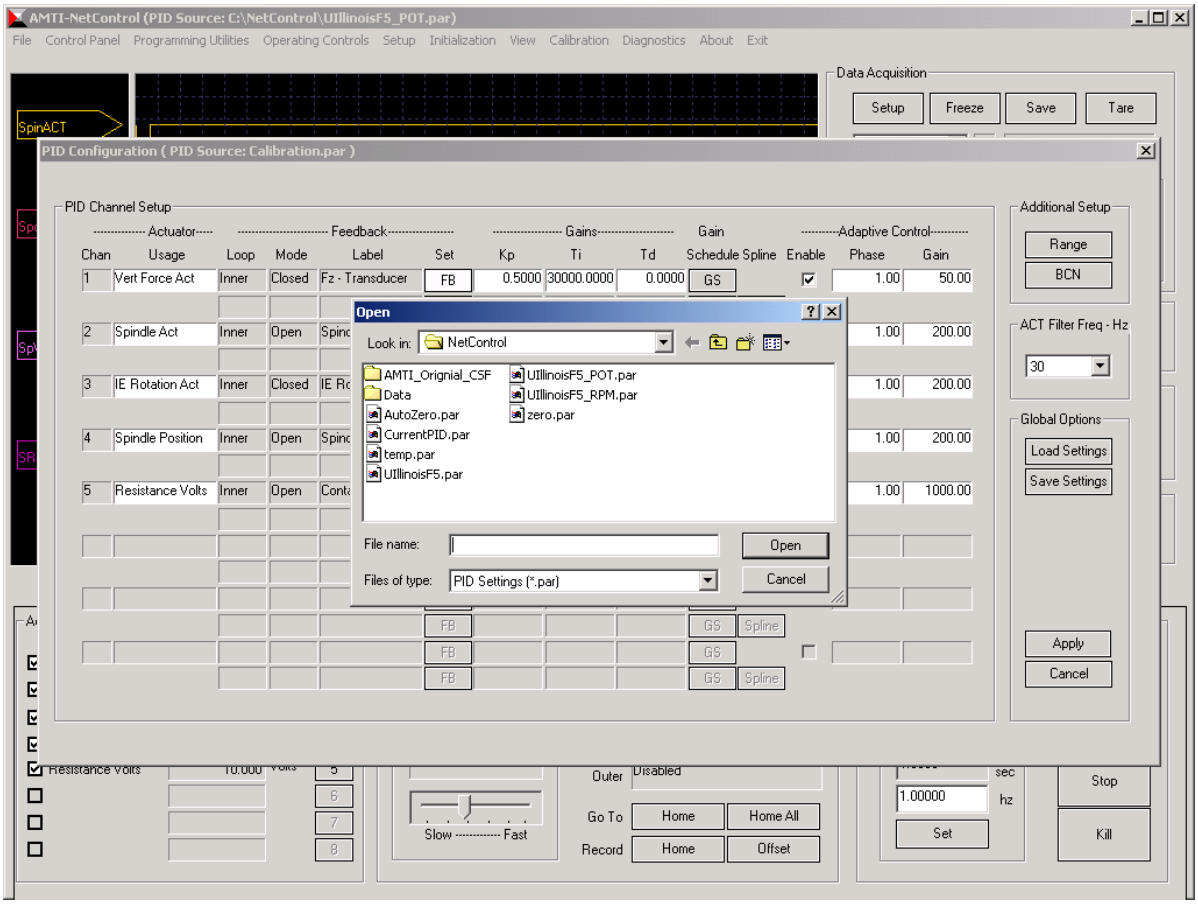

Figure A.10—PID files for unidirectional and oscillatory experiments.

Once the samples are appropriately place to start the test, go to **Initialization** on the top menu bar and select the **Transducer Autozero** (see Figure A.11) option to correct the strain-

gauge amplification for zero drift. After, the normal force shown below the jog on Figure A.4 will go to zero. In situation where the temperature of the chamber is increase above ambient temperature drift will occur and the **Tare** option shown in the upper right hand of Figure A.11 must be activated. Before starting an experiment the samples have to be preloaded, to do this use the **Jog** shown on Figure A.4 and move the bar close to the slow motion mode, then click on + sign in the **Jog**, the actuator should move upward to apply the normal load click + or – until you get ~10 lbs (this is an appropriate value for preload).

Before you start running the test, verify through the camera connected to the machine that the lower pin is sitting flat on the upper disk, this condition is necessary in the beginning of the experiments to avoid damage of the transducers. Close the chamber and open the valves to pressurize the chamber slowly (check that a pressure regulator is connected to the gas cylinders).

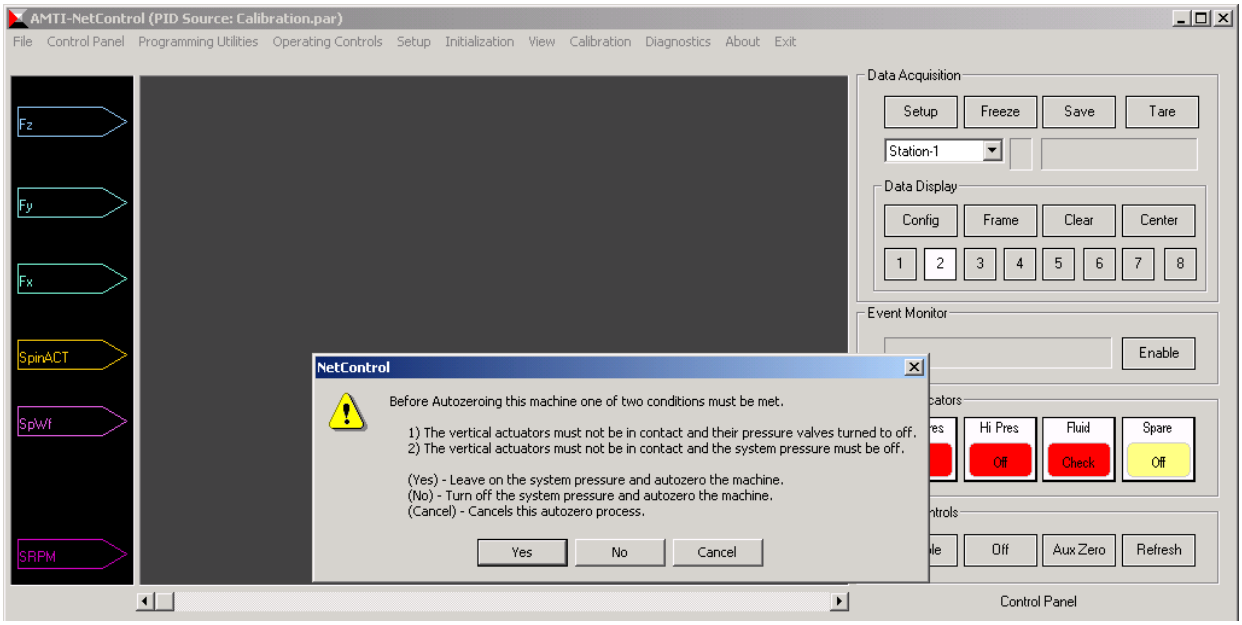

Figure A.11—Transducer Autozero operation to avoid drifting of the transducers.

To set up the duration of the experiments, the number of repetitions has to be calculated. For instance, a 10 minutes experiment performed using a waveform at a frequency of 2 Hz will need:

Repetitions=Frequency*duration (min)*(1/60) = 1200

The number of repetitions and the frequency must be type on the **Repetitions** and the **Frequency** boxes of the Global Control section as seen in Figure A.4, after typing these parameters click on **Set**. To start a test, click on **Setup** on the Data acquisition option a window similar to the one shown in Figure A.12. Type the duration of the experiment in seconds and name the file, then click **Ok**.

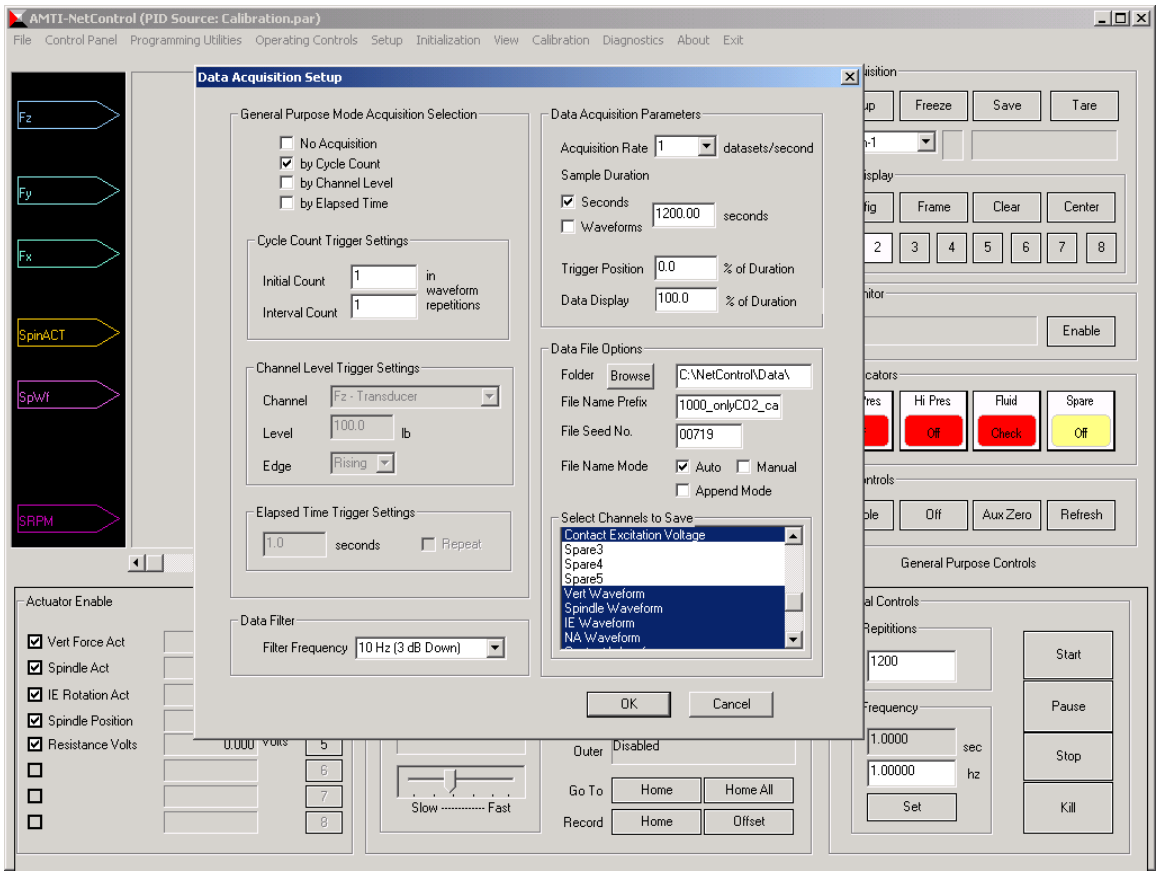

Figure A.12—Data acquisition set up to start a test.

To initiate the experiment click on the **Start** button as seen in Figure A.4, once the experiment starts monitor carefully the friction forces on the computer and observe the sliding interface (check the black monitor where the camera inside the UHPT is connected). Use your intuition and common sense, if you suspect weird noises coming from inside the chamber and the friction becomes high, stop the experiment immediately to avoid damage of the transducers. In the event that danger is imminent press the **Reset button** (red button shown in Figure A.1), this action will disengage the vertical actuator. Once the number of repetitions is reached, the experiment can be stop using the **Stop** button shown in Figure A.4. Similar procedure must be use for oscillatory experiments.

APPENDIX B

B.1. Effect of planarization on the contact behavior of patterned media

This study investigates the contact behavior of patterned media using a 2D plane strain finite element model. The effect of planarization on the resulting contact stresses for different filling materials were compared using a filling material in the area between patterns.

B.2. Introduction

In order to achieve higher densities in magnetic recording there is a lot of emphasis on the implementation of patterned media. Patterned media helps circumvent the problem of the superparamagnetic effect and provides thermal stability at higher densities [114, 115]. Two representative types of patterned media, namely bit-island type and discrete track recording (DTR)-type are being intensively investigated by researchers [116-118]. The structural stability of these patterns due to intermittent or sustained contacts with the magnetic recording head is also an important area of research. When the head flies over a patterned surface, the air-bearing pressure distribution will be influenced by the patterns and thus can significantly affect the head/disk dynamics. In order to overcome these potential dynamic instabilities, planarization of the patterned media is being investigated. This means that the region between adjacent patterned tracks is filled with a material. The contact behavior of patterned and planarized patterned media occurring from slider head features is examined in this appendix. Specifically, a comparative study of the effect of mechanical properties of the filling material on the contact behavior has been performed using finite element analysis (FEA).

B.3. Finite element model

A finite element method-based approach was adopted to examine this problem due to the complex nature of the contact involved. A quasi-static 2D plane strain model of a smooth rigid flat (representing the typically harder slider features) contacting a patterned media was modeled and solved using ABAQUS/Standard. Each pattern is composed of a magnetic layer material of 50 nm height and is coated with a 2.5 nm thick diamond-like carbon (DLC) overcoat. The DLC overcoat is typically not perfectly flat due to fabrication and deposition process and can be associated with some form of rounding. In this model, the DLC overcoat is taken as 1 nm at the edges of the patterns and 2.5 nm in the middle of each pattern, thus resulting in a radius of curvature of 834 nm. The pattern pitch is 300 nm as can be seen in Figure B.1, where the patterned media is depicted along with the filling material. In the FEA model we considered five patterns (in actuality these represent 10 patterns due to symmetry) since they provide sufficiently large contact width for the rigid flat whose length is representative of a head slider feature of the order of 3.0 μm. For simplicity, the remaining of the multilayers and the Glass or Aluminum-based substrate that are present in a magnetic media have not been considered. Instead, it was assumed that the whole region including the underlying substrate is made out of magnetic layer material (plus the DLC on top) denoted as "Bulk (Mag)" in Figure B.1. The mechanical properties of the DLC and magnetic layer are not bulk property values as they were based on actual sub-nm nanoindentation experiments using actual magnetic recording media samples [119]. The materials used are assumed to behave as elastic-perfectly plastic with no strain hardening and their mechanical properties are listed in Table B.1.

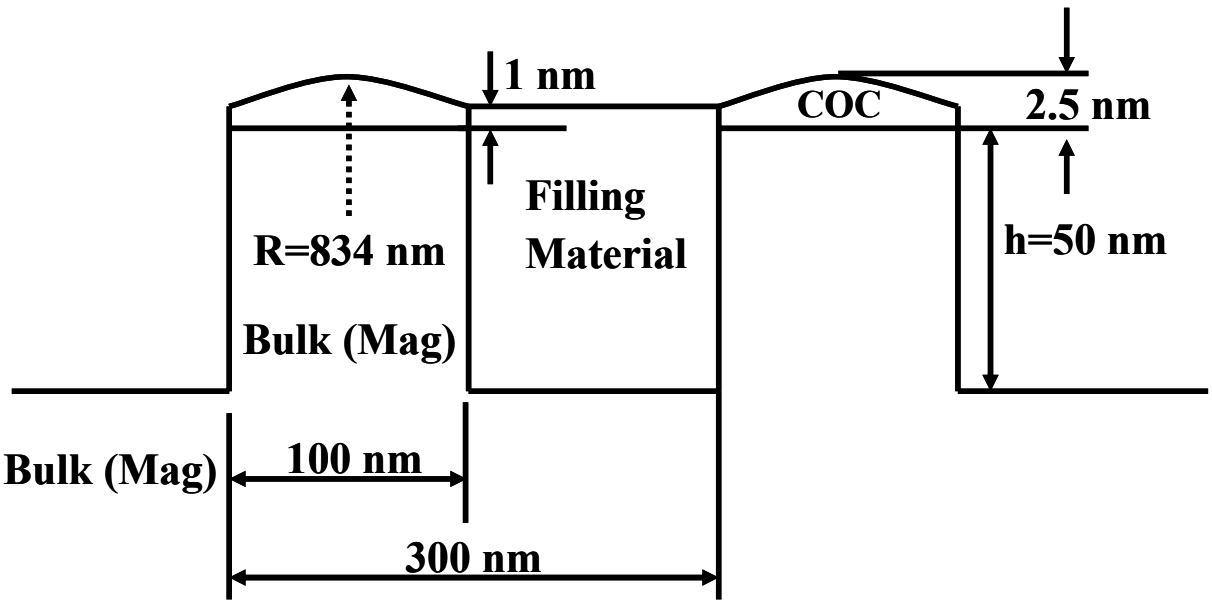

Figure B.1—Dimensions of patterned media (h is the pattern height).

Table B.1—Mechanical properties for the different layers

Layer	Elastic Modulus (GPa)	Poisson's Ratio	Yield Strength (GPa)
DLC	200	0.24	5.0
Magnetic Layer	100	0.30	3.0
Filling Material	Case (a): None	0	0
	Case (b): Mag	0.30	3.0
	Case (c): DLC	0.24	5.0

Four-node bilinear quadrilateral elements were used to mesh the patterned media with the smallest elements being used in the patterns close to the contact region. Mesh convergence studies have been performed to ensure that the current mesh configuration was optimized to obtain accurate results. Due to the existence of symmetry about the vertical y-axis, only half the geometry is modeled. The model is 6 μm in width and 5.95 μm in height (excluding the pattern region) and it consists of 21437 elements and 21577 nodes (Figure B.2). The model dimensions

were chosen so that the results were not affected by the boundary conditions and the stresses were well-contained.

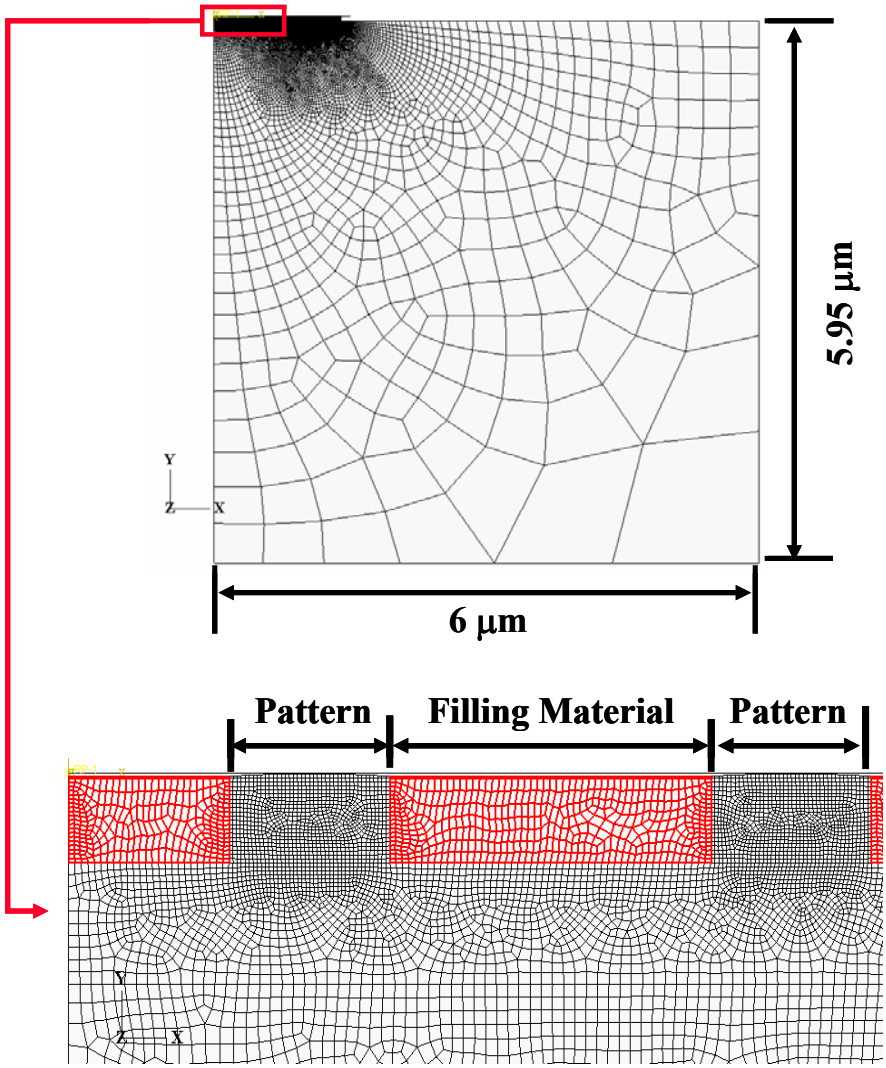

Figure B.2─FEA mesh used in the analysis.

Symmetry boundary conditions were applied on the left side constraining the horizontal motion (x-direction) of the left edge. The model was also constrained at the bottom, from moving in the vertical y-direction. An applied displacement δ of 50 nm was incrementally applied in a quasi-static manner to the rigid flat so that it contacts and compresses the patterned media. A Coulomb

friction model was used at the contact interface with a friction coefficient of 0.2. In order to perform a comparative study of the effect of the filling material on the contact behavior, three different simulation cases were considered: (1) No filling material (2) Filling material being the same as the magnetic layer and (3) Filling material being DLC (henceforth referred to as cases (a), (b) and (c) respectively). For simplicity, in this study, the filling material and the vertical walls of the patterns were assumed to be perfectly adhering. These simulations would provide an envelope of the resulting parameters when filling materials of different relative stiffness and hardness are used.

B.4. Results and discussion

B.4.1 Pattern stress imbalance due to contact

Figure B.3 depicts a contour plot of the normal (vertical) deformation of the media under a normal applied displacement of 50 nm. It is evident that although an equal displacement was applied to the top of the disk through the rigid flat, the normal displacement profile of the region under the patterns is not uniform. This displacement is higher near the center (symmetric boundary) and gradually decreases towards the edges of the contact. That is, despite the fact that all patterns were subjected to the same normal displacement, the displacement profile below the patterns changes when moving from the center pattern to the last pattern. The explanation for this behavior is because the whole geometry (mesh) used in this study is much larger than the region where the load is applied (normal displacement), representing realistic head/media contact. In such a case, the substrate displacement profile can be compared to the case of a simply supported beam with uniformly applied load at the center (Figure B.4), where the center pattern experiences the highest displacement and decreases when moving to the last pattern. Note that

the region at the right side of the last pattern provides additional structural stiffness, thus the displacement profile below the last pattern is smaller compared to the center pattern.

Also, owing to the normal deformation profile there is a net anticlockwise moment which becomes more prominent as one moves from the center pattern to the last one. This net moment results in higher shear stresses towards the lower-right edges of the patterns and are the highest in the last pattern, as can clearly been seen in Figure B.5. Interestingly this effect still exists with the presence of the filling material, but the magnitude of the stresses changes depending on the filling material's relative stiffness and hardness. Since the focus of this work is to examine the effect of using a filling material between the patterns, in what follows we focus on the stress results from the center pattern, since it was least affected by the stress imbalance discussed above.

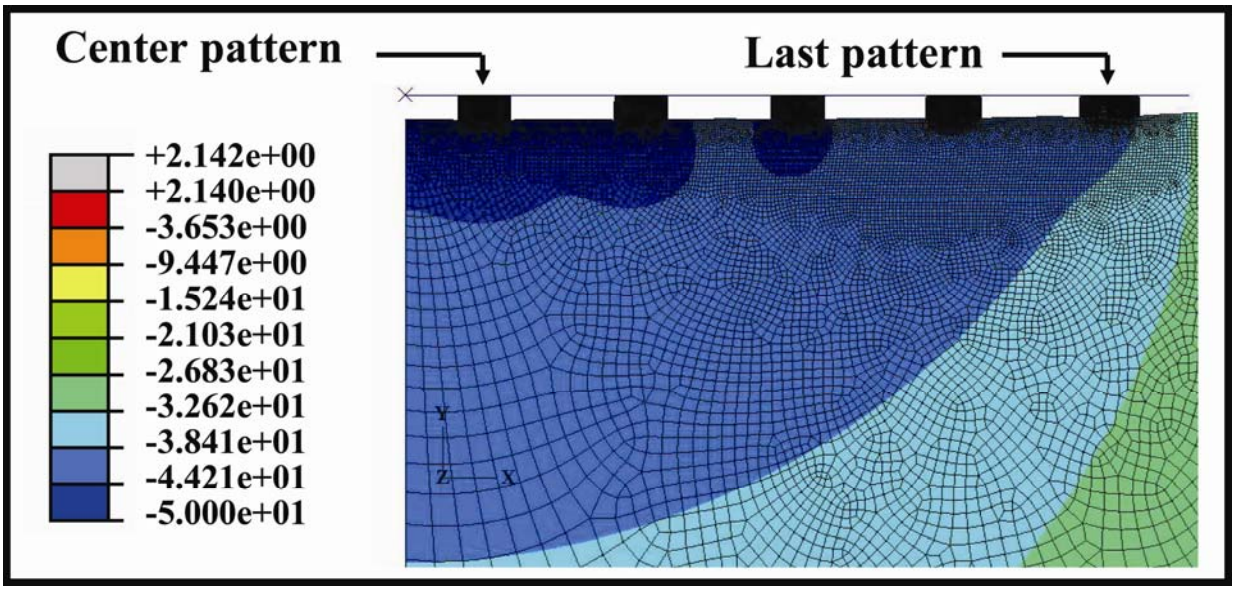

Figure B.3─Vertical deformation contour plot of the disk (units are in nm).

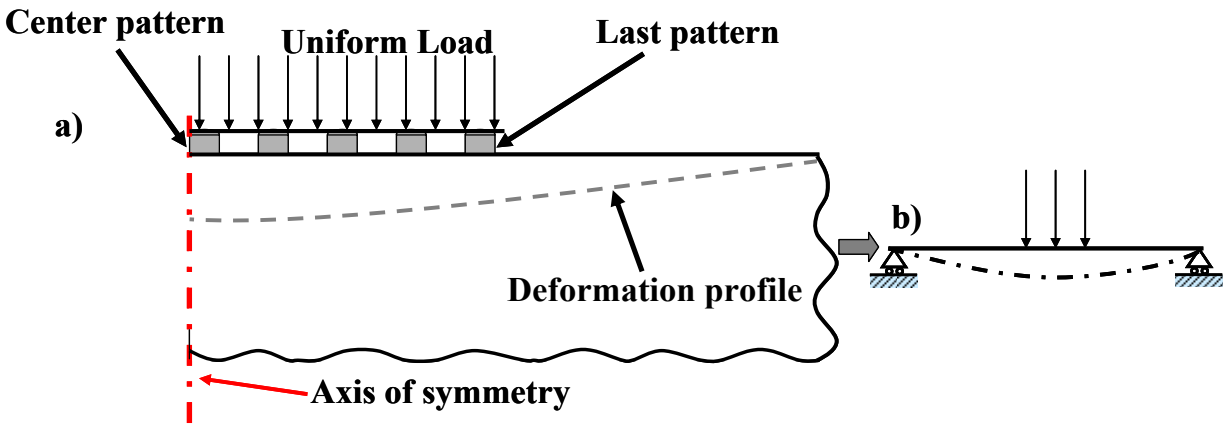

Figure B.4─(a) Displacement profile below the patterns, (b) analogy with a simply supported beam

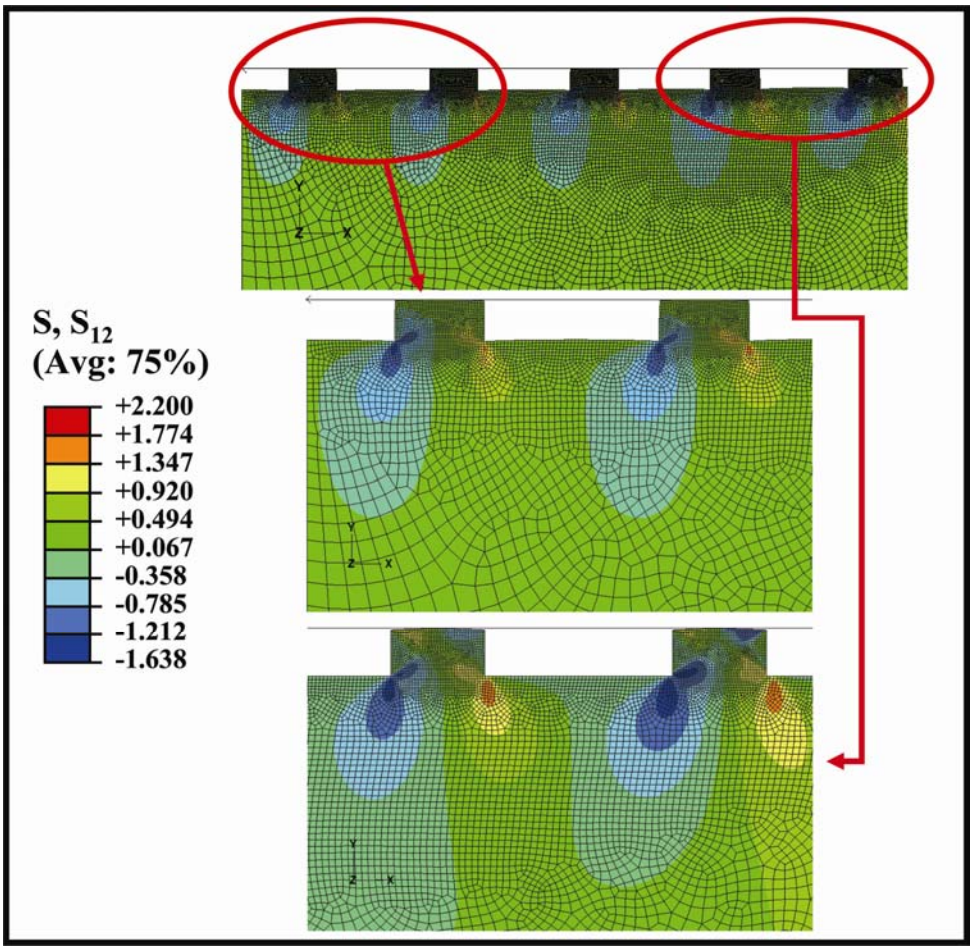

Figure B.5─Shear stress contour plots of the patterns (units are in GPa).

Figure B.6 shows the von Mises stress contours of a single pattern (center pattern) after an applied displacement of 50 nm. Note that the upper bound limit on the legend is set at 2.2 GPa to enable direct comparison of all 3 cases. The limit of 2.2 GPa is somewhat arbitrary and does not correspond to any material strength used in this work. Figure B.6(a) plots case (a), where there is no filling material. This represents a situation where the structural contribution of the filling material used for planarization is negligible. The magnetic layer region underneath the DLC has yielded (failed) indicating sub-surface yield. The gray region in Figure B.6(a) indicates the zone where the magnitude of the stress is higher than 2.2 GPa. Yielding of this region is more clearly observed in Figure B.7 (which is identical to Figure B.6(a)) but with the upper bound in the legend changed to 3 GPa which is the yield strength of the magnetic layer. This ensures that the highest stress contour represented by the red color in the legend in Figure B.7 is 3 GPa and indicates the region which has plastically yielded, which is significant.

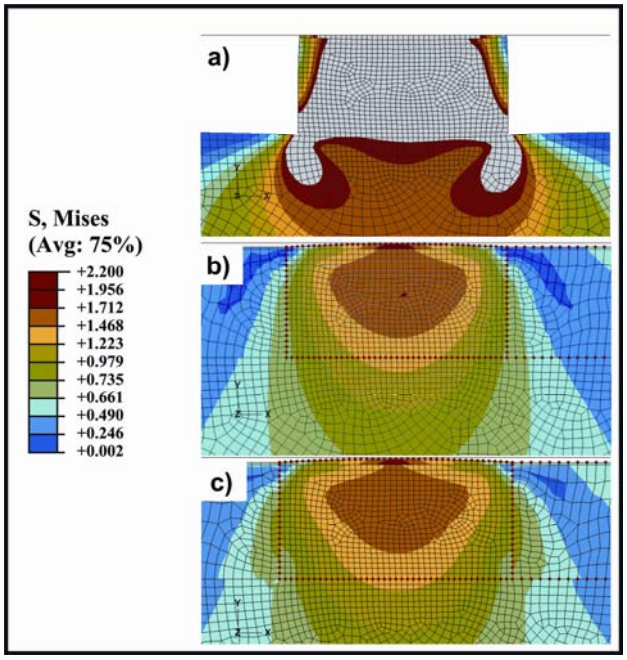

Figure B.6—von Mises stress contours of the center pattern for the three different cases of planarization materials (under 50 nm applied displacement, units are in GPa).

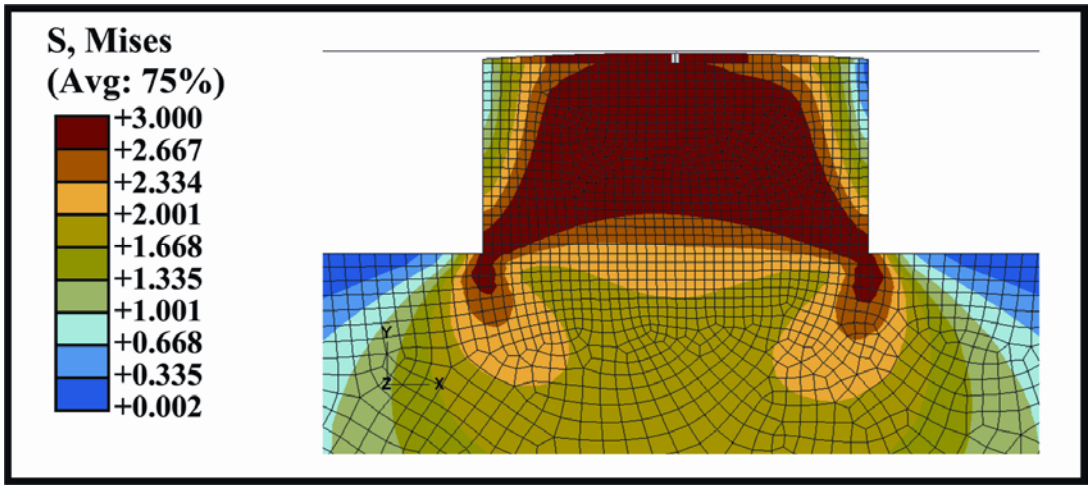

Figure B.7─von Mises stress contours for case (a) in Figure B.6 showing yielding underneath DLC layer (same as Figure B.6 (a) with upper limit set to 3.0 GPa). (units are in GPa)

Case (b) in Figure B.6 (b), in which magnetic layer material is used for planarization, is representative of a filling material which is marginally softer compared to the underlayers and the substrate. In this case, the stresses observed are not as high as in case (a) since the contact load is also shared by the filling material. It can also be seen that stresses of a lower magnitude exist in the filling material. Alleviation of the stresses in the pattern region due to the influence of planarization is more clearly observed in case (c) as shown in Figure B.6 (c), where DLC is used for planarization. In this case, DLC is harder than the magnetic layer and thus can sustain contact load more effectively, thus relieving stresses from the patterned region.

Figure B.8 shows the contact pressure distribution of all three cases when δ=10 nm and 50 nm. Note that when δ=50 nm, the rounding on the top of the patterns is flattened out, thus initiating contact in the filling material as well. The contact on the surface of the filling material causes normal displacement (downward) of the adjacent patterns, which results in lower contact stresses on the patterns. Thus the use of a filling material results in a decrease of the contact

pressure on the patterns. It can also be observed that the lowest contact pressure on the pattern is seen in case (c), with the difference between case (b) and (c) being small.

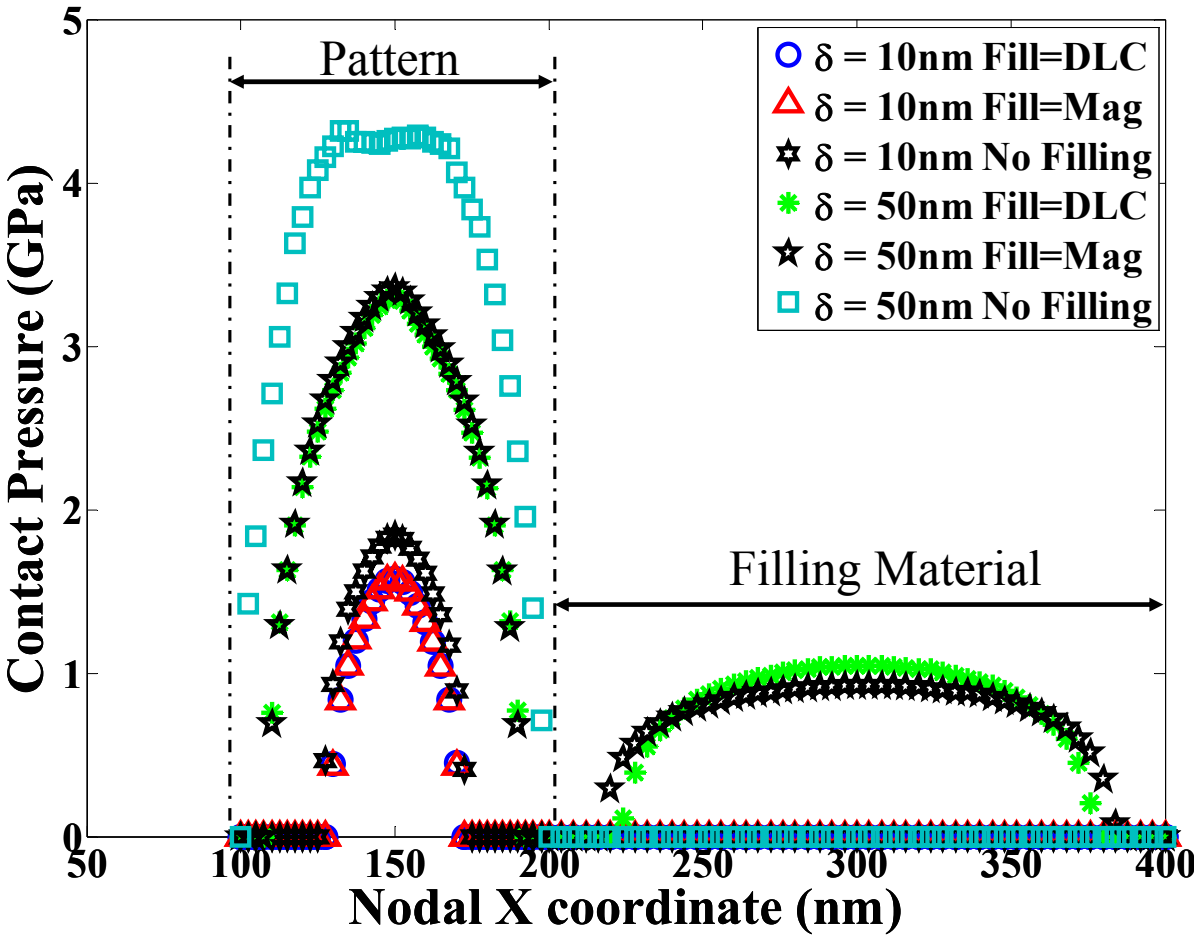

Figure B.8─Contact pressure distributions for the three different cases.

DLC material (case (c)) is much stiffer it exhibits lower contact deformation and the normal displacement applied on top of the DLC material is easily transported to the layer below, where the energy is going to be used up for the elastic deformation of the substrate. Therefore, since the stiffer filling material causes more normal displacement of the substrate below, it leads to less contact pressure on the pattern. Note that for case (a) when δ=50 nm we observe that the contact pressure is slightly asymmetric, being higher towards the left side of the pattern, compared to the right side. This will result in a net applied moment in the counterclockwise direction inducing higher stresses on the bottom right edge of the pattern. This effect is more prominent on the last (edge) pattern as discussed in Section B.4.1.

The net contact force (force per unit length due to the plane strain condition) and contact stiffness per unit area during the evolution of the contact are plotted in Figure B.9 and Figure B.10, respectively. In Figure B.9 for a chosen δ, the contact force for case (a) is lower than in cases (b) and (c). This difference increases as δ increases. However, in agreement with earlier observations, even though the contact force in case (b) is slightly lower than in case (c), it can be seen that for the magnitude of the loading involved, the difference is very small. The contact stiffness plot in Figure B.10 shows that a very steep slope exists during the initial loading stages, since the contact happens on the rounded (Hertzian) patterns, resulting in a rapid increase of the contact area. The rate of increase of the contact stiffness decreases and eventually reaches a steady state value. The contact stiffness for the patterned media planarized with the filling materials used here is higher than that of patterned media without planarization. This is due to the fact that the planarized patterns are inherently stiffer due to the presence of the current choice of filling materials. However, if a softer filling material (weaker than the magnetic layer) is used, it is expected that planarized pattern media behavior would be much closer to case (a).

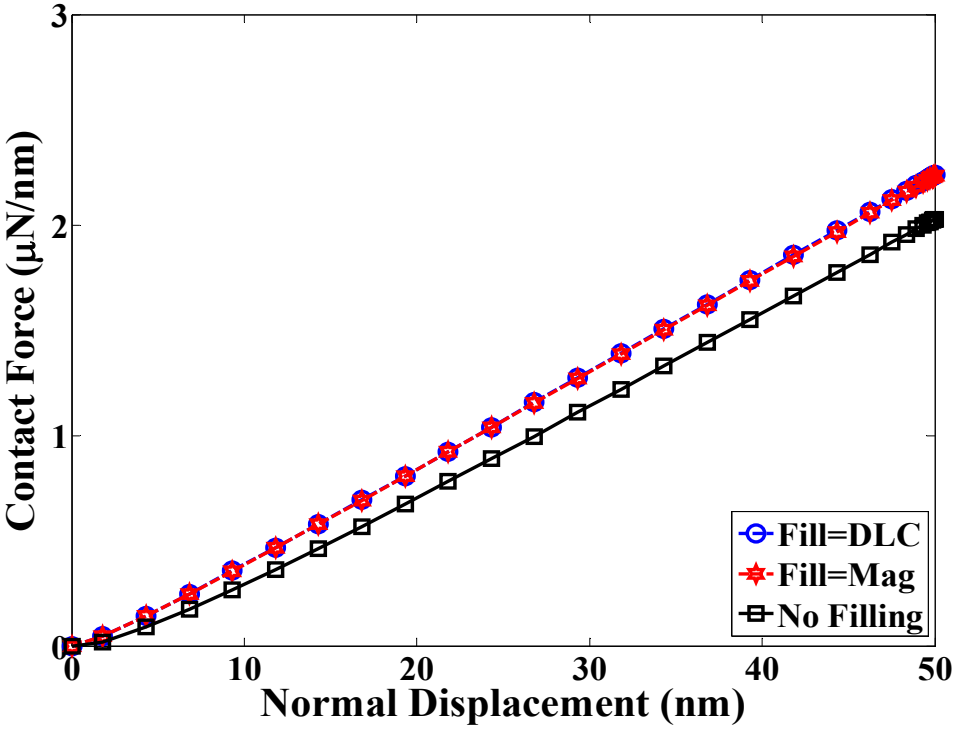

Figure B.9—Variation of contact force versus applied normal displacement.

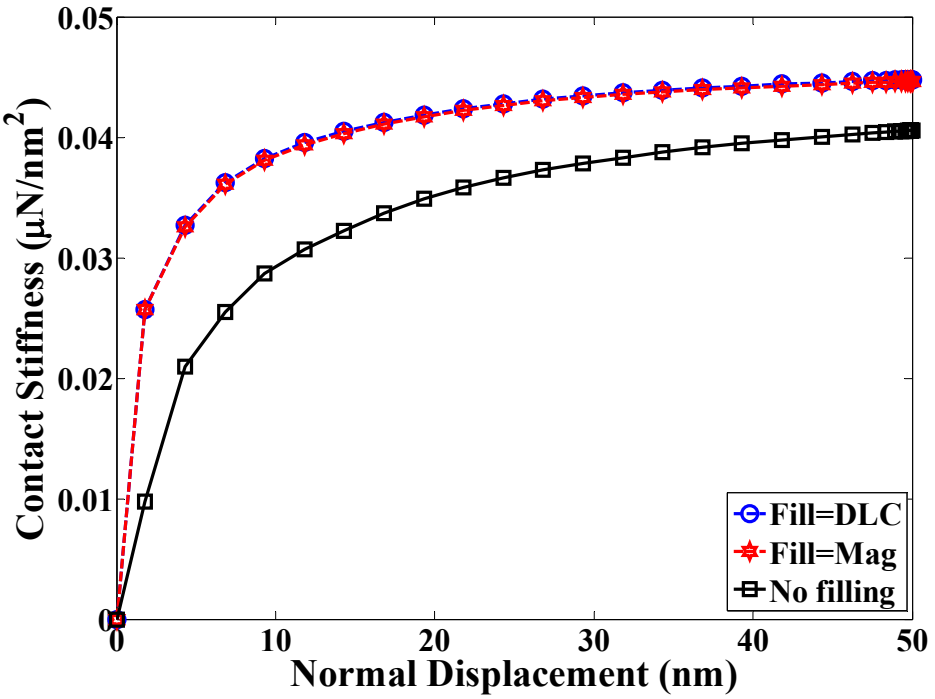

Figure B.10—Variation of contact stiffness versus applied normal displacement.

B.5. Summary

The contact behavior of planarized patterned media was examined and compared to non-planarized media (no filling in the gaps). For comparison purposes, DLC properties were used, representing a stiff filling material and typical magnetic layer properties representing a soft filling material. It was found that planarization in DTR-type media was useful in improving the contact performance compared to non-planarized DTR media. In other words, since the filling material can also support load during contact, it reduces the contact stresses on the patterns. Non-planarized DTR media plastically yielded in the magnetic layer which was not the case for planarized DTR media. Comparing the contact behavior between the stiffer filling material (DLC) and the softer filling material (magnetic material), no significant difference was observed under mild contact conditions.

APPENDIX C

C.1. The Effect of asperity interaction during the contact of rough surfaces

Modeling of rough surfaces is important for the understanding of the interaction of interfaces under static and sliding motion. This understanding becomes relevant for the reliability of devices from the nano to the macro level applications including hard drives, MEMS, compressors, gears, etc.

The pioneering probabilistic model of contact of rough surfaces was developed by J. A. Greenwood and J. B. P. Williamson back in the 1960's [120]. Even though, this model is still being used nowadays, it is only limited to contacts on the elastic range (light loads) and among its assumptions it assumes that the asperities are far apart, thus the interaction between them can be ignored. Other researchers, have focused on the improvement of the GW model [121, 122, 123], but scarce work related to asperity interaction of rough surfaces is available in the literature. For instance Ciavarella et al [124], studied the effect of asperity interaction considering heavier loads and treating the asperities as uniformly distributed over the apparent contact area. In their model the net deformation can be considered as uniform and the average deformation over a compact area A_n due to a uniform nominal pressure P acting over that area is:

$$\delta = m * P * \sqrt{\frac{A_n}{E^*}} \tag{C.1.1}$$

where the factor m equals 0.96 for a circular area, 0.95 for a square [125]. Cook and Bhushan [126] digitized measured profiles of contacting surfaces and used them for computer simulations. In addition, Eid and Adams [127] studied the effect of asperity interaction using an elastic-perfectly plastic finite element model of two hemispheres in contact with a rigid flat. The

contact behavior of rough surfaces can be studied using a deterministic approach were a real surface can be digitized and imported into a CAD model suitable for FEM simulations. However, the number of nodes and elements associated with the meshing of a real surface makes the likelihood of application of the FEM hardly possible.

The main objective of this study is to investigate the asperity interaction of contacting rough surfaces using a probabilistic approach. The asperity interaction will be evaluated by comparing the contact force and contact stiffness as a function of the normal approach distance obtained from FEA against GW and Ciavarella proposed models.

C.2. Finite element model

The finite element model was performed using ABAQUS standard and consists of a finite analytical rigid surface in contact with a deformable tri-dimensional array of asperities that follow a Gaussian distribution. The deformable mesh is made of ten nodes tetrahedral elements with full integration (C3D10M). The dimensions of the deformable mesh are 556 μm length x 25 μm height x 20 μm depth. The deformable mesh has been designed in such a way that small size elements are densely distributed along the hemispheres representing the contacting asperities while coarse elements were implemented away from this region. The number of elements used was 128972 and the number of nodes 217143. Contact was defined on the analytical rigid surface and the top surface of the deformable mesh, which ensure that proper contact pressures were applied. Boundary conditions were applied to the model to ensure appropriate capture of the interaction between neighboring asperities as follows: the rigid analytical surface was constrained from rotating, the bottom nodes of the mesh were constrained from moving vertically, and symmetric boundary conditions were applied to the front nodes. The size of the

geometry was designed in such a way that the gradient of the stresses are well contained and boundary effects can be neglected

The parameters used to generate the Gaussian distribution (see Figure C.1) were obtained from brass (typical material used in compressor applications with E=70 GPa and υ=0.27) using a contact profilometer. These roughness parameters (see Table C.1) were introduced in a Matlab code to generate a Gaussian distribution of the height of asperities and then the localization of the asperities into the FEA model was obtained by implementing a permutation of the position into the code. Figure C.2 shows the final and optimized mesh used during the analysis. For this model 41 asperities were selected and the mean was selected in such a way that the relationship between the density of asperities per unit area and the area of contact was satisfied. Using this number of asperities will cover up a maximum height of 2.2 times the standard deviation of asperity height ($2.2R_q$). The area of contact is assumed to be squared meaning that the mean of the distribution can be adjusted to satisfy equation C.1.2.

$$\eta_a = \frac{N}{A} \tag{C.1.2}$$

Where η_a represents the number of asperities per unit area, N the number of asperities, and A is the nominal area of contact.

In addition, a three asperity model was implemented and five different cases were studied. The basic geometry used is shown in Figure C.3 and the different cases are summarized in Table C.2.

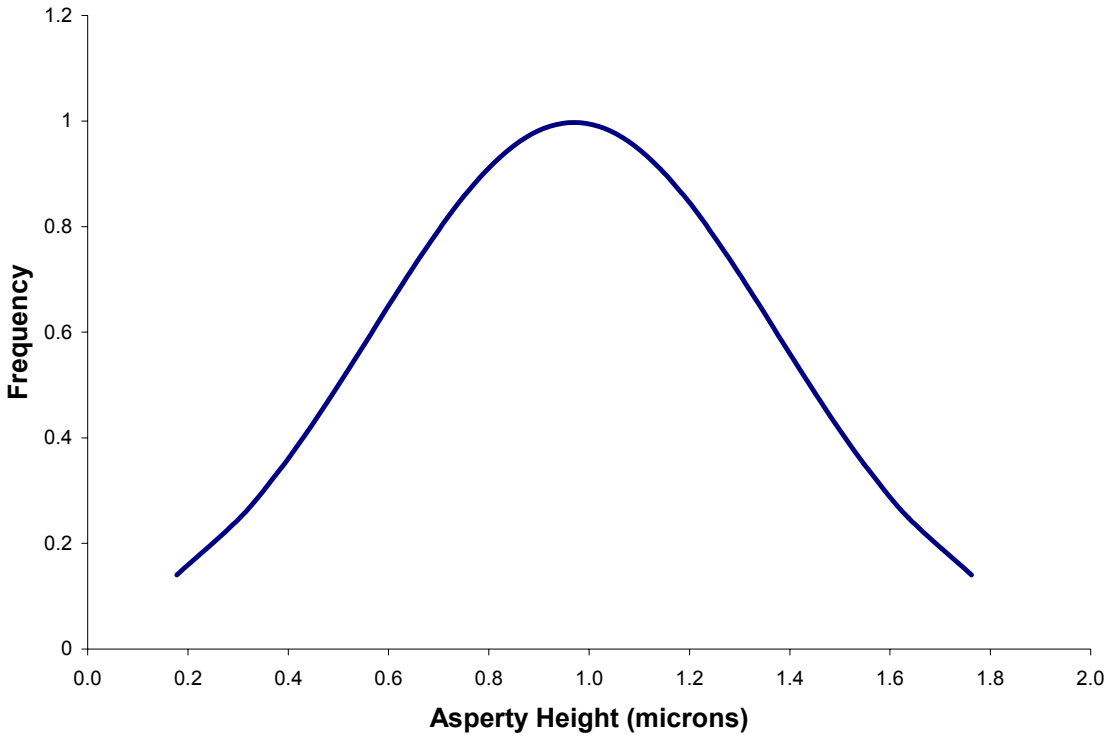

Figure C.1—Gaussian distribution of asperity heights

Table C.1—Roughness parameters for brass obtained using a contact profilometer

Parameter	**Specified roughness parameters for Brass**
	Scan size (500 μm^2)
R_q (μm)	0.43
R_a (μm)	0.32
R (μm)	21.7
Beta	0.06
Eta (μm^{-2})	0.006
Gamma	0.42
Mean (μm)	0.97

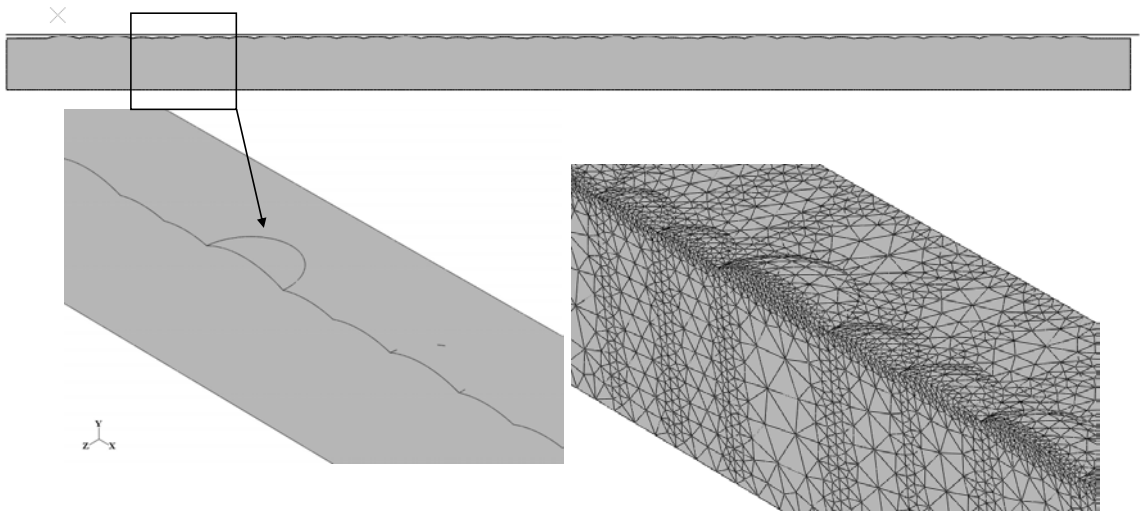

Figure C.2─Finite element mesh used to represent a Gaussian distribution of asperities along a line.

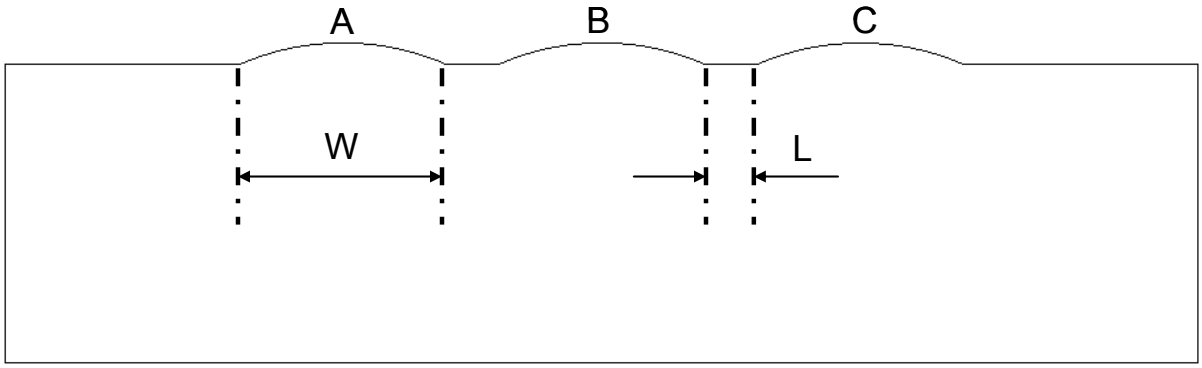

Figure C.3─Basic geometry used to simulate the contact of three asperities.

Table C.2—Cases under study in the three asperity simulation

Case	Ratio L/W	Asperity Height (μm)		
		A	B	C
1	0.08	1.4	1.77	1.4
2	0.08	1.77		
3	0.5			
4	1.5			
5	merged			

C.3. Results, analysis, and discussion

C.3.1 Gaussian distributed asperities

The gradient of the stress below the asperities upon the influence of normal approach of the rigid surface, is shown in Figure C.4. In this case the displacement used (δ=1.77 μm) was equivalent to the height of the tallest asperity. As can be seen in Figures C.4(a) and (b) the von Mises stress contour shows that the maximum stress occurred below the surface of the tallest asperity as it was expected. However, interestingly not all the asperities are being compressed by the analytical surface which points out the effect of the asperity interaction.

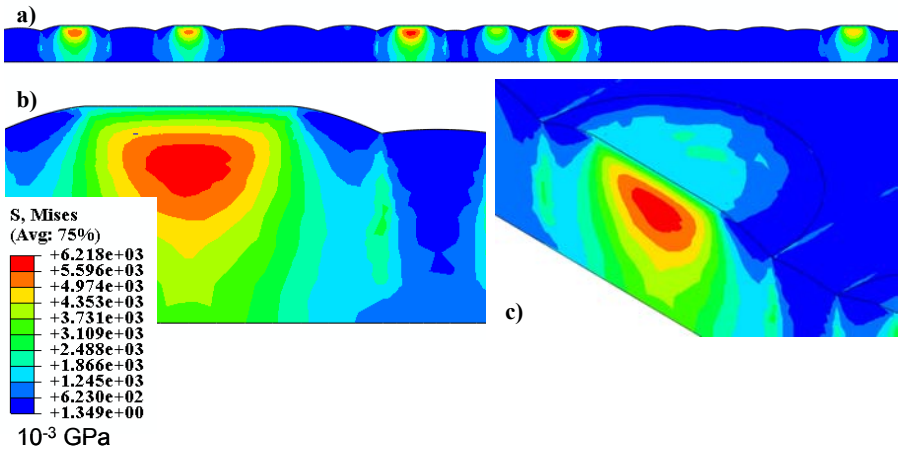

Figure C.4—von Mises contour below the surface of a Gaussian distribution of asperities randomly organized.

Figure C.5 shows the displacement profile below the surface of the asperities where it can be observed that the maximum interference is approximately 1 μm which is close to the location of the mean plane. The displacement on a large asperity can cause the neighboring asperities to move down even before they come into contact increasing the mean separation. It should be noted that this interference is high taking into account that the deformation is in the elastic regime pointing out again the effect of asperity interaction.

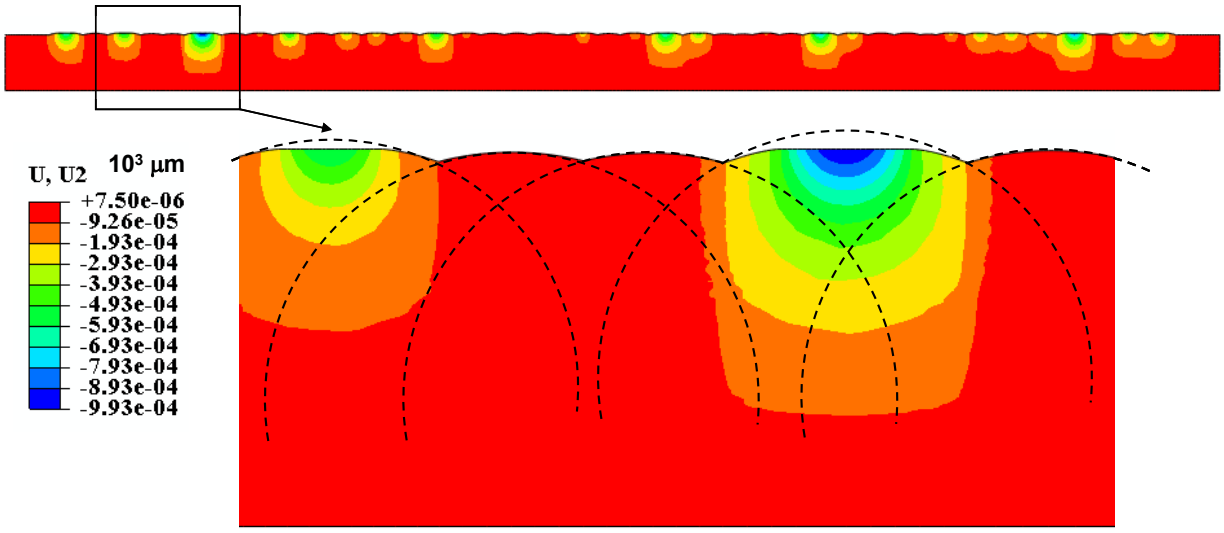

Figure C.5—Displacement profile of the asperities in the vertical direction.

A comparison of the FEA results against the GW and Ciavarella et al model was also performed. Contact force and contact stiffness as a function of the interference were analyzed to compare the different three models. Figure C.6 shows the contact force as a function of the interference. In this figure the contact force increases from the minimum negative interference (no contact) up to the maximum contact approach. It can be observed that the contact force is higher in the FEA model compared to Ciavarella et al, but lower compared to GW. An explanation for this is behavior is that in the FEA model the asperities are distributed in a line

while in the case of Ciavarella et al they are distributed in an area. Thus, during the contact of a tall asperity, the neighboring asperities will be displaced in the vertical direction and this displacement will be higher if the tall asperity is surrounded by more asperities. It is believed this is the reason why higher values of contact force are obtained in the FEA model compared to Ciavarella et al, yet, both model show lower contact loads compared to GW. Another way of explaining this behavior is based on the fact that as the taller asperity is being pushed in the vertical direction, the neighboring asperities are also displaced; consequently less contact force will be needed to cause the same amount of displacement.

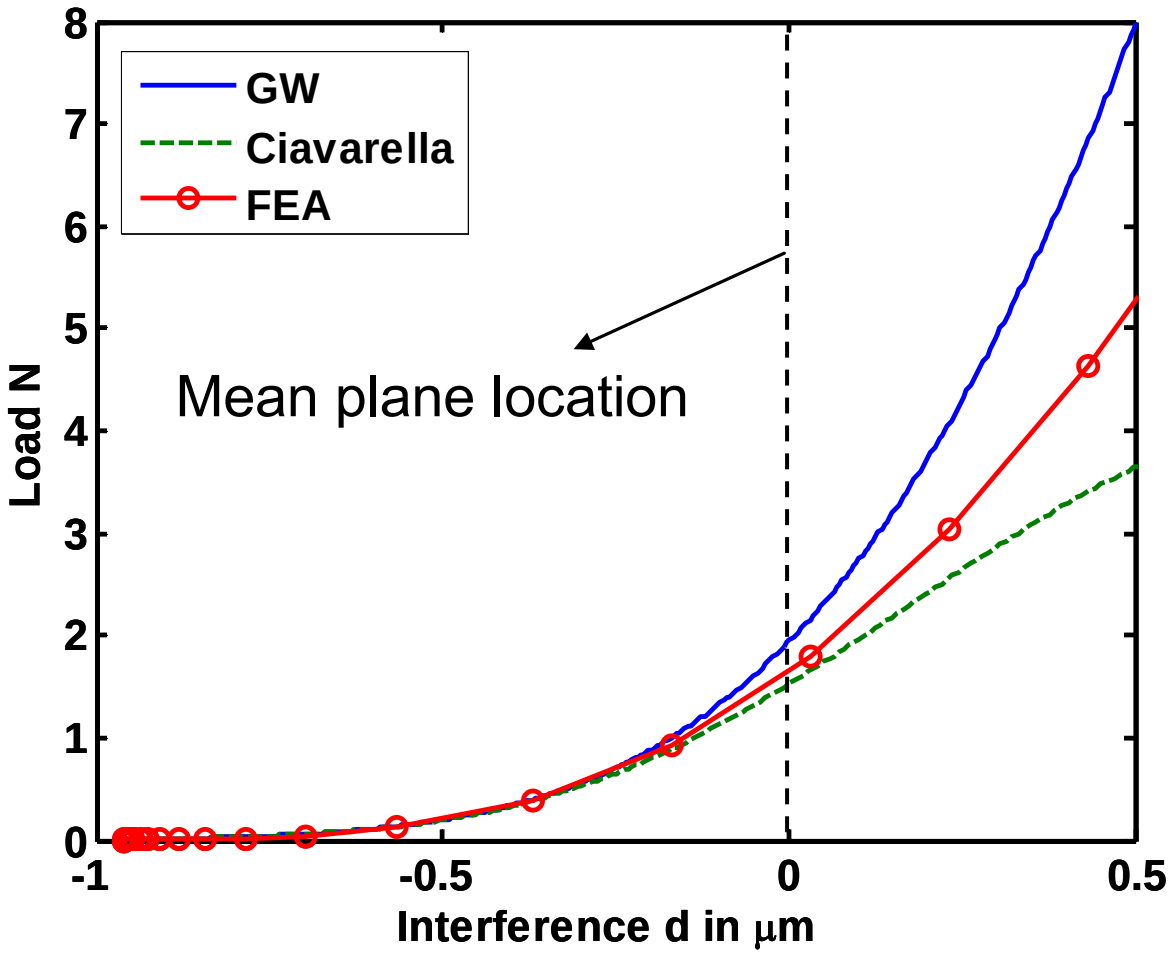

Figure C.6—Contact force vs interference for GW, Ciavarella and FEA.

C.4. Three asperity model

Figure C.7 (a) shows the von Mises stress profile for case 1, as noted stress in the central asperity (B) is higher compared to asperities A and C as would be expected. Figure C.7 (b) shows the vertical displacement contour which is continuous below the surface indicating interaction between neighboring asperities.

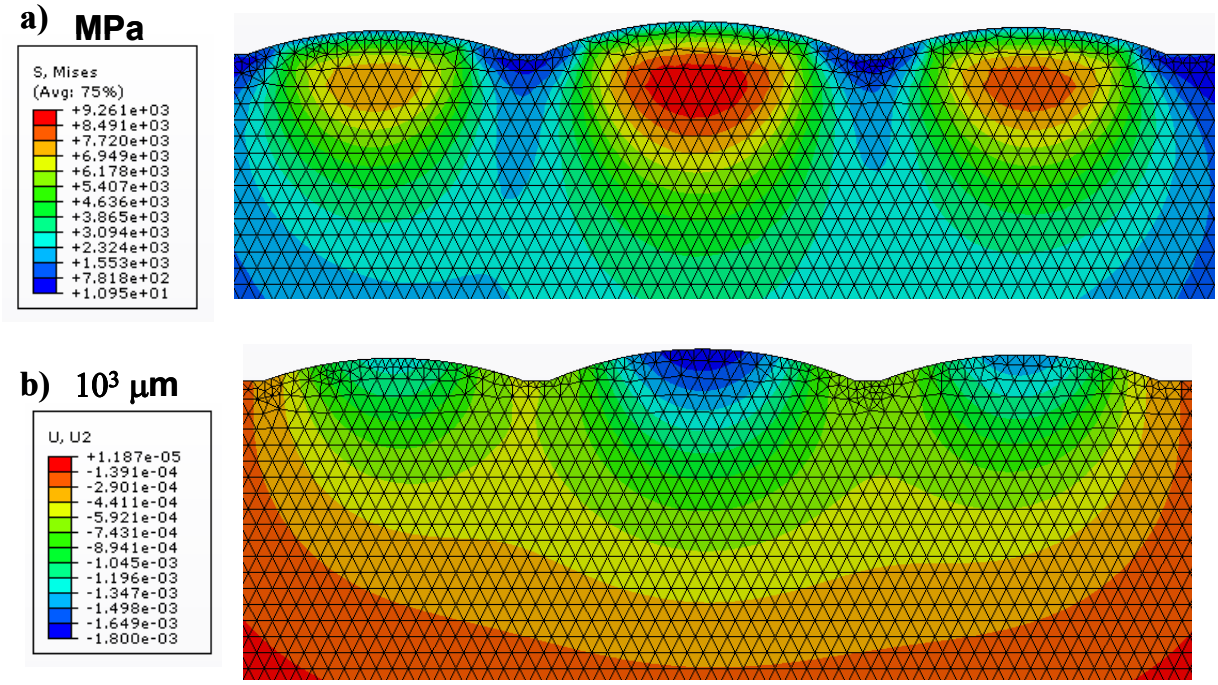

Figure C.7—(a) von Mises stress below the surface and (b) vertical displacement contour obtained for case 1.

Figures C.8(a) and (b) show the vertical displacement profiles for cases 2 and 4 respectively. In case 2 which is similar to case 1, but with asperities of similar height, it can be seen that the displacement profile below the surface is continuous and similar to case 1. Case 4, where the asperities are separate by a certain distance, shows discontinuity of the vertical displacement contour below the surface and points out the fact that neighboring asperities do not interact compared to cases 1 and 2.

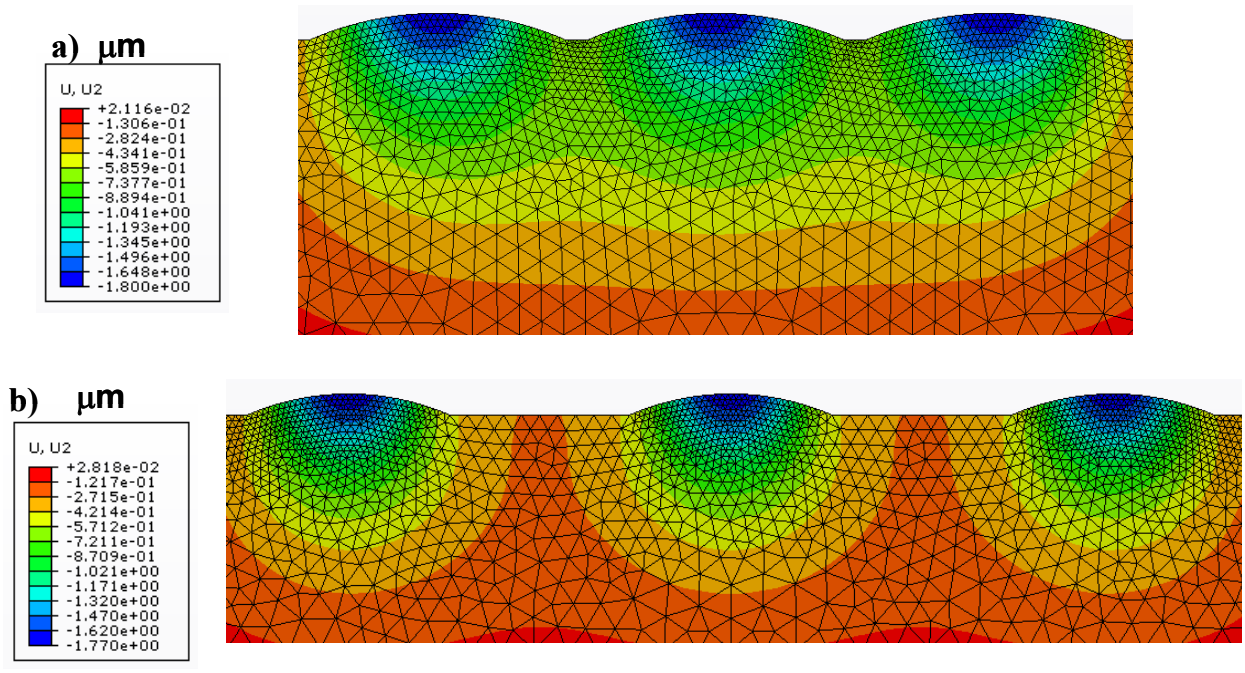

Figures C.8─(a) Vertical displacement obtained for case 2 and (b) vertical displacement contour obtained for case 4.

Figure C.9 shows the vertical displacement profile below the surface for case 5. In this situation where asperities are merged, the displacement profile below the surface is more continuous compared and deeper compared to cases 1 and 2. These results again evidence and proof the effect of asperity interaction in rough surfaces.

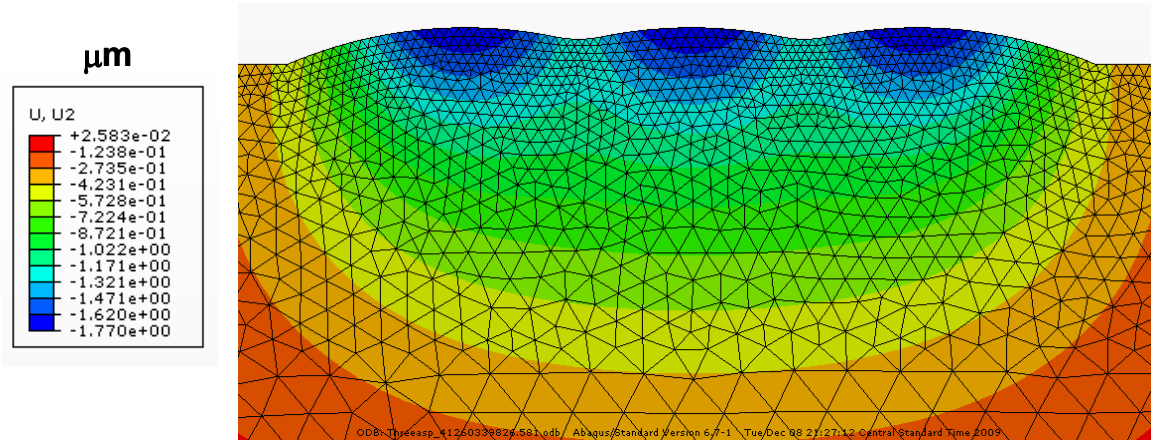

Figures C.9─Vertical displacement contour obtained for case 5.

Also Figures C.10 and 11 show the contact force and the contact stiffness plotted against the normal displacement of the analytical rigid surface. Unlike, cases 2 through 4 where the contact load and contact stiffness are similar, case 1 shows slightly higher values at the beginning of the normal approach (due to the difference in height between the asperities), but lower values when all asperities are being compressed. This can be explained taking into account that Case 1 is a situation where more initial load needs to be applied to bring all asperities into contact, yet once all three asperities are in contact the central asperity (B in Figures C.3) pushed the neighboring asperities downward. As a result the mean plane of asperity height will move (due to asperity interaction) decreasing the amount of applied load (contact force) needed to caused certain amount of unit displacement.

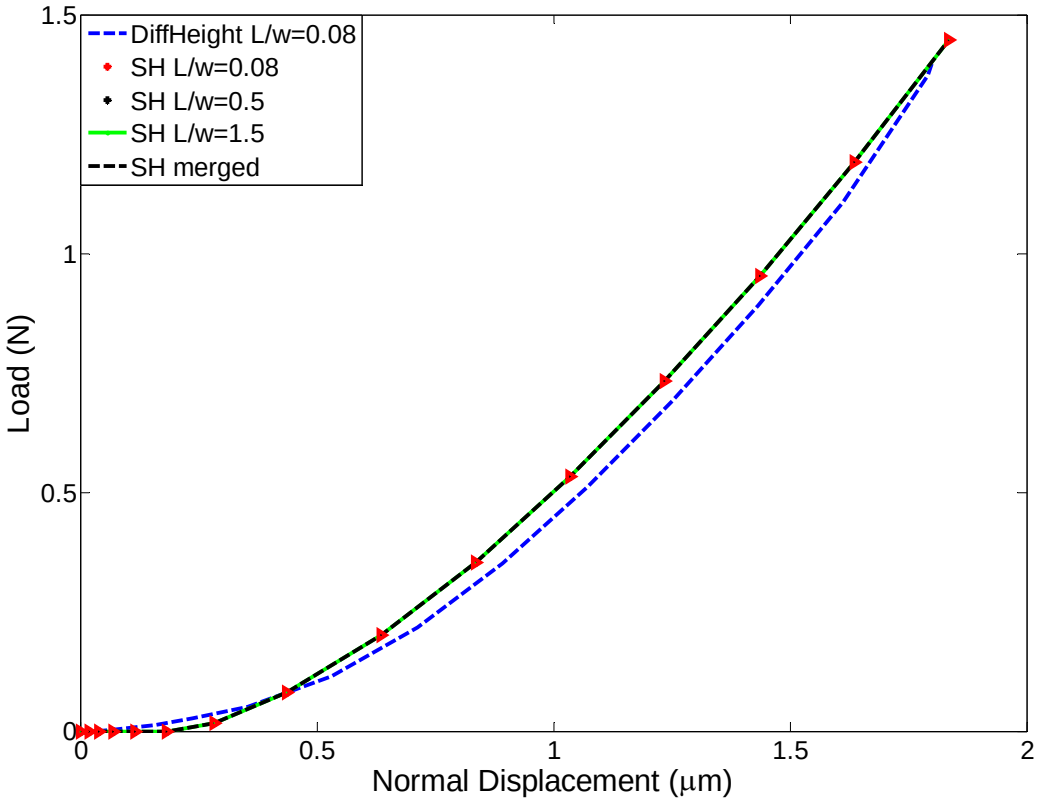

Figures C.10—Contact force vs normal displacement for cases 1 through 5.

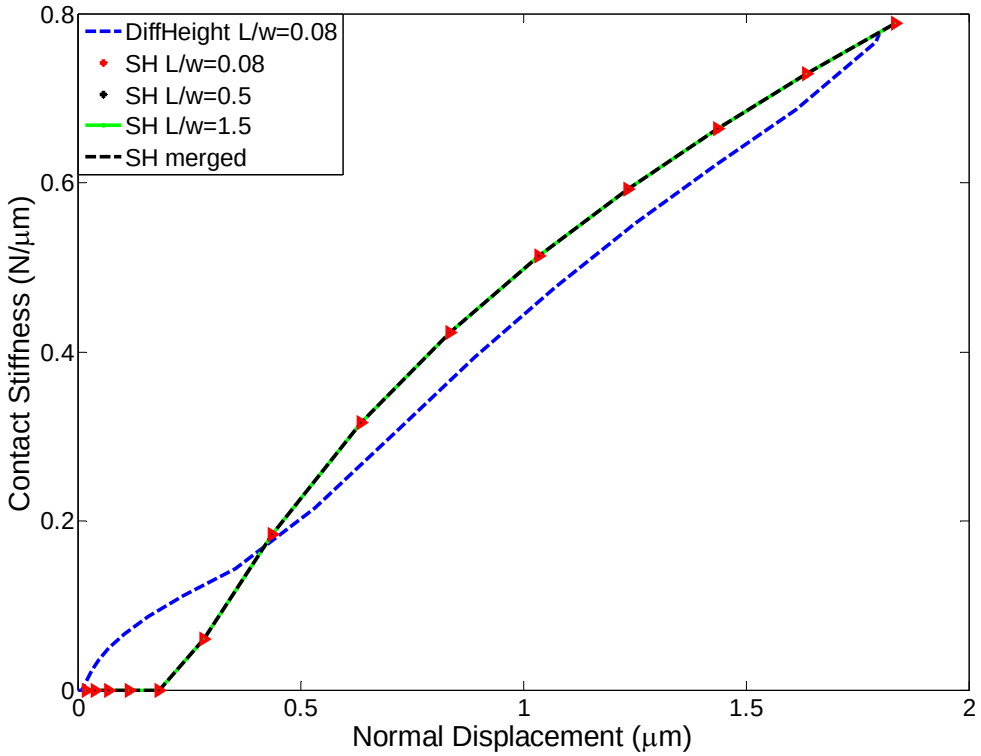

Figures C.11—Contact stiffness vs normal displacement for cases 1 through 5.

C.5. Summary

Different cases were analyzed to study the effect of asperity interaction. By using a Gaussian distribution of asperity height, it was shown that the contact force is lower compared to GW model and slightly higher compared to Ciavarella et al. In the case of a simple three asperity model, it was found that the vertical displacement contour below the surface is continuous in situations where the asperities are relatively closed (as in rough surfaces) and the contact force and contact stiffness decreased once all asperities are brought into contact in the scenario of having a difference in height between contacting asperities (Case 1). In the light of these findings, the effect of asperity interaction can not be ignored during the contact behavior of real rough surfaces. However, in order to improve this analysis, a more detailed three dimensional model is needed in order to capture with more accuracy the affect of asperity interaction where it would be expected that the density of asperities in every location would be

more similar to the real case scenario (where one single asperity is surrounded by other asperities in every direction on the same plane).

REFERENCES

1 Ayres, R. U., Ayres, L. W. Pokrovsky, V. (2005), "On the efficiency of US electricity usage since 1900", Energy 30, pp 1092-1145.

2 Molina, M. J., Rowland, F. S. (1974), "Stratospheric sinks for chlorofluoromethanes: chlorine atom-catalyzed destruction of ozone", Nature 249, pp 810-814.

3 Baek, J. S., Groll, E. A., Lawless, P. B. (2005), "Piston-Cylinder Work Producing Expansion Device in a Transcritical Carbon Dioxide Cycle. Part I: Experimental Investigation", International Journal of Refrigeration, 2, pp 141-151

4 Fukui, H., Sanechika, K. I., Masanori, I. (2000), "Novel Refrigeration Lubricants for Use with HFC Refrigerants", Tribology International, 33, No. 10, pp 707-713.

5 Lorentzen, G. (1995), "The use of natural refrigerants: A complete solution to the CFC/HCFC predicament", International Journal of Refrigeration, 18, pp 190-197.

6 Kim, M. H., Pettersen, J. Bullard, C. W. (2004), "Fundamental Process and Systems Design Issues in CO_2 Vapor Compression Systems," Progress in Energy and Combustion Science, 30, pp 119-174.

7 Demas, N. G., Polycarpou, A. A. (2006), "Ultra high pressure tribometer for testing CO_2 refrigerant at chamber pressures up to 2000 psi to simulate compressor conditions", Tribology Transactions, 49, pp 291-296.

8 http://www.1234facts.com/index.html

9 Misaki, S., Sekiya, A. (2000), "The potential of hydrofluoroethers to replace CFCs, HCFCs, and PFCs", Journal of Fluorine Chemistry, 101, pp 215-221.

10 McCulloch, A. (1999), "CFC and Halon replacements in the environment", Journal of Fluorine Chemistry, 100, pp 163-173.

11 Ludema, K. (1981), "A Review of Scuffing and Running-In of Lubricated Surfaces with Asperities and Oxides in Perspectives", Wear, 100, pp 315-331.

12 Salomon, G. (1976), "Failure criteria in thin film lubrication-the IRG program", Wear, 36, pp 1-6.

13 Bolliani, G. (1976), "Failure criteria in thin film lubrication film with EP additives", Wear, 36, pp 19-23.

14 Bowman, W., Stachowiak G. W. (1996), "A review of scuffing models", Tribology Letters, 2, pp 113-131.

15 Kwashniak, E., Pasierski, J., Stupnicki, J. (1997), "Some remarks concerning scuffing of ceramics slid against steel", Wear, 209, 219-228.

16 Wear Control Handbook, Peterson, and Winer editors, Glossary of Terms and Definitions in the Field of Friction, Wear and Lubrication, pp 1182.

17 Blok, H. (1937), "Theoretical Study of the Temperature Rise at Surfaces of Actual Contact Under Oiliness Conditions", Inst. Mech. Eng. General Discussion on Lubrication, 2, pp 222-235.

18 Abdel-Aal, H. A. (1997), "A Remark on the Flash Temperature Theory", Int. Comm. Heat Mass Transfer, 24, pp 241-250.

19 Somi Reddy, A., Pramila Bai, B. N., Murthy, K. S. S., Biswas, S. K. (1994), "Wear and Seizure of Binary Al-Si Alloys", Wear, 171, pp 115-127.

20 Yoon, H. K., Sheiretov, T., Cusano, C. (1998), "Scuffing under dry sliding conditions : Part II : Theoretical studies", Tribology Transactions, 41, pp 447-458.

21 Ajayi, O. O., Hersberger, J.G., Zhang, J., Yoon, H., Fenske, G. R.(2005), "Microstructural evolution during scuffing of hardened 4340 steel—implication for scuffing mechanism", Tribology International, 38, 3, pp 277–282.

22 Lee, K. M., Suh, A. Y., Demas, N. G., Polycarpou, A. A. (2005), "Surface and sub-micron sub-surface evolution of Al390-T6 undergoing tribological testing under submerged lubrication conditions in the presence of CO_2 refrigerant", Tribology Letters, 18, 1, pp 1-12.

23 Gravesen, J., Henriksen, C. (2001), "The Geometry of the Scroll Compressor", SIAM Review, 43, pp 113-126.

24 http://www.emgsi.com/scrolloperatingtheory.htm

25 Li, J., Elmagdali, M., Gertsman, V.Y., Lo, J., Alpas, A.T. (2006), "FIB and TEM characterization of subsurfaces of an Al–Si alloy (A390) subjected to sliding wear", Materials Science and Engineering A, 421, pp 317–327.

26 Saravanan, R. A., Lee, J. M., Kang, S. B. (1999), "Dry sliding wear behavior of A356-15 Pct SiCp composites under controlled atmospheric conditions", Metallurgical Materials Transactions A, 30, pp 2523–2538.

27 Sheiretov, T., Yoon, H., Cusano, C. (1998), "Scuffing Under Dry Sliding Conditions-Part I: Experimental Studies", Tribology Transactions, 41, 4, pp 435-446.

28 Pergande, S. R., Polycarpou, A. A., Conry, T. F. (2004), "Nanomechanical properties of Aluminum 390-T6 rough surfaces undergoing tribological testing", Journal of Tribology, 126, pp 573-582.

29 Riahi, A. R, Alpas, A. T. (2001), "The role of tribo-layers on the sliding wear behavior of graphitic aluminum matrix composites", Wear, 251, pp 1396-1407.

30 Elmadagli, M., Alpas, A. T. (2006), “Sliding wear of an Al-18.5 wt.% Si alloy tested in an argon atmosphere and against DLC coated counterfaces”, Wear, 261, pp 823-834.

31 Suh, A. Y., Patel, J. J., Polycarpou, A. A., Conry, T. F. (2006), “Scuffing of Cast Iron and Al390-T6 Materials used in Compressors Applications”, Wear, 260, pp 735-744.

32 Molgaard, J. (1976), “Discussion of oxidation, oxide thickness and oxide transfer in wear”, Wear, 40, pp 277-291.

33 Archard, J. F. (1986), “Friction between metals surfaces”, Wear, 113, pp 3-16.

34 Cutiongco, E. C., Chung, Y. W. (1994), “Prediction of scuffing failure based on competitive kinetics of oxide formation and removal: Application to lubricated sliding of AISI 52100 steel on steel”, Tribology Transactions, 37, pp 622-628.

35 Razavizadeh, K., Eyre, T. S. (1982), “Oxidative wear of aluminum alloys”, Wear, 100, pp 325-333.

36 Dorison, A., Ludema, K. C. (1985), “Mechanics and chemistry in lubrication”, Elsevier, Amsterdam.

37 Philipossian, A., Olsen , S. (2003), “Fundamental tribological and removal rate studies of inter-layer dialetric chemical mechanical planarization”, Japanese Journal of Applied Physics, 42, pp 6371-6379.

38 Nunez, E. E., Demas, N. G., Polychronopoulou, K., Polycarpou, A. A. (2008), “Tribological Study comparing PAG and POE Lubricants used in Air-Conditioning Compressors under the Presence of CO_2”, Tribology Transactions, 51, pp 1-8

39 Boyde, S. (2002), “Green lubricants. Environmental benefits and impacts of lubrication”, Green Chemistry, 4, pp 293-307.

40 Yokoseki, A. (2006), “Solubility Correlation and Phase behaviors of Carbon Dioxide and Lubricant Oil Mixtures”, Applied Energy, 84, No. 2, pp 159-175.

41 Hubacher, B. and Groll E., (2002), “Measurement of Performance of Carbon Dioxide compressors”, Air Conditioning Refrigeration and Technology Institute, ARTI-21 CR/611-10070-01.

42 Liu, H., Chen, J., Chen, Z. (2005), “Experimental Investigation of a CO_2 Automotive Air Conditioner”, International Journal of Refrigeration, 28, pp 1293-1301.

43 Sawyer, G. W., Freudenberg, K. D., Bhimaraj, P., Schadler, L. S. (2003), “A study on the friction and wear behavior of PTFE filled with alumina nanoparticles”, Wear, 254, pp 573-580.

44 Blanchet, T. A., Kennedy, F. E. (1992), “Sliding wear mechanism of polytetrafluoroethylene (PTFE) and PTFE composites”, Wear, 153, Issue. 1, pp 229-243.

45 Tanaka, K., Uchiyamaa, Y., Toyooka, S. (1973), "The mechanism of wear of polytetrafluoroethylene", Wear, 23, Issue. 2, pp 153-172.

46 Blundell, D. J., Osborn, B. N. (1983), "The morphology of poly(aryl-ether-ether-ketone)", Polymer, 24, Issue. 8, pp 953-958.

47 Lu, Z. P., Friedrich, K. (1995), "On sliding friction and wear of PEEK and its composites", Wear, 181-183, Issue. 2, pp 624-631.

48 Cannaday, M., Polycarpou, A. A. (2005), "Tribology of Unfilled and Filled Polymeric Surfaces in Refrigerant Environment for Compressor Applications", Tribology Letters, 19, 4, pp 249-262.

49 Shaffer, S. J., Rogers, M. J. (2007), "Tribological performance of various coatings in unlubricated sliding for use in small arms action components-A case study", Wear, 263, pp 1281-1290.

50 Demas, N.G., Polycarpou, A. A. (2008), "Tribological performance of PTFE-based coatings for air-conditioning compressors", Surface and Coating Technology, 203, pp 307-316.

51 Dascalescu, D., Polychronopoulou, K., Polycarpou, A. A. (2009), "The significance of tribochemistry on the performance of PTFE-based coatings in CO_2", Surface and Coating Technology, 204, 3, pp 319-329.

52 Demas, N. G., Polycarpou, A. A. Conry, T. F. (2005), "Tribological studies on scuffing due to the influence of CO_2 used as a refrigerant in compressors", Tribology Transactions, 48, pp 336-342.

53 Shabel, B.S., Douglas, A.G., Truckner, W.G. (1992), "Friction and wear of aluminum-silicon alloys", ASM Handbook 18, pp 785-794.

54 Sun, Y.S., Lorimer, G.W., Ridley., N. (1989), "Microstructure of high-tensile strength brasses containing silicon and manganese", Metallurgical and Materials Transactions, A 20A, pp1199-1206.

55 Pugacheva, N.B. (2007), "Structure of commercial $\alpha+\beta$ brasses", Metal science and Heat Treatment, 49,1-2, pp 67-74.

56 B46.1-1995 (1996), "Surface Texture (Surface Roughness, Waviness, and Lay): An American National Standard", ASME, New York.

57 Stout, K. J., Sullivan, P. J., Dong, W. P., Mainsah, E., Luo, N., Mathia, T., Zahouani, H. (1993), "The Development of Methods for the Characterization of Roughness in Three Dimensions", Commission of the European Communities, Brussels, Luxembourg.

58 Suh, A. Y., Polycarpou, A. A., Conry, T. F. (2003), "Detailed Surface Roughness Characterization of Engineering Surfaces Undergoing Tribological Testing Leading to Scuffing", Wear, 255, pp 556-568.

59 Cavatorta, M. P. and Cusano, C. (2000), "Running-in of Aluminum/Steel Contacts Under Starved Lubrication, Part II: Effects on Scuffing", Wear, 242, pp 133-139.

60 Seeton, C., Fahl, J., Henderson, D., (2000), "Solubility, Viscosity, Boundary Lubrication and Miscibility of CO2 and Synthetic Lubricants", Proc. 4th IIR-Gustav Lorentzen Conference on Natural Working Fluids, West Lafayette, IN, pp 446-454.

61 Briggs, D., Seah, M. P. (1990), "Practical Surface Analysis by Auger and X-Ray Photoelectron Spectroscopy", 2nd Edition, Wiley Interscience, Chichester, England, ISBN 0471920819.

62 Stoch, J., Gablankowska-Kukucz, J. (1991), "The Effect of Carbonate Contaminations on the XPS O 1s Band Structure in Metal Oxides", Surface and Interface Analysis, 17, pp 165-167.

63 Barton, A. F. M. (1975), "Solubility Parameters", Chemical Reviews, 75, pp 731-753.

64 Hsu, S.M. (2004), "Molecular Basis of Lubrication", Tribology International, 37, pp 553-559.

65 Hsu, S.M., Klaus, E.E. Cheng, H.S., (1988), "A Mechano-chemical Descriptive Model For Wear Under Mixed Lubrication Conditions", Wear, 128, pp 307-323.

66 Holloway, S., Bennemann, K.H. (1980), "Study of Water Adsorption on Metal Surfaces", Surface Science, 101, pp 327-333.

67 Lei, R. Z., Gellman, A. J. (2000), "Humidity Effects on PFPE Lubricant Bonding to a-CH_x Overcoats", Langmuir, 16, pp 6628-6635.

68 Yoon, H. K., Sheiretov, T., Cusano, C. (2000), "Scuffing behavior of 390 Aluminum against Steel under starved lubrication conditions", Wear, 237, pp 163-175.

69 Dwivedi, D.K. (2006), "Wear behavior of cast hypereutectic aluminum silicon alloys", Materials and Design, 27, pp 610-616.

70 J. Keller, J., Fridrici, V., Kapsa, P., Vidaller, S., Huard, J.F. (2007), "Influence of chemical composition and microstructure of gray cast iron on wear of heavy duty diesel engines cylinder liners", Wear, 263, pp 1158-1164.

71 Cho, M.H., Kim, S.J, Basch, R.H., Fash, J.W., Jang, H. (2003), "Tribological study of gray cast iron with automotive brake lining", Tribology International, 36, pp 537-545.

72 Waheed, A., Ridley, N. (1994), "Microstructure and wear of some high-tensile brasses", Journal of Materials Processing Technology, 114, pp 201-211.

73 Mindivan, H., Çimenoğlu, H., Kayali, E.S. (2003), "Microstructure and wear of brass synchronizer rings", Wear, 254, pp 532-537.

74 Sheiretov, T., Glabbeek, W.V., Cusano, C. (1995), "Evaluation of the tribological properties of polyimide and poly(amine-imine) polymers in a refrigerant environment", Tribology Transactions, 38, pp 914-922.

75 Hauk, A., Weidner, E. (2000), "Thermodynamic and Fluid-Dynamic Properties of Carbon Dioxide with Different Lubricants in Cooling Circuits for Automobile Application", Industrial & Engineering Chemistry Research, 39, pp 4646-4651.

76 Chastain, Jr. J., King, R. C. Handbook of X-ray Photoelectron Spectroscopy, Physical Electronics, Inc., MN (1995) ISBN 0-9648124-1-X.

77 http://srdata.nist.gov/xps/

78 http://www.tribology-abc.com/abc/solidlub.htm

79 Erdemir, A. (2000), "A crystal-chemical approach to lubrication by solid oxides", Tribology Letters, 8, pp 97-102.

80 Erdemir, A., Li, S., Jin, Y. (2005), "Relation of Certain Quantum Chemical Parameters to Lubrication Behavior of Solid Oxides", International Journal of Molecular Science, 6, pp 203–218.

81 Nunez, E. E., Demas, N. G., Polychronopoulou, K., Polycarpou, A. A. (2010), "Comparative scuffing performance and chemical analysis of metallic surfaces for air-conditioning compressors in the presence of environmentally friendly CO_2 refrigerant", Wear, 268, pp 668-676.

82 Yen, B. K. (1996), " Influence of water vapor and oxygen on the tribology of carbon materials with sp^2 valence configuration", Wear, 192, pp 208-215.

83 Pardee, R. P. (1967), "Moisture dependece of silver-graphite brushes in air, nitrogen, helium, and carbon dioxide", IEEE. Transactions of Power Apparatus and Systems,14, pp 747-762.

84 Robert, F., Paulmier, D., Zaïdi, H., Schouller, E. (1995), "Combined influence of an inert gas environment and a mechanical action on a graphite surface", Wear, 181, pp 987-690.

85 Zaïdi, H., Robert, F., Paulmier, D., Néry, H. (1993), "Correlation between the tribological behavior of graphite and its mechanical properties versus the interplan distance", Applied Surface Science, 70-71, pp 103-108.

86 Cannaday, M. L., Polycarpou, A.A. (2006), "Advantages of CO_2 compared to R410a refrigerant of tribologically tested aluminum 390-T6 surfaces", Tribology Letters, 21, pp 185-192.

87 Wu, X., Cong, P., Nanao, H., Minami, I., Mori, S. (2004), "Tribology behavior of 52100 steel in carbon dioxide atmosphere", Tribology Letters, 17, pp 925-930.

88 Carlès, P. (2010), "A brief review of the thermophysical properties of supercritical fluids", Journal of Supercritical fluids, 53, pp 2-11.

89 http://www.ecourses.ou.edu/cgi-bin/ebook.cgi?doc=&topic=fl&chap_sec=01.2&page=theory

90 Sugishita, J., Fugiyoshi, S. (1981), "The effect of cast iron graphites on the friction and wear performance II: variables influencing graphite film formation", Wear, 68, pp 7-20.

91 Heuer, J. K., Stubbins, J. F., (1999), "An XPS characterization of $FeCO_3$ films from CO_2 corrosion", Corrosion Science, 41, pp 1231-1243.

92 Shih, C. C., Shih, C. M., Su, Y. Y., Su, L. H. J., Chang, M. S., Ling, S. J., (2004), "The effect of surface oxide properties on corrosion resistance of 316L stainless steel for biomedical applications", Corrosion Science, 46, pp 427-441.

93 Wu, S. L., Cui, Z. D., He, F., Bai, Z. Q., Zhu, S.L., Yang, X.J., (2004), "Characterization of the surface film form from carbon dioxide corrosion on N80 steel", Materials Letters, 59, pp 1076-1081.

94 http://srdata.nist.gov/xps/

95 Sasaki, S., (2010), "Environmentally friendly tribology", Journal of Mechanical Science and Technology, 24, pp 67-71.

96 Park, J. G., Han, S. C., Jang, H. Y, Lee, S. M., Lee, P. S., Lee, J. Y., (2002), "The development of compressor-driven metal hydride heat pump (CDMHHP) system as an air conditioner", International journal of hydrogen, 27, pp 941-944.

97 http://www.swimpreglon.us/index.html

98 Zhang, G., Yu, H., Zhang, C., Liao, H., C, Coddet., (2008), "Temperature dependence of the tribological mechanisms of amorphous PEEK (polyetheretherketone) under dry sliding conditions", Acta Materialia, 56, pp 2182-2190.

99 Cebe, P., Hong, S., (1986), "Crystallization behavior of poly (ether-ether-ketone)", Polymer, 27, pp 1183-1192.

100 Blundell, D. J., (1987), "On the interpretation of multiple melting peaks in poly (ether-ether-ketone)", Polymer, 28, pp 2248-2251.

101 Tan, S., Su, A., Luo, J., Zhou, E., (1999), "Crystallization kinetics of poly (ether-ether-ketone) from its metastable melt", Polymer, 40, pp 1223-1231.

102 Lovinger, A. J., Hudson, S. D., Davies, D. D., (1992), "High-temperature crystallization and morphology of poly(aryl ether ether ketone)", Macromolecules, 25, pp 1752-1758.

103 Inami, S., Takayanagi, S., Kubo, T., Nanao, H., Minami, I., Mori, S., (2008), "Effects of fine-dispersed PTFE on load capacity of PEEK", Lubrication Science, 20, pp 299-310.

104 Minami, I., Kubo, T., Nanao, H., Mori, S., Iwata, H., Fujita, M., (2008), "Surface chemistry for improvement in load-carrying capacity of poly(ether-ether-ketone)-based materials by Poly(Tetrafluoroethylene)", Tribology Online, 3, pp 190-194.

105 Li, J., Liao, H., Coddet, C., (2002), "Friction and wear behavior of flame-sprayed PEEK coatings", Wear, 252, pp 824-831.

106 Eryilmaz, O. L., Erdemir, A., (2008), "TOF-SIMS and XPS characterization of diamond-like carbon films after tests in inert and oxidizing environments", Wear, 265, pp 244-254.

107 Feng, Z., Tzeng, Y., Field, J. E., (1992), "Friction of diamond on diamond in ultra-high vacuum and low-pressure environments", Journal of Physics. Division of Applied Physics, pp 1418-1424.

108 Gardos, M. N., (1999), "Tribological fundamentals of polycrystalline diamond films", Surface and Coating Technology, 113, pp 183-200.

109 Zhang, M. Q., Lu, Z. P., Friedrich, K., (1997), "On the wear debris of polyetheretherketone—fractal dimensions in relation to wear mechanisms", Tribology International, 30, pp. 87–102.

110 Schelling, A., Kausch, H. H., Roulin, A. C., (1991), "Friction behaviour of polyetheretherketone under dry reciprocating movement", Wear, 151, pp. 129–142.

111 Suh, N. P., (1977), "An overview of the delamination theory of wear", Wear, 44, pp. 1–16.

112 Godet, M., (1984), "The third-body approach: a mechanical view of wear", Wear, 100, pp. 437–452.

113 Rae, P. J., Brown, E.N., Orler, E. B., (2007), "The mechanical properties of poly(ether-ether-ketone)(PEEK) with emphasis on the large compressive strain response", Polymer, 48, pp 598-615.

114 White, R. L., New, R. M. H., Pease, R. F. W., (1996), "Pattern media: a viable route to 50 Gbites/in^2 for magnetic recording?", IEEE Transactions on Magnetics, vol. 2, pp 990-996.

115 Moser, A., Takano, K., Margulies, D. T., Albrecht, M., Sonobe, Y., Ikeda, Y., Sun, S., Fullerton, E. E., (2002), "Magnetic recording: advancing into the future", Journal of physics. Division: Applied physics, 35, pp157-167.

116 Terris, B. D., Thomson, T., Hu, G., (2007), "Magnetic media for future data storage" Microsystems Technology, 13, pp 189-196.

117 Wachenschwanz, D., Jiang, W., Roddick, E., Homola, A., Dorsey, P., Harper, B., Treves, D., Bajorek, C., (2005), "Design of a manufacturable discrete track recording medium", IEEE Transactions on Magnetics, 41, pp 670-675.

118 Lodder, J. C., (2004), “Methods for preparing patterned media for high-density recording”, Journal of magnetism and magnetic materials, 272-276, part 3, pp 1692-1697.

119 Lee, K.-M, Yeo, C. –D., Polycarpou, A. A., (2007), “Nanomechanical property and nanowear measurements for sub-10-nm thick films in magnetic storage”, Experimental Mechanics, 47, pp 107-121.

120 Greenwood, J. A., Williamson, J. B. P., (1966), “Contact of nominally flat surfaces”, Proceedings Royal Society of London, 295, pp 300–319.

121 Polycarpou, A. A., Etsion, I., (1999), “Analytical approximations in modeling contacting rough surfaces”, ASME Journal of Tribology, 121, pp 234-239.

122 Bhushan, B., (1998), “Contact mechanics of rough surfaces in tribology: multiple asperity contact”, Tribology Letters, 4, pp 1–35.

123 Chang, W. R., Etsion, I., Bogy, D. B., (1987), “An elastic-plastic model for the contact of rough surfaces”, ASME Journal of Tribology, 109, pp 257-263.

124 Ciavarella, M., Greenwood, J. A., Paggi, M., (2008), “Inclusion of interaction in the Greenwood and Williamson contact theory”, Wear, 265, pp 729-734.

125 Timoshenko, S., Goodier, J. N., (1951), “Theory of elasticity”, McGraw-Hill, New York.

126 Bhushan, B., Cook, N. H., (1975), “On the correlation between friction coefficients and adhesion stresses”, ASME Journal of Engineering and Materials Technology, 97, pp 285–287.

127 Eid, H., Adams, G. G., (2007), “An elastic–plastic finite element analysis of interacting asperities in contact with a rigid flat,” Applied Physics, 40, pp 7432–7439